

AN ABSTRACT OF THE DISSERTATION OF

Laxmikant Dhage for the degree of Doctor of Philosophy in Ocean, Earth and Atmospheric Sciences presented on December 17, 2019.

Title: Vertical Coastal Trapped Wave Propagation Produced by a Subsurface Ridge

Abstract approved: _____

Theodore S. Durland

The vertical propagation of Coastal Trapped Waves (CTWs) due to subsurface ridges is explored with the help of linear numerical and analytical models. Results show that submerged ridges projecting from the shoreline can scatter a horizontally propagating single baroclinic mode Kelvin wave into both upward and downward propagating Kelvin wave (KW) beams, emanating from the ridge top. The semi-infinite shelf response to an incident single mode KW reveals alongshore dependence of the vertical structure in the form of multi-modal ridge-top KWs, suggesting that the width (alongshore extent) of the ridge is an important factor in determining the basin response past the ridge. We hypothesize that over narrow ridges (less than twice the Rossby radius of deformation on ridge-top), the trapped solutions at the edges of the ridges overlap and interact to transmit horizontally propagating energy into the surface layer of the downstream basin. At the same time narrow ridges result in a weaker subsurface peak in velocity next to the ridge top in the downstream basin. This decreases the amplitude of vertically propagating KW beams.

The relative strengths of horizontally and vertically propagating KW modes, is explored by imposing the alongshore KW velocity profiles as a boundary condition next to edge of the ridge in the downstream basin. When the strength of the subsurface peaks in the vertical profile of alongshore currents is greater the basin response includes relatively stronger amplitudes of vertically propagating KW beams. On the other hand, when the

strength of the broader surface maximum is greater, the strength of the horizontal propagation of energy at the surface is higher relative to the amplitudes of upward propagating KW beams in the downstream basin.

The west coast of India near Kollam has a shelf-slope width comparable to that of the first mode Rossby radius of deformation, and vertical propagation of intraseasonal coastal trapped waves (CTWs) has been observed downstream of this ridge. To check the applicability of the KW experiments to such a situation, the numerical model was configured with a sloping coastal bottom similar to that found along the west coast of India, and an offshore ridge similar to the one used in the KW experiments. A first-mode CTW was imposed as the incident wave. The generation by the ridge of upward propagation was similar to that seen in the KW models. Close to the coast, however, the downward propagating beam quickly reflects from the sloping bottom into an upward propagating beam.

The effects demonstrated in these idealized experiments are likely to be found wherever KW or CTW propagation is important and the alongshore coastal bathymetry contains large changes in depth over short distances.

©Copyright by Laxmikant Dhage
December 17, 2019
All Rights Reserved

Vertical Coastal Trapped Wave Propagation Produced by a
Subsurface Ridge

by

Laxmikant Dhage

A DISSERTATION

submitted to

Oregon State University

in partial fulfillment of
the requirements for the
degree of

Doctor of Philosophy

Presented December 17, 2019
Commencement June 2020

Doctor of Philosophy dissertation of Laxmikant Dhage presented on December 17, 2019.

APPROVED:

Major Professor, representing Ocean, Earth and Atmospheric Sciences

Dean of the College of Earth Ocean and Atmospheric Sciences

Dean of the Graduate School

I understand that my dissertation will become part of the permanent collection of Oregon State University libraries. My signature below authorizes release of my dissertation to any reader upon request.

Laxmikant Dhage, Author

ACKNOWLEDGEMENTS

First and foremost, I would like to express sincere thanks to my adviser Ted Durland. Being an international student from a non-native English speaking country, it was difficult in the beginning but his assistance and guidance helped me through. He was supportive even during my difficult times of health and had an understanding of my family responsibilities and commitments. Secondly, I would like to thank my second adviser Ted Strub without whom this work would have never come together. He has been far more than an adviser, providing help, directions and guidance even at the personal level. I would also like to thank the other members of my committee Roger and Emily, who read the thesis and provided feedback on the work. A large thank you goes to Vincent Combes who helped me in setting up the numerical models and was available whenever I needed an assistance. Lastly, a bucket of thanks goes to my parents and my family members for being patient and providing me constant support and motivation. Special thanks to my wife Snehal and my daughter Sakshi, it would have not been possible without them.

TABLE OF CONTENTS

	<u>Page</u>
1 Introduction	1
2 Intra-seasonal sea level variability along the West coast of India	10
2.1 Introduction	10
2.2 DATA AND METHODS	12
2.2.1 Creation of Spatially Averaged Time Series	13
2.2.2 Lagged Correlations and Coherences	14
2.2.3 Regression Model	15
2.3 Results	15
2.3.1 The Intra-Seasonal Time Series	15
2.3.2 Lagged Correlation Analysis	16
2.3.3 Regression Model	18
2.3.4 Coherence and Phase Analysis	20
2.3.5 Hovmöller Diagrams	22
2.4 Discussion	24
2.5 CONCLUSION	27
3 Vertical Kelvin wave propagation produced by a subsurface ridge	44
3.1 Introduction	44
3.2 Analytical Approximation	47
3.2.1 Horizontal energy flux balances	49
3.2.2 Vertical mode projections	50
3.2.3 Limitations of the approximate solution	52
3.3 Numerical Model	53
3.4 Results	55
3.4.1 Response of a shallow shelf to an incident 1st mode Kelvin wave	55
3.4.2 Basin response downstream of a finite width ridge	56
3.5 Discussion	59
3.5.1 Alongshore Velocity in the downstream basin	60
3.5.2 Analytical Kelvin wave Current Boundary Conditions	61
3.5.3 Ridge waves: Wave D	62
3.5.4 Finite Ridges	63
3.6 Summary	64

TABLE OF CONTENTS (Continued)

	<u>Page</u>
4 Vertical propagation case of Coastal Trapped Waves	85
4.1 Introduction	85
4.2 Methods	86
4.2.1 Brink and Chapman Coastal wave program routines	86
4.2.2 Obtaining a clean CTW mode 1 to force the Numerical Model . .	88
4.2.3 Numerical Model	89
4.3 Results	90
4.3.1 CTW Model Run	91
4.3.2 KW Model Run	91
4.3.3 Comparison between CTW and KW model run amplitudes	92
4.4 Discussion	93
4.5 Conclusion	93
5 Conclusions	121
5.1 Summary of Chapter 2	121
5.2 Summary of Chapter 3	123
5.3 Summary of Chapter 4	124
Appendices	125
A Meridional Energy Flux Near an Eastern Boundary Within the Turning Latitudes of an Equatorial Basin	127
B Computation of N^*	152

LIST OF FIGURES

<u>Figure</u>	<u>Page</u>
1.1 A Figure in Amol et al. (2014), showing the bathymetry and locations of ADCP moorings along the west coast of India, with an addition of a schematic representing the seasonally varying monsoon current	5
1.2 Panel a) First 3 vertical modes derived from a typical stratification along the west coast of India; A Figure from Nethery and Shankar (2007): (from middle) Panel b) Monsoon Current south of Sri-Lanka with depth; Panel c) Alongshore velocity along the wall (at $x=0$, modelled as the west coast of India) at two different periods of forcing ($T = 30$ days and $T = 360$ days)	6
1.3 Figure-7 of Amol et al. (2014), showing the alongshore currents at Kollam mooring, demonstrating vertical propagation of energy in both directions, vertically up and down.	7
1.4 Schematic of an analytical model showing different regions to simplify the independent solutions. Region 1) Incident single mode baroclinic Kelvin Wave; region 2) basin response with the scattered Basin modes; region 3) topographic modes along the ridge away from the coastline; region 4) the region of adjustment close to the wall and the ridge, where transfer of energy from incident Kelvin wave takes place.	8
2.1 Basin-wide schematic of Oceanic wave propagation in the Northern Indian Ocean; Box H1 represents the region of interest	29
2.2 Sea Surface Height Boxes (in blue); Wind Boxes (in red); Open black arrows show the sub-boxes separated by dashed blue lines, representing respective coastal orientations within boxes TA3, TA4 and TA5.	30
2.3 H1 SLA Time-series; Top: Raw SLA overlapped on the seasonal cycle and trend in the dashed line; Middle: Seasonal Cycle and trend Removed; Bottom: Intra-seasonal 120 day high passed.	31
2.4 Power Spectrum of Normalized H3 and Normalized TA3; Vertical red lines represent the 90 % Confidence Interval (CI) for the peaks in Power Spectrum Density (PSD) plots to be significant; Red encirclement shows the significant coincident peak between 40-50 days in winds at TA3 and SLA at H3.	32

LIST OF FIGURES (Continued)

<u>Figure</u>	<u>Page</u>
2.5 Correlation of H1 SLA with: a) Coastal Stations H1, H2, H3 and H6 as well as H4 b) Rossby Wave Stations H4, H7 and H-Eq; Negative lag means H1 lags; Horizontal lines in respective colors represent the 95 % significant level for the correlations to be significant.	33
2.6 Correlation of H-Eq SLA with SLA at other stations; positive lag means H-Eq leads; Horizontal lines in respective colors represent the 95 % significant level for the correlations to be significant.	34
2.7 Correlation of H1 SLA with alongshore Wind Stress at different locations; Negative lag means H1 lags. Horizontal lines in respective colors represent the 95 % significant level for the correlations to be significant.	35
2.8 Regression Model for Hind-casting SLA at H1; Input Parameters : TA3, H4, H6, TA1	36
2.9 (Top Panel) Coherence and phase plots between SLA at H1 and along shore wind stress at TA1(a) and TA3(b); (Bottom Panel) Coherence and phase plots between H1 and TA12(c) and TA3 and TA1 (d). The dashed red line for the coherence and the red circles for the phase represent 95% significance levels. Black, Green and magenta lines represent corresponding values of phases and periods for a constant lag of 2 days, 6 days and 12 days respectively.	37
2.10 Correlation of SLA at H1 with alongshore Wind Stress at different locations with 40-60 day band pass filtered data; positive lag means H1 leads. Horizontal lines in respective colors represent the 95 % significant level for the correlations to be significant.	38
2.11 Boxes X4-X8 represent a Rossby wave path way and Boxes H1-X2-X3-X4-Y5-Y6-Y7 represent the pathway for a coastal trapped signal coming from the east coast of India.	39
2.12 Hovmöller plot from AVISO SLA(cm); H1-X2-X3 are on the west coast of India; X4-X8 are the Rossby pathway boxes; where as Y5-Y7 are the East Coast Pathway.	40

LIST OF FIGURES (Continued)

<u>Figure</u>	<u>Page</u>
2.13 Hovmöller plots of 40-60 day band pass filtered AVISO SLA, as in Figure 2.12, expanded to get an approximate estimate of the propagation speeds of the signals: a) Boxes H1-X2-X3 on the west coast for the year 2002 ; b) Boxes X4-X8 on the Rossby wave pathway for the year 2003.	41
2.14 ROMS model domain and Correlations: 1) On the left: ROMS model domain; horizontal arrows indicate the large scale wind forcing schematic. The black boxes are chosen with same sizes as in the altimeter analysis in order to compare the correlations of SLA at H1 with SLA at H3, H4 and H6. TA3 represents the wind forcing. 2) on the right: Lagged correlation of SLA at H1 with SLA at H3, H4, H6 and Wind Stress at TA3. The corresponding lags at maximum correlations are similar to what we expected from regression models and coherence analysis: (H1 vs H3: -1 day; H1 vs H4: -4 days; H1 vs TA3: -6 days)	42
3.1 Schematic of a coastal Kelvin wave in a basin of depth H_b incident upon a semi-infinite ridge of depth H_r	66
3.2 Panel a) and b) Show the bathymetry of a semi-infinite Shelf KW model including the terrain-following ROMS sigma-grid levels converging on ridge-top (coming from deep basin). Panel c) shows a snapshot of alongshore currents model run in YZ cross-section at wall.	67
3.3 I) ROMS solution for amplitude (a) and phase (b) for a 30-day Kelvin wave incident upon a semi-infinite shelf. II) Approximate solution for amplitude (a panel) and phase (b panel).	68
3.4 a) Bathymetry for a 200 km width ridge model run; b) Bathymetry for a 600 km width ridge model run. Top panel is in XY cross-section, whereas bottom panel is in YZ cross-section.	69
3.5 I) ROMS solution for amplitude (a) and phase (b) for a 30-day Kelvin wave incident upon a 600 km wide ridge. II) Approximate solution for amplitude (a panel) and phase (b panel).	70
3.6 I) ROMS solution for amplitude (a) and phase (b) for a 30-day Kelvin wave incident upon a 200 km wide ridge. II) Approximate solution for amplitude (a panel) and phase (b panel).	71

LIST OF FIGURES (Continued)

<u>Figure</u>	<u>Page</u>
3.7 I) ROMS solution for amplitude (a) and phase (b) for a 30-day Kelvin wave incident upon a 120 km wide ridge. II) Approximate solution for amplitude (a panel) and phase (b panel).	72
3.8 ROMS and Analytical approximate velocity amplitude solution for a 30-day Kelvin wave incident upon : I) 600 km wide ridge; II) 200 km wide ridge. The black dotted lines correspond to the transects in Z where the basin boundary currents are extracted for analytical and ROMS solutions.	73
3.9 Approximate analytical and ROMS velocity amplitudes for a 30 day period basin currents next to the (one grid-point) edge of the ridge at $y = Y_2$. . .	74
3.10 Figure: a) Amplitude and b) Phase for alongshore currents with a subsurface bottom currents above the forcing as a KW boundary condition next to the edge of the ridge; c) Time-series plot of vertical profiles of alongshore currents at $Y = 300$ km and wall ($X=0$).	75
3.11 Figure: a) Amplitude and b) Phase for alongshore currents with a weaker subsurface bottom current above the forcing as a KW boundary condition next to the edge of the ridge; c) Time-series plot of vertical profiles of alongshore currents at $Y = 300$ km and wall ($X=0$).	76
3.12 Figure: a) Amplitude and b) Phase for alongshore currents with a strong surface currents above the forcing as a boundary condition next to the edge of the ridge into the basin; c) Time-series plot of vertical profiles of alongshore currents at $Y = 300$ km and wall ($X=0$).	77
3.13 Figure: a) Amplitude and b) Phase for alongshore currents with stronger surface current and a weaker bottom subsurface current above the forcing as a KW Boundary Condition (B.C.); c) Time-series plot of vertical profiles of alongshore currents at $Y = 300$ km and wall ($X=0$).	78
3.14 Figure: a) Amplitude and b) Phase for alongshore currents with weaker surface current and a stronger bottom surface current above the forcing as a KW Boundary Condition (B.C.); c) Time-series plot of vertical profiles of alongshore currents at $Y = 300$ km and wall ($X=0$).	79

LIST OF FIGURES (Continued)

<u>Figure</u>	<u>Page</u>
3.15 Figure: a) Amplitude and b) Phase for alongshore currents corresponding to a 200 km wide ridge ROMS solution next to the downstream edge of the ridge as a Boundary Condition (B.C.); c) Time-series plot of vertical profiles of alongshore currents at $Y = 300$ km and wall ($X=0$).	80
3.16 Figure: a) Amplitude and b) Phase for alongshore currents corresponding to a 600 km wide ridge ROMS solution next to the downstream edge of the ridge as a Boundary Condition (B.C.); c) Time-series plot of vertical profiles of alongshore currents at $Y = 300$ km and wall ($X=0$).	81
3.17 Amplitude (a : downstream of the ridge; b : upstream of the ridge) and phase (c : upstream of the ridge) of wave D currents, along the the submerged ridge.	82
3.18 Bathymetry of a 600 km wide and 160 km long Ridge	83
3.19 Figure: a) Amplitude and Phase for alongshore currents at wall for a 30 day sinusoid for finite 600 km wide and 160 km long ridge; b) Amplitude and Phase for alongshore currents for a fully extended 600 km wide ridge (same as Fig 3.5 velocity instead of pressure)	84
4.1 Cross-shore Bathymetry along the west cost of India, showing different slopes along path A, B and C; represented by A (red), B (blue) and C (green) in the figure to the right. The downward black arrow shows the Kollam morring Depth (KMD). Two different slopes in black, one with coastal decay and one on top of the ridge ($Y=3000$ km) in the CTW model domain are plotted on top.	95
4.2 Bathymetry along the west coast of India. Black lines represent the off-shore path for Station 1, 2, 3 and 4, located on the coastline.	96
4.3 The bottom topography of the cross-shore paths starting from Station 1, 2, 3 and 4. Δ_x represents the shelf-slope width at each of these locations.	97
4.4 Pressure structures of eigen mode 1 in arbitrary units at Station 1. ($C1=285$ cm/s), $S = 0.26$	98
4.5 Pressure structures of eigen mode 1 in arbitrary units at Station 2. ($C1=289.82$ cm/s), $S = 0.25$	99

LIST OF FIGURES (Continued)

<u>Figure</u>	<u>Page</u>
4.6 Pressure structures of eigen mode 1 in arbitrary units at Station 3. (C1=285 cm/s), $S = 0.41$	100
4.7 Pressure structures of eigen mode 1 in arbitrary units at Station 4. (C1=286 cm/s), $S = 0.29$	101
4.8 Dispersion curve for mode 1 CTW eigen structure along the path of Station 3.	102
4.9 The velocity structure of mode 1 CTW obtained from Brink and Chapman solution for a typical slope along the west coast of India.	103
4.10 The velocity structure of mode 1 CTW after eliminating the off-shore discrepancies of the Brink and Chapman solution for a steep slope bathymetry. The obtained modal structure is not perfect and contains the contamination from higher modes, although, with low amplitudes.	104
4.11 Bathymetry and slope along the west coast of India.	105
4.12 Snapshots of alongshore currents for the contaminated mode 1 CTW, at a 450 m deep off-shore transect in YZ at $t = 148$ days; $t = 142$ days; $t = 136$ days.	106
4.13 Snapshots of alongshore currents for the clean mode 1 CTW, at a 450 m deep off-shore transect in YZ (from left to right) at $t = 136$ days; $t = 142$ days; $t = 148$ days.	107
4.14 Right panel : The velocity structure of clean mode 1 CTW after eliminating all the contamination from higher modes, for a typical slope along the west coast of India. Left Panel: Same as Figure 4.10.	108
4.15 Figure to the left shows a bathymetry of the CTW domain with a 200 km wide and 80 km long ridge. The Figure to the right shows the coastal decay slope overlapped on top of ridge slope at $y = 3000$ kms.	109
4.16 a) The cross-shore amplitude structure of alongshore current boundary forcing for a clean mode 1 CTW b) The CTW model output in terms of Amplitude and Phase for alongshore currents (V) at Kollam Mooring Depth (KMD) in Y-Z cross-section. T represents the time period (30 days), used to extract the sinusoidal Amplitude and Phase	110

LIST OF FIGURES (Continued)

<u>Figure</u>	<u>Page</u>
4.17 a) Bathymetry of KW domain with a 200 km wide and 80 km long ridge b) The cross-shore amplitude structure of alongshore current boundary forcing for a mode 1 KW c) KW model output in terms of Amplitude and Phase for alongshore currents (V) at wall. T represents the time period (30 days), used to extract the sinusoidal Amplitude and Phase	111
4.18 The amplitude of alongshore current boundary forcing for CTW and KW domain is plotted with a unit amplitude normalization for the maximum amplitude.	112
4.19 The surface amplitude decay of alongshore current boundary forcing for CTW and KW mode 1.	113
4.20 Comparison of alongshore currents 30 day period Amplitude for a) KW model run b) CTW model run	114
4.21 Bathymetry of a 50 km long and 200 km wide Ridge	115
4.22 Bathymetry of a 50 km long and 100 km wide Ridge	116
4.23 Bathymetry of a 50 km long and 40 km wide Ridge	117
4.24 ROMS Amplitude and Phase of alongshore currents at a certain depth off-shore transect in YZ for a 50 km long and 200 km wide Ridge. Black Arrow show the direction of phase propagation	118
4.25 ROMS Amplitude and Phase of alongshore currents at a certain depth off-shore transect in YZ for a 50 km long and 100 km wide Ridge. Black Arrow show the direction of phase propagation.	119
4.26 ROMS Amplitude and Phase of alongshore currents at a certain depth off-shore transect in YZ for a 50 km long and 40 km wide Ridge. Black Arrow show the direction of phase propagation.	120

Chapter 1: Introduction

Understanding the coastal circulation along the west coast of India is important because of the highly productive fisheries in the region (Bakun et al. 1998; Gopalakrishna et al. 2008; Manjusha et al. 2013). Both modeling and observational studies indicate that the West India Coastal Circulation (WICC) is substantially influenced by remote forcing over a wide range of time-scales, with coastal signals propagating poleward from the southern tip of Sri Lanka at roughly the Kelvin wave speeds associated with the lowest two baroclinic modes (McCreary et al. 1993; Shankar and Shetye 1997; Shankar 2000; Shankar et al. 2002; Vialard et al. 2009; Rao et al. 2010; Amol et al. 2012). More recently, a modelling study by Suresh et al. (2016) elucidated the importance of wind forcing south of India and Sri-Lanka for the WICC, signifying the importance of Coastal Trapped Waves (CTWs) generated by distant forcing. At seasonal and longer time scales the coastal signals can radiate off-shore as Rossby waves, affecting, for instance, the seasonally oscillating Lakshadweep High and Low, as well as other circulation patterns of the Arabian Sea (Shankar and Shetye, 1997). The shorter time scale coastal signals in the intra-seasonal band, however, can be completely trapped along the coast.

In Chapter 2 we investigate the importance of different forcing factors, remote versus local, for the sea level variability in the intra-seasonal band of periods (30-120 days). The analysis uses 10 years of satellite altimeter data along with model and scatterometer winds. The dominant period of frequencies associated with these intra-seasonal oscillations is also deduced for the maximum variance. This research plays an important role in selecting the period of forcing used to analyse the coastal dynamics along the west coast of India in subsequent chapters.

Chapter 3 examines a possible source of vertical propagation within the CTWs along the west coast of India. Using a semi-analytic formulation, Nethery and Shankar (2007) predicted the possibility of downward propagating Kelvin wave energy on the west coast of India, forced by variability in the zonally flowing monsoon current south of Sri-Lanka [Figure 1.1]. They modeled the west coast of India as a straight meridional barrier extending equatorward to 5° N (the latitude of the southern tip of Sri Lanka). At the

tip of the barrier they imposed a zonal current with a meridional and vertical structure similar to that of the monsoon current, and the contact of this current with the boundary generated a Kelvin wave propagating poleward on the western side of the barrier. The vertical structure of the monsoon current doesn't match with a single baroclinic mode in the unforced, quiescent basin, leading to excitation of multiple vertical modes and resultant vertical energy propagation of the freely propagating Kelvin wave [Figure 1.2].

The National Institute of Oceanography (NIO) at Goa has Acoustic Doppler Current Profiler (ADCP) moorings at several locations along the west coast of India [Figure 1.1]. Amol et al. (2014) analyzed the data from these moorings and supported the prediction of Nethery and Shankar (2007), showing evidence of downward propagating Kelvin beams. Moreover, observations of an upward vertical propagation of energy can also be witnessed in the alongshore current profiles of the Kollam mooring, which sits at the edge of ridge-like structure near the south west tip of India [Figure 1.3]. Although the vertical propagation of energy shown in Figure 1.3 is for the band of 100-250 days, a similar upward and downward propagation of energy can be observed for other bands of frequencies, including the intra-seasonal band. The forcing mechanism for the observed upward vertical propagation of energy, however, has not been thoroughly explored.

Given the significance of coastal circulation along the west coast of India and the impact on the WICC of remotely forced CTWs, along with their observed bi-directional vertical propagation of energy, it is important to understand the dynamics and physics behind this phenomenon and quantify its affect on the vertical structure of the currents. In chapter 3 we investigate the generation of bi-directional vertically propagating Kelvin beams using idealized models in a continuously stratified ocean configured to shed light on the observations of Amol et al. (2014).

We propose that the observed upward, and perhaps the downward vertical propagation of Kelvin wave energy observed on the west coast of India is due to the scattering of a low baroclinic mode Kelvin wave incident upon a sudden change in the bottom topography. A number of past studies have addressed the interaction of Kelvin or coastal-trapped waves with bottom topography, but many of these involved a homogenous ocean (e.g., Longuet-Higgins 1968; Killworth 1989a; ER Johnson 1990, ER Johnson 1993), which does not support vertical propagation. (Killworth, 1989b) studied the effect of a submerged ridge on a Kelvin wave in a two-layer baroclinic ocean, but this model cannot represent well the vertical propagation in a continuously stratified basin. Wilkin and Chapman (1987)

presented an analytic solution for the scattering of a coastal trapped wave by variations in the shelf width in a barotropic ocean. Wilkin and Chapman (1990) supplemented this with numerical solutions for a stratified ocean but did not address bottom irregularities or vertical propagation of the scattered waves. Generation of internal tides by the interaction of the barotropic tide with bottom topography is a problem that has been studied extensively (e.g., Baines 1973; Baines 1982; Holloway and Merrifield 1999) and provides a useful analogy to the vertical aspect of our problem. The dynamics are not identical, though, and the internal tide generation mechanism does not answer all the questions that arise in the Kelvin wave problem.

As a first simplifying step, we configured the Regional Ocean Modeling System (ROMS) model with a subsurface ridge of “semi-infinite” extent: a ridge that spans the entire model basin combined with a sponge layer to absorb the cross-shore signals traveling along the ridge. The vertical coastal boundary supports Kelvin waves, but because of ROMS requirements, the sides of the subsurface ridge are sloping and instead support topographic ridge waves. The above configuration allows us to separately define the topographic wave response and the Kelvin mode response to propagation directly over the ridge. In the case of the semi-infinite ridge, topographic waves cannot reach or affect the downstream basin. Chapter 3 contains numerical results of a series of such semi-infinite ridge model runs and their comparison with approximate analytical solutions. Semi-infinite submerged ridges simplify the dynamics and allow an examination of the problem through the analytical approximations. In nature, however, the bathymetry is always more complex and hard to model analytically. The submerged ridges are finite in length, and the basin response past the ridge contains the contribution from topographic ridge waves traveling along and around the ridge. Numerical solutions for finite-length ridges are compared with those for the semi-infinite ridges.

Chapter 4 analyzes the vertical propagation of energy by modeling the west coast of India with a sloping bottom. This is preliminary work done to assess how a more realistic sloping coastal boundary would affect the solutions in Chapter 3. The ROMS model is run for a finite submerged ridge on a sloping bottom bathymetry, typical of the west coast of India, with an incoming single mode 1 CTW from the southern boundary. The Chapter includes comparisons between various finite ridge numerical model runs, mainly: 1) on a sloping bottom incoming mode 1 CTW 2) on a flat bottom incoming mode 1 Kelvin wave.

For the given slope and stratification, the first mode baroclinic CTW eigen solution is computed using the Brink and Chapman coastal trapped wave routines (http://www.whoi.edu/cms/files/Fortran_30425.htm). The CTW solution for a typical slope along the west coast of India was hard to obtain, as the shelf-slope width is very small compared to the first internal Rossby radius of deformation, and the Brink and Chapman routines do not work very well in those scenarios. The correct solution was obtained by forcing the model without a ridge with the contaminated first baroclinic CTW mode and letting it run for a long distance. The first baroclinic mode has the highest phase speed, and with time it leaves behind the lower modes to obtain a clean first mode.

Chapter 5 summarizes the conclusions from Chapters 2, 3 and 5. Appendix A of the thesis does not necessarily relate to the core of the PhD research work. It is in the form of a term paper based on Durland et al., 2014 AGU poster. This work shifts the focus on equatorial dynamics to better understand the process of transfer of energy (within the turning latitudes of equatorial basin) from equatorial trapped KWs (equator-ward of turning latitude) to the meridional CTWs (pole-ward of turning latitude) when the equatorial trapped KWs reflect back from an eastern meridional boundary.

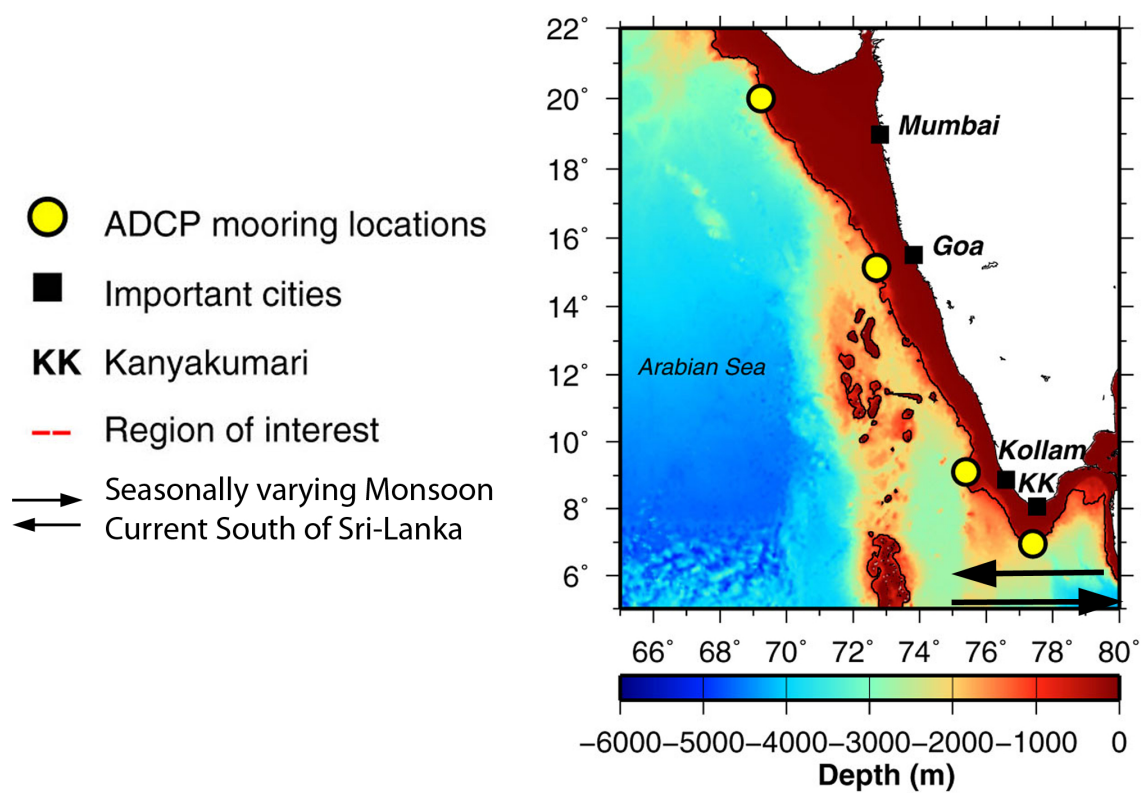


Figure 1.1: A Figure in Amol et al. (2014), showing the bathymetry and locations of ADCP moorings along the west coast of India, with an addition of a schematic representing the seasonally varying monsoon current

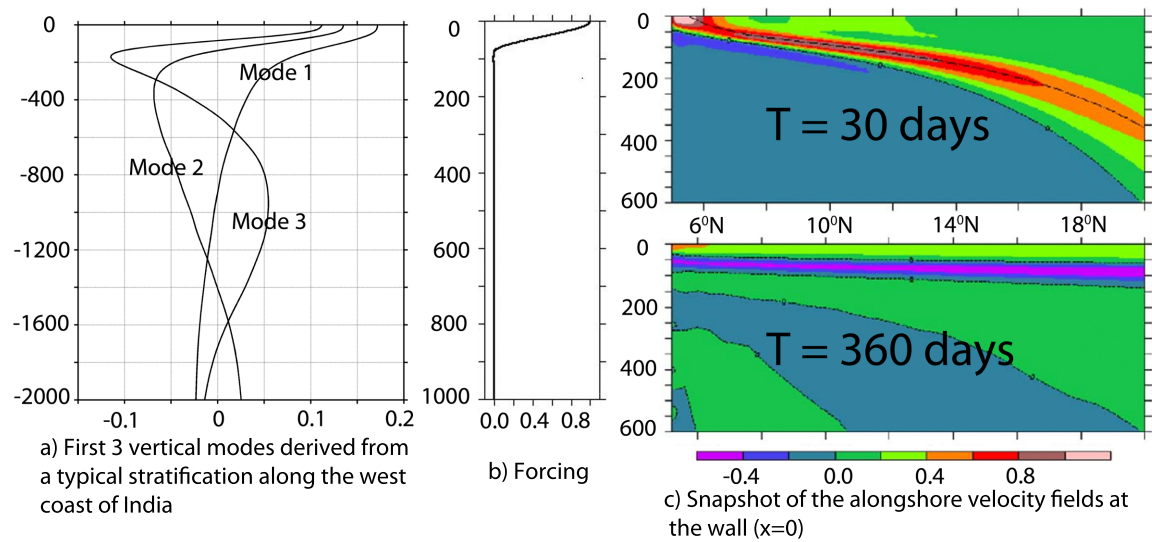


Figure 1.2: Panel a) First 3 vertical modes derived from a typical stratification along the west coast of India; A Figure from Nethery and Shankar (2007): (from middle) Panel b) Monsoon Current south of Sri-Lanka with depth; Panel c) Alongshore velocity along the wall (at $x=0$, modelled as the west coast of India) at two different periods of forcing ($T = 30$ days and $T = 360$ days)

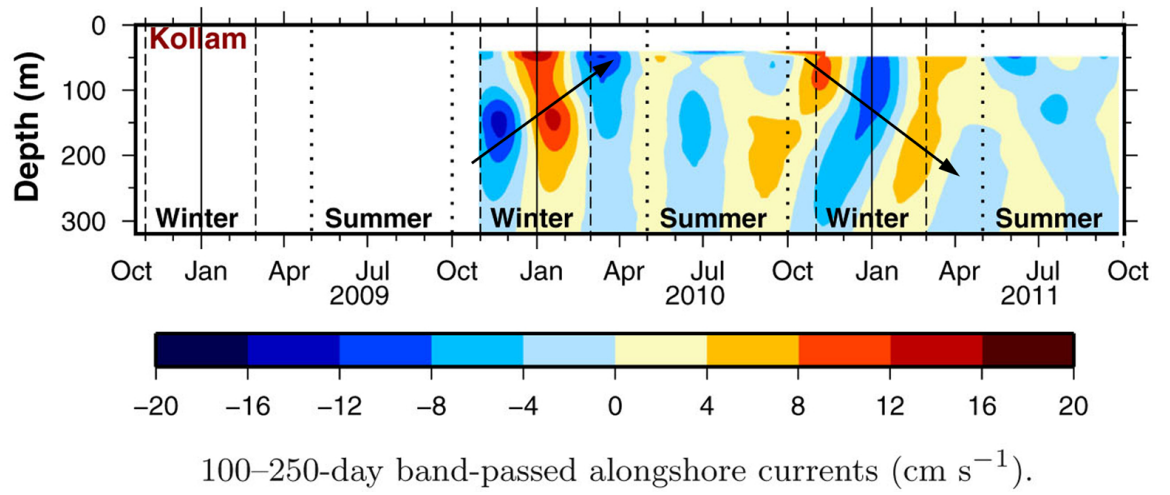


Figure 1.3: Figure-7 of Amol et al. (2014), showing the alongshore currents at Kollam mooring, demonstrating vertical propagation of energy in both directions, vertically up and down.

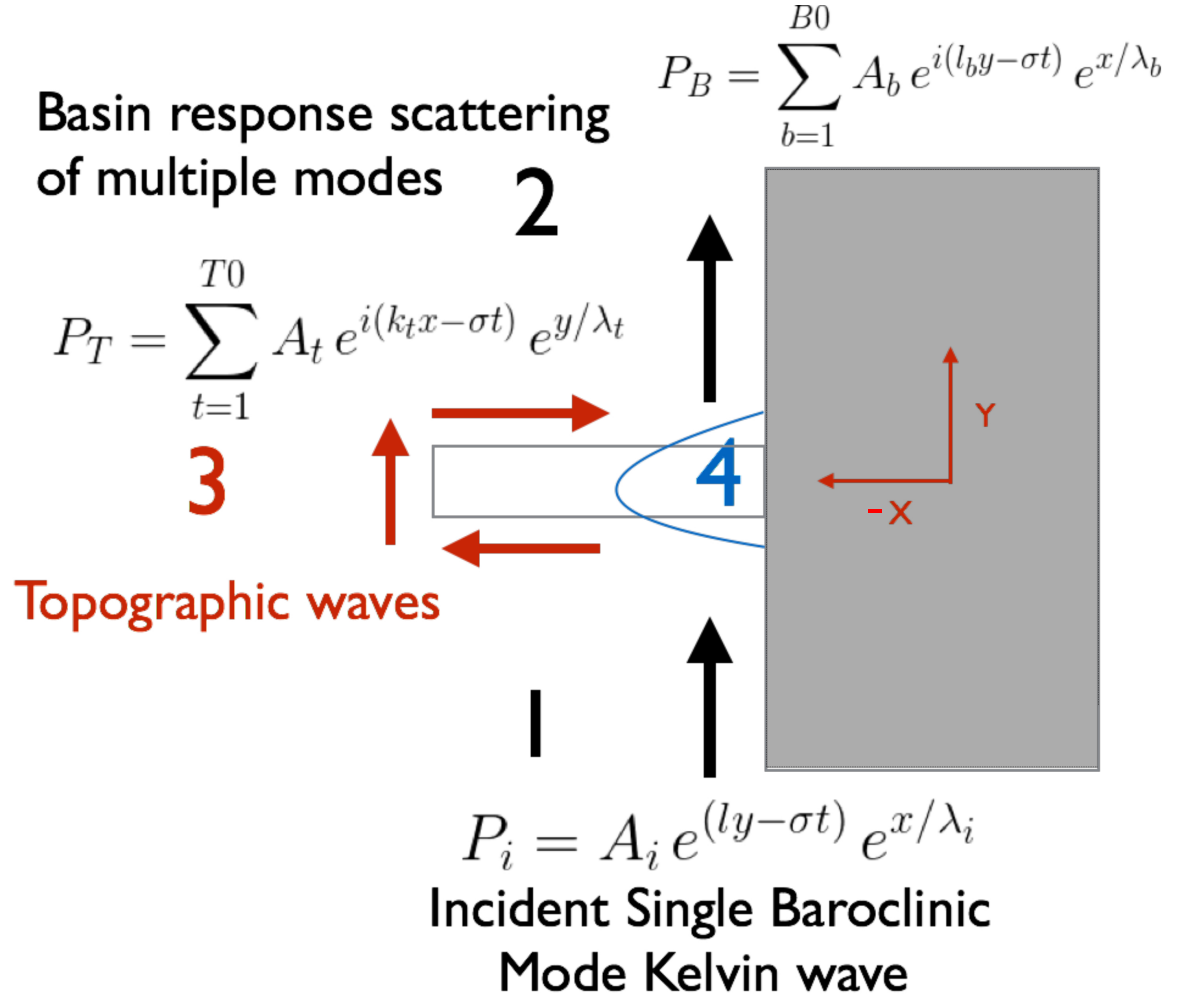


Figure 1.4: Schematic of an analytical model showing different regions to simplify the independent solutions. Region 1) Incident single mode baroclinic Kelvin Wave; region 2) basin response with the scattered Basin modes; region 3) topographic modes along the ridge away from the coastline; region 4) the region of adjustment close to the wall and the ridge, where transfer of energy from incident Kelvin wave takes place.

Intra-seasonal sea level variability along the West coast of India

Laxmikant Dhage and P. Ted Strub

Journal of Geophysical Research, Oceans

Vol. 121 (11), 8172-8188, 2016.

<https://doi.org/10.1002/2016JC011904>

Chapter 2: Intra-seasonal sea level variability along the West coast of India

2.1 Introduction

Over the past twenty years, progress has been made in defining the circulation on seasonal time scale along the east and west coasts of India, as well as in the Bay of Bengal (BOB)-that part of Indian Ocean directly east of the Indian sub-continent. We refer to the coastal currents as the East India Coastal Current (EICC) and the West India Coastal Current (WICC). This progress has been accomplished through traditional oceanographic hydrographic cruises [Shetye et al., 1990; Shetye et al., 1991; Shetye et al., 1996], analytic and numerical modeling studies [McCreary et al. 1996; Shankar and Shetye 1997; McCreary et al. 1993] and (more recently) the use of satellite altimeter data [Babu et al. 2003; Durand et al. 2009; Vialard et al. 2009; Shenoi 2010; Rao et al. 2010]. Recent modelling work by Suresh et al. (2016) has showed the importance of distant remote-wind forcing from east of Sri-Lanka as a major driving factor for sea level variations along the west coast of India, again on seasonal time scales. In addition to the wind forcing, an important aspect of the Indian Ocean is the degree to which equatorial motions impact coastal circulation via Coastal Trapped Waves (CTWs), generated where the Equator meets the eastern boundary (McCreary et al., 1996).

Sea level variability serves as an indicator of upwelling and downwelling along the west coast of India and is of particular interest because the region supports an important fisheries, with increased productivity during upwelling periods (Gopalakrishna et al., 2008). The sea level along the west coast, in direct relation to the WICC in particular has significant intra-seasonal variability (Vialard et al., 2009). In contrast to the more thoroughly studied seasonal variability, the coastal circulation on these shorter time scales is only now being addressed [Amol et al. 2014; Amol et al. 2012; Suresh et al. 2013; Girishkumar et al. 2013].

Recent studies provide evidence for the importance of intra-seasonal variability in the coastal circulation [Durand et al. 2009; Suresh et al. 2013; Vialard et al. 2009; Amol

et al. 2012; Girishkumar et al. 2013; Amol et al. 2014]. Durand et al., 2009 quantify the importance of the intra-seasonal variability of currents and sea level along the coasts of India, superimposed on the seasonal cycle, with the use of along-track satellite data . The National Institute of Oceanography (NIO) at Goa has deployed Acoustic Doppler Current Profiler (ADCP) moorings at several locations along the east and west coast of India. Amol et al. (2012) use data from these ADCP moorings to elicit the propagation of CTWs along the west coast of India although the emphasis is on periods shorter than the 30 days cut-off in our analysis. In addition, Amol et al. (2014) show evidence for vertical propagation of energy at intra-seasonal periods from the tip of India and Sri-Lanka along the west coast of India. This vertical propagation reduces correlations in surface signals along this path. In the present work we extend the previous analysis of local and more remote connections through altimeter derived Sea Level Anomalies(SLAs), quantifying the decrease in correlations along this pathway.

Vialard et al. (2009) showed that intra-seasonal variability along the west coast of India is a part of a basin scale phenomenon. The magnitude of alongshore wind stress is maximum at the tip of India and Sri-Lanka, which induces two opposite SLA signals, one at the Equator and one at the tip of India, with a potential to influence the intra-seasonal SLA variability along the west coast of India [ibid.; Webber et al. 2010]. The SLA signal at the Equator propagates to Sumatra in the form of an equatorial Kelvin wave and then reflects back westward across BoB as a Rossby wave and northward around the BoB as a CTW going north along the coastal wave-guide of the BoB in the northern Indian ocean. Vialard et al. (2009) and Webber et al. (2010) show that the Rossby wave signal interacts with the CTWs from the east coast of India and is also reinforced by favourable winds when it reaches the tip of Sri-Lanka. It is clear that the Rossby wave signal reaches the tip of Sri-Lanka. However the significance of its contribution to the intra-seasonal SLA variations in the northern Indian ocean is not thoroughly understood.

Modelling work by Suresh et al. (2013), suggests that most of the intra-seasonal sea level variability in the northern Indian Ocean originates along the equator via equatorially and coastally-trapped waves. In their model, the percentage of intra-seasonal variability attributable to an equatorially generated signal is 80-90% along the north-east coast of the BoB, decreases to 50% north-east of Sri-Lanka along the wave guide next to south-east India, and then increases to 60-70% along the west coast of India, for reasons not fully understood. We provide evidence that the source for this increase in energy

is from Rossby waves incident upon the south-east tip of Sri-Lanka, generated in the south-central or eastern boundary of the BoB. Both the incoming Rossby waves and the alongshore winds can generate CTWs that propagate up the west coast of India, and the two generation mechanisms can interact constructively or destructively with each other and with CTWs propagating down the east coast of India. The net result is that SLA variability along the Indian west coast can be influenced by remote forcing via multiple wave pathways [Fig 2.1].

Our work aims to understand the contributions of the various forcing factors and pathways to the intra-seasonal Sea Surface Height (SSH) variability on the west coast of India. This is investigated using correlations of altimeter SLAs and European Centre for Medium-Range Weather Forecasts (ECMWF) winds at various key locations and by building a multivariate regression model to identify the forcing mechanisms that explain the greatest amount of the intra-seasonal variability of SLA along the west coast of India. Correlations are then extended to analyse the frequency dependent coherences and corresponding phases, identifying the importance of a narrower band in which the winds are most strongly correlated with intra-seasonal SLA. Finally, Hovmöller diagrams are used to illustrate the large-scale propagation of oceanic signals.

2.2 DATA AND METHODS

The primary data sets used are 10 years (October 1999 to November 2009) of altimeter sea level anomaly fields (SLA, also referred to as sea surface height anomaly, SSHA) from the Archiving, Validation and Interpretation of Satellite Oceanographic data project (AVISO), and coincident alongshore wind stress derived from surface wind velocities over the ocean from ECMWF. Both types of data are gridded with spatial separation of 0.25×0.25 degrees between grid points, at daily time steps. The use of this ten-year period allows us to check the results of wind forcing with the winds from QuikSCAT scatterometer. This period also has the best coverage by multiple altimeters. The satellite sampling and AVISO optimal interpolation apparently attenuate periods shorter than a few weeks (DB Chelton et al., 2011). We accordingly low pass filter the ECMWF winds with a cosine-squared weight function that has a cut-off period of 30 days and is centered on the AVISO time grid. The means, trends and seasonal cycles (annual cycle plus first three harmonics) are removed from both data sets prior to a 120-day high pass filter,

retaining intra-seasonal periods of approximately 30-120 days. Our processing ensures that both AVISO SLA and ECMWF winds have the same timing and similar frequency roll-offs.

2.2.1 Creation of Spatially Averaged Time Series

Both SLA and surface wind data were averaged over the rectangular areas shown in Fig 2.2, to create the time series used in our analyses. Three boxes for SLA are located over the continental slope along the Indian west coast (H1-H3), with another (H6, centered at $\sim 10.5^\circ\text{N}$) over the slope along the Indian southeast coast. H1 is centered at $\sim 13^\circ\text{N}$ (100-200 km south of Goa), and our primary interest is to predict SLA variability at this location. Boxes H1, H2 ($\sim 10^\circ\text{N}$) and H3 ($\sim 7.5^\circ\text{N}$) are chosen such that they are under the “reference” altimeter tracks on the west coast of India (those occupied by TOPEX/Poseidon, Jason-1 and Jason-2). For instance, track 181 passes through H1, track 03 passes through H2 and track 79 passes through H3. Even though we have not used the along track data for this analysis, choosing the boxes under the altimeter tracks ensures that more precise altimeter data are included in our primary time series. Box H4, centered at $\sim 5.5^\circ\text{N}$ and $\sim 85^\circ\text{E}$, is intended to capture the SLA signature of Rossby waves that are either generated in the southern BoB, or that propagate from the eastern boundary after the reflection of equatorial Kelvin waves. Box H-Eq (centered at $\sim 93^\circ\text{E}$) on the equator and Box H7 (centered at $\sim 5^\circ\text{N}$ and $\sim 93^\circ\text{E}$) off the coast of Sumatra, are intended to capture the latter process.

The boxes located on the slope (H1, H2, H6) have a width of about 1.5° longitude and a height of about 1° latitude, encompassing approximately 10-15 grid points. The size of these boxes is chosen such that they can capture the CTW signal on the slope; large enough to have improved statistical reliability by averaging multiple grid points but small enough to be comparable to the local Rossby deformation radius (typically ~ 80 -120 km for mode 1 (DB Chelton et al., 1998)). Box H3 is comparatively larger in size (longitudinal-width of about 2° and latitudinal-height of about 1.5°), as the SLA signal at the tip of India can also include Rossby waves from south-west of Sri-Lanka which are expected to have a smaller amplitude but larger spatial scale compared to the CTW signals. Box H4 is even bigger in size (longitudinal-width of 2.5° and latitudinal-height of about 3.5°), as it is solely meant to capture Rossby waves.

Similar to SLA, wind boxes are chosen along the west coast near the SLA boxes [Figure 2.2]. One surrounds box H1 (TA1), one surrounds box H2 (TA2) and one lies in between the SLA boxes (TA12). The choice of larger boxes for the winds is required to reduce the smaller-scale noise in the data and improve the correlations with the SLA. Three additional wind boxes represent different areas near southern India: on the southern tip of India, TA3 surrounds SLA box H3, TA5 lies along the western side of Sri-Lanka and TA4 covers the region south of Sri-Lanka and along its east coast. One more box, TA6 is north of Sri-Lanka, surrounding box H6, to represent the winds along the south east coast of India. A single time-series for each box is constructed to represent variations of alongshore wind stress (even away from the coast), positive in the downwelling sense. The alongshore component of wind stress is calculated at each ECMWF grid point within a box before averaging to obtain an effective alongshore stress for the entire box. This is particularly important for boxes TA3, TA4, TA5 and TA6 which involve more than one sub-box [Fig 2.2], which have different angles for computing the alongshore wind stress at each ECMWF grid point, taking into account the corresponding alongshore angle nearest to each grid point. The alongshore wind stresses for all the grid points falling inside the corresponding wind boxes are then spatially averaged with equal weights to obtain a single time-series for the entire box. Time-series of wind stress curl for each of the wind boxes are average values of all grid points within the box and labelled similarly to the alongshore wind stress time series (C1, C12, C2, C3, C4, C5, C6).

For most of the analyses, the intra-seasonal time-series for SLA, alongshore wind stress and wind stress curl are normalized with their respective standard deviations from each box.

2.2.2 Lagged Correlations and Coherences

Between any two time series, correlation co-efficients are obtained for different lags. The 95% confidence level for each lag is calculated using a significance test for sample cross correlation (DB Chelton, 1983). The number of independently occurring events/degrees of freedom (N^*) used in the computation of 95% confidence levels is estimated using the Artificial Skill Method(ASM) (*ibid.*), as described in the Appendix. The correlations of the 30-120 day time series are supplemented with coherence calculations that identify narrow period bands within which the correlations are highest.

2.2.3 Regression Model

A multivariate linear regression model is built to hind-cast the SLA on the west coast of India from SLA and alongshore wind stress at other locations. For most comparisons, the SLA in box H1 is the estimand. An underlying problem common to analyses of geophysical signals occurs when there are significant correlations among the different input fields, which lead to high error bars on each of the regression coefficients in the regression model. In that case, it is difficult to estimate the importance of one factor over the other, as the error bars on each of those coefficients are large enough to include the others. In our analysis, the final model is thus constructed with the input parameters and lags that are consistent with the dynamics which are thought to govern the physics of the processes: wind stress, CTWs and Rossby waves.

2.3 Results

In this Section we quantify the statistical connection of the coastal ocean's intra-seasonal response in sea level along the west coast of India to distant and local wind forcing and sea level signals at other locations. There are five sub-sections. The first one discusses the strength of time-series in different frequency bands, with periods corresponding to seasonal, non-seasonal and intra-seasonal bands. The next two sub-sections focus on simple two-point lagged correlations and a multiple regression model that helps to identify the importance of different forcing signals. The fourth sub-section turns the attention to coherence calculations that reveal the significance of a narrower 40-60 day band, which produces maximum correlations among the important signals. The last sub-section looks at the propagation of oceanic signals with the help of Hovmöller diagrams.

2.3.1 The Intra-Seasonal Time Series

Time series of SLA in box H1 are shown in Fig 2.3 for the raw and filtered data: (Top) Raw: AVISO daily; (Middle) Non Seasonal: after removing trends, means and seasonal cycles (annual plus first three harmonics); and (Bottom) Intra-seasonal: 120-day high pass filtered non-seasonal time series. The seasonal time scale is the most visually dominant aspect of the raw time-series. The variance of the intra-seasonal band (7.6 cm^2) accounts for half the variance of the non-seasonal time-series (15 cm^2). The presence of a significant

intra-seasonal signal on the west coast of India is consistent with the findings of Vialard et al. 2009, that the WICC has a significant intra-seasonal variability.

Time series for alongshore wind stress boxes show similar dominance of the seasonal cycles for the raw data set and significant intra-seasonal variability for Non-Seasonal time series. For instance, the alongshore wind stress in box TA3 has a variance of $2.7 \times 10^{-4} N^2/m^4$ in the non-seasonal time-series, and $1.8 \times 10^{-4} N^2/m^4$ in the 30-120 day time-series.

Power spectra for each intra-seasonal time series contain consistent peaks between 40-60 day periods in both winds and SLA. Figure 2.4 shows power spectra of the normalized timeseries, for SLA in H3 and alongshore wind stress at TA3. There are coincident significant peaks between 40-50 days, and marginally significant peaks between 50 and 60 days. This is within the period range of Madden-Julian Oscillations (MJOs), well known signals in the ocean and atmosphere in the Indian Ocean.

2.3.2 Lagged Correlation Analysis

Intra-seasonal normalized SLA time-series from all regions are correlated with SLA at H1. Fig 2.5 and Table 2.1 show that the boxes on the west coast of India are highly correlated with H1 with a lead of 0-1 days, suggesting events that appear almost at the same time all along the west coast. The magnitudes of the correlations decrease to approximately 0.69 at H2 and 0.56 at H3, somewhat consistent with decorrelation in currents found by Amol et al., 2014. The next highest correlation is with SLA at H4, east of Sri Lanka. This suggests that the Rossby-wave mechanism which is presumably represented by SLA variability in H4, is indeed important for estimating SLA variations in H1 (Table 2.1). However, the lag of 2 days between H4 and H1 is too short as described in the Discussion. Along the south-east coast of India, the SLA at H6 is significantly correlated with H1 SLA, but at a much lower level than locations along the west coast. Combined with the ~ 11 day lead from H6 to H1, this suggests a tenuous coastal connection between the east and west coast of India, possibly due to the convoluted pathway around Sri Lanka and the southern tip of India.

Significant correlations of H-Eq with SLA signals along the Rossby wave path-way (H-Eq-H7-H4-H1) with an increase in the lead as we move from H7 (off of Sumatra) to H4 (east of Sri-Lanka) and H1 (west coast of India) [Fig 2.6] suggest the connection of

the equator with the west coast of India along the Rossby wave path-way. The decrease in the correlation between the Equator and the south-east coast of India(H6), followed by an increase of correlation with the west coast of India, suggests that the Rossby wave path is a more important connection between the equator and the west coast of India than the coastal path around the BoB. This is consistent with the model results of Suresh et al. (2013).

Figure 2.7 shows the correlations of the alongshore wind stress with SLA at H1. The highest correlation of H1 is with TA3 and the lowest correlation is with TA1, suggesting the importance of remote winds from the tip of India over the local winds for intra-seasonal sea level variations at H1. This can be understood by the fact that winds are almost perpendicular to the west coast farther north, and the alongshore component of the wind stress increases as we move southward, with a maximum at the tip of India [Figure 3, (Vialard et al., 2009) and Figure 4, (Webber et al., 2010)]. These results are consistent with the study by Amol et al. (2012), suggesting the importance of distant winds from the tip of India for intra-seasonal SLA variations along the west coast of India, an indication of CTW dynamics. The next highest correlation of alongshore wind stress comes from the winds at the tip Sri-Lanka (TA4), which are very similar to TA3. Moving to the south-east coast of India, winds at TA6 are significantly correlated with SLA at H1 with a slightly longer lead. The correlations with TA5 along western Sri Lanka changes sign due to the fact that the same winds affect the tip of India and the western coast of Sri Lanka in an opposite sense (winds toward the southwest between India and Sri Lanka cause downwelling on the Indian coast and upwelling next to Sri Lanka).

Correlations of the wind stress curl [Table 2.1] with H1 generally follow the same pattern as the wind stress but with opposite sign, as negative wind stress curl causes positive (downwelling) SLA. The maximum correlation is found with C3 and C4. This again suggests the importance of wind forcing to the south of India and Sri-Lanka for predicting the SLA on the west coast of India, whether the more important forcing is alongshore wind stress or wind stress curl. Differentiating wind stress from wind stress curl is complicated by the fact that coastal alongshore winds are often slowed by friction with the land and other processes next to the coast (Bakun and Nelson, 1991), causing high correlations between the coastal wind stress curl and the alongshore wind stress [Table 2.1].

Winds at the tip of India (TA3) show the maximum correlation for a lead of 6

days. Correlations with more local winds (TA1, TA12, TA2) are similar but slightly less in magnitude, with a lead of 5-6 days. These leads are longer than expected for local upwelling and downwelling sea level responses to imposed wind stress, which are expected to be in the 1-2 day range (Denbo and JS Allen, 1987). All of these wind signals with the longer leads may represent the strong inter-correlation between these local winds and winds at the tip of India and Sri-Lanka, which have the highest correlation with H1 and leads of 6 days (discussed in detail in Coherence and Phase results).

The interpretation of the wind stress correlations at different locations is made difficult by the fact that the winds are highly inter-correlated, due to the influence of the basin-wide signals. Table 2.2 shows the correlation of daily TA3 alongshore wind stress with wind stress and wind stress curl in all other wind boxes, quantifying the degree to which the different forcing functions are inter-correlated with each other. An Empirical Orthogonal Function (EOF) analysis of the alongshore wind stress at these several locations produces a first mode that explains almost 54% of the total variance, with highest amplitudes coming from TA3 and TA4, suggesting the importance of larger-scale wind forcing, best represented by winds from the southern tip of India and Sri-Lanka (TA3 and TA4). The second EOF explains another 31% of the variance, with approximately equal positive amplitude at TA1, TA12, TA2, TA3, TA4 and even stronger negative amplitude at TA6. This demonstrates another mode of large-scale coherence between winds along the west, south and east coast of India. This wide-scale nature of wind forcing is in agreement with Vialard et al. (2009) and Webber et al. (2010) and confirms the results of Amol et al. (2012).

2.3.3 Regression Model

In order to investigate the relative importance of multiple forcing signals, we employ multivariate regressions, building a model that uses the variables (parameter, location and lag) that explain significant amounts of variance in H1. Input parameters and their corresponding lags are chosen such that they are consistent with the dynamics of the dominant physical processes and are statistically significant, explaining the maximum amount of the variance.

Very high correlations among H1, H2 and H3 with a lag of near 0 days suggest that time-series of H1, H2 and H3 are quite similar, representing the regional west coast

response. Therefore, H2 and H3 are not used as the input parameters for predicting the SLA at H1, the target response. The most distant signal, H7, is also not used in building a final statistical model, since we assume that Rossby wave signals from H7 must pass through H4 before reaching the west coast of India. H4 is used to represent the Rossby wave contribution. To include the different dynamic processes which are considered to have a potential to influence the SLA variability at H1, we choose following four major input parameters for the regression model: 1) TA3: representing the winds at the tip of India which are also correlated with the larger-scale patterns of wind forcing represented by first mode of EOF (54% of the variance) described above; 2) H4: representing Rossby wave signals coming from east of Sri-Lanka; 3) H6: representing CTWs coming from the east coast of India and 4) TA1: representing local wind forcing.

The model with just TA3 winds at the lag of 6 days explains 24.7% of the variance, suggesting the importance of regional winds, represented by the winds from the tip of India. H4, with a lead of 4 days, explains the next largest amount of variance, increasing the total by 4-5% to 28.9%. The next in line is H6 from the east coast of India, with a lead of 11 days, increasing the variance by 2-3%. The final model consist of the following variables: 1) TA3 (-6 day) 2) H4 (-4 days) 3) H6 (-11 day) 4) TA1 (0 day). Figure 2.8 shows a two-year subset of the time series during 2005-2006, comparing the observed H1 to the model reconstructions of H1. The skill of the model is 32% implying there is still significant percentage of unexplained variance. In Figure 2.8, the model doesn't capture a few of the peaks that are observed in SLA at H1 (for eg. Nov 2005, Mar 2006), which can be associated with some of the other crucial factors not accounted for in this simple regression model. Some of these factors may include alongshore winds between TA1 and TA3 (through CTWs) and offshore-onshore transport by regional mesoscale fields (eddies etc.).

Although, the high inter-correlations between input variables create large uncertainties in the regression coefficients, we interpret correlations and regression models as identifying 4 regional input variables, with characteristic lags:

- 1) The strongest input is from winds south of India and Sri Lanka, which we regard as representative of large-scale winds because of it's strong inter-correlation with winds at other locations (Table 2.2);
- 2) There is a significant and moderate input from SLA south-east of Sri Lanka, with a lead of 4 days. This signal appears to originate next to Sumatra and propagate westward

over a period of about 3 weeks (Discussed in the Hovmöller section below);

3) There is a significant but weak input from winds and SLA from the south east coast of India, with a lead of approximately 11-13 days;

4) There is a significant but weak input from local winds with a lead of 0-2 days.

2.3.4 Coherence and Phase Analysis

In the last section, the regression model identifies some of the connections between sea level along the Indian west coast and signals in other regions that were first identified using lagged correlations. This section uses coherence and phase computations to identify the dominant 40-60 day period in the system. Finally, an additional band-pass filter is applied to examine the coherent wind and sea-level connections in the narrower 40-60 day period band.

The coherence plot of SLA at H1 with winds at TA1 shows that the maximum coherence comes from the periods 40 to 60 days and the phase plot shows that the leads corresponding to those periods are between 0 to 2 days (Figure 2.9). Previous correlation of H1 with TA1 showed a lead of 5 days, which is longer than expected for a coastal response to the local winds. However, the multivariate regression model suggests a lead of around 0-2 days using local forcing. Moving from local winds along the west coast to the winds south of India and Sri Lanka, coherence magnitudes of H1 with TA12, TA2, TA3 and TA4 again show similar peaks for periods of 40 to 60 days. However, the leads increase from 0-2 days locally to 6 days in the south at TA3 (Figure 2.9). The coherence plots for TA3 and TA4 are very similar and the 6 day lead obtained from the coherence is consistent with the leads from previous correlations and the multivariate regression model. Along the south-east coast of India, the coherence plot for TA6 (not shown) indicates winds shows two peaks; one at 30-35 days and another in the 45-65 day band. The phase plot shows that the corresponding lead is close to 8-12 days, similar to results from the regression model.

In summary, the coherence analysis is consistent with the multivariate regression model for the frequency band of 40-60 days. The previous correlations between winds at all locations and SLA at H1 produced leads of 5 to 7 days (close to a 6 day lead). This is in contrast to the shorter leads for local winds and longer leads for winds along the south-east coast of India obtained from regression models and coherence calculations for

the band of 40-60 days. A possible explanation for this is the high correlation of winds at different locations with the winds from south of India and Sri-Lanka (TA3 and TA4), which have a lead of 6 days with SLA at H1. In the coherence plots for H1 and winds, we see the more realistic leads for periods of 40-60 days. Local winds have high coherence with SLA at H1 for the band of 40-60 days. However there is also high coherence between local winds(TA1) and the winds at the tip of India and Sri-Lanka (TA3 and TA4) for frequencies outside of the 40-60 day band(Figure 2.9). Our hypothesis is that the longer lead for the correlation of local winds with H1 is due to the frequencies outside of the band of 40-60 days, which have high coherence with the winds at TA3 and TA4 (which leads of 6 days with SLA at H1 for all periods).

Given the strength of signals in the 40-60 day periods, we band pass filter the data in order to look at the sea level response in the dominant and narrow band. Fig 2.10 shows the correlations of the H1 sea levels with all of the wind stress variables after the data have been band-pass filtered to keep periods between 40 and 60 days. The first apparent change is the increase in correlation coefficients of all of the wind variables with H1. There is also a significant decrease in the lag between the sea level and local winds, from 5 days to 2 days. This demonstrates that the periods outside of the 40-60 day band contributed to the longer lags of the previous correlations between H1 and local winds. Using the 40-60 day band-pass filtered data set in the final model derived in Section 3.3 (using the same lags) now explains 48% of the total variance compared to the previous 32%, a significant increase.

Our interpretation of the wind forcing is as follows: Winds at all locations used in our analysis are significantly correlated with the wind from south of India and Sri-Lanka, which are represented by TA3 and TA4 winds. This wind signal produces a lead of 6 days with the SLA on the west coast of India for reasons that are unclear as explored in the Discussion section. Hence, when SLA on the west coast is correlated with the winds at any location, the correlations and corresponding leads are primarily due to the large scale wind relationship, as represented by the 6 day lead at TA3. However, the multivariate regression model and coherence plots help to separate this large-scale signal and give a more realistic lag due to the interaction of SLA and winds within a narrower band of 40-60 day periods.

2.3.5 Hovmöller Diagrams

In the previous section, coherence and phase analysis demonstrated the importance of the 40-60 day band for the intra-seasonal SLA variations on the west coast of India. In this section we try to interpret the statistics with visual means, that is, by constructing the time-distance plots of 40-60 day band pass filtered SLAs.

The propagation of signals from the south east coast of India (H6) to H1 and from Sumatra (H7 through H4) to H1 are investigated with Hovmöller plots of 40-60 day band pass filtered AVISO SLA. In Fig 2.11, boxes H1-X2-X3 (on the west coast), X4 (south of Sri-Lanka), X5-X8 (along the Rossby wave guide path going to the east of Sri-Lanka) are chosen to investigate the Rossby wave pathway by capturing the signals generated along the pathway as well as signals coming all the way from the coast of Sumatra. Rossby waves consist of a variety of meridional modes; among these, the first meridional mode has a symmetric off-equatorial maxima. The distance of the maxima away from the Equator depends upon the Rossby radius of deformation (D Chelton et al., 2003). The first mode, which typically has a SSH maxima near $4-5^\circ$ latitude, appears to dominate intra-seasonal periods compared to higher modes (Webber et al., 2012). Rossby wave pathway boxes from X4-X8 are chosen along the $4-6^\circ$ latitude to capture the SSH maxima due to the first meridional mode of Equatorial Rossby waves. The critical latitude for the first baroclinic mode near the tip India forces the signals with periods greater than 60 days to radiate away as Rossby waves (Vialard et al., 2009), allowing only periods less than 60 days to propagate farther north along the west coast. This shows the capability of Rossby waves within the band of 40-60 day period to affect the SLA variability farther north on the west coast of India once they reach the tip of India. Boxes H1-X2-X3 and X4-Y5-Y6-Y7 (going around Sri-Lanka to the east coast of India) are chosen to investigate the signals coming from the south-east coast of India. H1, X2, X3, Y5, Y6, Y7 are chosen on the slope to capture the CTW signals.

Fig 2.12 shows the Hovmöller plots of the Rossby and the East coast pathways for a 500 day subset of the 10-year period. Significant propagation of both upwelling and downwelling signals along the Rossby wave pathway (between X8 and X4) can be seen from May 2003 to Aug 2003. There is a slight intensification of the signal near X5, suggesting the importance of local winds at X5 for intensifying the Rossby wave signal through wind stress curl. For the case of the east coast pathway, the propagation of the

signal is not as robust as for the Rossby wave pathway. The propagation of signals can also be seen on the west coast of India as a CTW signal, for instance during Sep-Dec 2002. X4 is the primary site where the two SLA signals can interact, one coming from the south-east coast of India and another as a Rossby wave from the east of Sri-Lanka. The Hovmöller plots show that the signals from the Rossby wave path are often stronger than the signals coming from the east coast of India. For instance, a downwelling signal (high SLA) started from the east coast of India (Y7) around mid-May 2003. However it does not reach the southern tip of Sri-Lanka (X4), because a strong upwelling (low sea level) signal from the Rossby wave pathway reaches X4 almost at the same time, completely subduing the downwelling signal from the east coast pathway. The upwelling signal continues to the Indian west coast. There are several examples of strong and robust propagation along the Rossby wave pathway, travelling all the way to H1 (mid-Oct 03 from X6 to H1).

There is an apparent southward propagation observed between the tip of India (X3) and the tip of Sri-Lanka (X4). This apparent southward propagation doesn't necessarily mean that signals propagate from X3 to X4, but it certainly suggests that a signal sometimes appears at X3 before a signal appears at X4. The appearance of a signal at X3 is due to the intensification of alongshore winds at the tip of India; the appearance of a signal at X4 is coming either through a Rossby wave pathway and/or due to local winds at X4. The alongshore wind stress signals at both of these locations appear almost at the same time [Table 2.2 : Lagged correlation between TA3 and TA4], meaning this apparent southward propagation between X3 and X4 happens due to the intensification of alongshore wind stress at the tip of India (X3) before the Rossby wave signal reaches at the tip of Sri-Lanka (X4). At times, there are also slight apparent southward propagation events on the west coast of India, for instance mid-June 2003 between X3 and X2. This is due to the fact that local winds near X2 appear first, followed by the local wind forcing at H1, before the subsequent intensified appearance of winds at the tip of India and Sri-Lanka [see the lags in Table 2.2].

Figure 2.13 shows an expanded view of the Hovmöller diagrams, in order to estimate the propagation speeds of Rossby and Kelvin wave signals along the Rossby wave pathway and along the CTW pathway on the west coast of India, respectively. The phase speed of a Rossby wave varies with baroclinic and meridional mode number of the wave. Rossby waves follows the dispersion relation

$$c_R = \frac{-\beta}{\kappa^2 + (2n + 1)\beta/c_k} \quad (2.1)$$

where $\beta \simeq 2.3 \times 10^{-11} \text{ m}^{-1}\text{s}^{-1}$ is the meridional gradient of coriolis parameter f , κ is the zonal wavenumber, n is the meridional mode number and c_k is the Kelvin wave phase speed of the baroclinic mode in question. In the case of the long Rossby wave approximation, Rossby waves are approximately non-dispersive in nature. For the case of $n = 1$, the Rossby wave would propagate almost at one third of the speed of the first baroclinic Kelvin wave (DB Chelton et al., 1998). The first baroclinic Kelvin wave speed in this region is often around 240-280 cm/s (ibid.). This suggests that the theoretical first baroclinic Rossby mode wave speed (under the long wave approximation) would be around 80-90 cm/s . However the observational speed is often slightly less than the theoretical speed, as phase speed is often weakly dependent on the wave number. Webber et al. (2012) estimated the phase speed for the first baroclinic mode along the similar latitude in the Indian ocean for the intra-seasonal periods to be around $50 \pm 10 \text{ cm/s}$. We estimate the phase speed of the Rossby waves from the slope of the lines in Fig 2.13, which is around 57 cm/s . This observation is in fairly good agreement with the observation of Webber et al. (ibid.). Using this estimated phase speed for Rossby waves, it takes 3 to 4 weeks for the SLA signal to travel from X8 (west of Sumatra) to X4 (south of Sri Lanka) ($\sim 1200 \text{ km}$). The signal then propagates very quickly from X4 to H1, in the form of CTWs. The phase speed of the CTWs is also estimated from the slope of the Hovmöller plots on the west coast of India, which is around 178 cm/s [Figure 2.13]. This phase speed results in a travel time close to a couple of days from X3 to H1. In general the first baroclinic Kelvin wave speed is often thrice the speed of the first baroclinic Rossby waves. Using this rule, the estimation of phase speed for the Kelvin waves seems fairly consistent with the theory.

2.4 Discussion

Inclusion of 10 years of altimeter data (October 1999 to November 2009) in this analysis ensures the robustness of the use of grided SLA data near the coast. During this period there are times with 3-4 altimeters, producing higher resolution in time and space in the grided SLA fields. We also limit our analysis for the period of 10 years from October

1999 to November 2009 so that we can correlate our results with the use of QuikSCAT scatterometer winds(1999-2009). The use of scatterometer winds instead of model winds does not alter the overall results (not shown), giving us further confidence in the datasets used in our analysis, especially near the coast. In our final analysis, we prefer the use of ECMWF model winds, which are without data-gaps in time and space, reducing small scale noise in the coastal region.

One set of results, concerns the relative influence of equatorial signals arriving through Rossby waves from east of Sri-Lanka compared to CTW signals travelling around the BoB. Robust propagation on the Rossby wave pathway can be seen with a lead of 3 to 4 weeks from Sumatra to the tip of Sri-Lanka; propagation is not as robust in the case of the east coast CTW pathway. This result provides support for the result found in the modelling study by Suresh et al. (2013) referenced above, suggesting that the increase in the correlation between the Equator and the west coast of India compared to the south-east coast, may be due to the signals arriving along the Rossby wave pathway. In fact, our Hovmöller Diagram (Figure 2.12) analysis suggests that the energy arriving from east of Sri-Lanka in the form of Rossby waves does not simply add to the energy arriving around the BoB boundaries. We hypothesize that the Rossby wave energy can act to cancel and replace the signals travelling from the south-east coast of India. As discussed below, large-scale wind forcing south of India and Sri-Lanka also strongly affects the signals moving up the west coast of India and is the major driving force for SLA variability, as seen in the regression model.

An additional complication in the lagged correlation analysis is the short lag of 2 days between H4 and H1. A longer lag of 4 days is found in the regression analysis but this is still short. Below, in discussing the response to the winds, we hypothesize that the winds are large-scale and generate multiple signals throughout the basin, which arrive at H1 via different pathways, producing artificial lags in the simple correlation. Thus, those correlations are only a starting point.

The other set of results consist of responses to large-scale and local winds. Interpretation of the point to point lagged correlations for the wind forcing are difficult because of the strong coherence between the winds at the tip of India (represented by TA3) and winds at other locations. Correlations of winds from the tip of India (TA3) with other winds [Table 2.2], along with the EOF analysis mentioned earlier (Section 3.1), suggests the dominance of these large-scale winds. The large scale nature of wind forcing for

the intra-seasonal sea-level response in the northern Indian ocean is consistent with the previous studies from Vialard et al. (2009) and Webber et al. (2010). This wind signal produces a lead of 6 days with the SLA on the west coast of India, for reasons not fully understood.

CTW theory, along with the correlations between the H3 and H1 suggest the travel time for the SLA signals on the west coast to be approximately 2 days. This leaves open the question of how the large-scale winds represented by TA3 can produce a lead of 6 days with SLA along the west coast of India? Another question is the reason for the short lead (2-4 days) between sea level at H4 and H1. We offer two hypothetical mechanisms to explain these observation. 1) One possible explanation related to both of unrealistic leads is that these winds produce simultaneous signals with the same frequency at different locations, creating multiple signals which arrive at H1 with different travel times and corresponding phase leads. The combination of these signals can create an artificial lead between the large-scale winds and the signal at H1. As an example, consider large scale winds blowing to the east between the tip of India and the Equator. These winds will generate two different SLA signals: low sea level signal at the tip of India due to upwelling; and high sea level at the Equator due to downwelling (exactly opposite in sign). Both of these signals will ultimately reach to the west coast of India following pathways shown in Fig 2.1. The fact that the SLA on the west coast is a combination of the two signals can create an observed but artificial lead. The observed lead depends upon the separate travel times to reach H1, along with the frequency and relative amplitudes of the wind forcing and arriving signals. 2) A second possible explanation behind the approximate 6-day lead (winds at TA3 and SLA at H1) lies in the fact that the time-series used for making all of these computations is an average of the signals inside corresponding boxes. In particular, the box H1 is offshore over the slope. The average time-series in box H1 might include the SLA signal which has travelled to the west (off-shore) from the coast in the form of slowly moving Rossby waves. The H1 time-series may represent a sum of two travel times: I) CTW travelling on the west coast of India II) slowly moving Rossby waves carrying the signal slightly farther off-shore to the sampling box; producing an apparent lag of 6 days.

In preliminary tests, we have used an idealized configuration of the Regional Ocean Modeling System (ROMS) model with reduced gravity and a flat bottom topography, using a depth that matches the observed first mode Kelvin wave phase speed in the region

of interest. A large-scale analytical east-west wind forcing is applied between the tip of India and the Equator, with a 50 day sinusoid period in time and a Gaussian horizontal structure in space, centred between the Equator and the tip of India. Correlations of Sea level and winds from this idealized model produce similar results to those obtained in the analysis of altimeter SLA and ECMWF winds. The correlations use the identical boxes for SLAs as used with altimeter SLAs and produce approximate 6-day leads with winds at TA3 and close to 4 day lead with SLA at H4 when correlated with SLA at H1 [Figure 2.14]. This very preliminary model experiment demonstrates that a narrow frequency band of large scale winds can produce the observed lags. To quantify and understand the mechanisms producing these lags, future studies should use more realistic stratification, realistic bottom topography and wind forcing from QuikSCAT or ECMWF model winds.

2.5 CONCLUSION

Analysis of 10 years of altimeter SLA data and the ECMWF winds on intra-seasonal time scales of 30-120 days are consistent with previous studies that report the presence of CTW dynamics along the west coast of India. Sea level at H1 (the west coast of India) is highly correlated with sea level and alongshore winds farther south along the coastal wave guide. Sea level at H1 is also moderately well correlated with the sea level east of Sri-Lanka and along the Sumatra coast, implying a more distant connection to the Equator. Sea level at H1 is also weakly correlated with sea level and winds along the south east coast of India. Leads of 3 to 4 weeks are found for sea level between Sumatra and Sri Lanka, followed by a lead of several days between Sri Lanka and H1. Between the south-east coast of India and H1, the leads are 11 to 12 days for sea level.

The highest correlation for the wind forcing when correlated with SLA at H1 comes from the winds at the tip of India(TA3) with a lead of 6 days, which is too long to represent the creation of CTWs at the tip of India that propagate to H1. Wind forcing from other key locations also produce a lead close to 6 days when correlated with SLA at H1, suggesting the large scale nature of wind forcing. However, a multivariate regression model and coherence calculations give more realistic leads due to the interaction of SLA and winds within a narrower band of 40-60 day periods. In this narrow band, high coherences between H1 and local alongshore winds identify lags of 0-2 days, more realistic for a coastal response to local winds. High coherences between H1 and the south-east

coast of India correspond to lags of 8-12 days for the same band. A final band-pass filtering of winds and sea levels to reduce periods outside of the 40-60 day band brings the lags from the correlation calculations of H1 sea level and winds into agreement with the coherence calculations and the regression model. In particular, the lead between local winds and sea level at H1 reduces to a more realistic 0-2 days lead.

Hovmöller diagrams illustrate the propagation of signals through a Rossby wave pathway and an east coast pathway. Rossby wave phase speeds estimated from the slope of Hovmöller plots are around 57 cm/s which is consistent with the previous observations by Webber et al. (2012) for intra-seasonal periods. The observed phase speed produces a lead of 3 to 4 weeks for SLA signals near Sumatra(X8) to travel to a location south of Sri-Lanka(X4), and then to travel quickly in the form of CTWs to reach H1. The phase speed of CTWs along the west coast of India is also estimated from the Hovmöller plots to be around 178 cm/s . Propagation on the east coast pathway is not robust and does not occur as often as along the Rossby wave pathway. This result provides a possible explanation for the modelling study by Suresh et al. (2013), in which the contribution of equatorial forcing for intra-seasonal SLA variability decreases as we move along the coastal wave guide from the northern Bay of Bengal to the eastern coast of Sri Lanka. The correlations then increase along the wave guide from south of Sri Lanka to the west coast of India. The Hovmöller diagrams provide evidence that the increased connection between the west coast of India and the equator is explained by the signals arriving along the Rossby wave pathway.

Table 2.1: Highest correlation of H1 SLA with other time-series and corresponding Lags: AVISO Daily SLA and ECMWF daily Winds. Shown in bold are the input variables selected by the regression models.

Max. Correlation of H1 SLA with other variables									
Wind Stress(WS)	H1	Lag	WS Curl	H1	Lag	SSH	H1	Lag	
TA1	0.3143	- 5 days	C1	-0.2087	- 6 days	H1	1.0000	0 days	
TA12	0.3465	- 5 days	C12	-0.3452	- 5 days	H2	0.6882	- 1 days	
TA2	0.3634	- 5 days	C2	-0.2990	- 6 days	H3	0.5559	0 days	
TA3	0.5028	- 6 days	C3	-0.4121	- 6 days	H4	0.3243	- 2 days	
TA4	0.4572	- 6 days	C4	-0.4348	- 6 days	H6	0.2335	- 11 days	
TA6	0.2122	- 8 days	C6	-0.2984	- 6 days	H7	0.2607	- 21 days	

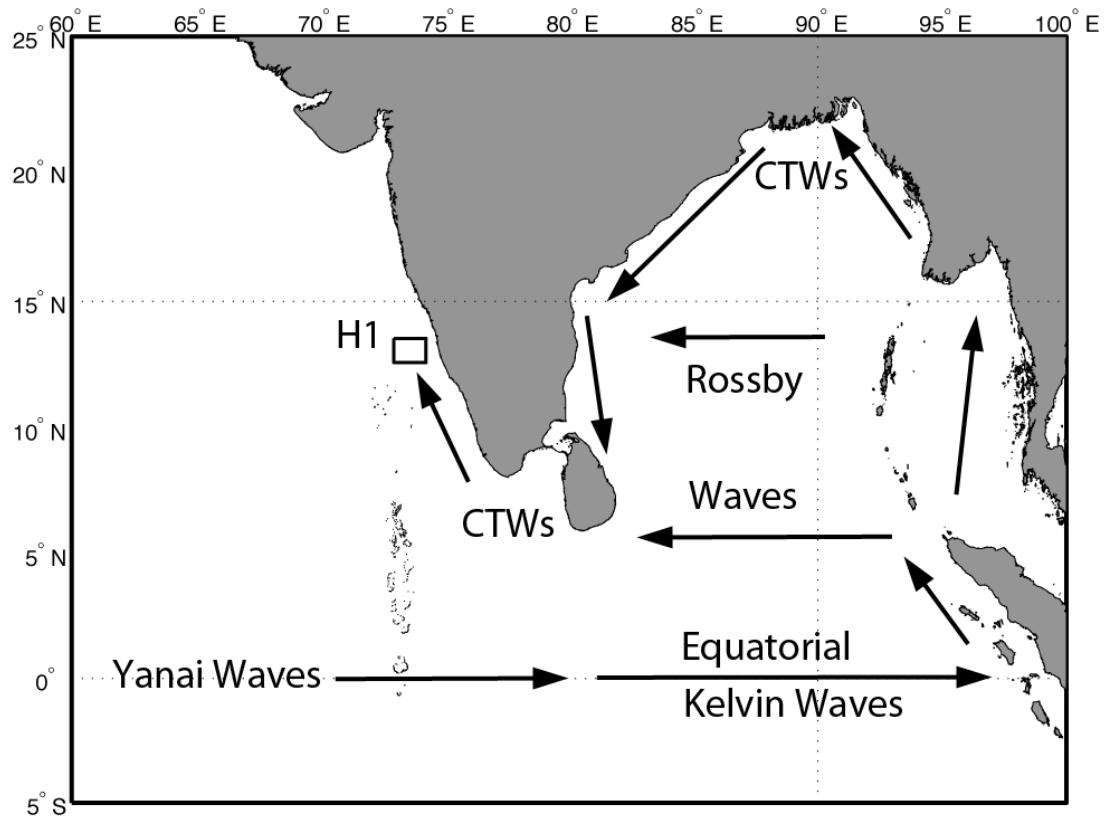


Figure 2.1: Basin-wide schematic of Oceanic wave propagation in the Northern Indian Ocean; Box H1 represents the region of interest

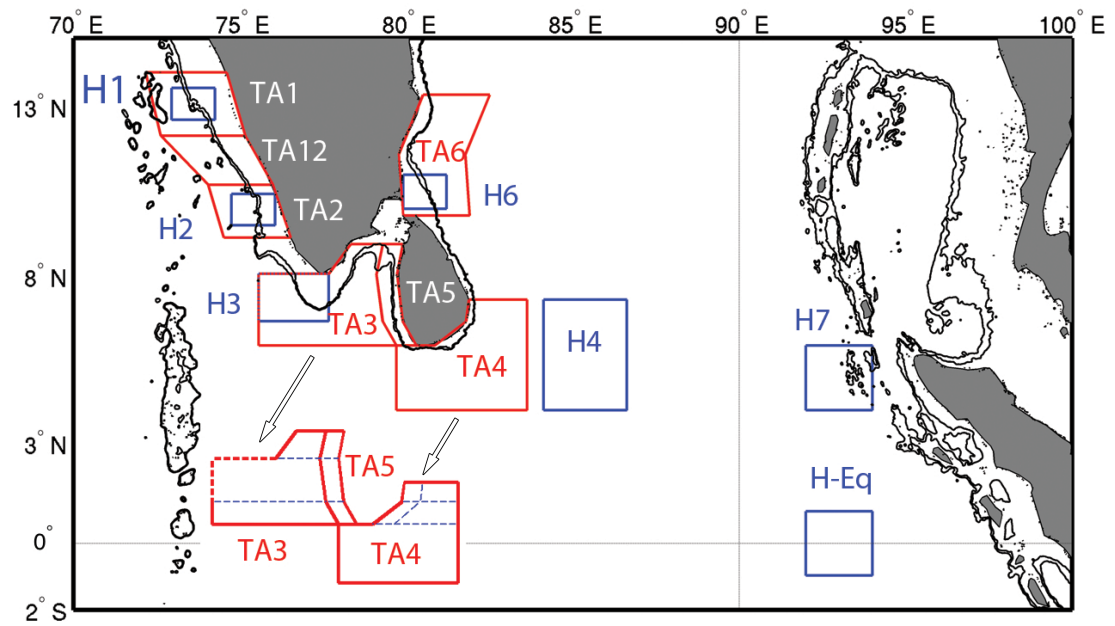


Figure 2.2: Sea Surface Height Boxes (in blue); Wind Boxes (in red); Open black arrows show the sub-boxes separated by dashed blue lines, representing respective coastal orientations within boxes TA3, TA4 and TA5.

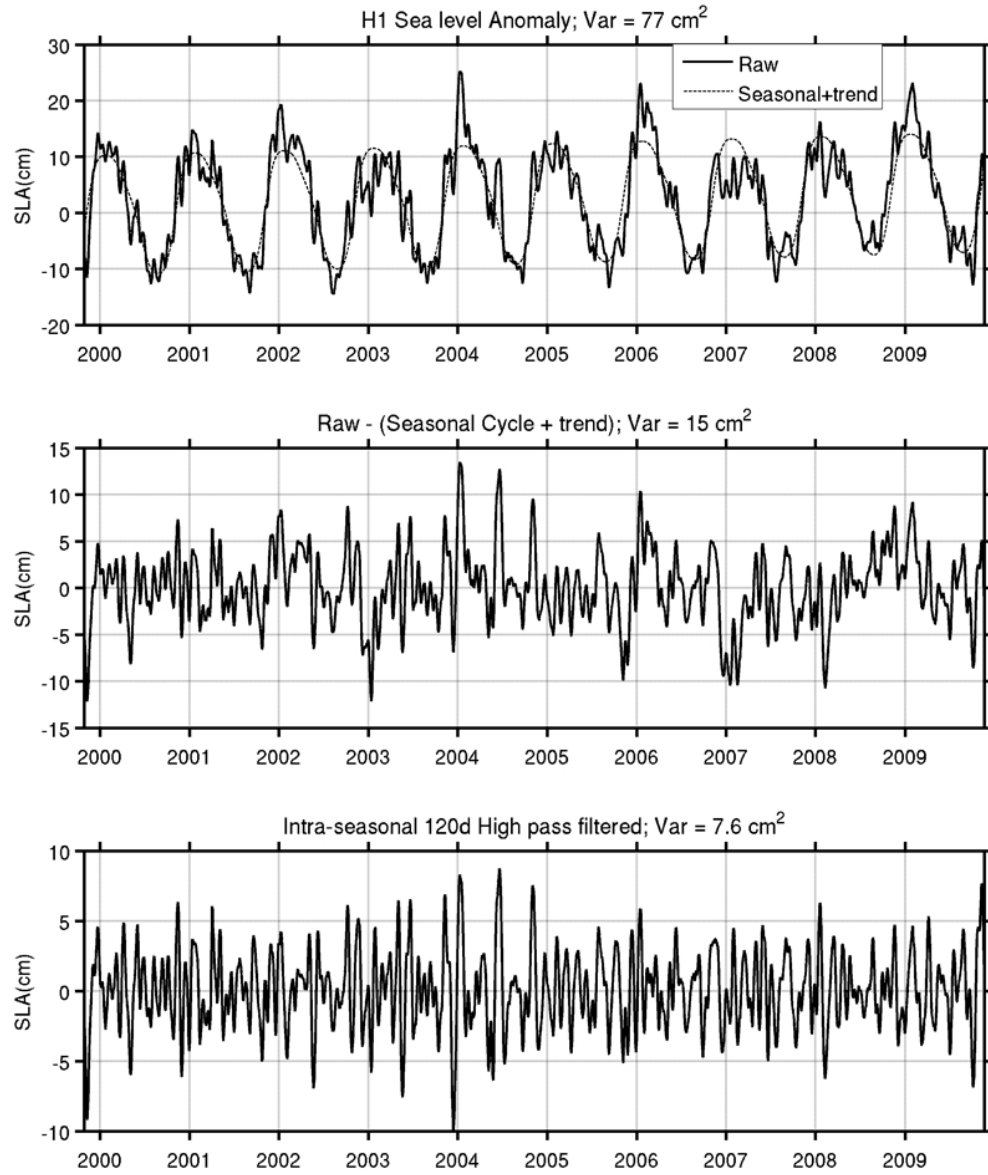


Figure 2.3: H1 SLA Time-series; Top: Raw SLA overlapped on the seasonal cycle and trend in the dashed line; Middle: Seasonal Cycle and trend Removed; Bottom: Intra-seasonal 120 day high passed.

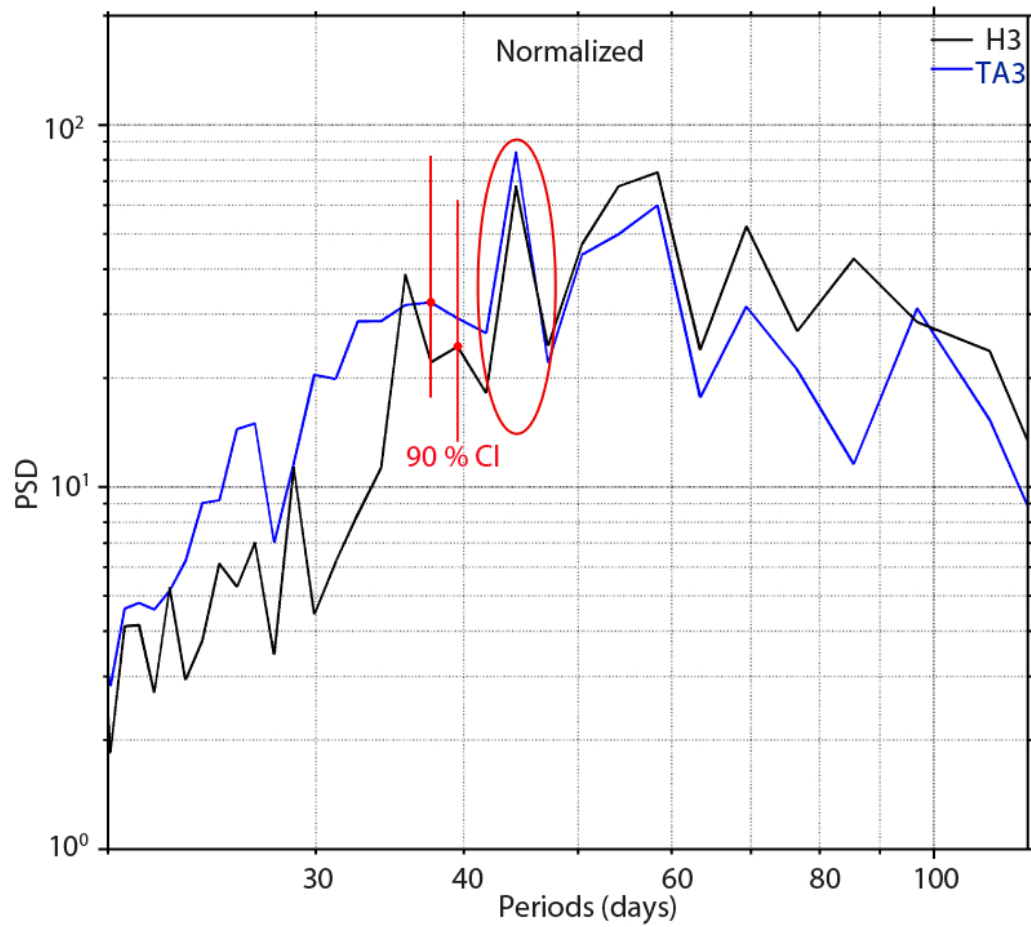


Figure 2.4: Power Spectrum of Normalized H3 and Normalized TA3; Vertical red lines represent the 90 % Confidence Interval (CI) for the peaks in Power Spectrum Density (PSD) plots to be significant; Red encirclement shows the significant coincident peak between 40-50 days in winds at TA3 and SLA at H3.

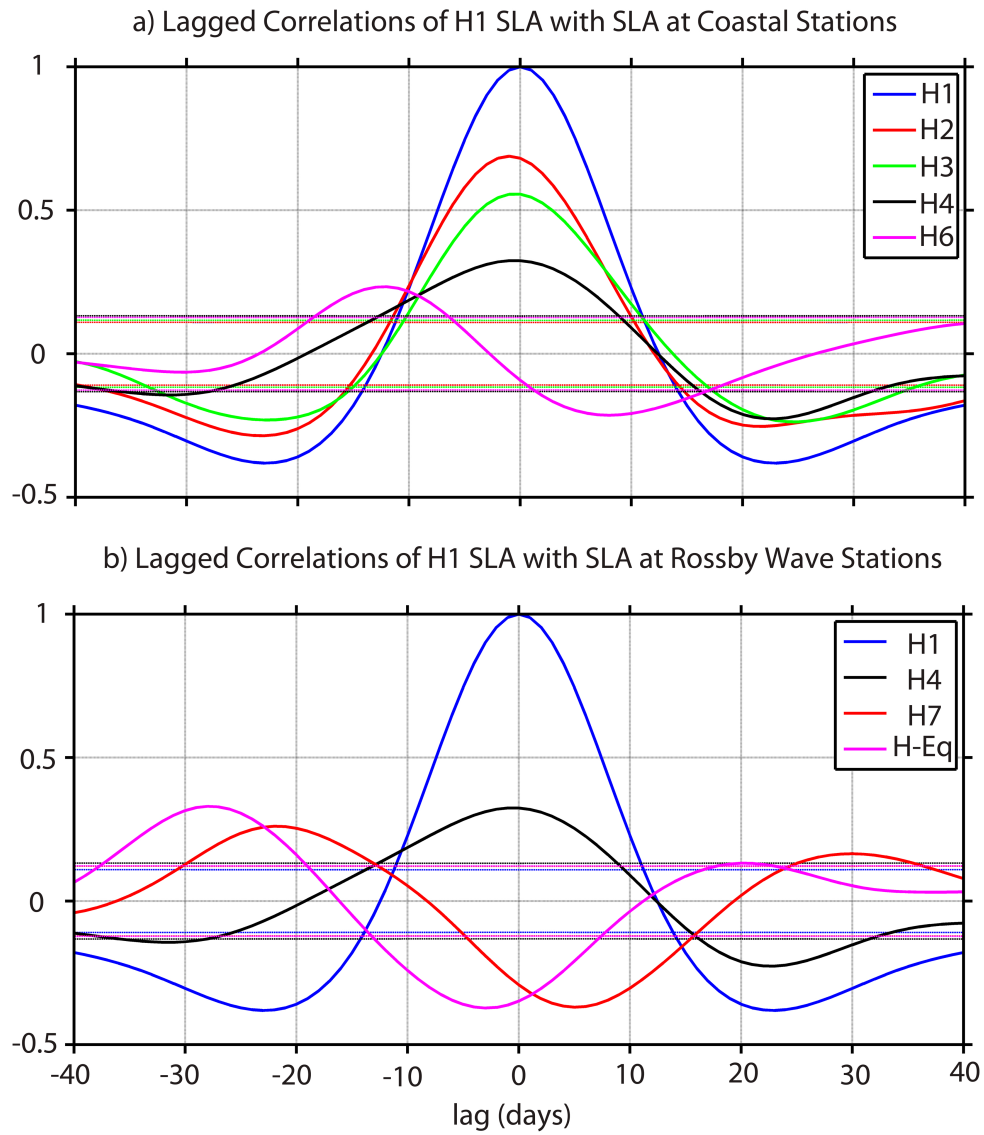


Figure 2.5: Correlation of H1 SLA with: a) Coastal Stations H1, H2, H3 and H6 as well as H4 b) Rossby Wave Stations H4, H7 and H-Eq; Negative lag means H1 lags; Horizontal lines in respective colors represent the 95 % significant level for the correlations to be significant.

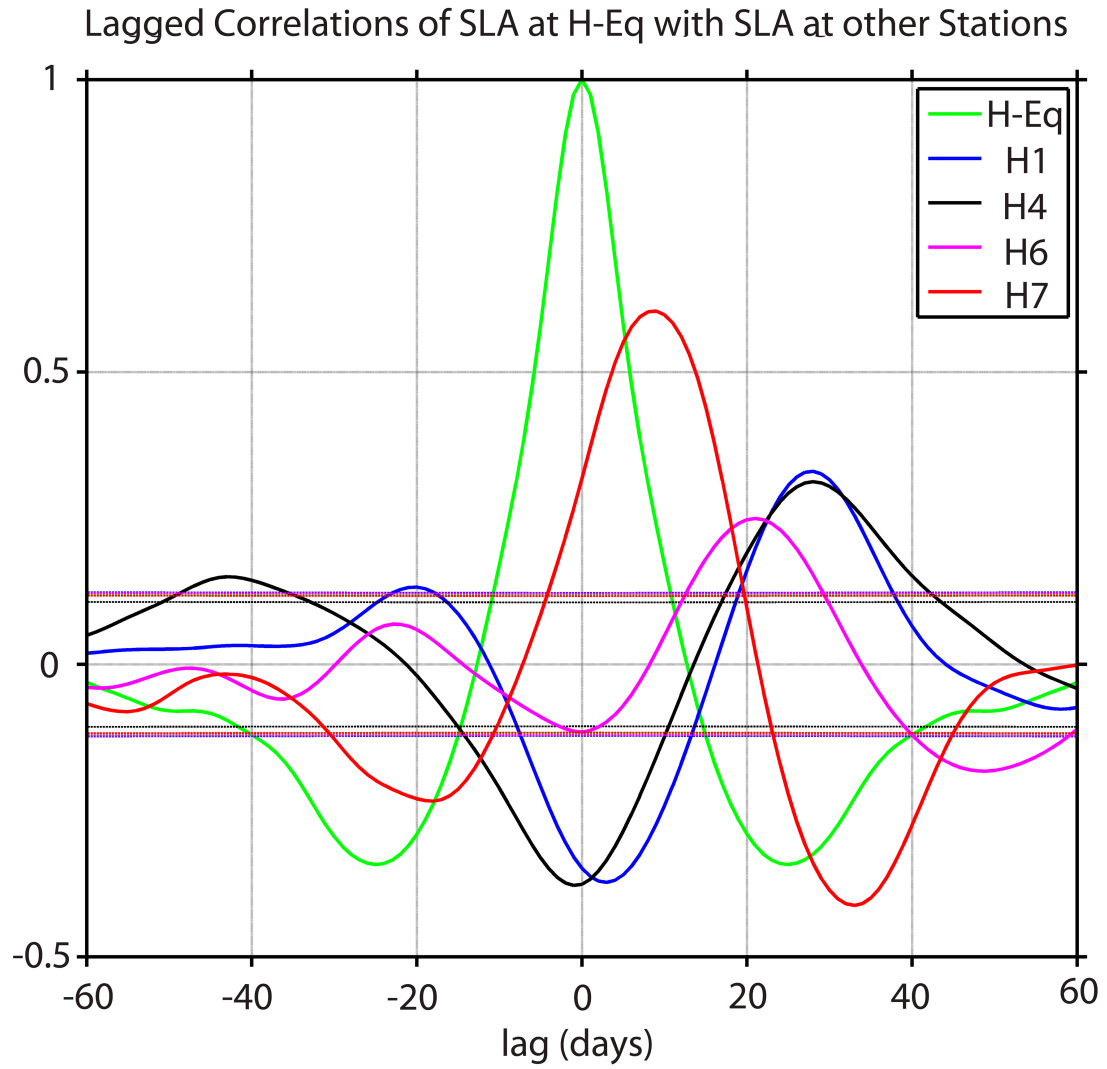


Figure 2.6: Correlation of H-Eq SLA with SLA at other stations; positive lag means H-Eq leads; Horizontal lines in respective colors represent the 95 % significant level for the correlations to be significant.

Lagged Correlations of SLA at H1 with Alongshore Wind Stress at other Stations

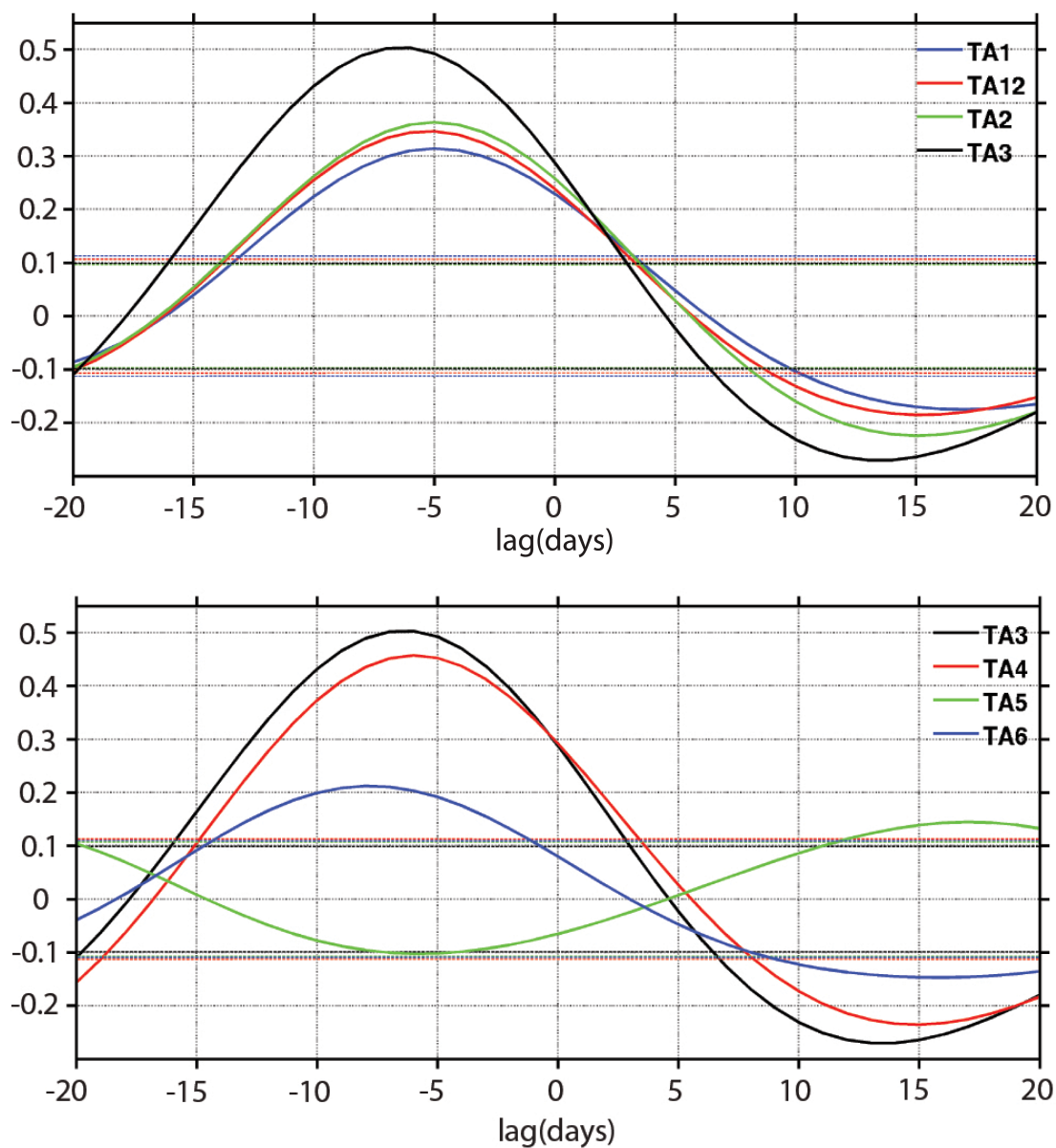


Figure 2.7: Correlation of H1 SLA with alongshore Wind Stress at different locations; Negative lag means H1 lags. Horizontal lines in respective colors represent the 95 % significant level for the correlations to be significant.

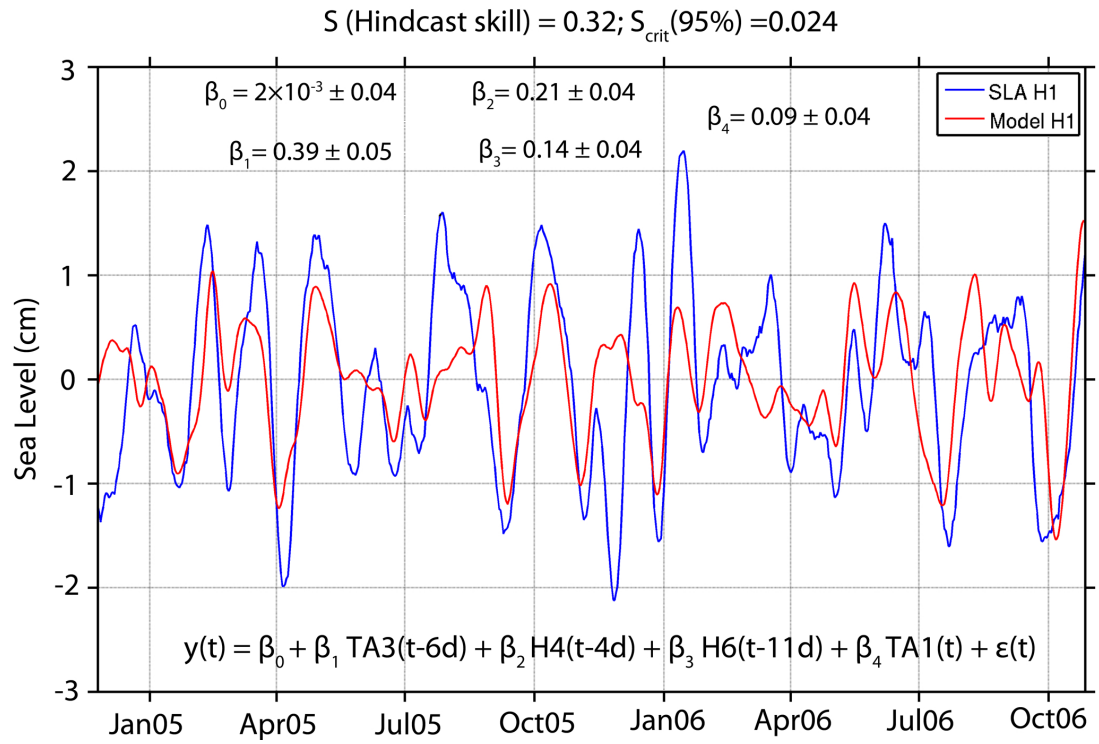


Figure 2.8: Regression Model for Hind-casting SLA at H1; Input Parameters : TA3, H4, H6, TA1

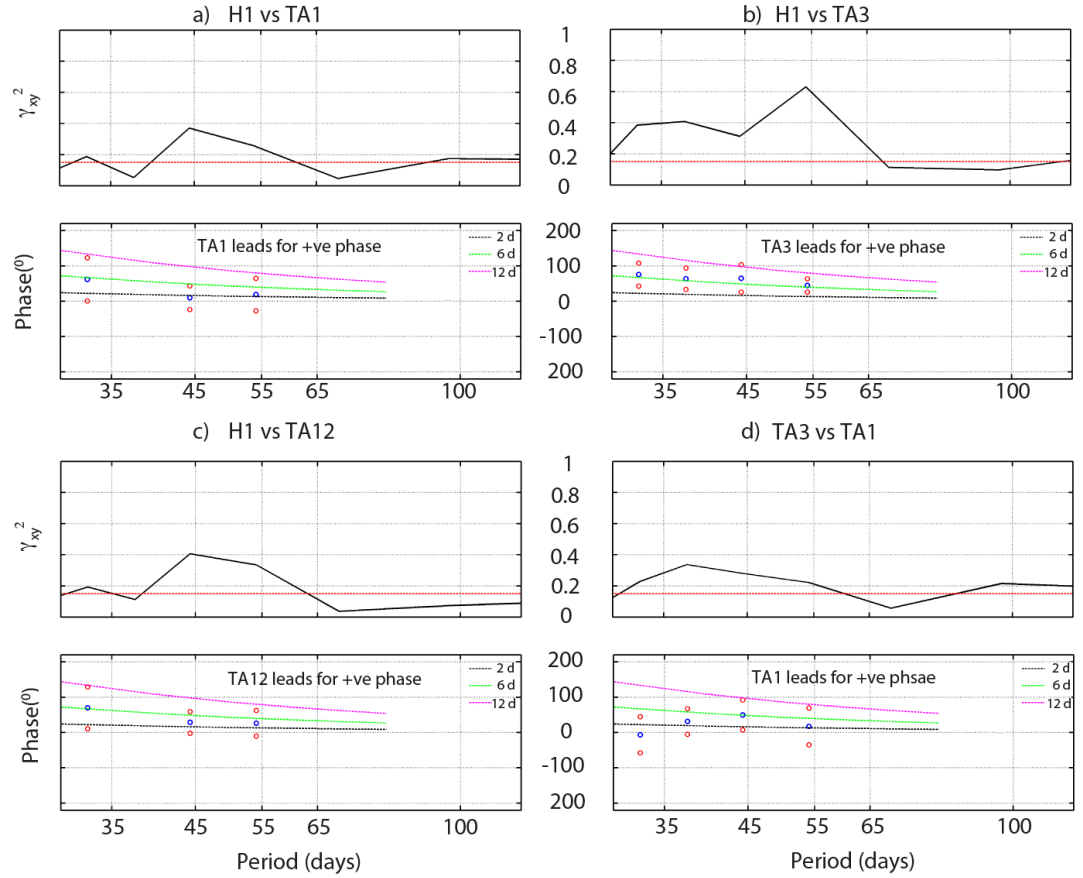


Figure 2.9: (Top Panel) Coherence and phase plots between SLA at H1 and along shore wind stress at TA1(a) and TA3(b); (Bottom Panel) Coherence and phase plots between H1 and TA12(c) and TA3 and TA1 (d). The dashed red line for the coherence and the red circles for the phase represent 95% significance levels. Black, Green and magenta lines represent corresponding values of phases and periods for a constant lag of 2 days, 6 days and 12 days respectively.

Lagged Correlations of H1 SLA with Alongshore Wind Stress (40-60 d band pass)

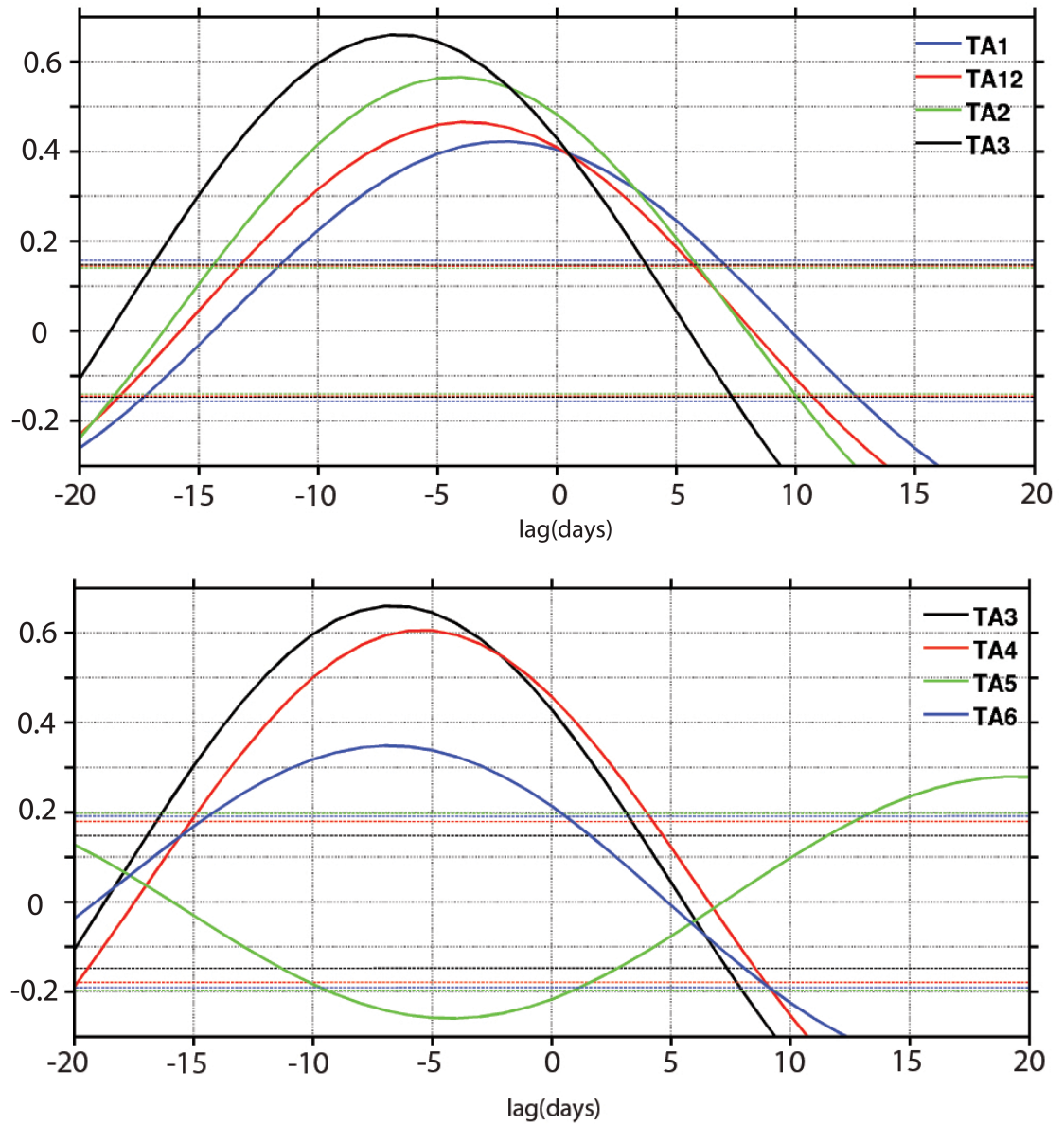


Figure 2.10: Correlation of SLA at H1 with alongshore Wind Stress at different locations with 40-60 day band pass filtered data; positive lag means H1 leads. Horizontal lines in respective colors represent the 95 % significant level for the correlations to be significant.

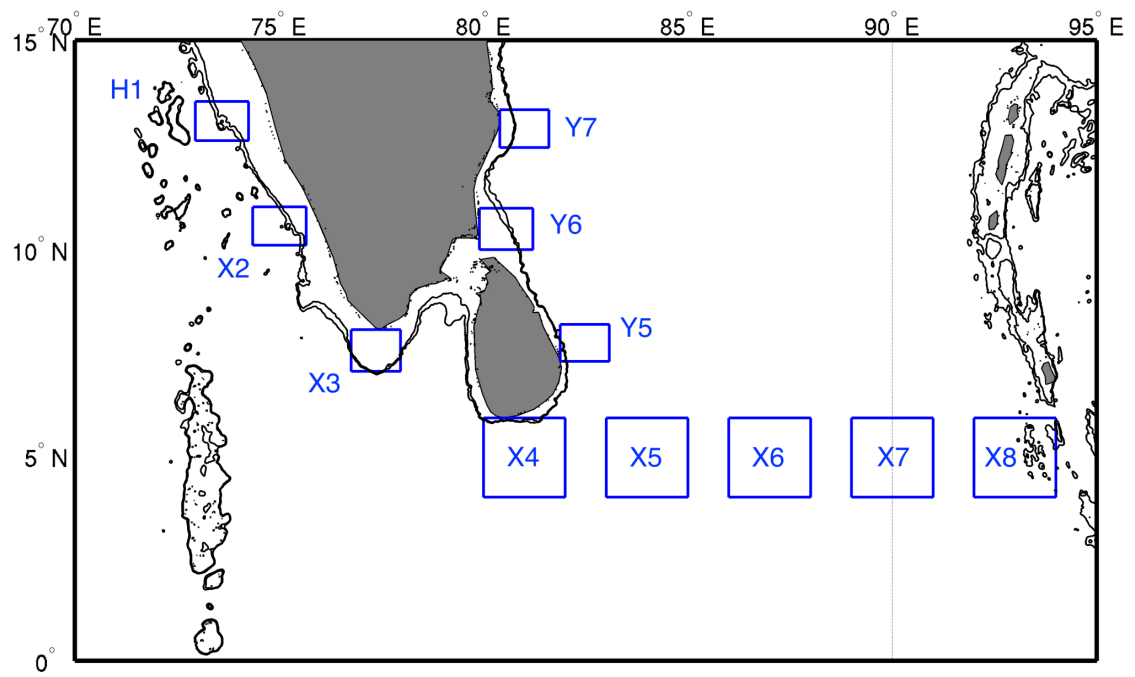


Figure 2.11: Boxes X4-X8 represent a Rossby wave path way and Boxes H1-X2-X3-X4-Y5-Y6-Y7 represent the pathway for a coastal trapped signal coming from the east coast of India.

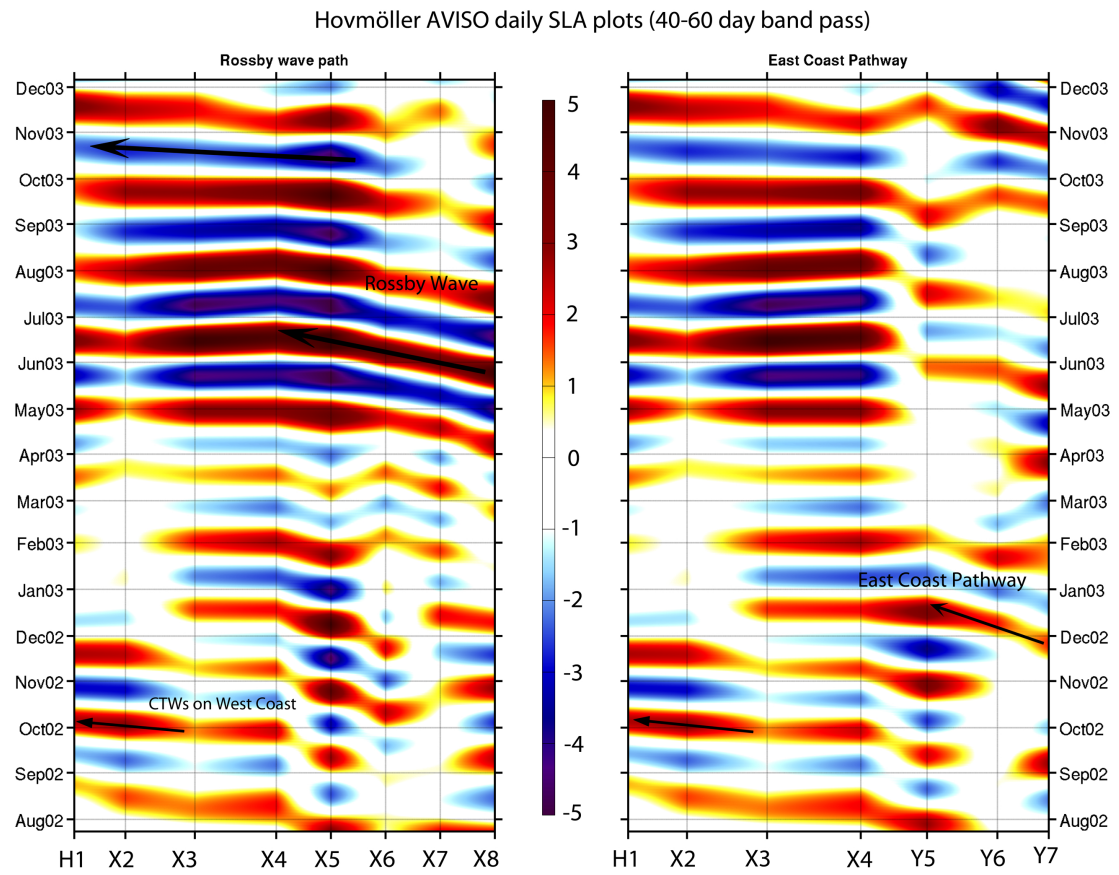


Figure 2.12: Hovmöller plot from AVISO SLA(cm); H1-X2-X3 are on the west coast of India; X4-X8 are the Rossby pathway boxes; where as Y5-Y7 are the East Coast Pathway.

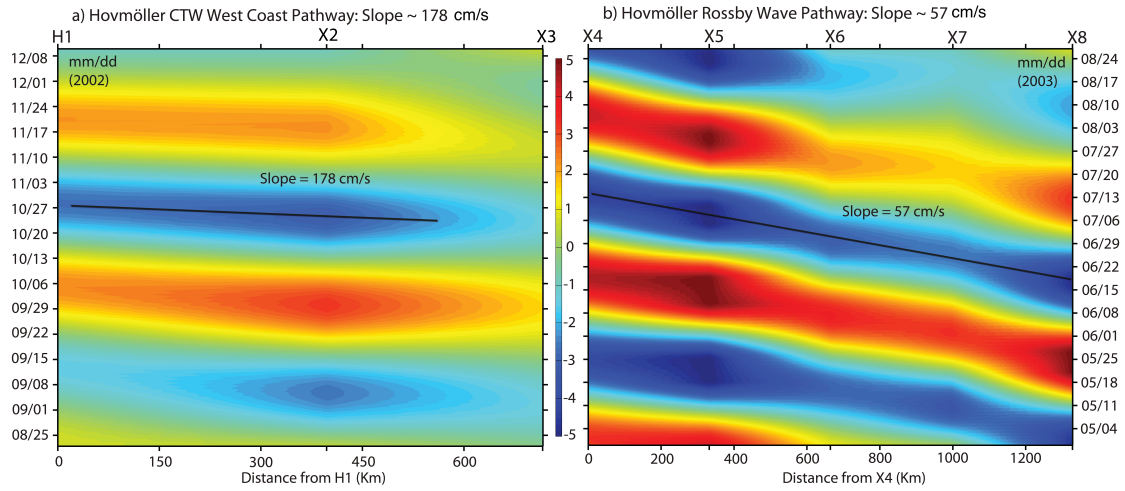


Figure 2.13: Hovmöller plots of 40-60 day band pass filtered AVISO SLA, as in Figure 2.12, expanded to get an approximate estimate of the propagation speeds of the signals: a) Boxes H1-X2-X3 on the west coast for the year 2002 ; b) Boxes X4-X8 on the Rossby wave pathway for the year 2003.

Max. Correlation Daily TA3 wind stress with other wind stress							
Wind Stress(WS)	TA1	TA12	TA2	TA3	TA4	TA5	TA6
TA3	0.4160	0.5532	0.5509	1.000	0.8379	-0.3357	0.4216
Lag	+1 day	+2 day	+1 day	0 day	0 day	+1 day	+1 day
WS Curl	C1	C12	C2	C3	C4	C5	C6
TA3	-0.3246	-0.6035	-0.4695	-0.7872	-0.7350	-0.1870	- 0.5508
Lag	-1 day	0 day	-1 day	-1 day	0 day	-3 day	+1 day

Table 2.2: Highest correlation of TA3 alongshore wind stress with other box wind stress and wind stress curl

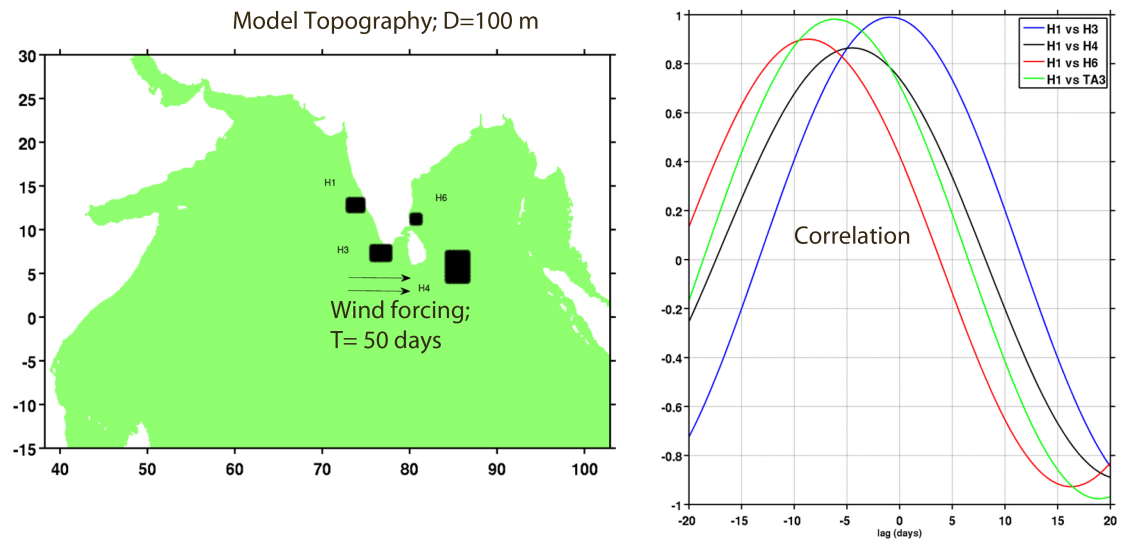


Figure 2.14: ROMS model domain and Correlations: 1) On the left: ROMS model domain; horizontal arrows indicate the large scale wind forcing schematic. The black boxes are chosen with same sizes as in the altimeter analysis in order to compare the correlations of SLA at H1 with SLA at H3, H4 and H6. TA3 represents the wind forcing. 2) on the right: Lagged correlation of SLA at H1 with SLA at H3, H4, H6 and Wind Stress at TA3. The corresponding lags at maximum correlations are similar to what we expected from regression models and coherence analysis: (H1 vs H3: -1 day; H1 vs H4: -4 days; H1 vs TA3: -6 days)

Vertical Kelvin wave propagation produced by a subsurface ridge

Laxmikant Dhage, Ted Durland, Ted Strub and Vincent Combes

Journal of Geophysical Research, Oceans
(IN PREPARATION)

Chapter 3: Vertical Kelvin wave propagation produced by a subsurface ridge

3.1 Introduction

Using numerical process modeling supplemented by analytical approximations, we examine the impact of a submerged ridge on a coastal Kelvin wave in a continuously stratified basin. We show that such a ridge projecting from the shoreline can scatter a horizontally propagating, single baroclinic mode Kelvin wave into both upward and downward propagating Kelvin waves emanating from the ridge top. We are motivated in particular by ADCP mooring observations of coastal trapped signals reported by Amol et al. (2014), showing evidence of both downward energy propagation (which they expected), and upward energy propagation (which they did not expect). Both directions of propagation were evident at the Kollam mooring, located just down the coastal wave guide from a protruding subsurface ridge on India's west coast. We suspect that such subsurface irregularities are common in the world's coastal topography. It is worth understanding how they might affect waves that propagate along, and are trapped to the coastline.

Previous studies have long sought to understand the dynamic effects of bathymetric irregularities in relation to the scattering of coastal trapped waves. Longuet-Higgins (1968) studied the generation of topographic waves (Double Kelvin waves) due to step-up/down topography for a barotropic system. Chao et al. (1979) looked at the scattering of continental shelf waves due to isolated topographic irregularities, again for a barotropic inviscid ocean. Killworth (1989a) looked at a coastally trapped Kelvin wave hitting a ridge in a barotropic system and Killworth (1989b) did the same for a more complex two-layered system. The above research, however, did not focus on the vertically propagating part of the solution in a continuously stratified basin. In later years, ER Johnson (1990) looked at the scattering of low-frequency Kelvin wave beams over a stepped topography and ER Johnson (1991) extending for continuously sloping topography. Both of these studies again involved a barotropic system and did not include vertically propagating beams as part of the solution.

Another set of studies which relate to this work is the generation of internal tides due to ridges and sea-mounts. Baines (1973) and Baines (1982) looked at the generation mechanisms of vertically propagating internal tides due to changes in topography. Holloway and Merrifield (1999) investigated internal tide generation through numerical studies with barotropic tidal forcing. All of the above studies provide a useful analogy to the vertical aspect of our problem. The dynamics are not identical, though, and the internal tide generation mechanism does not answer all the questions that arise in the Kelvin wave problem.

Since our purpose is to shed light on the basic physics of the problem, our modeling is highly idealized including only the most fundamental features required to produce a qualitatively relevant response. In light of the above motivation, we focus on a 30-day, 1st baroclinic mode incident Kelvin wave in stratification typical of the west coast of India. We restrict our modeling to an f -plane at the latitude of the Kollam mooring: 9.10°N . At this latitude, the Coriolis parameter changes rapidly along the west coast of India, but motions with 30-day periods are trapped to the coast (do not radiate Rossby waves), and such intraseasonal signals have been demonstrated to make important contributions to the local coastal circulation (Amol et al. 2012, Suresh et al. 2013, Amol et al. 2014, Dhage and Strub 2016). Furthermore, the mechanism that we investigate occurs over a small range of latitudes, over which the Coriolis parameter can be considered constant. Finally, we seek to understand the most fundamental aspects of the Kelvin wave-topography interaction, and insights from this study are likely to be applicable to situations at higher latitudes, where the f -plane approximation is more appropriate. In light of the Kollam mooring motivation, we model only ridges with a top at the 250 m depth, similar to the depth of the ridge south of the mooring. To demonstrate the important dynamics, we primarily investigate the effects of the ridge width (alongshore extent) on the basin response, with some additional consideration of ridge length (offshore extent).

We refer to the side of the ridge from which the incident Kelvin wave approaches as the upstream side, and the other side as the downstream side. The main part of our analysis focuses on a semi-infinite ridge, modeled as a ridge that extends from the Kelvin wave boundary at the coast completely across the numerical basin, with a sponge layer at the far end. An incident Kelvin wave can scatter into motions on the ridge top that will then force the downstream basin, and it can also scatter into waves that propagate along the upstream side of the submerged ridge. In the case of the semi-infinite ridge,

these latter waves cannot reach or affect the downstream basin - in the numerical model they are absorbed in the sponge layer far from the coast. When the length of the ridge is finite, they can propagate around the perimeter of the ridge and recombine with motions forced by propagation over the ridge top. After analyzing the semi-infinite ridge problem, both analytically and numerically, we use numerical experiments to examine how finite ridge lengths alter the solution.

The problem we study has some similarities to that studied by Nethery and Shankar (2007), who modeled the effect on the west coast of India of variability in the monsoon current flowing south of Sri Lanka. The vertical structure of this current does not project perfectly onto a single baroclinic mode of the basin, and it thus excites coastal waves containing a spectrum of vertical modes, which thereby exhibit vertical propagation. In our case, the incident wave structure does not in general project perfectly onto a single ridge-top baroclinic mode, and the resultant ridge-top flow does not project perfectly onto a single baroclinic mode of the downstream basin. A spectrum of vertical modes is excited, and vertical propagation is produced in each case. The solutions of Nethery and Shankar (*ibid.*) exhibited only downward energy propagation, but some of our solutions exhibit both downward and upward energy propagation in the downstream basin. We show that the degree to which upward propagation is evident depends on the vertical profile of the ridge-top alongshore current. This in turn depends on the width of the ridge, due to the vertical propagation of the ridge-top wave¹. Because of the dynamical similarity between our problems, we suggest that the Nethery and Shankar (*ibid.*) solutions could also have produced upward energy propagation, but that the vertical structure of the monsoon current was not conducive to this.

In section 3.2, we present an approximate analytical solution for the problem of a Kelvin wave propagating over a semi-infinite ridge. Section 3.3 describes the numerical model configuration, and section 3.4 compares the numerical model results with the approximate analytical model predictions. In Section 3.5, we discuss questions arising

¹It also depends on the structure of the ridge-top boundary current, but we do not analyze this in detail. In this draft we demonstrate the effect of the vertical structure of the downstream basin's Kelvin wave current at the intersection of the ridge-top and downstream basin domains. The connection between this current structure and that of the ridge-top Kelvin wave current at the same location is a matter of ongoing investigation. The two currents are not identical, because evanescent Poincare modes complete the solution near domain changes, and these modes are not included in the analytical approximate solutions.

from the solutions, exploring analytical approximations for alongshore currents as a KW boundary condition into the basin. In the later part of the section we show numerical solutions for parts of the problem that we do not address analytically. Our results are summarized in section 3.6.

3.2 Analytical Approximation

In this section we present analytical approximations for important aspects of the problem of a Kelvin wave propagating over a semi-infinite subsurface ridge in a continuously stratified ocean. We consider an incident wave of a single frequency and a single vertical mode, because we are interested in how the ridge can scatter a horizontally propagating wave into vertically propagating waves. Ours is not a rigorous approach, but the assumptions made are physically reasonable, and we test the validity by comparing the predictions with results of a linear numerical model. The analysis is on a northern hemisphere f -plane at a subinertial frequency, for which the Kelvin wave is the only free wave solution to the linear, in-viscid equations of motion. A time dependence of $e^{-i\omega_0 t}$ will be assumed wherever it is not included explicitly in the equations.

Figure 3.1 shows the geometry of the problem in a Cartesian coordinate system (x, y, z) , with the water surface at $z = 0$ and a solid boundary at $x = 0$. There are three distinct, flat-bottom domains: the upstream basin, the ridge top, and the downstream basin. In each, the motions can be projected onto a series of shallow-water, horizontal problems for the vertical modes of the particular domain. At an intersection between two domains, the sum of solutions on one side of the intersection must match that on the other side. We simplify the problem by considering only a match of the integrated alongshore energy flux at each intersection at the wall ($x = 0$), allowing us to treat only the Kelvin wave parts of the total solution. Thick arrows in Fig. 3.1 represent the permissible Kelvin wave solutions in each of the domains. A known incident Kelvin wave (A) in an upstream basin of depth H_b propagates along the boundary at $x = 0$ until it encounters a semi-infinite ridge at $y = Y_1$. The ridge is perpendicular to the basin boundary, has a water depth $H_r < H_b$, and extends from the boundary to $x = -\infty$. At $y = Y_1$, the incident wave excites Kelvin wave B along $x = 0$ on the ridge top. It also excites Kelvin wave D , which is trapped to the subsurface ridge and propagates toward $x = -\infty$ along $y = Y_1$. At $y = Y_2$, the ridge-top Kelvin wave B excites Kelvin wave C

in a basin of depth H_b . This wave propagates along $x = 0$ toward $y = \infty$. A radiation condition specifies that there is no incoming Kelvin wave from $x = -\infty$ along $y = Y_2$, so wave C is the only permissible Kelvin wave solution in the downstream basin.

We expect that in general, waves B , C , and D will each contain a spectrum of vertical modes, due to the failure of an upstream incident wave to project perfectly onto a single vertical mode of the adjacent downstream domain. The vertical modal solutions for wave D are special cases of the submarine canyon solutions developed by Grimshaw et al. (1985). In our case, the canyon is infinitely wide, the “continental slope” is horizontal, and the frequency is subinertial. The Poincare modes that complete the solution near $y = Y_1$, $z = -H_r$ are thus evanescent, and do not contribute to the energy flux budget. We are primarily concerned with predicting wave C , and we will address wave D only to the extent that it extracts energy flux from incident wave A . Evidence of this wave in the numerical results will be shown in the Discussion. A barotropic double Kelvin wave (Longuet-Higgins, 1968) can also propagate toward $x = -\infty$ along $y = Y_1$. Our numerical experiments show little evidence of this wave, likely because the incident wave is baroclinic. Accordingly, we will not include the double Kelvin wave in our approximation.

At the intersections between the various domains (at $y = Y_1$ and $y = Y_2$), the Kelvin wave solutions by themselves cannot necessarily meet all of the no-normal-flow boundary conditions, and they do not provide continuity of pressure and velocity across the intersections at every value of x and z . There are additional Poincare modes with imaginary wavenumbers that decay away from $(x = 0, y = Y_1)$ and $(x = 0, y = Y_2)$ on the scale of the appropriate deformation radius. These trapped solutions provide the pressure and velocity continuity, in addition to satisfying any boundary conditions that the Kelvin wave solutions fail to satisfy. An example of the individual Kelvin wave and evanescent Poincare solutions (together with their superposition) at a domain discontinuity in a two dimensional problem can be seen in Fig. 2 of Durland et al. (2009). An isolated evanescent solution cannot carry an energy flux, in which case the energy flux balance must be provided solely by the Kelvin waves. This is the foundation of our approximation, and it depends on $Y_2 - Y_1 \gg L_{dr}$, where L_{dr} is the appropriate deformation radius for the ridge-top domain. When this condition is not met and the solutions trapped to Y_1 and Y_2 overlap on the ridge top, additional energy flux can tunnel between the evanescent modes, thus degrading our approximation. A more rigorously complete treatment could include the evanescent Poincare modes at $y = Y_1$ and $y = Y_2$, as well as the barotropic

and baroclinic components of “wave D” along $y = Y_1$. For a lowest order approach however, we proceed under the assumption that the energy flux balance is dominated by the Kelvin wave contributions. We then compare our solutions with numerical results for progressively narrower ridges, to determine the validity limits of our approximations. Velocities, pressures and energy flux values in what follows refer only to the Kelvin wave solutions.

3.2.1 Horizontal energy flux balances

Vertically propagating Kelvin waves can carry a vertical energy flux, but all following references to energy fluxes and their balances apply only to the horizontal fluxes. The alongshore fluid velocity (V) of the Kelvin wave is in exact geostrophic balance with the pressure (P):

$$V = (\rho_0 f_0)^{-1} \partial_x P, \quad (3.1)$$

where f_0 is the Coriolis parameter and ρ_0 is the Boussinesq mean density. In a periodic solution, the period averaged alongshore horizontal energy flux is

$$F = \int_{z=-H}^0 dz \int_{x=-\infty}^0 dx V P / 2. \quad (3.2)$$

Taking advantage of (3.1) and the fact that the Kelvin wave decays toward $x = -\infty$, the energy flux at a given y_0 is

$$F = (2\rho_0 f_0)^{-1} \int_{z=-H}^0 dz \int_{x=-\infty}^0 dx \partial_x P^2 / 2 = (4\rho_0 f_0)^{-1} \int_{z=-H}^0 dz P^2(x = 0, y_0, z). \quad (3.3)$$

At each of the domain intersections, this integral evaluated for the wave on one side of the intersection must equal the integral evaluated for the wave on the other side of the intersection.

We make the further assumption that the cross-intersection energy flux balance holds at every z level. This may not be precisely true, but it is a reasonable lowest order expectation. For instance, this assumption forces the energy flux into the downstream basin at $y = Y_2$ to emanate from depths shallower than the submerged ridge top, rather than from the solid boundary below that level. Applying this principle at $y = Y_1$ implies

that the energy flux in wave B comes from the incident wave energy flux above $z = -H_r$, and the energy flux in wave D comes from the incident wave energy flux below $z = -H_r$. Consequently, we expect the following matches of Kelvin wave pressures along the solid boundary ($x = 0$) at the domain intersections:

$$P_B(x = 0, y = Y_1, z) = P_A(x = 0, y = Y_1, z), \quad -H_r < z < 0, \quad (3.4)$$

$$P_D(x = 0, y = Y_1, z) = P_A(x = 0, y = Y_1, z), \quad -H_b < z < -H_r, \quad (3.5)$$

$$P_C(x = 0, y = Y_2, z) = P_B(x = 0, y = Y_2, z), \quad -H_r < z < 0, \quad (3.6)$$

$$P_C(x = 0, y = Y_2, z) = 0, \quad -H_b < z < -H_r. \quad (3.7)$$

The subscripts on P refer to the Kelvin waves shown in Fig. 3.1.

3.2.2 Vertical mode projections

For a given profile of buoyancy frequency, $N(z)$, we solve the vertical eigenvalue problems in each of the domains to yield the structures of the vertical modes, and their associated Kelvin wave speeds (eigenvalues). For the upstream and downstream basins (depth H_b), these are labelled $Z_{bn}(z)$, $-H_b < z < 0$, and C_{bn} , $n = 0, 1, 2, \dots$, where $n = 0$ denotes the barotropic mode.² For the ridge top domain (depth H_r), they are labelled $Z_{rn}(z)$, $-H_r < z < 0$, and C_{rn} . The associated deformation radii are $L_{bn} = f/C_{bn}$ and $L_{rn} = f/C_{rn}$. In each domain, the eigenfunctions are normalized so that

$$\int_{-H}^0 dz Z_m Z_n = \delta_{mn}, \quad (3.8)$$

where δ_{mn} is the Kronecker delta. For each vertical mode n , the expressions for the Kelvin wave pressure and velocity are:

$$Pk_n = P_n Z_n(z) \exp \left[\frac{x}{L_n} + i\omega_0 \left(\frac{y}{C_n} \right) \right] e^{-i\omega_0 t}, \quad (3.9)$$

$$Vk_n = 1/(A_0 f_0 L_n) Pk_n \quad (3.10)$$

²Although the incident wave A is baroclinic, it will in general project onto the ridge-top barotropic mode, and the ridge-top pressure may project onto the barotropic mode in the downstream basin.

The $e^{-i\omega_0 t}$ factors out of summations of vertical modes and will be implied but not explicitly included in the equations to follow.

The pressure of the incident wave (A) has a unit amplitude, a vertical structure $Z_{b1}(z)$, and a spatial phase of 0 at $y = Y_1$. The ridge-top pressure of wave B at Y_1 is

$$P_B(x=0, y=Y_1, z) = \sum_{n=0}^{\infty} P_{Bn} Z_{rn}(z), \quad (3.11)$$

where the ridge-top modal amplitudes are calculated from the pressure match with Z_{b1} :

$$P_{Bn} = \int_{z=-H_r}^0 Z_{b1}(z') Z_{rn}(z') dz'. \quad (3.12)$$

The full solution for the pressure of Kelvin wave B is

$$P_B(x, y, z) = \sum_{n=0}^{\infty} P_{Bn} Z_{rn}(z) \exp \left[\frac{x}{L_{rn}} + i\omega_0 \left(\frac{y - Y_1}{C_{rn}} \right) \right], \quad -H_r < z < 0. \quad (3.13)$$

The vertical structure of Kelvin wave B is y dependent, so the pressure match that determines wave C will depend on the width of the ridge ($Y_2 - Y_1$):

$$P_C(x=0, y=Y_2, z) = \sum_{m=0}^{\infty} P_{Cm} Z_{bm}(z) \quad (3.14)$$

$$= \sum_{n=0}^{\infty} P_{Bn} Z_{rn}(z) \exp[i(\omega_0/C_{rn})(Y_2 - Y_1)], \quad -H_r < z < 0, \quad (3.15)$$

$$= 0, \quad -H_b < z < -H_r. \quad (3.16)$$

The complex modal amplitudes for wave C are

$$P_{Cm} = \sum_{n=0}^{\infty} P_{Bn} \exp[i(\omega_0/C_{rn})(Y_2 - Y_1)] \int_{z=-H_r}^0 Z_{bm}(z') Z_{rn}(z') dz', \quad (3.17)$$

and the full solution for the pressure of wave C is

$$P_C(x, y, z) = \sum_{m=0}^{\infty} P_{Cm} Z_{bm}(z) \exp \left[\frac{x}{L_{bm}} + i\omega_0 \left(\frac{y - Y_2}{C_{bm}} \right) \right], \quad -H_b < z < 0. \quad (3.18)$$

The infinite summations above are truncated to include a finite number of vertical modes

that provide reasonable convergence.

The velocities for waves B and C are

$$V_B(x, y, z) = (\rho_0 f_0)^{-1} \sum_{n=0}^{\infty} \frac{P_{Bn}}{L_{rn}} Z_{rn}(z) \exp \left[\frac{x}{L_{rn}} + i\omega_0 \left(\frac{y - Y_1}{C_{rn}} \right) \right], \quad (3.19)$$

$$V_C(x, y, z) = (\rho_0 f_0)^{-1} \sum_{n=0}^{\infty} \frac{P_{Cn}}{L_{bn}} Z_{bn}(z) \exp \left[\frac{x}{L_{bn}} + i\omega_0 \left(\frac{y - Y_2}{C_{bn}} \right) \right]. \quad (3.20)$$

3.2.3 Limitations of the approximate solution

The approximate solution depends on a pressure match at a domain discontinuity, which in turn depends on all of the alongshore energy flux being carried by Kelvin waves. This latter requirement is satisfied for an incident basin Kelvin wave encountering a shallower, semi-infinite shelf, or for an incident Kelvin wave on a semi-infinite shelf encountering a drop into a deeper downstream basin. Evanescent Poincare modes that are trapped to either of these domain discontinuities cannot carry an energy flux.

In the case of the finite-width ridge, however, evanescent modes can tunnel an alongshore energy flux if the decaying modes trapped to the two domain discontinuities overlap between the discontinuities. The amount of the energy flux depends on the amplitudes of the decaying modes at the region of overlap (or alternately, the amplitude of one at the location of the other discontinuity). For a particular vertical mode, an evanescent Poincare mode will decay from a domain discontinuity at the relevant deformation radius. The deformation radii for the barotropic and first two baroclinic modes on the 250 m deep shelf are roughly 2200, 52 and 23 km. The evanescent barotropic modes atop a ridge of realistic width would clearly have significant overlap, but we still do not expect them to carry a significant energy flux because the associated alongshore velocity is proportional to the inverse of the deformation radius. As a lowest order prediction, we would expect the approximate solution to degrade as the ridge width decreases to the order of perhaps two deformation radii of the first baroclinic mode, or roughly 100 km. This prediction in itself can be problematic, because the energy fluxes in the individual vertical modes are not necessarily orthogonal: the velocity of one mode can act on the pressure field of another. Further analysis is beyond the scope of this work, and we rely now on comparisons of the approximate solutions with numerical solutions.

Because of the difference between vertical eigen solutions on either side of a domain

discontinuity, the Kelvin wave pressure matches at $(x = 0, y = Y_1)$ and $(x = 0, y = Y_2)$ imply that the Kelvin wave pressures *do not* match at Y_1 and Y_2 for $x \neq 0$. The Kelvin wave velocities also do not, in general, match at Y_1 and Y_2 . The velocity matches, and the pressure matches for $x \neq 0$ must be provided by the evanescent modes, which we have ignored.

3.3 Numerical Model

For the purpose of this paper, we consider the true response of an upstream Kelvin wave propagating over a ridge to be given by the numerical solutions, for which we use the Regional Ocean Modeling System (ROMS) (Shchepetkin and McWilliams, 2005). To these solutions we will compare the solutions described in Section 3.2, which we refer to as the “approximate analytic solutions.” For best comparison with the approximate analytic solutions, ROMS is configured without viscosity, without non-linear momentum terms and with a constant Coriolis parameter, appropriate for 9°N . The basin depth is 3000 m, and the stratification is sub-sampled at 40 sigma levels from the stratification used in the approximate solution (consistent with values from the 2009 World Ocean Atlas along the west coast of India). Horizontal grid spacing is $5\text{ km} \times 5\text{ km}$. There is a solid meridional eastern boundary at $x = 0$, and sponge layers along the northern and western boundaries, with horizontal viscosity of $1500\text{ m}^2/\text{s}$ for 100 km away from the western boundary. To simulate a semi-infinite ridge, the offshore ridge projects from $x = 0$ to the sponge layer at the western boundary. The southern edge of the ridge ($y = Y_1$) is at 900 km from the southern boundary of the model domain, and the northern boundary is between 3000 and 6000 km from the southern boundary, depending on the experiment. The ridge top is at a depth of 250 m for all experiments.

The bathymetry for the ROMS configurations of the above scenarios is shown in Figs. 3.2 b) and 3.4, along with the depths of the sigma levels for undisplaced fluid in the basin. Because ROMS uses terrain following (sigma) vertical coordinates, the model is unstable for a bottom slope that is too steep. The maximum recommended value of the slope parameter ($|\frac{h_2 - h_1}{h_2 + h_1}|$) is 0.25. For this reason, the sides of the subsurface ridges are not vertical; a possible source of discrepancy between the ROMS and approximate solutions. The slope of the bathymetry along the ridge is smoothed with a slope parameter of 0.20. This smoothing leads to a gradually sloping of the ridge edges at $y = Y_1$ and $y = Y_2$.

The slope deformation of the sigma levels between a basin and the ridge top is shown in Fig. 3.2 a).

Although we are initially motivated by observations of vertically propagating coastal waves on the west coast of India, our solutions clearly are not intended to represent realistic solutions over the full range of latitudes implied in the model configuration. Our intent is to show the effect on a Kelvin wave of the large change in depth that occurs at both the upstream and the downstream edge of a ridge. Each of these effects occurs over a small enough range of latitudes that the dominant local physics can be approximated by f -plane dynamics. The large range of latitudes (y coordinate) for which we show solutions just simplifies the interpretation of what happens at the depth discontinuities.

A first baroclinic mode Kelvin wave is generated at the southern boundary by imposing the appropriate meridional velocity there, with a sinusoidal time dependence at a 30 day period. The maximum amplitude for the meridional velocity forcing is 0.06 m/s . After transients generated by the initial wavefront have been absorbed by the sponge layers, a time series two periods long is regressed onto a 30 day cycle to determine the amplitude and phase at each point in the domain.

Because we expect a y dependence of the ridge-top solution (eq. 3.15), we begin by examining a ROMS solution for a semi-infinite shelf, extending from $y = Y_1$ to the northern boundary. This is referred to as the shelf solution, and it will be compared with a comparable approximate shelf solution. We then calculate ROMS solutions for finite ridge widths of $Y_2 - Y_1 = 600, 200, \text{ and } 120\text{ km}$. The comparable approximate solutions use vertical profiles from the approximate shelf solution for the pressure matches at $y = Y_2$, and we expect that these approximations will degrade as the width is decreased, due to tunneling by the evanescent modes.

ROMS does not explicitly provide pressure as an output. Potential temperature and salinity from the output is used to obtain the potential density profile at each grid point (using the linearized equation of state). The vertical integration of the hydrostatic balance from surface to a certain depth provides the pressure at that depth. The pressure perturbation associated with the wave dynamics is obtained after removing the mean background hydrostatic pressure.

3.4 Results

This section displays both the ROMS and the approximate solutions for the scenarios described above. For both ROMS and approximate solutions, each figure shows a y - z contour plot of the perturbation pressure amplitude (panel a) and phase (panel b) at $x = -\Delta x/2$, the closest that the pressure grid points get to the boundary at $x = 0$ in the ROMS staggered C-grid. However, the pressure match that conserves alongshore energy flux is at $x = 0$, in the approximate solution. Thus, the figures for the approximate solution at $x = -\Delta x/2$ show a slight discontinuity at domain intersections in the approximate analytic solutions.

3.4.1 Response of a shallow shelf to an incident 1st mode Kelvin wave

To understand the shelf response on the ridge-top we designed a numerical model with a semi-infinite shelf. Panel b) of Figure 3.2 shows the bathymetry of the domain. A forced mode-1 KW propagates from the southern boundary and hits the southern edge of the shelf ($y = Y_1$) to generate the shelf response on the ridge-top. In the Panel c) of Fig. 3.2, we show a snapshot of alongshore currents from the ROMS solution for the shelf scenario. The zero crossing of the incident Kelvin wave is at ~ -890 m in the upstream basin, so the incident alongshore currents are unidirectional above the 250 m depth of the shelf. Nevertheless, the alongshore currents along the shelf quickly develop a bi-directional vertical structure. The pressure match at the southern edge of the shelf includes a significant contribution from the shelf's barotropic mode, but this mode contributes little to the alongshore velocity. This is because the Kelvin wave velocity is inversely proportional to the deformation radius, and the deformation radii for the barotropic and first baroclinic modes above the shelf are roughly 2200 km and 52 km, respectively.

The approximate analytical solution with the pressure match at ($y = Y_1$) is compared with the numerical ROMS solution. Figure 3.3 I a) and I b) show the amplitude and phase of ROMS perturbation pressure at $x = -\Delta x/2$, extracted through a least-squared regression analysis in YZ for a 30 day period, where as, II a) and II b) show the analytical approximate solution amplitude and phase for the same. The slight discontinuity at the domain intersection in the approximate solution at $x = -\Delta x/2$ (mentioned above) is evident.

The approximate solution gives a very close match with the numerical solution. The incident KW pressure has an amplitude maximum near the surface, and it decreases with depth with no vertical phase change above the level of the ridge top. On the shelf, however, the amplitude and phase show a multi-modal vertically propagating KW beam pressure structure emanating from the southern edge of the shelf. The multiple modes are demonstrated by the horizontally changing vertical structure of the amplitudes over the shelf.

As these modes travel with different phase speeds, the vertical pressure structure depends on y . For instance, the pressure amplitude is highest near the surface at the southern edge of the ridge. At $y = 2000$ km, however, the pressure amplitude is greater near the bottom. The y -dependence of the vertical structure on top of the shelf implies different boundary conditions at $y = Y_2$ for ridges of different widths, which then forces the responses in the downstream basin.

In the next section, we focus our attention on finite width ridges, where the width of the ridge is varied and the corresponding basin responses past the ridge are compared.

3.4.2 Basin response downstream of a finite width ridge

In the previous section, the ROMS model run and solutions from the analytical approximations showed that the vertical structure on top of the semi-infinite shelf is dependent on the y -location. This suggests that different widths of ridges would have different boundary conditions for the basin response past the ridge. In this section, we display the output from several numerical model runs with varying ridge widths: 1) 600 km width, 2) 200 km width, and 3) 120 km width. The first two are categorized as wide ridges (wider than twice the mode 1 baroclinic Rossby radius of deformation on the shelf: $2\lambda_1 \simeq 104$ km) and the last one as a narrow ridge (close to the limit of twice the Rossby radius of deformation on the ridge top).

To obtain the response in the downstream basin for the analytical approximation, we match the pressure at the wall at the southern end of the ridge ($y = Y_1$) and at the northern end of the ridge ($y = Y_2$).

3.4.2.1 Wide Ridges: 600 km and 200 km

The top panel of Figure 3.4 shows the bathymetry used for the ROMS model run for a) a 200 km wide ridge and b) a 600 km wide ridge. The southern boundary is to the right of the domain at $y = 0$, where the known incident mode 1 KW is forced. The wall representing the west coast of India is located along $x = 0$. The bottom panels show the vertical slope of the ridge on either side. Black arrows show the northern and southern end of the ridges where the pressure match is carried out in the approximate solution (with straight vertical walls) to obtain the basin response on the ridge-top and past the ridge.

Figures 3.5 and 3.6 show the amplitude and phase for the KW perturbation pressure for these 2 cases: I) ROMS model run; and II) Basin Response through the analytical approximations, for a 30 day period. Panel a) represents the amplitude and panel b) shows the associated phase. The basin response past the ridge for 600 km and 200 km width ridges are different, which can be seen in both amplitude and phase plots of ROMS as well as the analytical approximations. The robust feature in both of the cases is a distinct upward propagating KW beam in amplitude and phase plots emanating from the top of the ridge at $y = Y_2$. This upward propagating KW beam amplitude intensifies as it propagates upward. The downward propagating KW beam, however, is lower in amplitude, possibly because the stratification decreases with depth.

Low latitude f -plane internal Kelvin wave (IKW) beams propagate vertically on a sloping IKW ray path, which is a function of depth, due to $N(z)$:

$$\frac{dz}{dy} = \pm \frac{\sigma}{N(z)}, \quad (3.21)$$

where $N(z)$ is the buoyancy frequency (Romea, 1983). These are plotted as green lines in Figures 3.5-3.7. The obtained amplitude and phase structures approximately follow the IKW ray path (also known as Wentzel–Kramers–Brillouin [WKB] ray path when derived with the WKB approximations) with the existence of multiple modes in the downstream basin.

The green lines representing IKW ray paths follow the upward and downward beams fairly closely. The phase travels from red to blue (in the negative direction; Green arrow), suggesting a downward phase propagation (upward energy propagation) in the

top 250 meters and a upward phase propagation (downward energy propagation) below 250 meters (across the IKW rays).

One of the differences between the 600 and 200 km width ridges is the width of the upward propagating KW beam. The amplitude and phase plots for the 600 km width ridge show a wider upward propagating beam when compared to the 200 km width ridge (Figure 3.5 and 3.6). We believe this is due to the different vertical structures of the forcing at $y = Y_2$. The criteria to generate a wider upward propagating beam in relation to the vertical structure at the northern end of the ridge is addressed in detail in section 3.5.

There are several differences between the ROMS and analytical approximation amplitude and phase plots. For instance the amplitude intensification of the upward propagating beam, as it propagates upward, is more pronounced and robust in the approximate solution when compared to ROMS. This is seen in the greater pressure amplitude of the approximate solution at $y = 2000\text{ km}$ along the IKW ray. Overall the match between the approximate solution and ROMS is fairly good for the first 100 - 200 m below the level of the ridge top, but less good below that. We believe that the increasingly coarse sigma level spacing in the deep basin may contribute to this discrepancy (see Fig 3.2 a). ROMS uses terrain following sigma co-ordinates in Z with a higher resolution of sampling for first few hundred meters below the free surface, and a progressively coarser resolution of sampling at greater depths, following the bathymetry. Another key difference between the ROMS model and the approximate solution is that the edge of the ridge in the latter problem has a sharp corner with a straight vertical wall in Z, whereas ROMS has smoothly rounded bathymetry with a gradual sloping edge of the ridge. We believe this may contribute to the difference in width of the upward propagating beam between the approximate and numerical solutions.

The ROMS solutions contain the trapped Poincare modes at the ridge edges, which are not present in the approximate solutions. Much of the discrepancy between ROMS and the analytical approximations near the ridge corners can be associated with these differences.

3.4.2.2 Narrow Ridge: 120 km

Figure 3.7 shows the amplitude and phase for the perturbation pressure structure for : I) ROMS model run II) approximate analytic solutions for the narrow 120 km ridge. The panel a) represents the amplitude and the panel b) shows the associated phase for a 30 day period sinusoid. The distinct change from the wide ridges to this narrow one is that the upward propagating KW beam as in the earlier cases is not as robust. This is especially evident from the plots of ROMS amplitude. There is also a significant difference between ROMS and the approximate solution. The phase plot of ROMS suggests that the phase is moving upward (green arrow) throughout, suggesting a downward propagation of energy. On the other hand, the approximate solution continues to show an upward propagating beam. Compared to the wide ridge, however, this upward propagating beam is much narrower in pressure amplitude and phase for the narrow ridge.

As discussed in the earlier Section 2.3, for narrow ridges, the ridge trapped Poincare modes interact with each other significantly enough to contribute an alongshore energy flux into the downstream basin. The approximate solution does not include this energy flux and so degrades as the ridge width decreases to the order of two deformation radii of the first baroclinic mode (~ 104 km). The narrower the width of the ridge, the greater is the contribution of the trapped modes to the alongshore energy fluxes. Thus, narrow ridges don't have a sufficient width to generate a strong upward propagating beam in the ROMS solution, as seen in Figure 3.7.

3.5 Discussion

In the last section we discussed the influence that the ridge width has on the response of the downstream basin. Pressure solutions for 600 km and 200 km width ridges showed different widths of the upward propagating KW beams past the ridge. We have noted that the Kelvin wave currents are not continuous between the ridge top and the downstream basin ($y = Y_2$). In this section we address the issue by examining how the vertical profile of the Kelvin wave current at the beginning of the downstream basin ($y = Y_2$) affects the characteristics of the upward propagating beam.

In the latter part of this section we discuss model solutions for ridges with finite lengths. Evidence for the wave trapped to the subsurface ridge (wave D, Fig,1) is

shown, and the downstream basin response to the finite-length ridge is compared to the semi-infinite ridge solution.

3.5.1 Alongshore Velocity in the downstream basin

Figure 3.8 shows the alongshore velocity amplitudes at the wall for both the ROMS and the approximate analytical solutions for 600 km and 200 km ridge widths. Unlike the approximate solution, the ROMS velocities are continuous at the domain discontinuities. The continuity in the ROMS velocity is provided by the trapped modes not present in the approximate solutions. Velocities on top of the ridge next to the bottom indicate vertical propagation caused by scattering of multiple shelf-KW modes. In the ROMS solution these modes appear smoothed by processes generated in the trapped modes at the leading edge of the ridge. Velocities near the surface are reduced in both ROMS and approximate solutions for the wider ridge. For the narrower ridge velocities in the ROMS solution maintain most of their strength near the surface.

In the downstream basin, velocity amplitudes show a wide and robust upward propagating KW beam for the 600 km width ridge. The 200 km width ridge has a narrower upward propagating KW beam. We are interested in how the different vertical structures at the northern edge of the ridge in pressure and alongshore currents are related to the different basin responses.

Figure 3.9 shows the alongshore current amplitude profiles in the deep basin next to the ridge at $y = Y_2$ and $x = 0$ for the two ridge widths [a) Approximate b) ROMS]. At $y = Y_2$, the KW basin boundary currents are determined by the KW pressure match at the discontinuity for the approximate solutions. In the ROMS solutions, alongshore velocities at $y = Y_2$ include components from both the KWs and trapped Poincare modes. The current amplitude profiles for both solutions include local broad maxima near the surface and sharper peaks just above the height of the ridge top. Surface currents are greater for the narrower ridge (especially for ROMS), while subsurface peaks are greater for the wider ridge.

3.5.2 Analytical Kelvin wave Current Boundary Conditions

In this section we examine the basin responses to different possible KW boundary conditions in the form of vertical structures of alongshore current at $y = Y_2$. We impose a boundary condition at $(x = 0, y = Y_2)$ for the Kelvin wave solutions in the downstream basin, and examine how changes in the vertical structure of this boundary condition affect the upward propagating beam. In particular we are interested in the relative importance of local surface maxima in comparison to that of the sharper subsurface peaks.

Figures 3.10 - 3.16 display the analytical solution past the ridge for various vertical structures of alongshore KW current amplitudes as the basin KW boundary conditions. We first start with a subsurface peak at the depth of the ridge top as KW boundary condition (Figure 3.10-3.11), followed by broad surface maxima (Figure 3.12). We next present the basin response for both maxima, with a stronger (Figure 3.13) or a weaker (Figure 3.14) subsurface maxima. Finally, we use smoothed versions of ROMS alongshore velocity amplitude profiles next to the downstream edge of the 200 km wide ridge (Figure 3.15) and the 600 km wide ridge (Figure 3.16).

The presence of the subsurface peaks in the KW boundary condition produces distinct upward and downward propagating KW beams. The width of these vertically propagating KW beams decrease as the width of the subsurface peaks in the KW boundary current is reduced. This is clearly seen in panels c where we plot alongshore velocity amplitude as a function of time and depth at $x = 0$, $y = 300$ kms downstream (dashed line in panels a and b). Note the decrease in the width of the amplitude in the colorbar in (Figure 3.10-3.11 c).

The presence of a broader local surface (0 - 100 m) maximum in the alongshore velocity amplitude at $y = Y_2$ is associated with a combination of horizontal propagation of energy (in the surface 100 meters) and broadly downward propagating KW modes. The time-series in panel c demonstrates a stronger horizontal propagation of amplitude and a weaker amplitude of downward propagating energy.

Figures 3.13-3.14 combines the effects of the broader surface local maxima with the effects of the subsurface velocity peaks in the KW boundary current profiles at $y = Y_2$. When the strength of the surface maximum is greater the basin response includes relatively stronger horizontal propagation of energy at the surface than in the subsurface vertically propagating KW beams (Figure 3.13). On the other hand, when the strength of the

surface maximum is weaker, the strength of the horizontal propagation of energy at the surface is also weaker than the upward propagating KW beam (Figure 3.14). These idealized profiles relate to the vertical structures of alongshore currents next to the downstream edge of the ridge in the ROMS solutions, in the subsurface peaks and the broader surface maxima in the alongshore velocity amplitudes. The narrower ridge has a stronger surface local maximum (Figure 3.9) relative to the subsurface peak similar to Figure 3.13. The wider ridge has a stronger subsurface peak relative to the surface maximum, similar to Figure 3.14. It's important to note that the ROMS velocity profiles include contributions from the trapped Poincare modes. However, the velocity profiles derived from the approximate analytic KW solutions (Figure 3.9) show a similar increase in relative strength of the subsurface peaks as the ridge becomes wider.

For better comparisons of the basin's analytical response to the ROMS solution, we used smoothed vertical velocity profiles at the upstream edge of the basin (Figure 3.9 b) as KW boundary conditions. Figures 3.15-3.16 present the analytical basin response to smoothed ROMS velocity profiles for the 200 km (Figures 3.15) and 600 km wide (Figures 3.16) ridges. These can be compared to the basin responses to more idealized velocity profiles in Figures 3.13 - 3.14 and more realistic ROMS basin responses in Figure 3.8 a). In Figure 3.8 a) the contribution from the trapped modes becomes negligible approximately 200 kms (2 Rossby radii) downstream of the ridge. In contrast the contributions of the trapped modes to the ROMS velocity profiles used as boundary conditions in Figures 3.15-3.16, become the part of the KW solutions that propagate through the entire basin. In spite of this contamination from trapped modes, the analytic representation of the basin response using the total ROMS velocity profiles includes the basic characteristics of the basin response to the idealized forcing (3.13-3.14) and the full ROMS response (Figure 3.8 a)). Those characteristics are : wider ridges result in a stronger upward propagating KW beam of energy; narrower ridges result in a stronger horizontal propagation of energy in a surface layer.

3.5.3 Ridge waves: Wave D

All of the previous numerical and analytical experiments were carried out for the fully extended submerged ridges. In reality, however, the submerged ridges are finite in length and the basin response past the ridge contains a contribution from ridge waves traveling

along the ridge. To explore the ridge wave (wave D) dynamics, we extract the cross-shore (U) currents along the fully extended ridge. The brown dotted lines in the upper 500 m (Figure 3.4 bottom panel a) indicate the XZ transect across which the currents along the ridge (U) are extracted. Figure 3.17 shows the amplitude and phase for these currents: panel a) north of the ridge and panel b and c) for south of the ridge. Along the southern side of the ridge, there are significant amplitudes of cross-shore currents. Phase contours for the same suggest the existence of a multi-modal vertically propagating ridge wave. This confirms that wave D exists and can extract energy from the incident KW. As expected for the fully extended ridge, the amplitude of the cross-shore currents (U) is very low on the northern transect (panel a), showing that the wave D is absorbed by the off-shore sponge layer. If the ridge is finite in length, however, wave D can propagate around the ridge and affect the downstream response. Along the northern side of the ridge, energy generated at $x = 0$ by the trapped modes cannot travel off-shore with the wall to the left.

3.5.4 Finite Ridges

As explained earlier, the motivation behind this work came from the observations of alongshore currents at Kollam mooring which sits close to the ridge-like structure along the west coast of India. The dimensions of the submerged ridge near Kollam were hard to model analytically, as the depth of the ridge varies spatially and makes it difficult to approximate with a single, simple ridge with fixed values for the width, length and the exact depth. In the previous sections, we discuss the effects of the different ridge widths on the upward propagation of energy in the downstream basin in the absence of ridge waves. In this section, we provide a discussion of ridge waves that affect the downstream basin response through their propagation around finite ridges. Because of the difficulty of obtaining analytic solutions for the topographic waves in a stratified ocean, results from the numerical model are shown. Figure 3.18 shows the dimensions of the ridge bathymetry for the numerical model. The depth of the ridge is 250 m and the offshore elongation is 160 kms. The model is 3000 m deep everywhere else in the domain. To compare to the fully extended solution with a least influence of the trapped modes, the ridge is 600 kms in width. The wall is at $x = 0$. The model is forced from the southern boundary with a 30-day sinusoid mode 1 KW. Panels a) show the amplitude and phase

of 30-day period alongshore currents after the model run is complete.

The finite ridge bathymetry produces a wider and higher amplitude KW beam [Figure 3.19 panel a)] when compared to the fully extended ridge model run [panel b)]. Profiles of alongshore velocity amplitude in the downstream basin next to the ridge (not shown) reveal much stronger peak at the depth of the ridge top than for the fully extended ridge. This also implies a stronger upward propagating beam. We believe the reasons behind these differences include the contribution of ridge waves traveling along the ridge and affecting the basin response past the ridge. Thus, for a wide finite ridge the propagation of ridge waves around the ridge strengthens the upward propagating KW beam. However, it does not change the qualitative nature of the downstream basin velocity response found for both approximate analytic and numerical solutions for extended ridges (Figures 3.8 and Figure 3.19).

3.6 Summary

Numerical process modeling supplemented by analytical analysis shows that submerged ridges projecting from the shoreline can scatter a horizontally propagating single baroclinic mode Kelvin wave into both upward and downward propagating Kelvin wave beams, emanating from the ridge top. Numerical model experiments in the form of semi-infinite (fully-extended) ridges are designed to prevent the ridge waves from traveling around the ridge to affect the basin responses. These are compared with the analytical approximate solutions. The semi-infinite shelf response to the incident single mode KW reveals along-shore dependence of the vertical structure in the form of multi-modal ridge-top KWs, suggesting that the width of the ridge is an important factor in determining the basin response past the ridge. The approximate analytical solutions confirm that the upward propagating beam becomes weaker and narrower as the width of the ridge gets narrower (approaching the order of two Rossby radii of deformation on the shelf-top).

A series of numerical model runs further demonstrate the effects of varying the widths of the extended ridges. Decreasing the ridge width from 600 km to 120 km greatly reduces the strength of the upward propagating beam. We hypothesize that over narrow ridges, the trapped solutions at the edges of the ridges overlap and interact to transmit horizontally propagating energy into the surface layer of the downstream basin. At the same time narrow ridges result in a weaker subsurface peak in velocity next to the ridge

top in the downstream basin. This decreases the amplitude of vertically propagating KW beams.

The relative strengths of horizontally propagating KW modes to that of vertically propagating KW modes, is explored with the help of broad surface maxima and sharp subsurface peaks in the alongshore KW velocity profiles as a boundary condition next to edge of the ridge in the downstream basin. When the strength of the subsurface peaks in the vertical profile of alongshore currents is greater, the basin response includes relatively stronger amplitudes of vertically propagating KW beams. On the other hand, when the strength of the surface maximum is greater, the strength of the horizontal propagation of energy at the surface is higher relative to the amplitudes of upward propagating KW beams in the downstream basin.

Numerical model runs are carried out for the somewhat more realistic case scenario in the form of a finite ridge for an incoming single mode baroclinic KW. The basin response past the ridge contains additional energy coming in the form of ridge waves. For the wide ridge considered here, the ridge wave strengthens the upward propagating KW beam compared to a semi-infinite ridge where the ridge waves are eliminated in the basin response. The qualitative nature of the upward propagating beam in the semi-infinite ridge, however, is not changed for the wide ridges. A more complete examination of the affect of the finite ridges of different lengths and widths is a topic for further study.

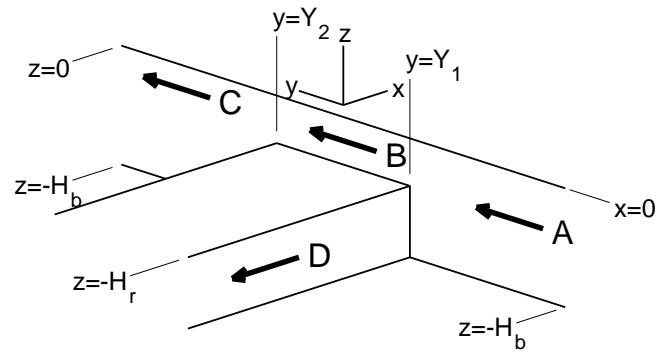


Figure 3.1: Schematic of a coastal Kelvin wave in a basin of depth H_b incident upon a semi-infinite ridge of depth H_r .

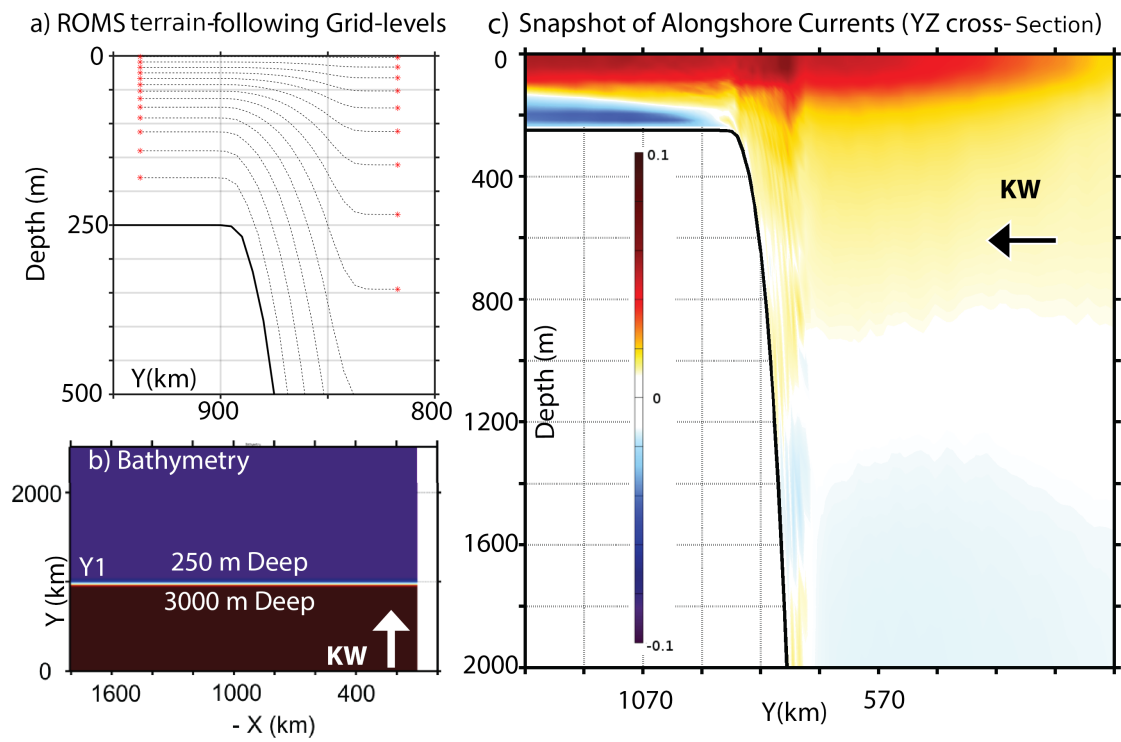


Figure 3.2: Panel a) and b) Show the bathymetry of a semi-infinite Shelf KW model including the terrain-following ROMS sigma-grid levels converging on ridge-top (coming from deep basin). Panel c) shows a snapshot of alongshore currents model run in YZ cross-section at wall.

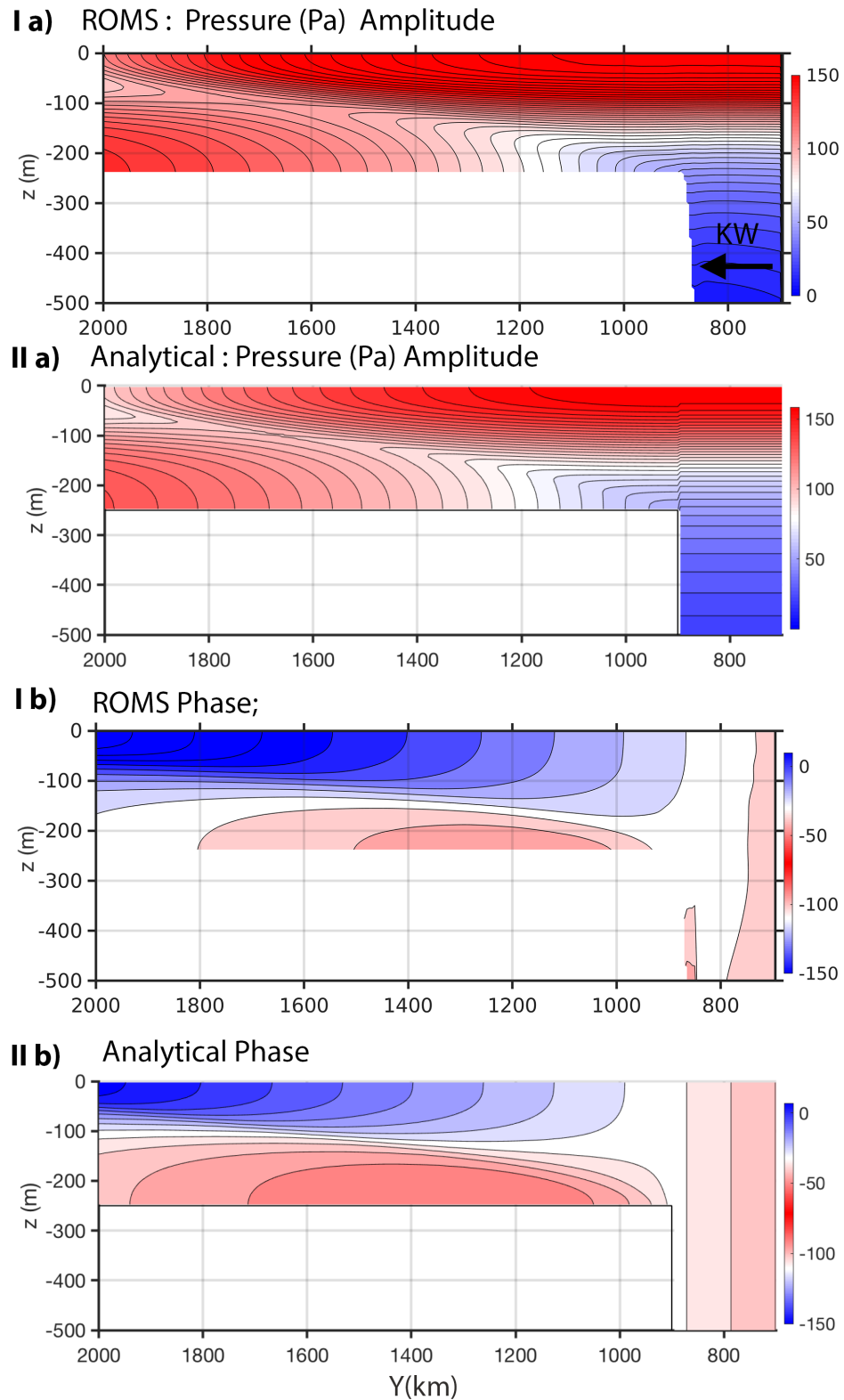


Figure 3.3: I) ROMS solution for amplitude (a) and phase (b) for a 30-day Kelvin wave incident upon a semi-infinite shelf. II) Approximate solution for amplitude (a panel) and phase (b panel).

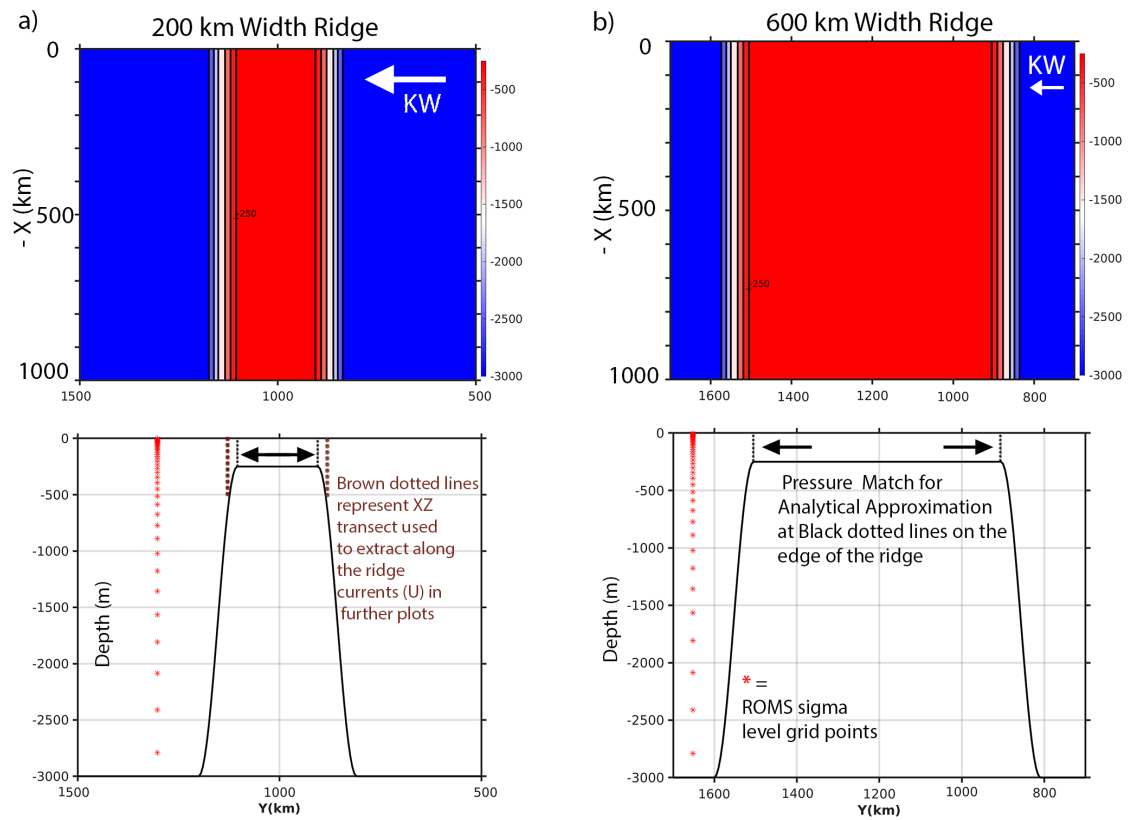


Figure 3.4: a) Bathymetry for a 200 km width ridge model run; b) Bathymetry for a 600 km width ridge model run. Top panel is in XY cross-section, whereas bottom panel is in YZ cross-section.

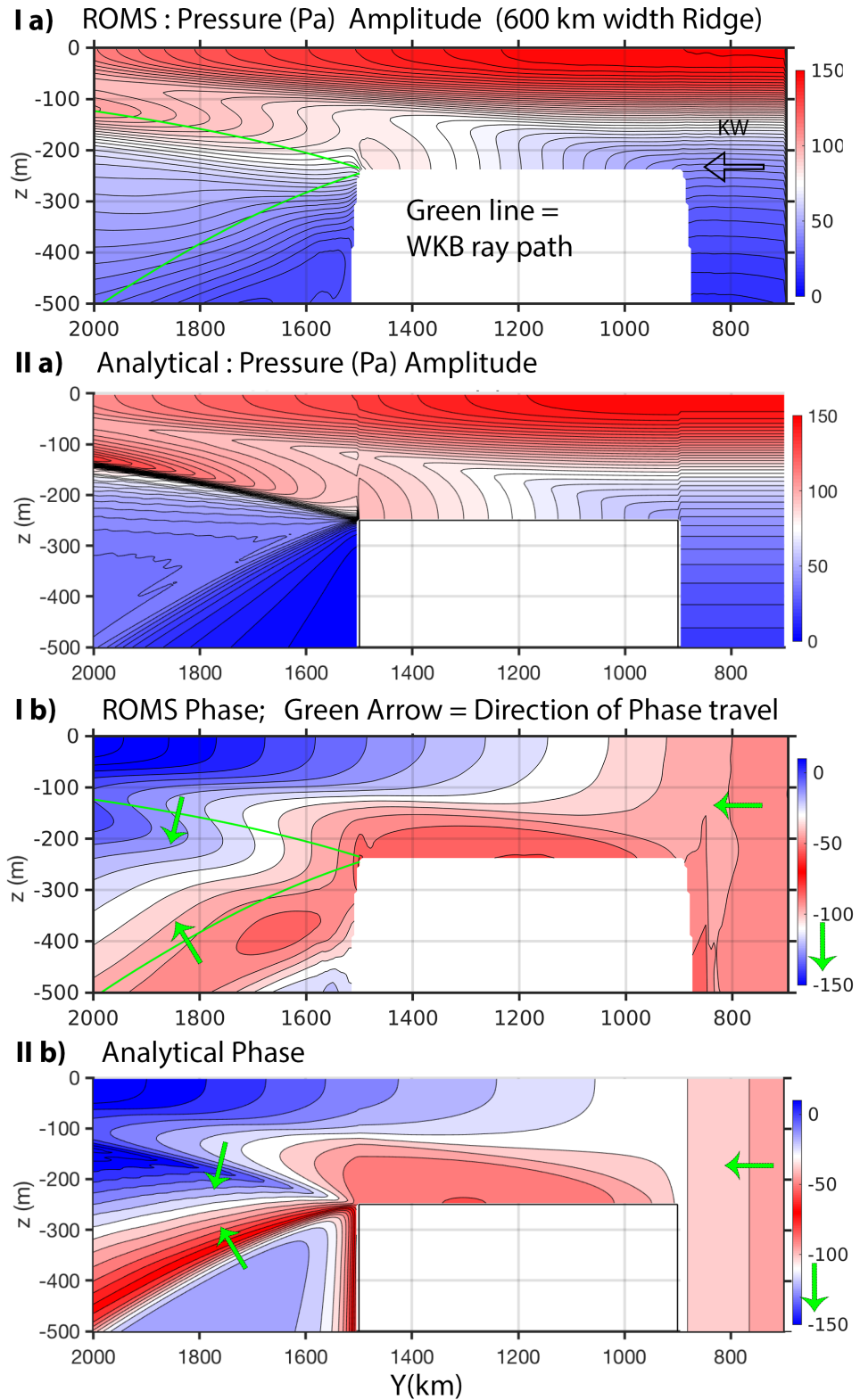


Figure 3.5: I) ROMS solution for amplitude (a) and phase (b) for a 30-day Kelvin wave incident upon a 600 km wide ridge. II) Approximate solution for amplitude (a panel) and phase (b panel).

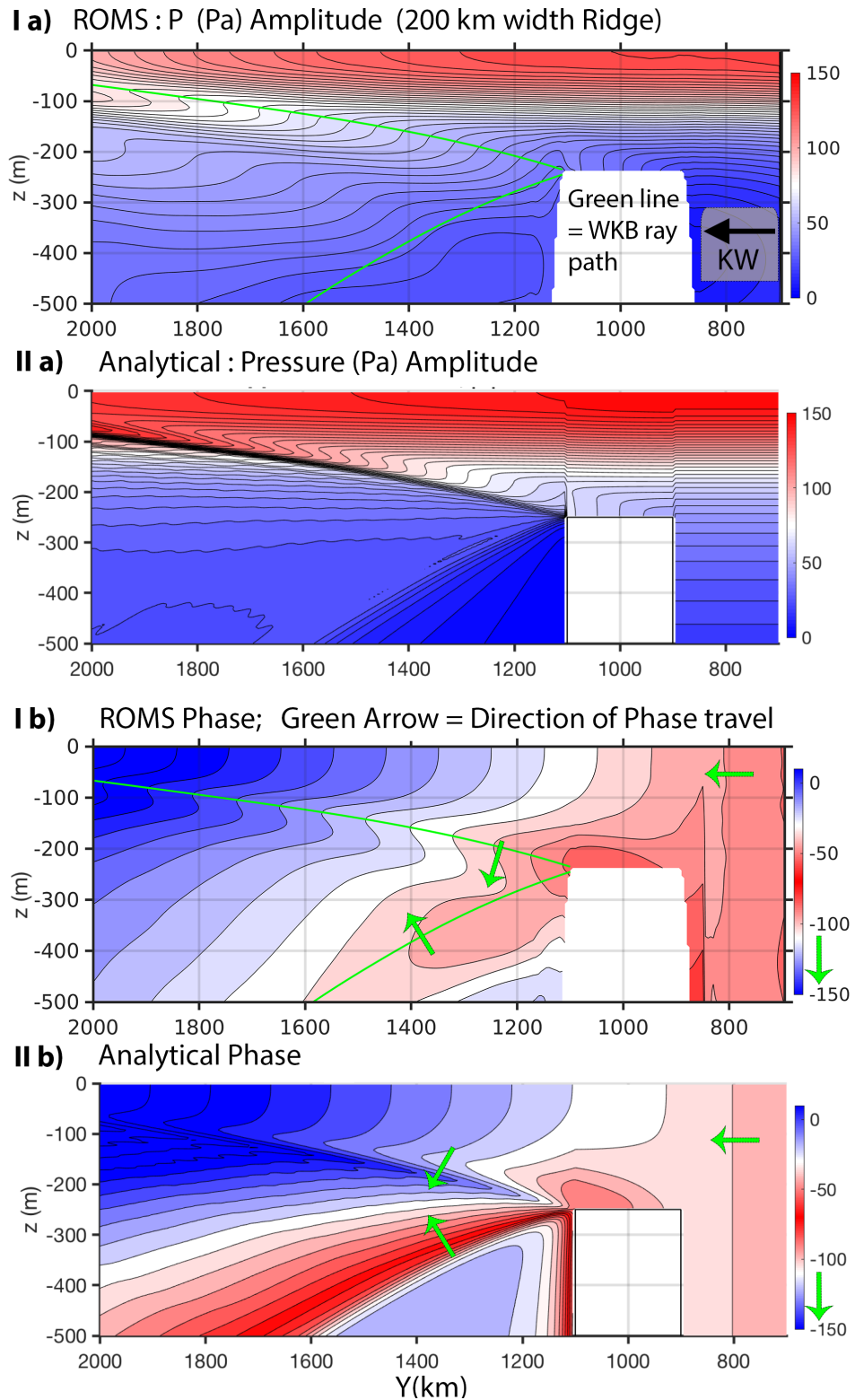


Figure 3.6: I) ROMS solution for amplitude (a) and phase (b) for a 30-day Kelvin wave incident upon a 200 km wide ridge. II) Approximate solution for amplitude (a panel) and phase (b panel).

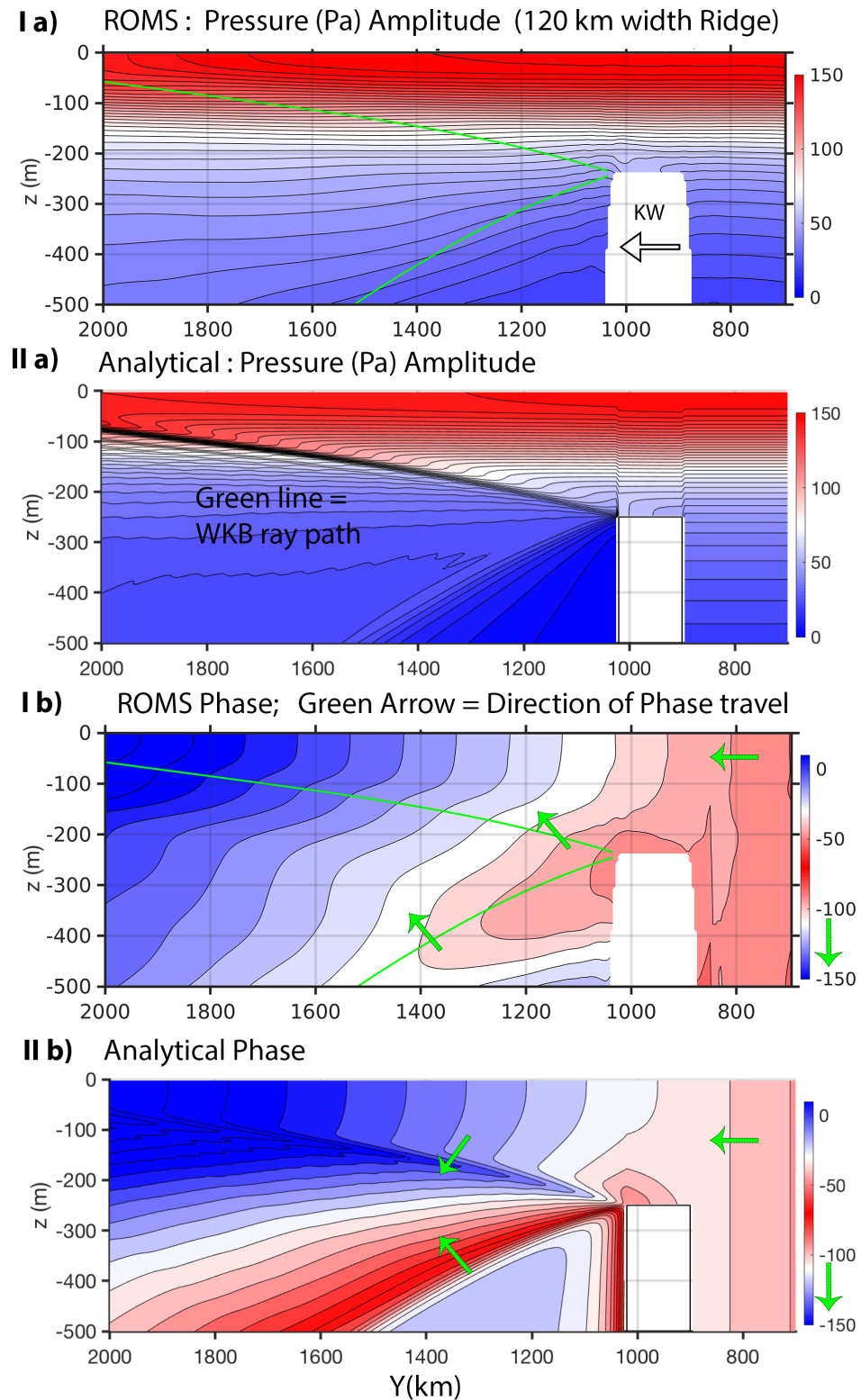


Figure 3.7: I) ROMS solution for amplitude (a) and phase (b) for a 30-day Kelvin wave incident upon a 120 km wide ridge. II) Approximate solution for amplitude (a panel) and phase (b panel).

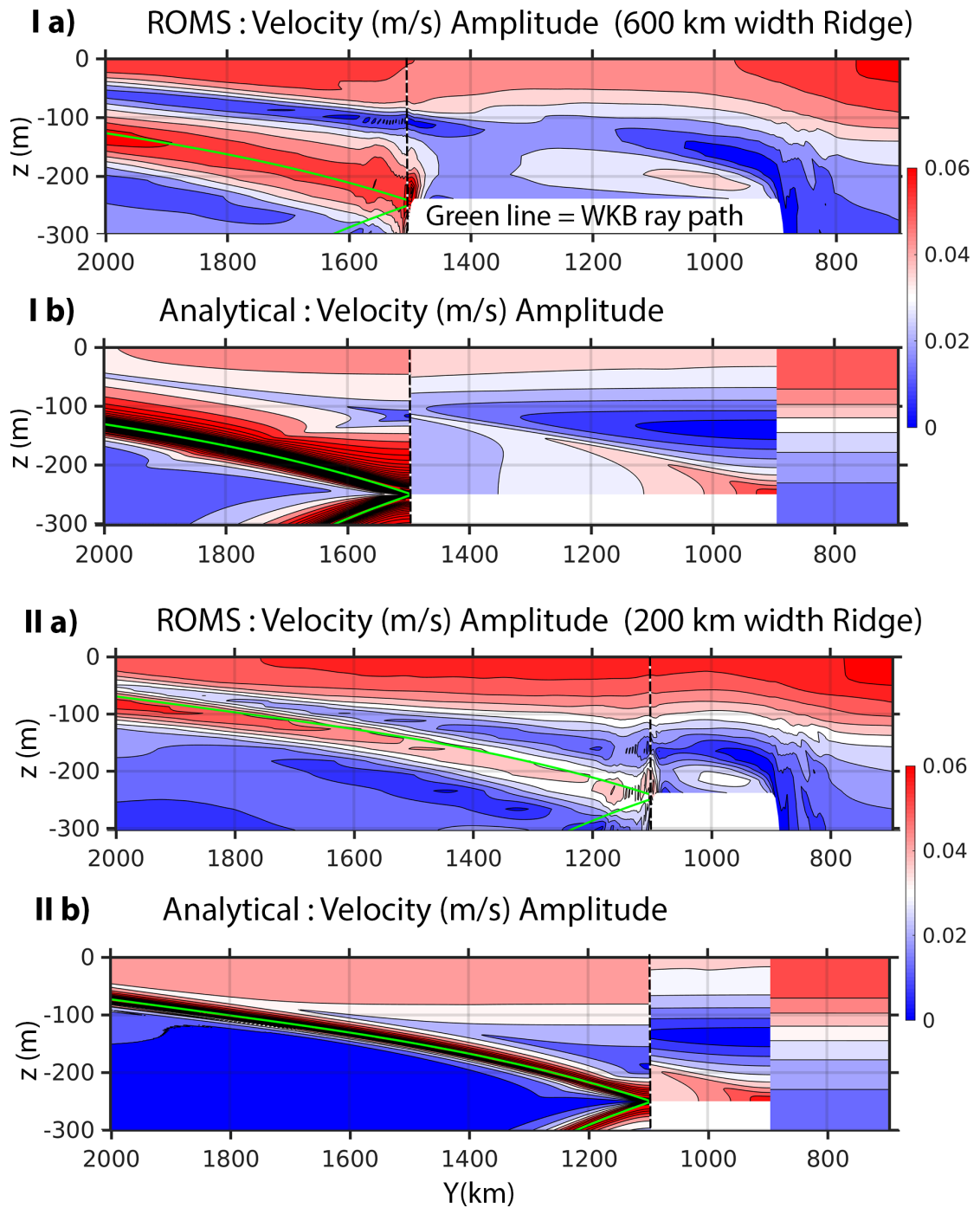


Figure 3.8: ROMS and Analytical approximate velocity amplitude solution for a 30-day Kelvin wave incident upon : I) 600 km wide ridge; II) 200 km wide ridge. The black dotted lines correspond to the transects in Z where the basin boundary currents are extracted for analytical and ROMS solutions.

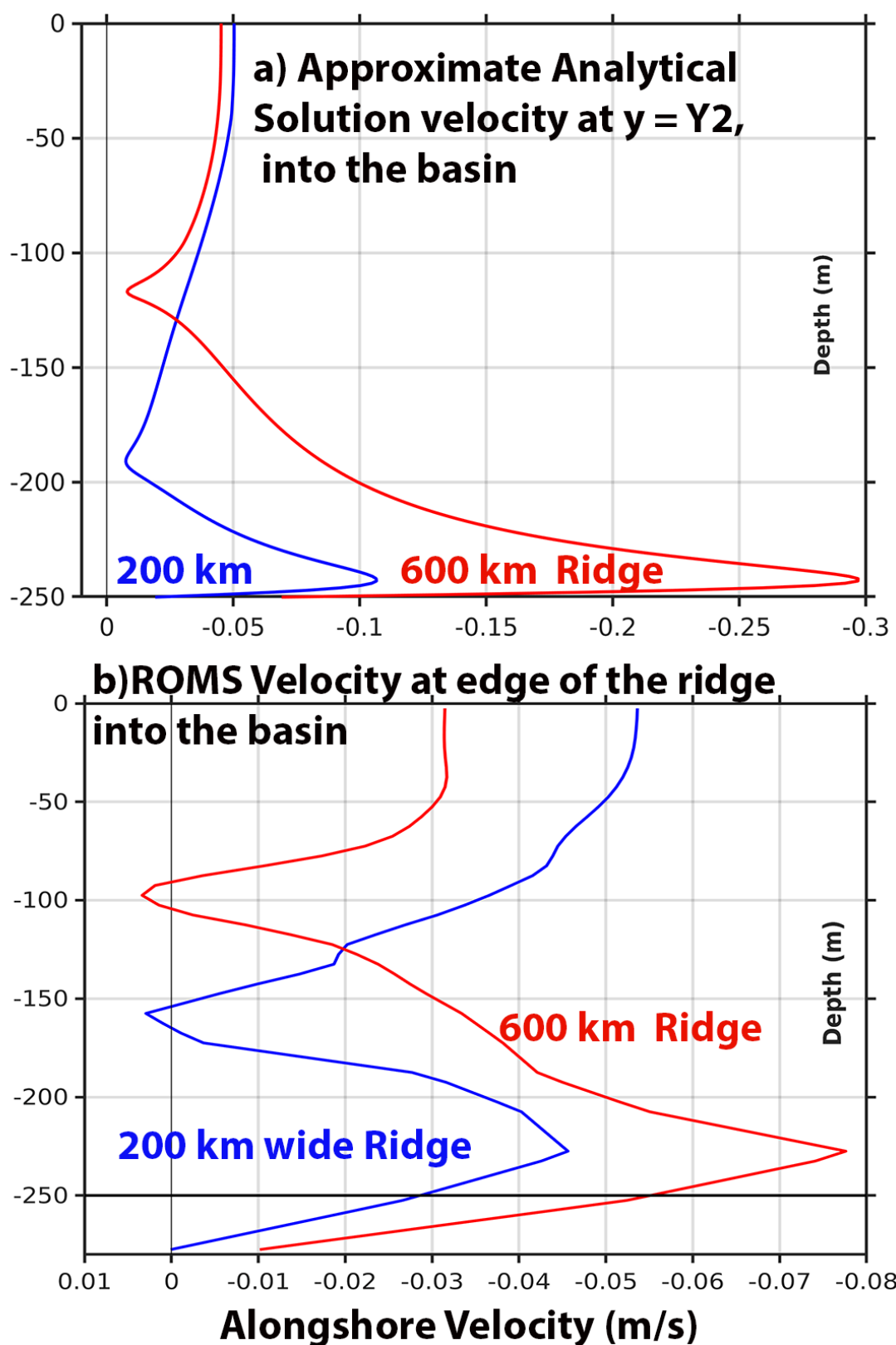
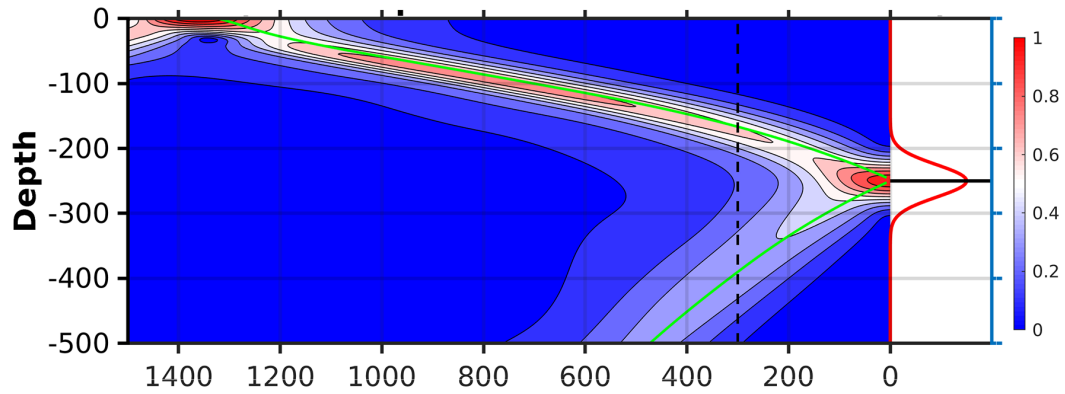
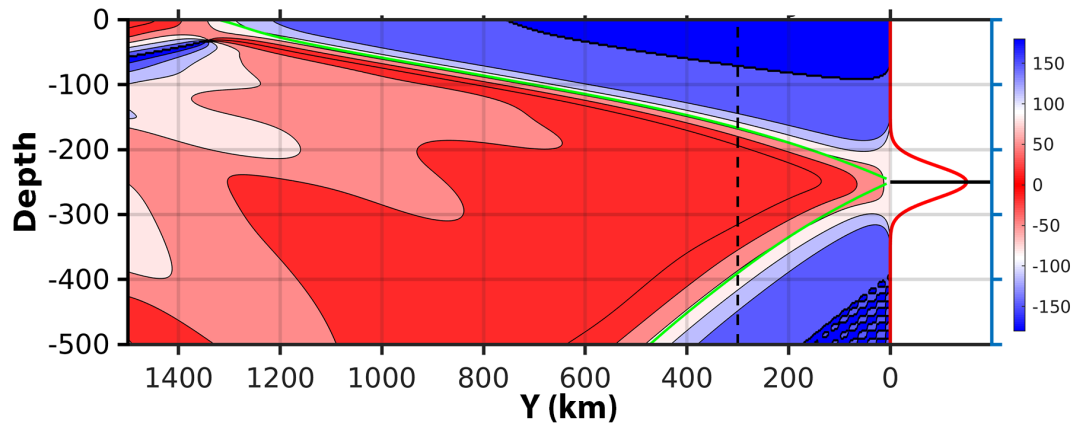


Figure 3.9: Approximate analytical and ROMS velocity amplitudes for a 30 day period basin currents next to the (one grid-point) edge of the ridge at $y = Y_2$.

a) Analytical Amplitude (V) : Wide Bottom velocity B.C.



b) Phase ; Green line = WKB ray



c) Vertical Profile of V at Y = 300 km and wall

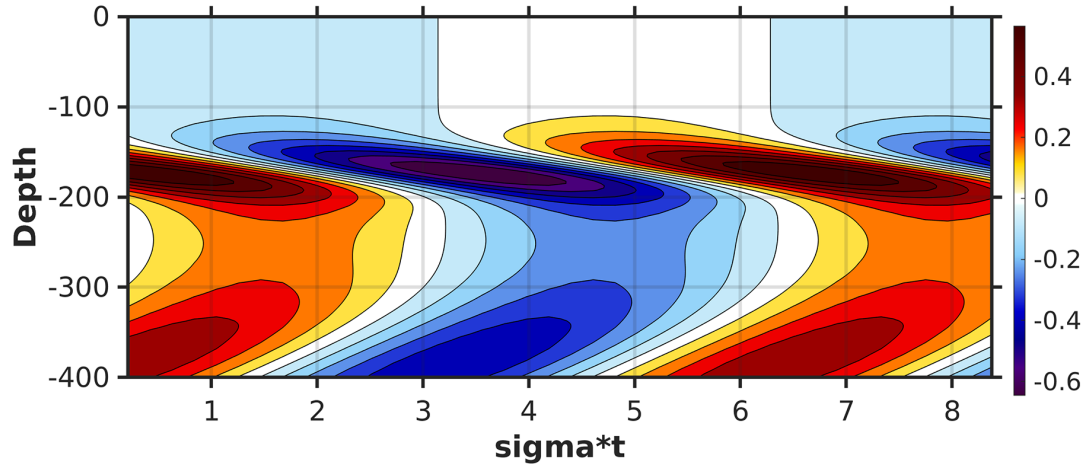
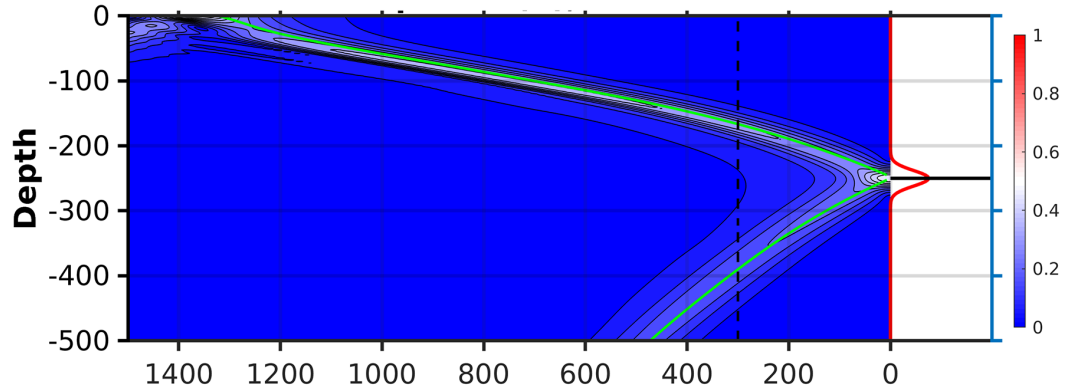
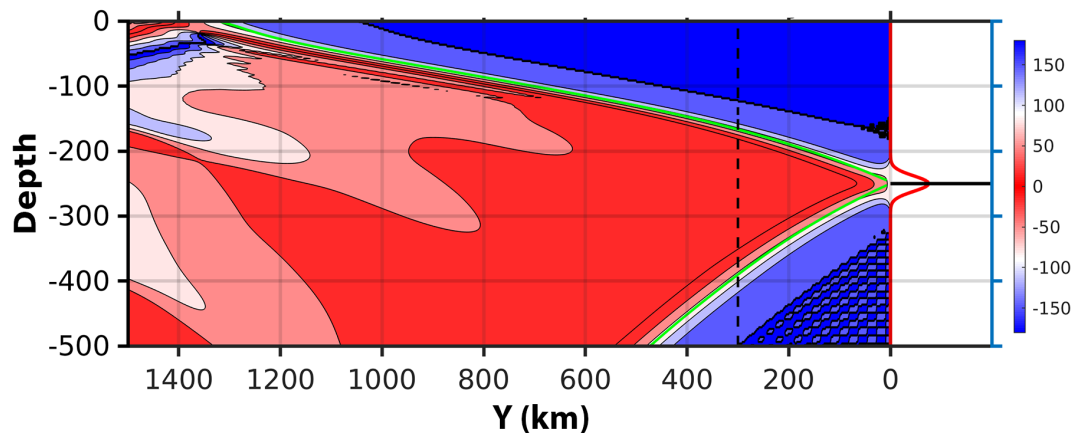


Figure 3.10: Figure: a) Amplitude and b) Phase for alongshore currents with a subsurface bottom currents above the forcing as a KW boundary condition next to the edge of the ridge; c) Time-series plot of vertical profiles of alongshore currents at Y = 300 km and wall (X=0).

a) Analytical Amplitude (V) : Narrow Bottom Velocity B.C.



b) Phase ; Green line = WKB ray



c) Vertical Profile of V at Y = 300 km and wall

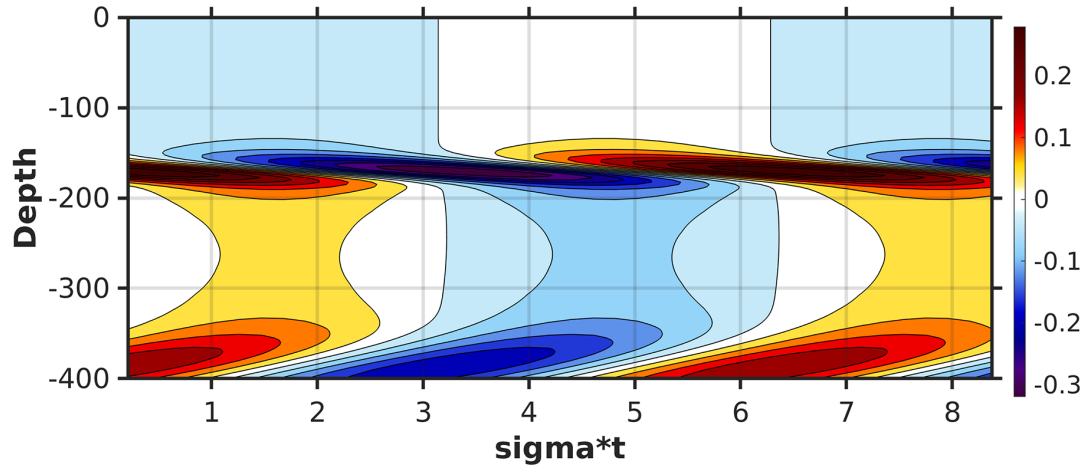
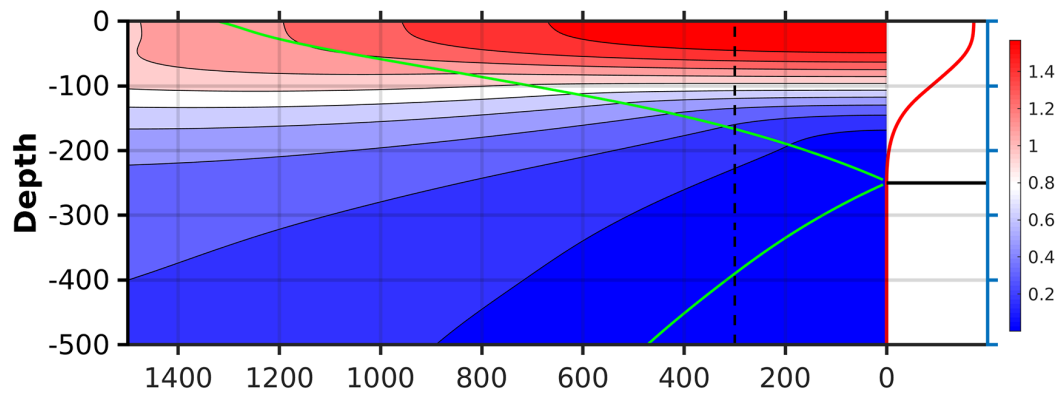
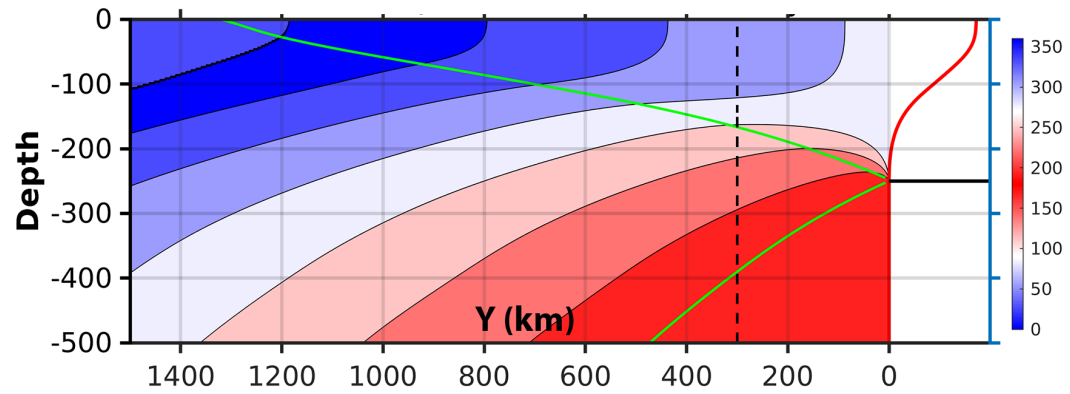


Figure 3.11: Figure: a) Amplitude and b) Phase for alongshore currents with a weaker subsurface bottom current above the forcing as a KW boundary condition next to the edge of the ridge; c) Time-series plot of vertical profiles of alongshore currents at Y = 300 km and wall (X=0).

a) Analytical Amplitude (V) : Strong Surface Velocity B.C.



b) Phase ; Green line = WKB ray



c) Vertical Profile of V at Y = 300 km and wall

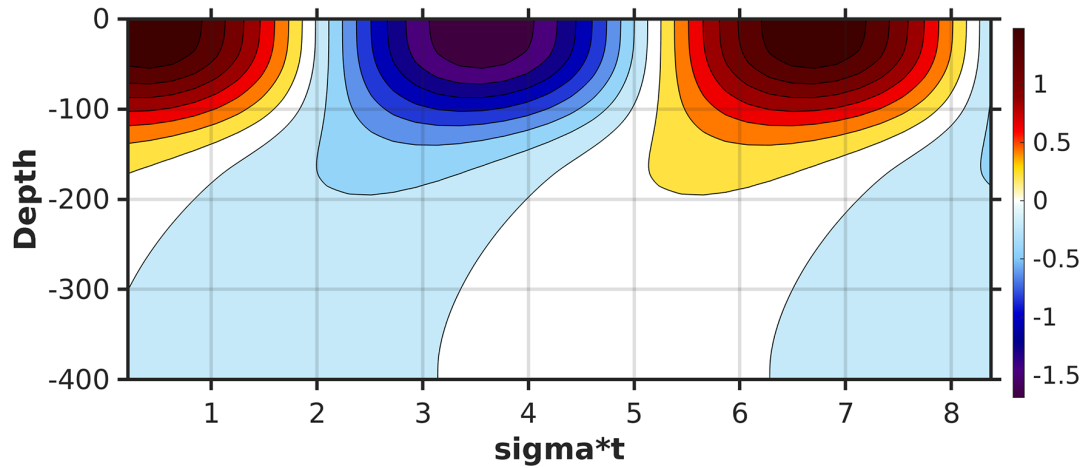
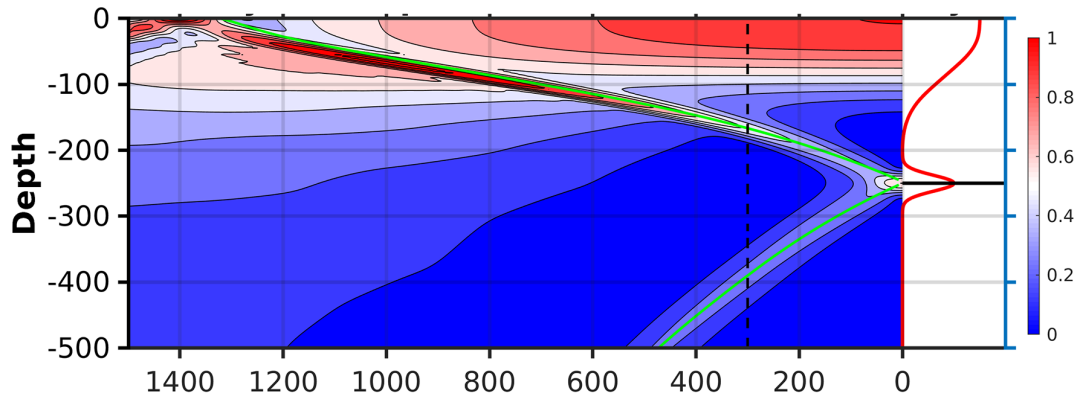
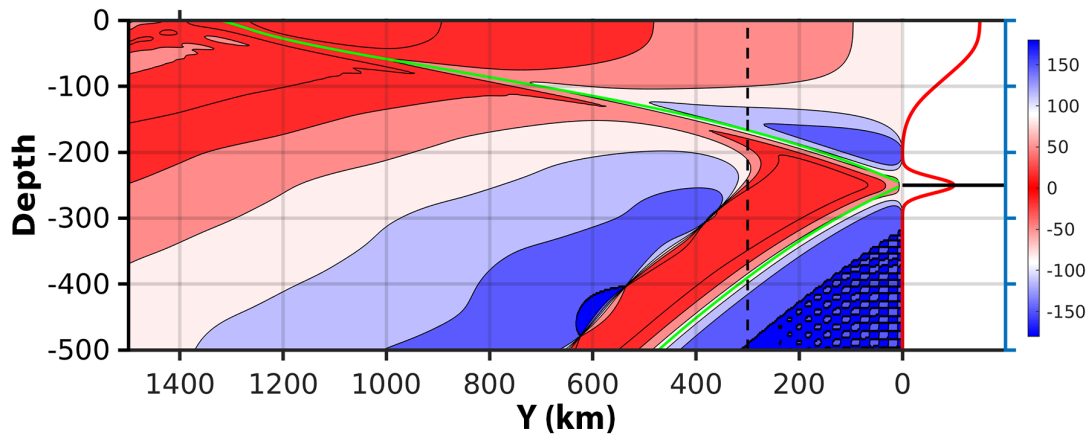


Figure 3.12: Figure: a) Amplitude and b) Phase for alongshore currents with a strong surface currents above the forcing as a boundary condition next to the edge of the ridge into the basin; c) Time-series plot of vertical profiles of alongshore currents at Y = 300 km and wall (X=0).

a) Analytical (V) : Strong Surface Weak bottom Velocity B.C.



b) Phase ; Green line = WKB ray



c) Vertical Profile of V at Y = 300 km and wall

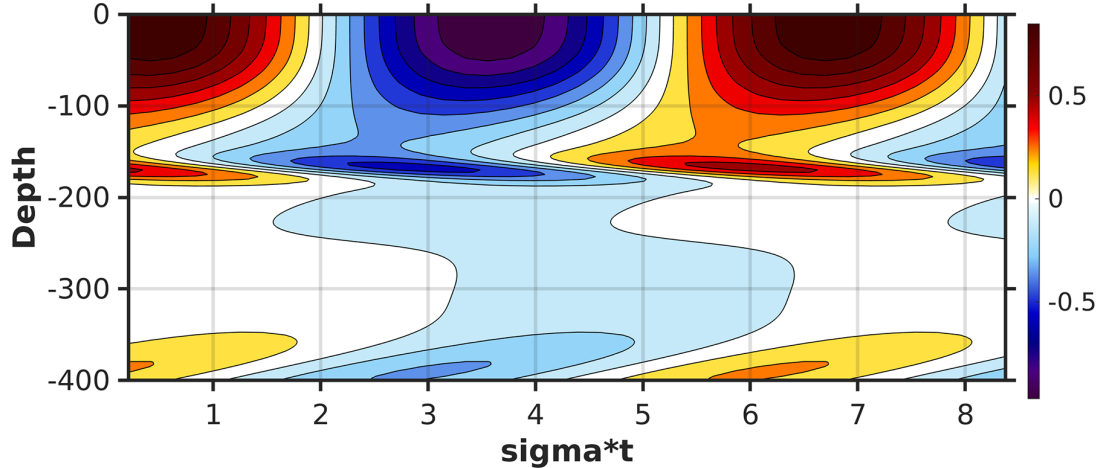
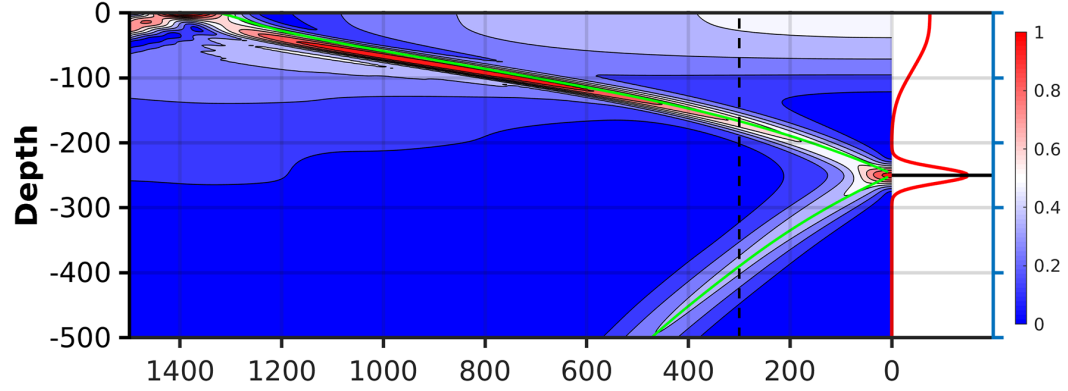
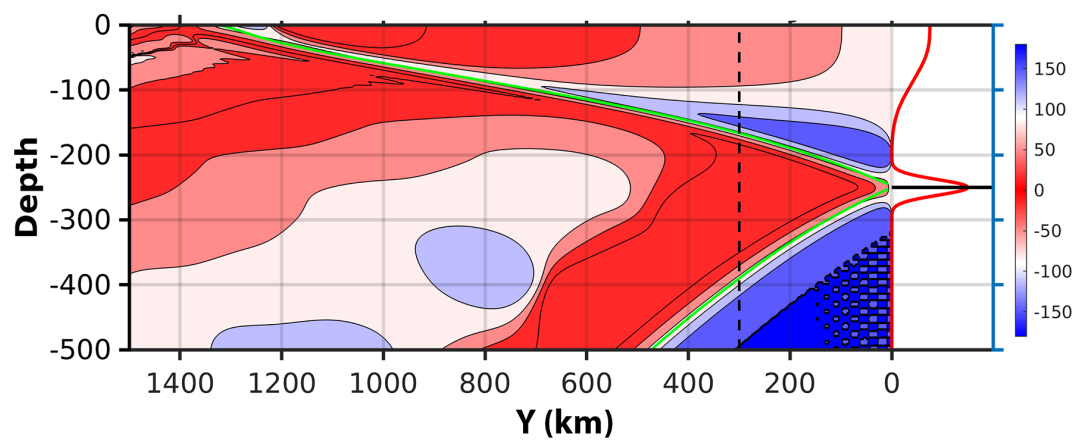


Figure 3.13: Figure: a) Amplitude and b) Phase for alongshore currents with stronger surface current and a weaker bottom subsurface current above the forcing as a KW Boundary Condition (B.C.); c) Time-series plot of vertical profiles of alongshore currents at Y = 300 km and wall (X=0).

a) Analytical (V) : Strong bottom Weaker Surface Velocity B.C.



b) Phase; Green line = WKB ray



c) Vertical Profile of V at Y = 300 km and wall

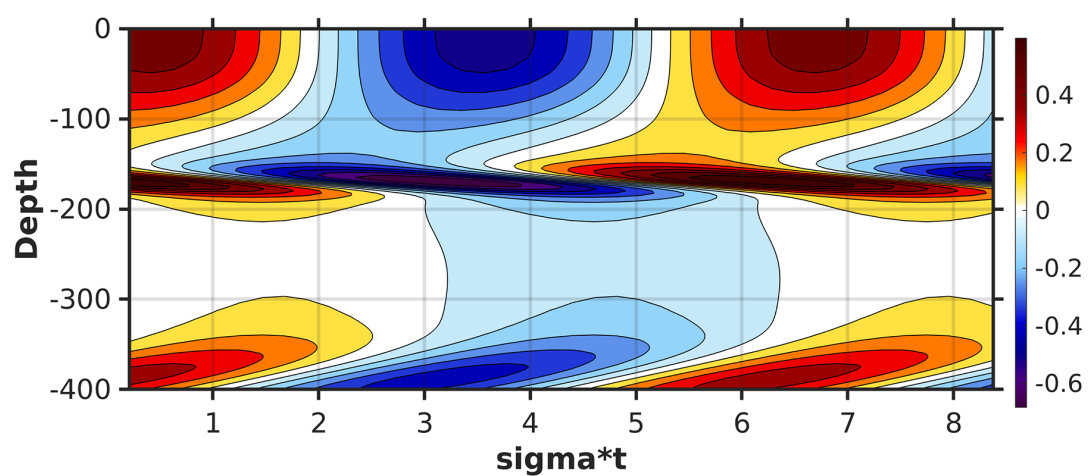


Figure 3.14: Figure: a) Amplitude and b) Phase for alongshore currents with weaker surface current and a stronger bottom surface current above the forcing as a KW Boundary Condition (B.C.); c) Time-series plot of vertical profiles of alongshore currents at Y = 300 km and wall (X=0).

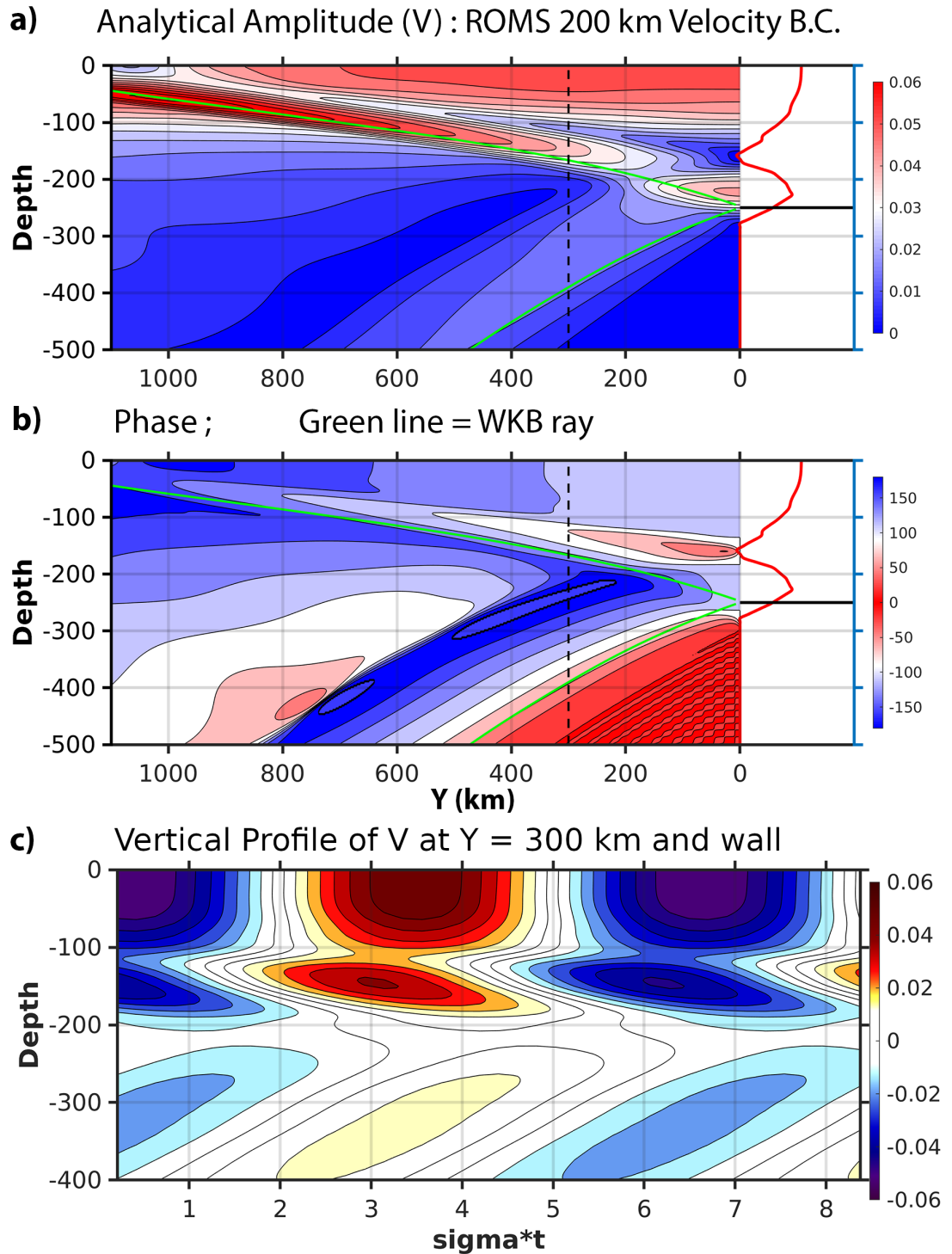


Figure 3.15: Figure: a) Amplitude and b) Phase for alongshore currents corresponding to a 200 km wide ridge ROMS solution next to the downstream edge of the ridge as a Boundary Condition (B.C.); c) Time-series plot of vertical profiles of alongshore currents at Y = 300 km and wall (X=0).

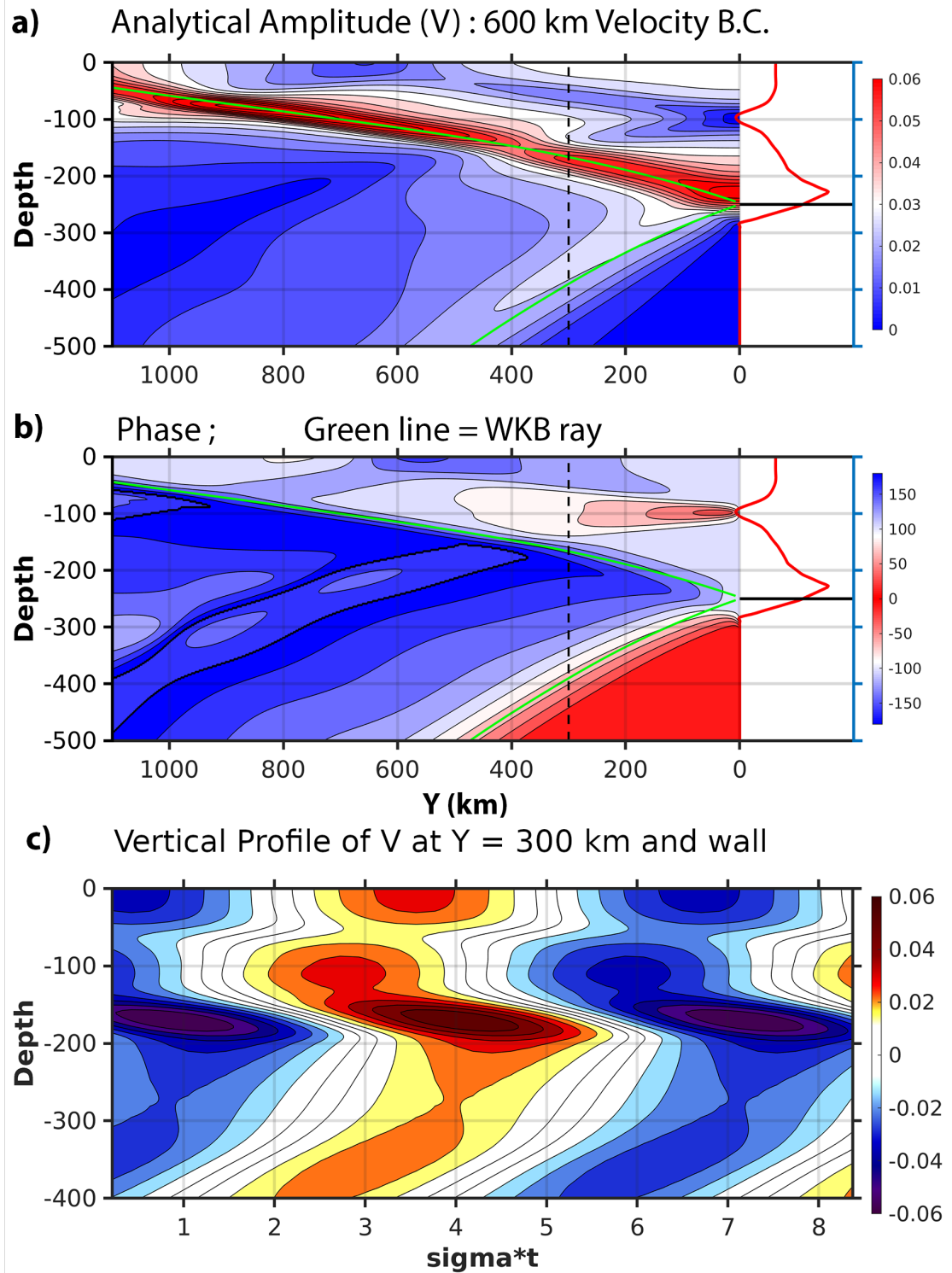


Figure 3.16: Figure: a) Amplitude and b) Phase for alongshore currents corresponding to a 600 km wide ridge ROMS solution next to the downstream edge of the ridge as a Boundary Condition (B.C.); c) Time-series plot of vertical profiles of alongshore currents at Y = 300 km and wall (X=0).

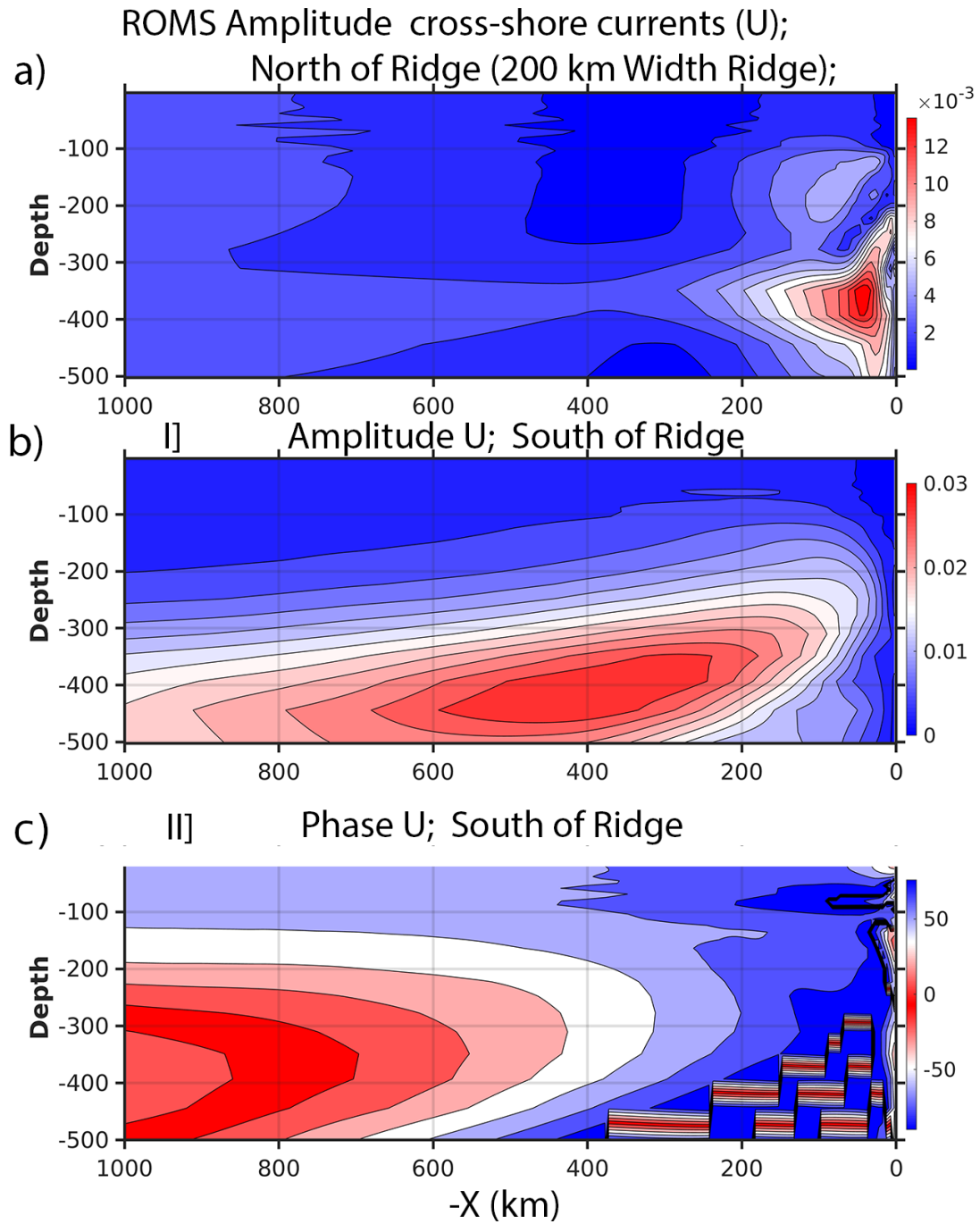


Figure 3.17: Amplitude (a : downstream of the ridge; b : upstream of the ridge) and phase (c : upstream of the ridge) of wave D currents, along the the submerged ridge.

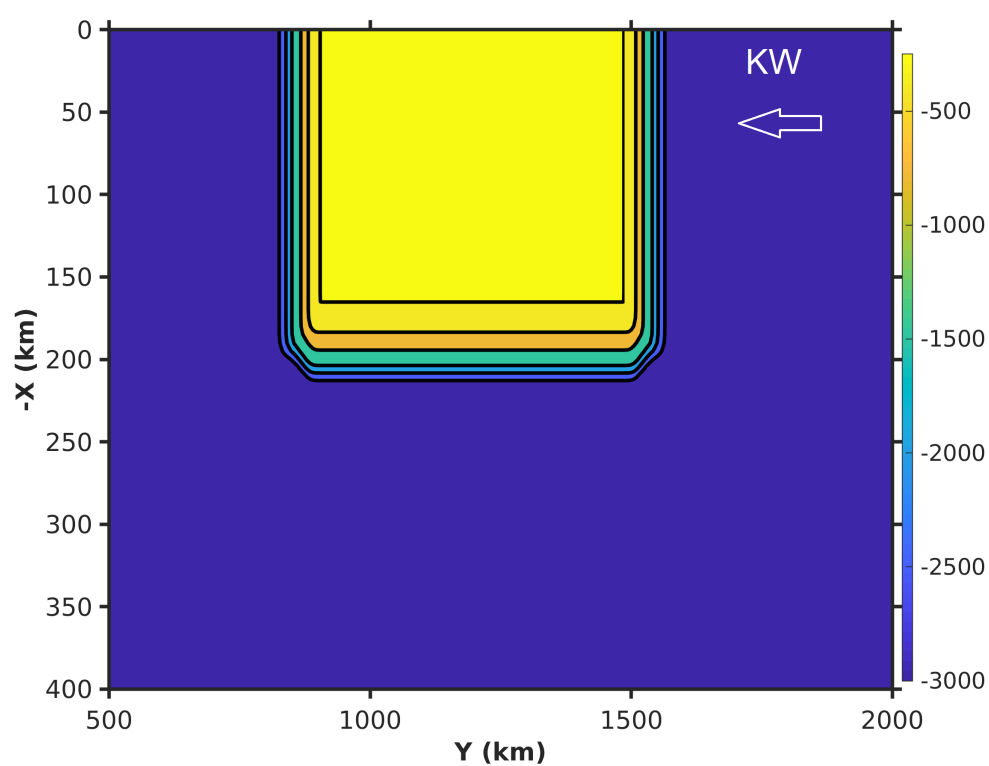


Figure 3.18: Bathymetry of a 600 km wide and 160 km long Ridge

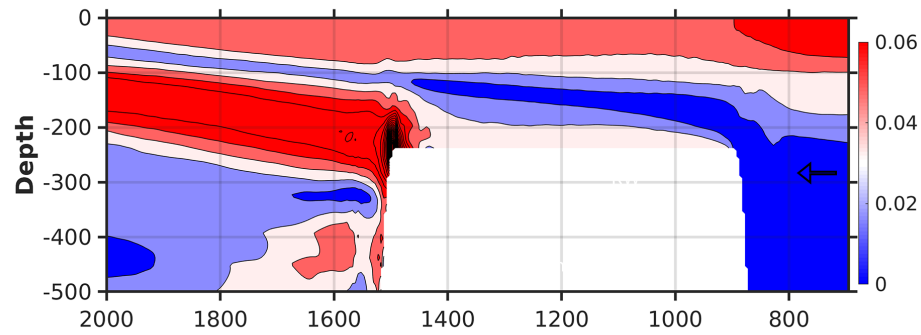
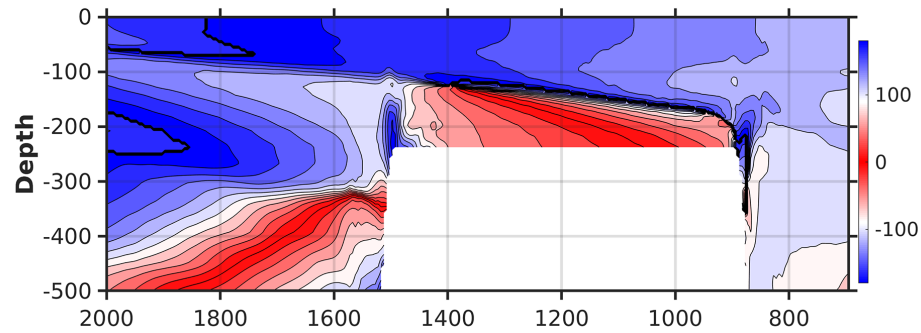
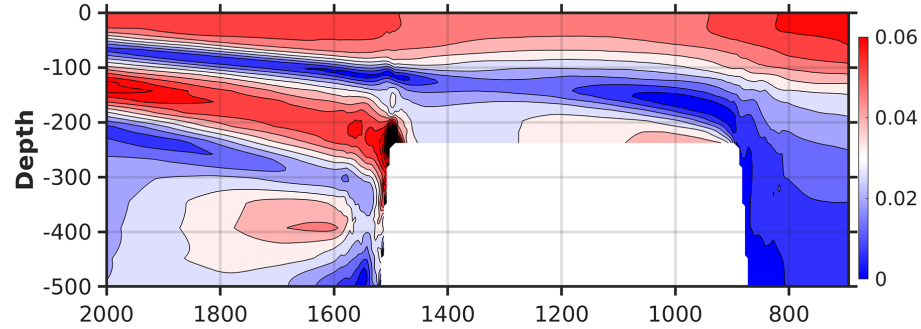
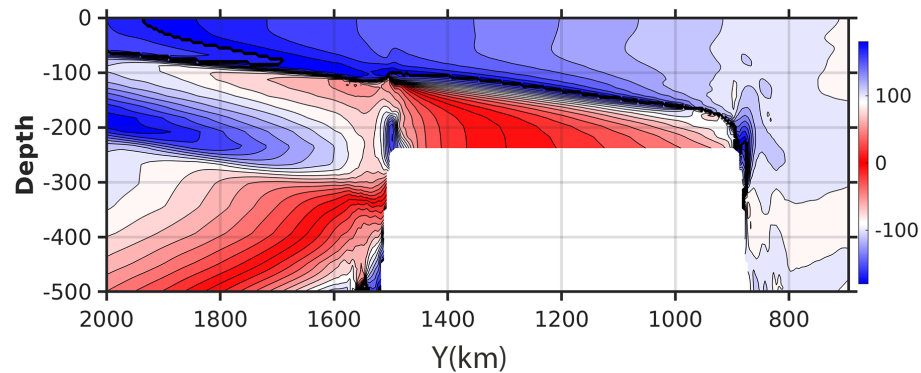
I a) ROMS :V Amplitude (160 km long Ridge)**II a)** Phase**I b)** ROMS V Amplitude fully extended Ridge**II b)** Phase

Figure 3.19: Figure: a) Amplitude and Phase for alongshore currents at wall for a 30 day sinusoid for finite 600 km wide and 160 km long ridge; b) Amplitude and Phase for alongshore currents for a fully extended 600 km wide ridge (same as Fig 3.5 velocity instead of pressure)

Chapter 4: Vertical propagation case of Coastal Trapped Waves

4.1 Introduction

The motivation behind this work comes from the observed vertical propagation of energy at the Kollam mooring (Figure 4.1) and at various other locations along the west coast of India. In the previous chapter we assumed the west coast of India to be a straight vertical wall with a flat bottom topography. In this chapter we focus our attention on the differences between the flat-bottom KWs and the sloping bottom Coastal Trapped Waves (CTWs) in relation to vertically propagating energy beams downstream of the ridge.

Previous studies have long represented the west coast of India as a flat-bottom meridional boundary (Nethery and Shankar 2007; Shankar and Shetye 1997). The bottom bathymetry along with the stratification play an important role in determining whether the coastal free wave solution behaves as an internal Kelvin wave (IKW) or a CTW. Comparing the relative magnitudes of shelf slope width (Δ_x) and the internal Rossby radius of deformation δ_R is key (J Allen 1975; Huthnance 1978; JS Allen and Romea 1980).

The relative effects of bottom topography and stratification can be combined into a single variable S , defined as: $(\delta_R / \Delta_x)^2$. According to Brink (1982), for high latitudes, a typical value of S (< 0.25) is very low, and the generalized phase velocity approaches that of barotropic shelf waves. The modal structures have nearly vertical isopleths over the shelf. At low latitudes, the values of S are usually greater and modal structures can clearly be identified as IKWs, with isopleths that slant outwards considerably. At extremely low latitudes ($S > 4$), the phase speed approaches that of a Kelvin wave, as the shelf width becomes small relative to the Rossby radius. At moderately low latitudes, the free (hybrid) long CTW mode 1 phase speed is slightly lower than the IKW phase speed. However, farther poleward, at intermediate latitudes when the Rossby radius of deformation is comparable to the shelf slope width ($0.25 < S < 4$), the free (hybrid) long CTW phase speed is slightly higher than the mode 1 IKW phase speed due to the gradual transition to topographically supported waves.

The stratification, bathymetry and the latitude close to the Kollam mooring (region of interest) (Figure 4.1) suggest that the free wave along the coastline behaves more like an IKW. The phase speed and the eigen-mode structure corresponding to the hybrid coastal trapped wave, however are not well represented by a flat-bottom IKW. Thus it is important to study shelf-slope dynamics in that region to obtain an accurate phase speed and modal structure corresponding to the CTW eigen-mode. We use Brink and Chapman coastal trapped wave routines (http://www.whoi.edu/cms/files/Fortran_30425.htm) to determine the CTW eigen-mode structure and the corresponding phase speeds, close to the Kollam mooring region. The effects of the CTWs on the establishment of vertically propagating energy beams due to submerged ridges is explored by forcing the numerical models with the mode 1 CTW eigen-function on a sloping bottom bathymetry.

In section 4.2, we present the step-wise procedures that were carried out to obtain a clean CTW mode 1 structure using Brink and Chapman routines for the average bathymetry, Coriolis parameter and stratification near Kollam mooring. The later part of the section describes the numerical model and its configuration in detail. Section 4.3 of the chapter show numerical model run results for the case of CTWs, and their comparison with the KW model runs. In section 4.4, we discuss questions arising from the solutions. Section 4.5 summarizes the overall results.

4.2 Methods

4.2.1 Brink and Chapman Coastal wave program routines

In several existing papers (Brink 1982; Chapman 1983; Clarke and Brink 1985), a number of computer programs have been described which compute properties of linear coastal-trapped waves and wind-driven motions over the continental shelf. These programs, since they allow rather arbitrary choices of topography, stratification, etc., may be of fairly general use to the oceanographic community. A few assumptions are common to all programs below. First, only linear problems are considered. Second, the water depth is always assumed to be a function of x only. Third, the Buoyancy frequency may vary in z only, and must be non-zero everywhere. The general free-wave programs search for free-wave solutions using resonance iteration. The general approach is to assume that the dependent variables are sinusoidal in time and the along-shelf direction, e.g. $U(x,y,t)$

$= U(x) \exp[i(\omega t + ly)]$. These programs calculate free-wave dispersion curves (ω, l pairs) by resonance iteration, given input parameters including arbitrary bottom topography and stratification. Options include the choice of a free-surface or a rigid-lid boundary condition. The user must supply stratification, topography, the Coriolis parameter, and other information. The programs, after converging to a free wave solution, print out frequency, wave-number and the modal structure. All program outputs are either in arbitrary or cgs units.

For instance, the Brink and Chapman coastal wave routines are used to compute the wave properties at 4 different cross-shore transects along the west coast of India, passing through; Station 1: 8.39° N, Station 2: 8.74° N, Station 3: 9.38° N, Station 4: 10.53° N (Figure 4.2). Data from World Ocean Atlas 2009 are used to get the Buoyancy structure at these locations. For this computation, we assumed a rigid lid and no planetary β component. High resolution bathymetry etopo2 from NOAA is used for this analysis. Figure 4.3 shows the topography and the approximate off-shore slope width along these various cross-shore transects. Figures 4.4-4.7 show the associated modal structures of pressure across the pathways. The phase speeds for mode 1 CTW for Station 1-4 are 285, 289.82, 285, 286 cm/s respectively. The isopleths slant considerably outwards (more horizontal) on the shelf-slope for all the modal structures, suggesting these waves behave more like IKWs. The phase speed for a mode 1 IKW for the averaged stratification in this region is $\simeq 245$ cm/s. The values of scale ratio S are obtained for all of these cases using Δ_x and $\delta_R = C_{IKW}/f$, where C_{IKW} is the phase speed for the IKW mode and f is the Coriolis parameter. The values of S for all of these cases (0.26, 0.25, 0.41, 0.29) lie between 0.25 and 4. This suggests that the shelf-slope width is comparable to the first Rossby radius of deformation and the hybrid free CTW phase speed should be slightly higher than the IKW phase speed. Our results from the Brink and Chapman routine seem to agree with this as the CTW phase speeds ($\sim 285, 289.82, 285, 286$ cm/s) for all of the Stations are higher than the IKW mode 1 phase speed ($\simeq 245$ cm/s).

The dispersion curve of a free CTW solution is investigated for the intra-seasonal band of frequencies. The dispersion curve for the mode 1 CTW along the cross-shore path of station 3 suggest that the waves are mostly non-dispersive close to the frequencies of our interest (Figure 4.8).

4.2.2 Obtaining a clean CTW mode 1 to force the Numerical Model

We are motivated by the observations of vertical energy propagation at the Kollam mooring. To set up the numerical model bathymetry analytically, we choose the topography slope steep enough to represent the observed slope along path A (Figure 4.1) which sits within the constraints of ROMS allowed maximum slope. The left panel of Figure 4.1 shows three different cross-shore transect paths used for the reference. The bottom slope topography for paths A, B and C are shown in the right panel in color, whereas the black lines show the chosen analytical coastal decay slope used for numerical model runs. The Coriolis parameter (f) is set to the latitude of the Kollam mooring, and the rest-state stratification of the model is taken from local stratification reported by the 2009 World Ocean Atlas. For the given slope (without the ridge) and stratification the first mode baroclinic CTW eigen solution is computed using the Brink and Chapman coastal trapped wave routines, for a wider off-shore domain extending more than 1200 kms from the coast.

Figure 4.9 shows the mode 1 CTW velocity structure for the analytical slope. The CTW solution for that typical coastal decay slope along the west coast of India for a wider domain produces discontinuities in the form of spurious currents in the region more than a 1000 kms away from the wall. The manual for the Brink and Chapman routines state that the program does not perform very well with high slope steepness in the bathymetry for a wide off-shore domain. To get rid of these spurious currents we either need to truncate our solution in the off-shore direction and choose a smaller domain (as in the case of Figures 4.4-4.7), or change the bathymetry to reduce the steepness of the slope. Neither of the above solutions provides us with a required CTW to force the numerical model, which has a wider domain and steep slope bathymetry representing a typical slope close to the Kollam region.

We carry out the following steps to obtain a clean CTW mode 1 eigen structure. First we truncate the solution to only 600 kms off-shore and let the off-shore amplitude decay to zero exponentially in X for all Z . This takes out the off-shore bipolar current discontinuity from the eigen structure. Figure 4.10 show this truncated CTW mode 1 eigen structure for a wider domain. We force the Regional Ocean Modeling System (ROMS) model with the obtained eigen structure for a 30 day period (period of interest for this study) for a sloping bottom bathymetry without a ridge. The domain of the

model is extended in Y to incorporate a length of more than 21,000 kms. Figure 4.11 shows the bathymetry of the model domain (the y-extension is shown only for first 6200 kms). Figure 4.12 shows the snapshot of alongshore currents for the model run at a 450 m deep off-shore transect in YZ. The snapshots of alongshore currents when forced by the obtained CTW eigen mode clearly show the signs of more than one vertical mode while sampling at 136 days, 142 days and 148 days (slanted amplitude lines), suggesting the contamination with higher modes.

The first baroclinic mode CTW has the highest phase speed and with time it leaves behind the higher modes. At a sufficient distance away from the southern boundary the amplitude and phase of alongshore currents in the XZ transect are extracted (through least-square regression analysis) for the time-period when the higher modes do not reach that location for atleast one period of time (30 days). We then re-run the ROMS model by forcing with the extracted mode 1 eigen structure. Figure 4.13 show the snapshot of alongshore currents for the above case at a 450 m deep along an alongshore transect in YZ (from 0-2800 km). The snapshots of alongshore currents show vertical lines of amplitudes at all times, suggesting a single vertical mode in the eigen function. Figure 4.14 compares the CTW mode 1 eigen structure for: a) Contaminated CTW mode 1 b) Clean CTW mode 1.

4.2.3 Numerical Model

The ROMS numerical model is used to carry out a series of experiments. For this study, we configured the ROMS model in an idealized version of the west coast of India/Sri Lanka, including a short subsurface ridge extending from the coastline for a distance. The model basin is 3000 m deep, and has an off-shore slope similar to that of a typical off-shore decay along the west coast of India. The depth of the subsurface ridge near Kollam in the real case scenario varies spatially with an average minimum depth of 250 meters. In the model domain we chose ridge-top depths between 200 and 250 meters. Figure 4.15 shows the bathymetry for one such model run that has a 200 km wide and 80 km long ridge. The width of the ridge represents alongshore distance and the length of the ridge represents the off-shore distance away from the wall. The coastal decay slope in the domain is shown in the right-hand panel, overlapped with a ridge slope at $y = 3000$ km from the southern boundary.

There are 40 sigma (terrain following) levels in the model. The grid resolution is $5\text{ km} \times 5\text{ km}$ in alongshore and cross-shore directions. The model has open boundaries to the north and to the west of the domain. The boundary to the west is more than 1000 km away from $X=0$ (eastern boundary) and the boundary to the north is between 3000 and 6000 km from $Y = 0$ (southern boundary). A viscous sponge layer is placed on the north and the west boundaries of the domain with a viscosity of $1500\text{ m}^2/\text{s}$ for 100 kms extending away from each boundary. This viscous sponge layer plays an important role in absorbing the forced coastal wave signal when it reaches the boundary. A no-slip condition is present at bottom, creating a bottom boundary layer.

We are interested in frequencies at which Rossby waves cannot propagate freely, so to simplify the dynamics, we start with solutions on an f -plane. The Coriolis parameter (f) is set to the latitude of the Kollam mooring, and the rest-state stratification of the model was taken from local stratification reported by the 2009 World Ocean Atlas. We force the model with a 30-day frequency by varying the southern boundary normal velocity, appropriately as per the first eigen mode velocity structure (Figure 4.16 a). The model is run for 150 days.

After transients generated by the initial wavefront have been absorbed by the sponge layers, a time series two periods long is regressed onto a 30 day cycle to determine the amplitude and phase at each point in the domain.

4.3 Results

This section summarizes the results from several numerical model runs. First we show the results from a CTW model run having a coastal slope comparable to that of typical slopes along the west coast of India. We then show the results from a KW model run having a flat-bottom bathymetry with a vertical wall representation of the west coast of India. Both the model domains have a ridge in the middle of the domains, with similar dimensions. The results from the KW model run are qualitatively compared with the CTW model run. It is shown that the Kelvin wave assumption yields similar upward propagation of energy results to that of the CTW scenario, but the extent of downward propagation in amplitude is missing in case of the CTWs.

4.3.1 CTW Model Run

The best way to interpret the results for vertical propagation is to look at the amplitude and phase for alongshore currents for the applied frequency. Figure 4.16 b) shows the amplitude and phase of alongshore currents extracted through a least-squared regression analysis along a 300 m deep cross section in YZ (black arrow in panel a). The middle of the ridge is at 3000 kms away from the southern boundary. The upper right panel represents the amplitude and the lower right panel shows the associated phase. The CTW reaches the ridge top with almost a constant amplitude in the horizontal direction and the associated phase changes with distance in Y (alongshore) with mostly vertical contours suggesting not a significant vertical propagation of phase before the CTW hits the ridge. Past the ridge, both amplitude and phase lines show signs of vertical propagation. The phase travels from red to blue (decreasing), suggesting a downward phase propagation (upward energy propagation) in the top 250 meters and a slight upward phase propagation (downward energy propagation) below 250 meters. The corresponding amplitudes show a clear beam emanating from the top of the ridge above 250 meters. The downward propagating beam below 250 meters reflects back from the bathymetry (300 meters deep for the extracted cross-section) giving rise to interference, henceforth it is difficult to see a clean downward propagating beam unless we look at a cross-section farther offshore. Both, the amplitude and phase suggest a significant upward propagation of energy above 250 meters past the ridge.

4.3.2 KW Model Run

To determine the similarities between a CTW numerical solution to that of a KW scenario we design a KW numerical model with similar ridge dimensions as that of CTW case. We assume the west coast of India as a vertical wall with a flat bottom topography. Figure 4.17 a) shows the bathymetry of a KW domain. The ridge dimensions are similar to that of the CTW case that is 200 km wide and 80 km long. We force the model with the first vertical mode eigen structure of alongshore currents from the given stratification (Figure 4.17 b)) with a 30 day period.

The comparison between the boundary forcing of a mode 1 KW alongshore velocity structure to that of CTW eigen function is shown in Figure 4.18. The phase speed of

mode 1 CTW in that region is slightly greater than the IKW mode 1 phase speed in the deep ocean. The surface amplitude for the KW decays off-shore faster than the CTW. Figure 4.19 shows the exponential decay rates for the surface amplitude for CTW as well as KW scenarios.

A similar amplitude and phase extraction is carried out through a least-squared regression analysis for a 30 day period along a YZ cross section for alongshore currents at the wall ($X=0$). Figure 4.17 c) shows the extracted amplitude and phase past the ridge. The difference between the CTW domain with that of KW domain is that the depth of the YZ cross section past the ridge for KW, will always be at 3000 meters (although in figure we show top 1200 meters only). The upper right panel presents amplitude and the bottom right panel presents the associated phase. Before hitting the ridge, KW has an amplitude mostly horizontal with the highest amplitude largely concentrated in the top 100 meters. The associated phase is mostly constant in the vertical direction and changes with a 180° phase shift at 800 to 1000 meters depth. This is due to the zero crossing (depth) in first eigen mode vertical structure of alongshore currents (Figure 4.17 b)) in the forcing. The amplitude past the ridge shows a clear beam emanating from top of the ridge suggesting a similar upward propagation of energy as that of the CTW case. The downward propagating beam is weaker in amplitude due to the fact that the stratification amplitude decreases with depth. The phase lines show a distinct downward propagation of energy (upward propagation of phase) below 250 meters (phase travels from red to blue, with decreasing values).

4.3.3 Comparison between CTW and KW model run amplitudes

We ran several numerical model runs to compare the vertically upward propagating beams in amplitude for different cases of KWs and CTWs. One case is shown in Figure 4.20, where both the domains have a ridge at 1000 kms from the southern boundary. The length and width of the ridge is same in both cases, as is the maximum amplitude with which the models are forced. Qualitatively both the cases yield a distinct upward propagating energy beam.

4.4 Discussion

In the previous chapter we demonstrate that the width of the ridge plays a key role in producing a wide and robust upward propagating energy beam. For a given forcing in the numerical model solutions the observed upward propagation of energy gets weaker as the width of the ridge narrows. In this section we investigate the effects of varying widths of the ridges on CTW upward propagating energy beams, for finite ridges.

We design several numerical model runs where we change the width of the ridge, keeping all other parameters the same. Figures 4.21 - 4.23 show the bathymetry of three different model domains that have a ridge widths of 200 km, 100 km and 40 kms respectively with a constant off-shore length of 50 km at the top of the ridge. The remaining dimension of the domain are kept the same for all the three scenarios. The left panels show the contours of the bathymetry and the right panels give the decay slope of the model bathymetry overlapped with the ridge decay slope at $y = 1000$ kms.

After the model runs are complete, the amplitude and phase of alongshore currents are extracted through a least-squared regression analysis at a depth of 300 meters along an alongshore transect in YZ. Figures 4.24 - 4.26 show the amplitude and phase corresponding to regression over the three 30 day periods between 30-89 days. The phase plots of all the three cases show slanted contours at the bottom in each of the YZ transects. This is probably due to a bottom boundary layer. Hence we neglect the vertical propagation of phase at the bottom, as the dynamics in that region is dominated by the bottom drag.

The upward propagation of energy is more robust in the case of the 200 km width ridge, and it gets weaker as the width of ridge gets narrower. The amplitude and phase plots of 40 km wide ridge does not produce a significant upward propagation of energy (Black arrows show the direction of phase propagation).

The above results are similar to that of KW model runs with varying widths of the ridges (Chapter 3) suggesting a minimum width of the ridge is required to produce a strong and robust upward propagating energy beams.

4.5 Conclusion

The differences between the flat-bottom KWs and sloping bottom CTWs in response to a sudden change in bathymetry in the form of a submerged ridge are investigated with

the help of numerical model runs. The west coast of India near Kollam has a comparable shelf-slope width to that of that of the first mode Rossby radius of deformation. The scale ration S in this region suggests that free wave solutions close to Kollam mooring behave more like IKWs. The corresponding phase speed and modal structure of IKWs however, does not accurately represent the hybrid mode 1 CTW phase speed and cross-shore structure.

In this study, we put-forth step by step procedures used to obtain a clean CTW mode 1 eigen function when the Brink and Chapman routines fail for the cases of steep bottom slopes and wide domains in cross-shore directions. Two different models runs in terms of a CTW domain and a KW domain, with a similar ridge dimensions, yield qualitatively similar upward propagating energy beams.

The effect of varying widths on the upward propagation of energy for CTWs is carried out using three different model runs of the widths of 200 km, 100 km and 40 kms by keeping all other dimensions the same. The upward propagation of energy gets weaker as the width of ridge gets narrower.

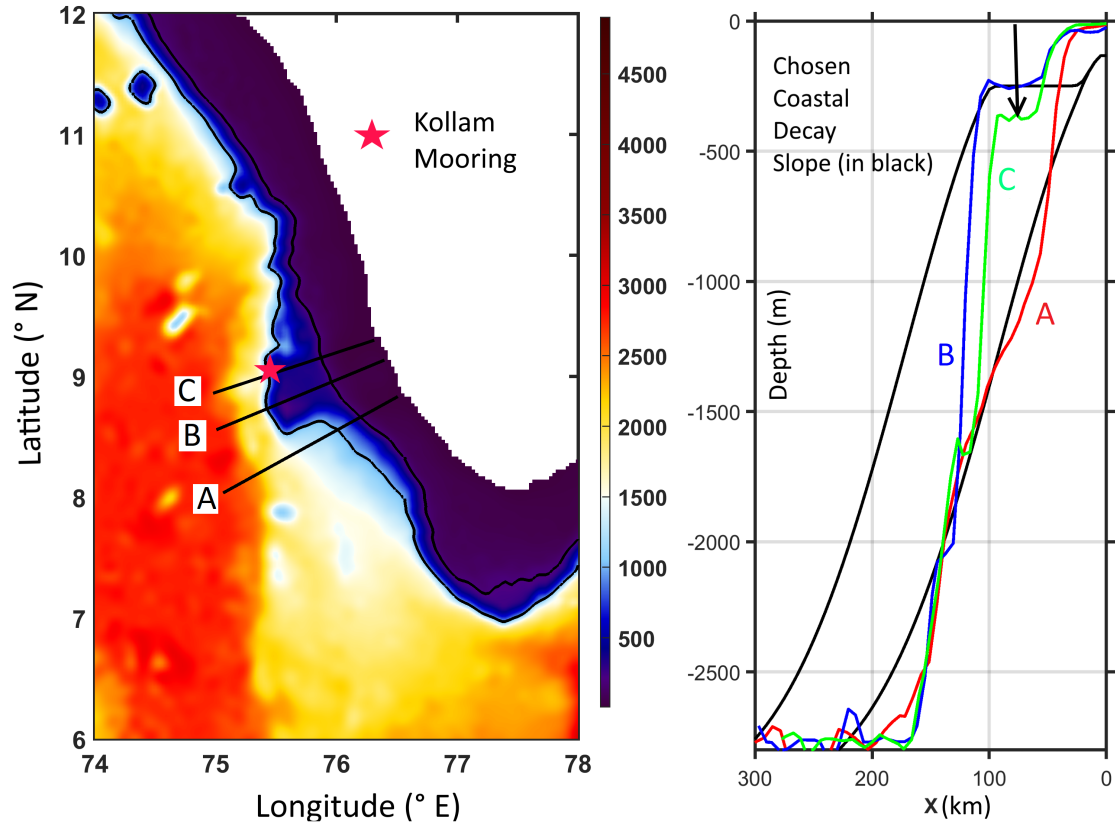


Figure 4.1: Cross-shore Bathymetry along the west cost of India, showing different slopes along path A, B and C; represented by A (red), B (blue) and C (green) in the figure to the right. The downward black arrow shows the Kollam morring Depth (KMD). Two different slopes in black, one with coastal decay and one on top of the ridge ($Y=3000$ km) in the CTW model domain are plotted on top.

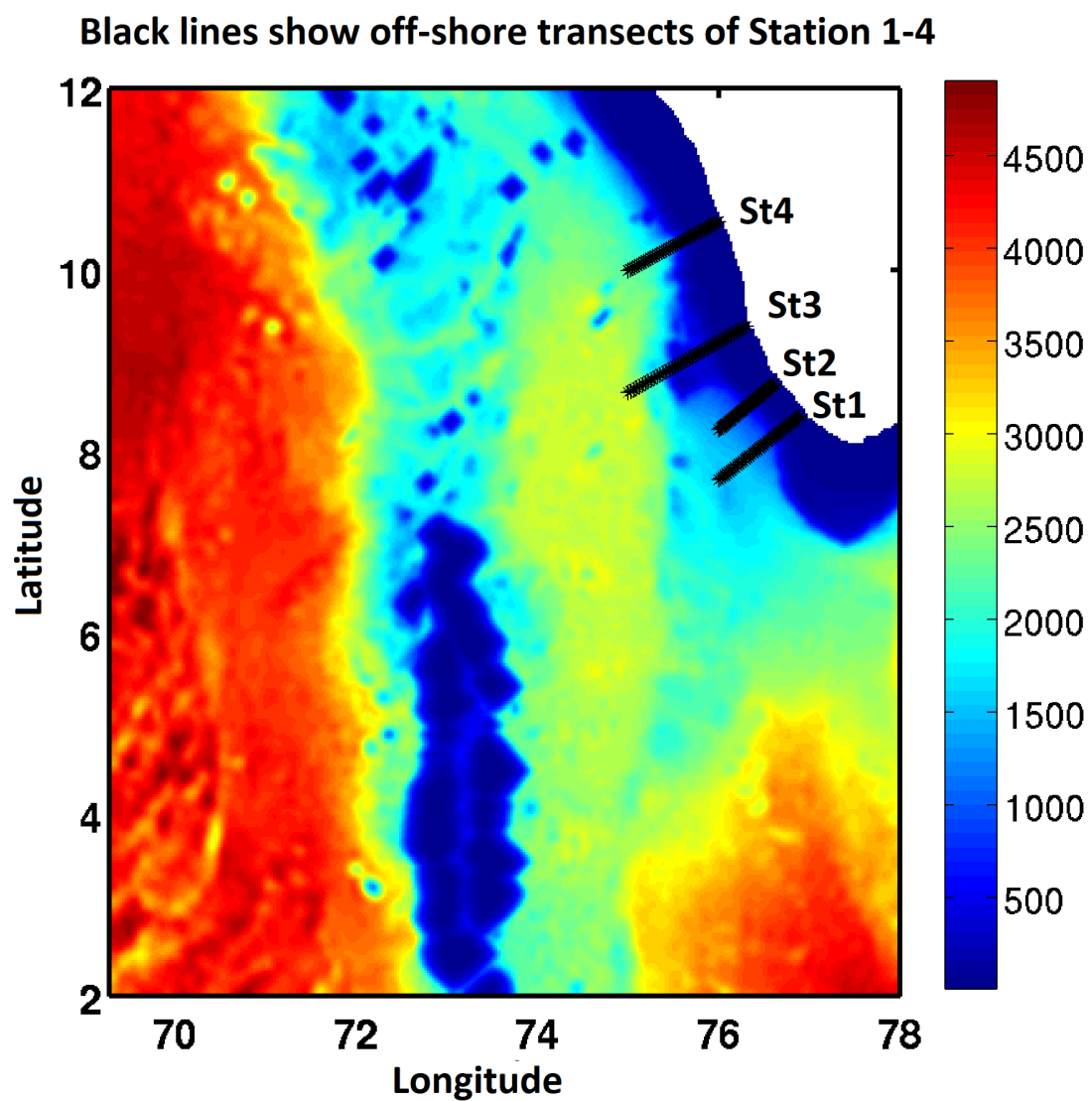


Figure 4.2: Bathymetry along the west coast of India. Black lines represent the off-shore path for Station 1, 2, 3 and 4, located on the coastline.

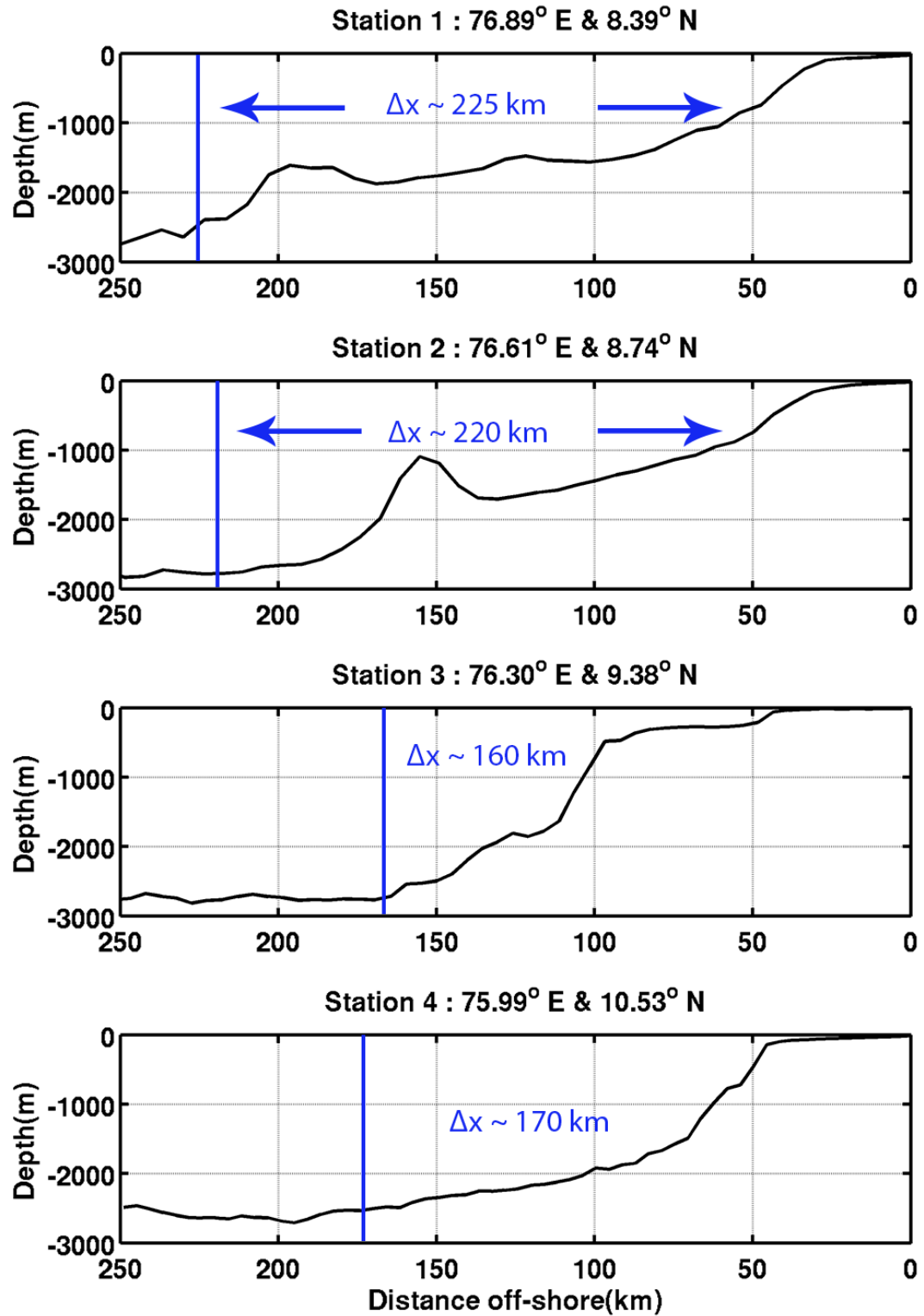


Figure 4.3: The bottom topography of the cross-shore paths starting from Station 1, 2, 3 and 4. Δ_x represents the shelf-slope width at each of these locations.

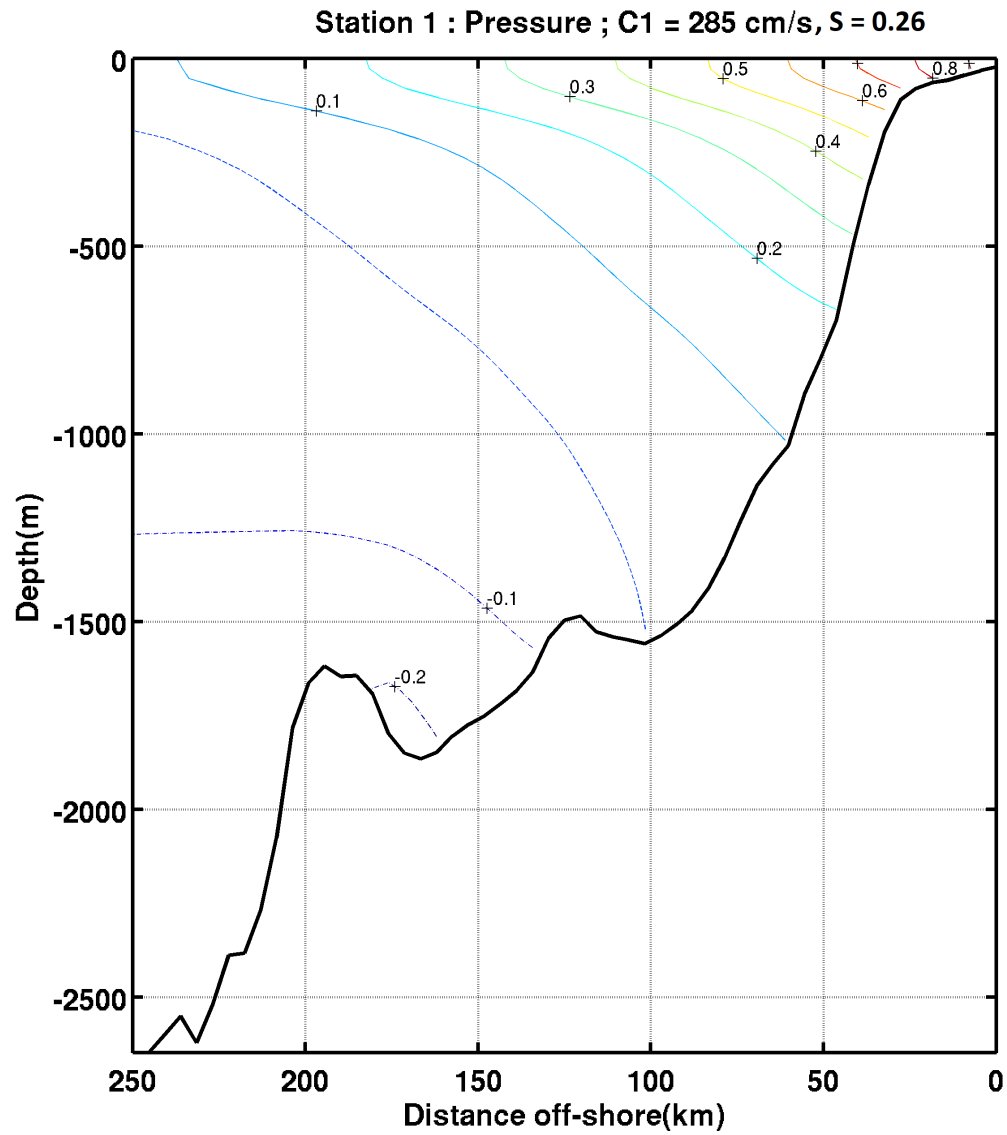


Figure 4.4: Pressure structures of eigen mode 1 in arbitrary units at Station 1. ($C1=285 \text{ cm/s}$, $S = 0.26$)

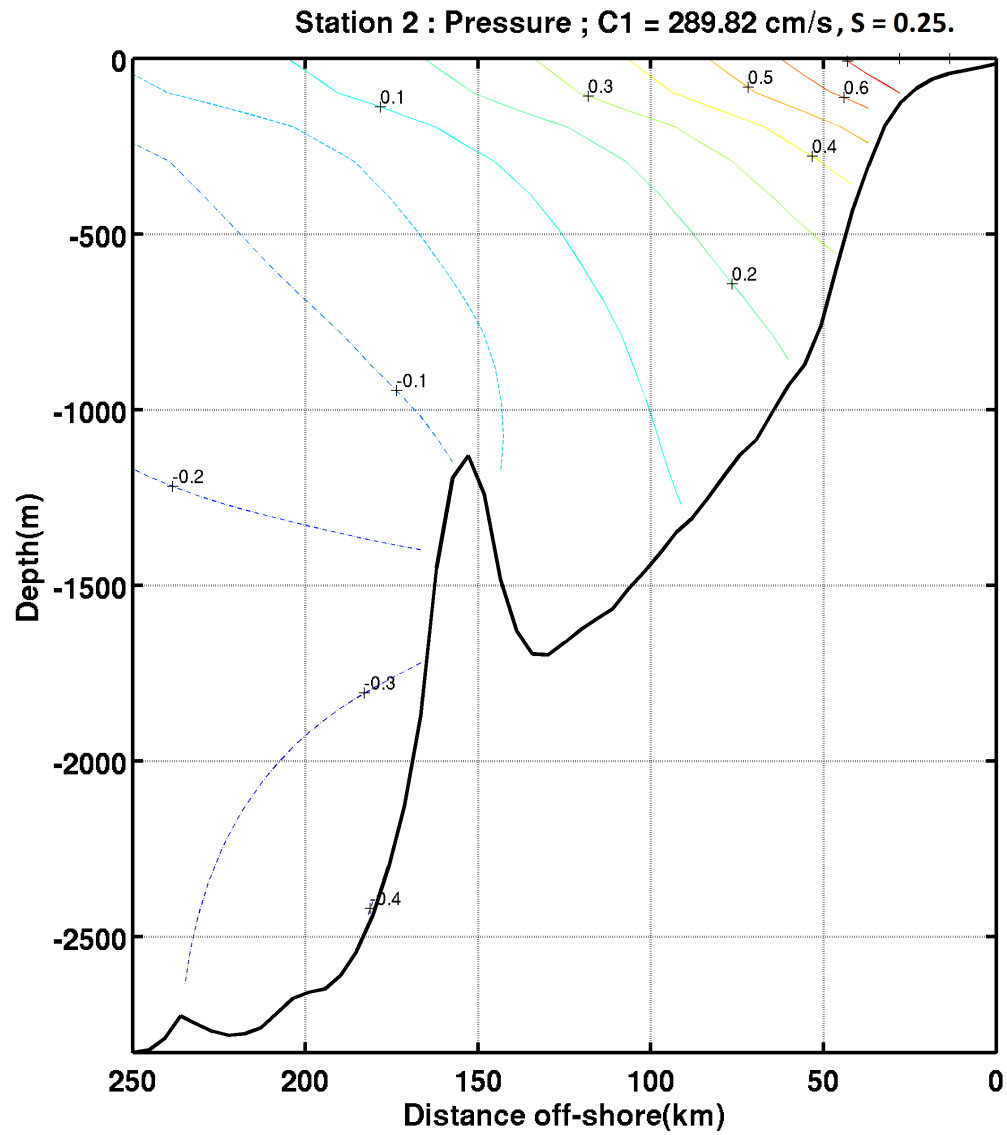


Figure 4.5: Pressure structures of eigen mode 1 in arbitrary units at Station 2. (C1=289.82 cm/s), S = 0.25

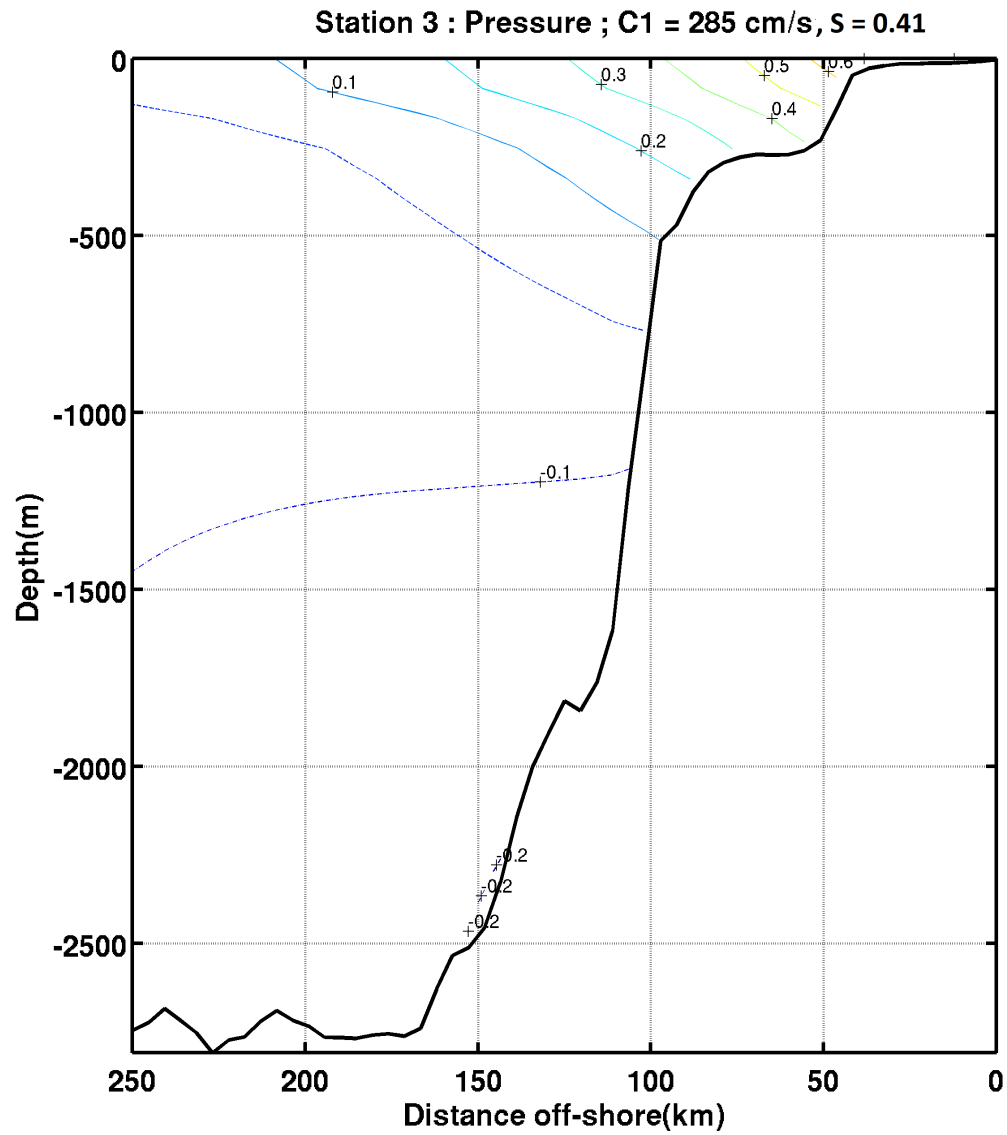


Figure 4.6: Pressure structures of eigen mode 1 in arbitrary units at Station 3. (C1=285 cm/s), S = 0.41

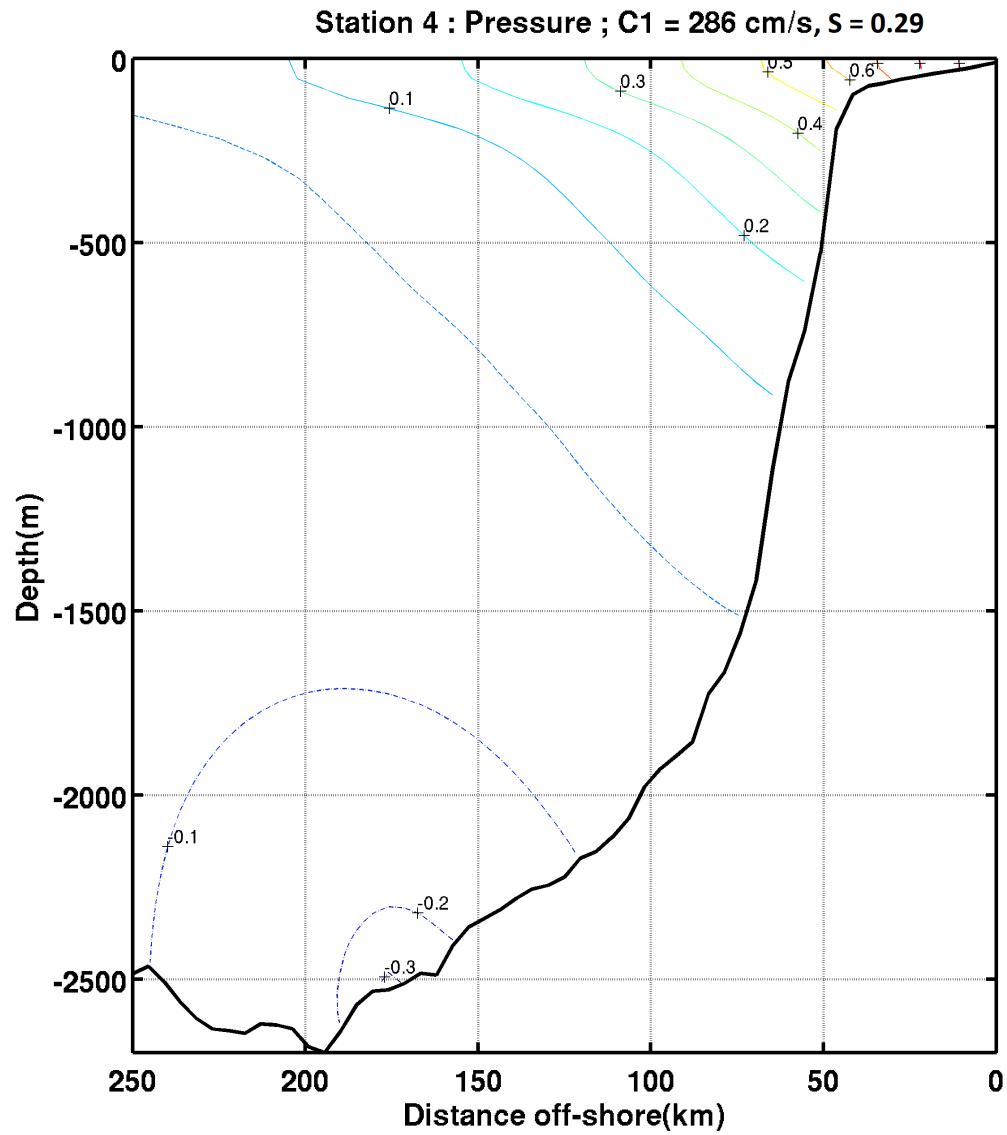


Figure 4.7: Pressure structures of eigen mode 1 in arbitrary units at Station 4. (C1=286 cm/s), S = 0.29

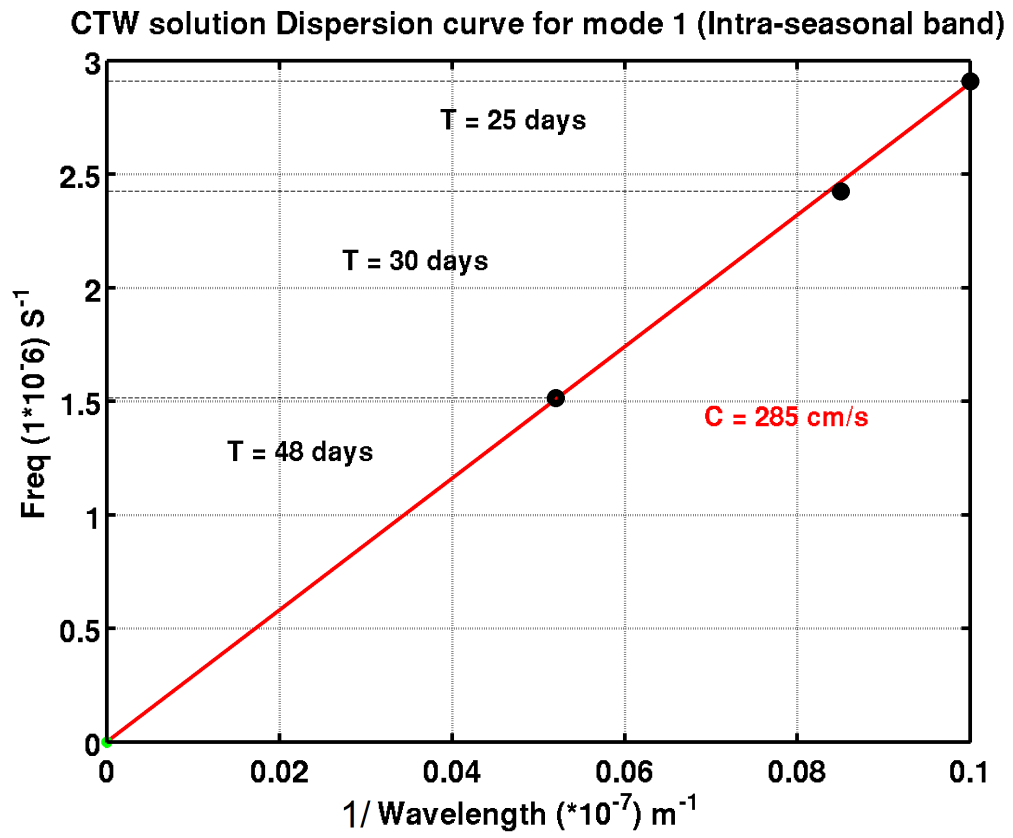


Figure 4.8: Dispersion curve for mode 1 CTW eigen structure along the path of Station 3.

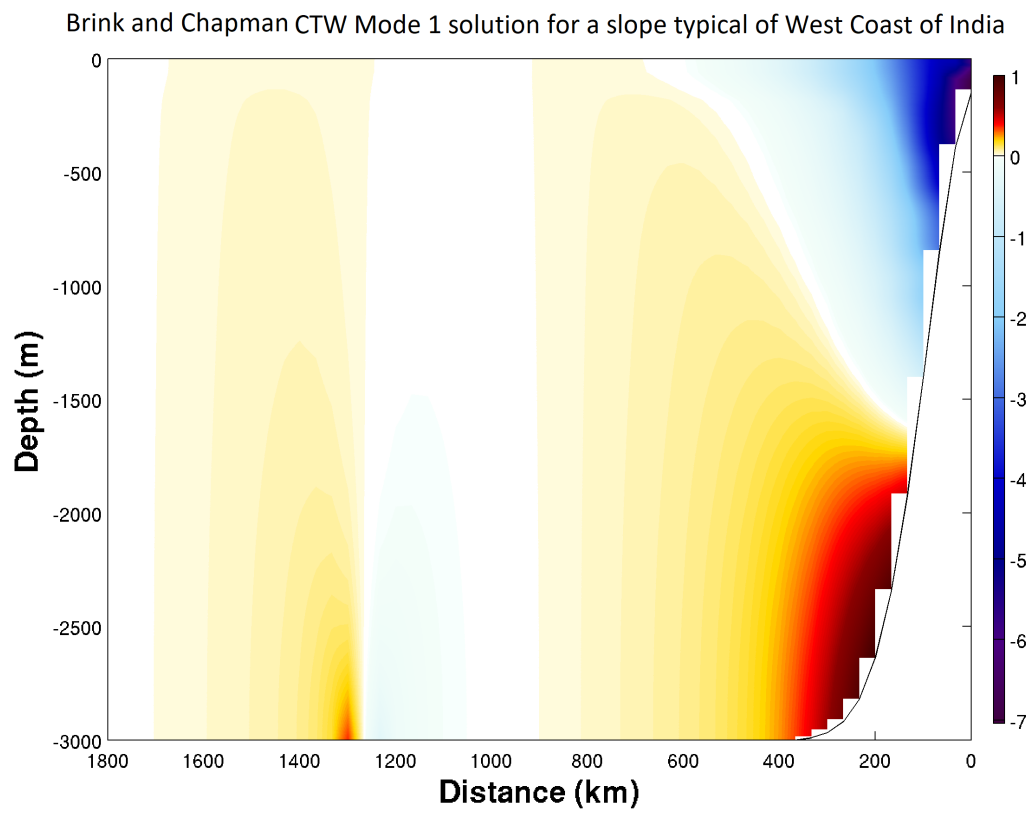


Figure 4.9: The velocity structure of mode 1 CTW obtained from Brink and Chapman solution for a typical slope along the west coast of India.

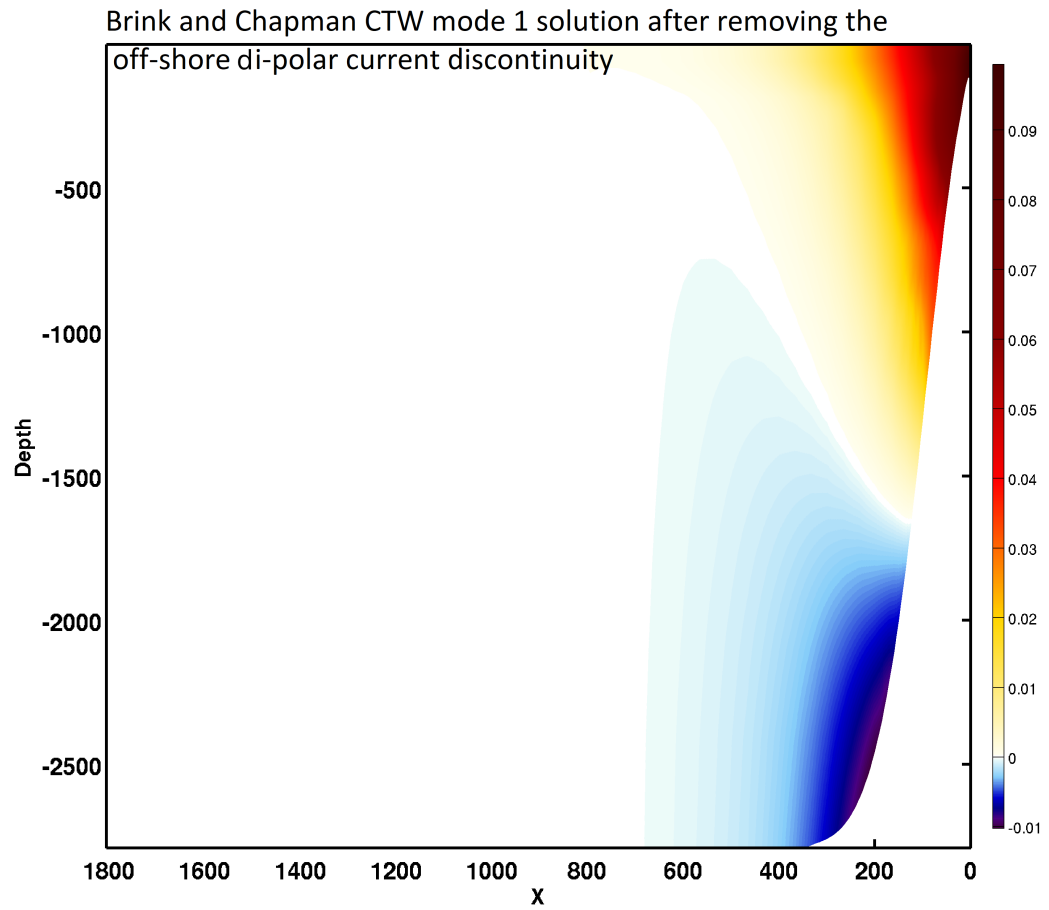


Figure 4.10: The velocity structure of mode 1 CTW after eliminating the off-shore discrepancies of the Brink and Chapman solution for a steep slope bathymetry. The obtained modal structure is not perfect and contains the contamination from higher modes, although, with low amplitudes.

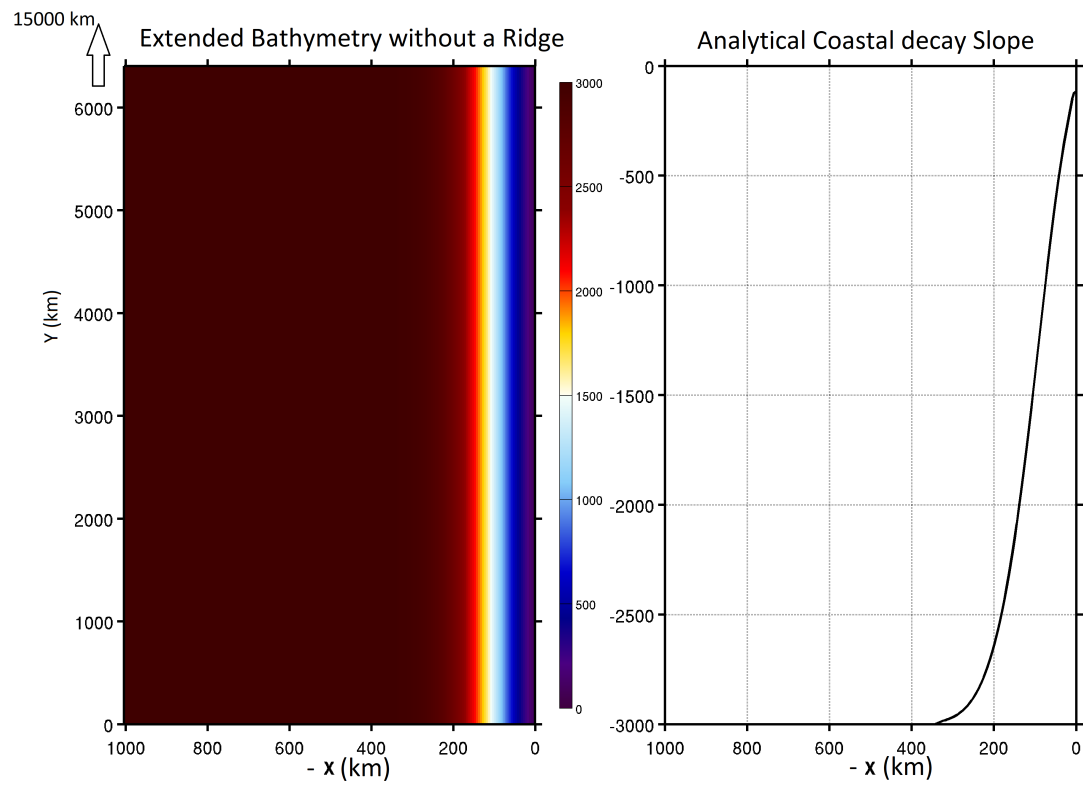


Figure 4.11: Bathymetry and slope along the west coast of India.

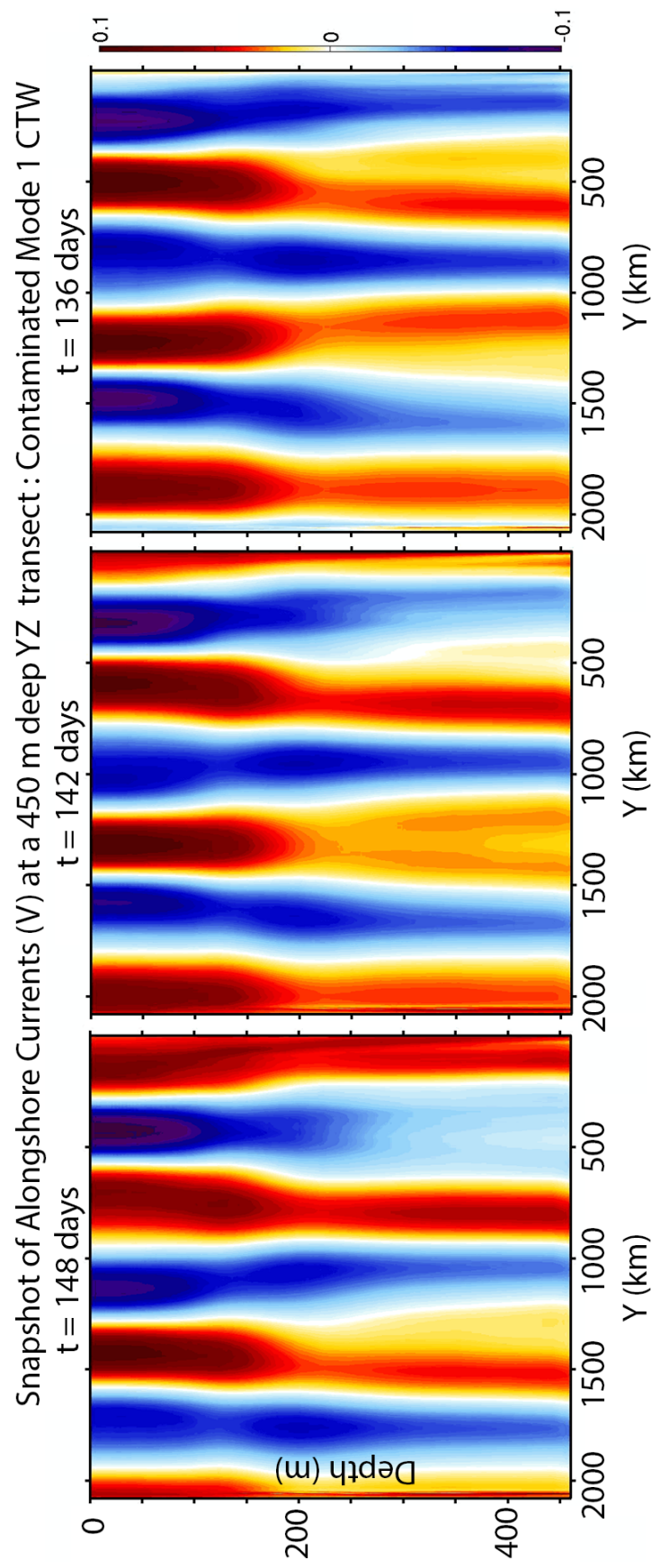


Figure 4.12: Snapshots of alongshore currents for the contaminated mode 1 CTW, at a 450 m deep off-shore transect in YZ at $t = 148$ days; $t = 142$ days; $t = 136$ days.

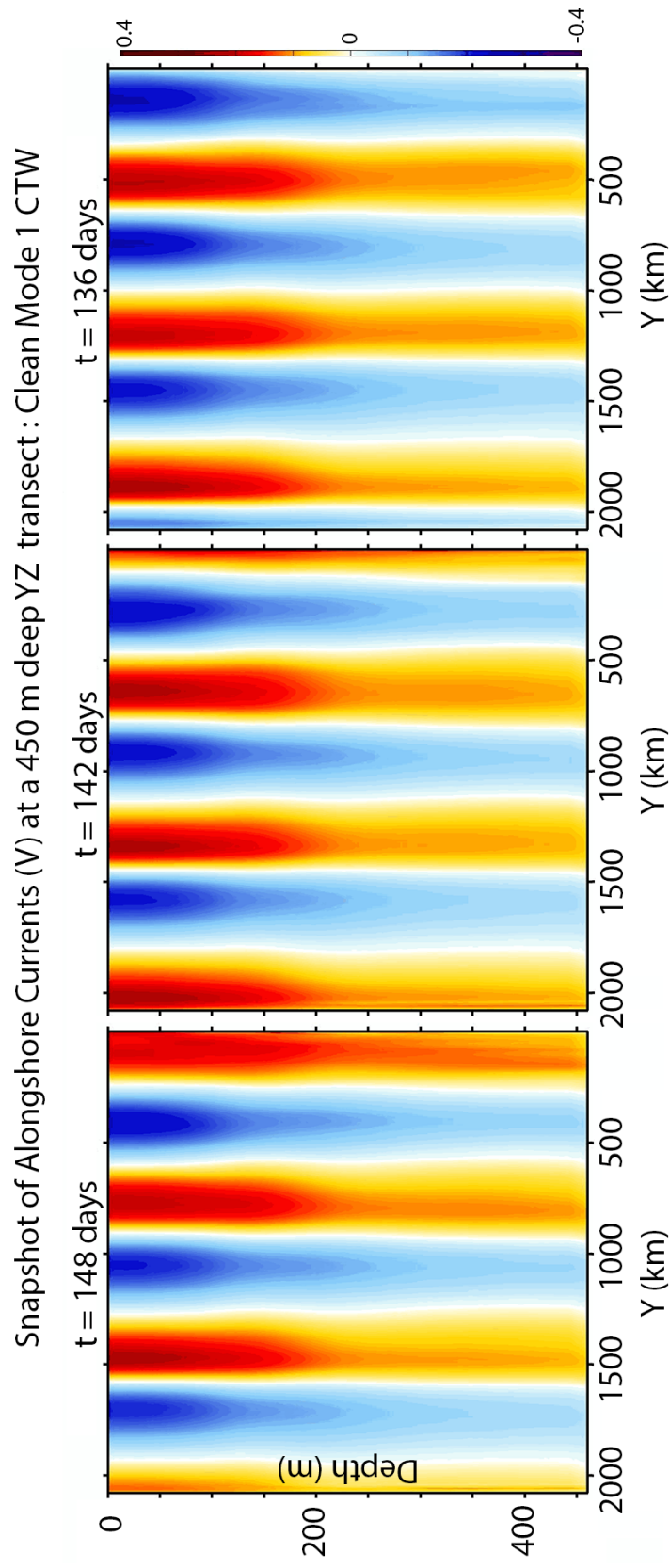


Figure 4.13: Snapshots of alongshore currents for the clean mode 1 CTW, at a 450 m deep off-shore transect in YZ (from left to right) at $t = 136$ days; $t = 142$ days; $t = 148$ days.

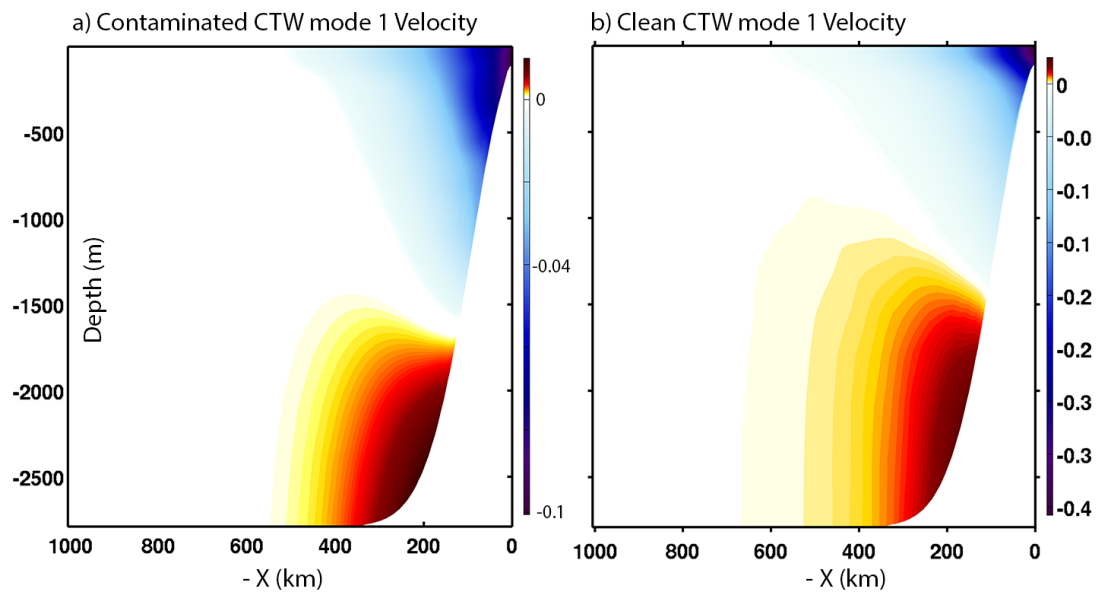


Figure 4.14: Right panel : The velocity structure of clean mode 1 CTW after eliminating all the contamination from higher modes, for a typical slope along the west coast of India. Left Panel: Same as Figure 4.10.

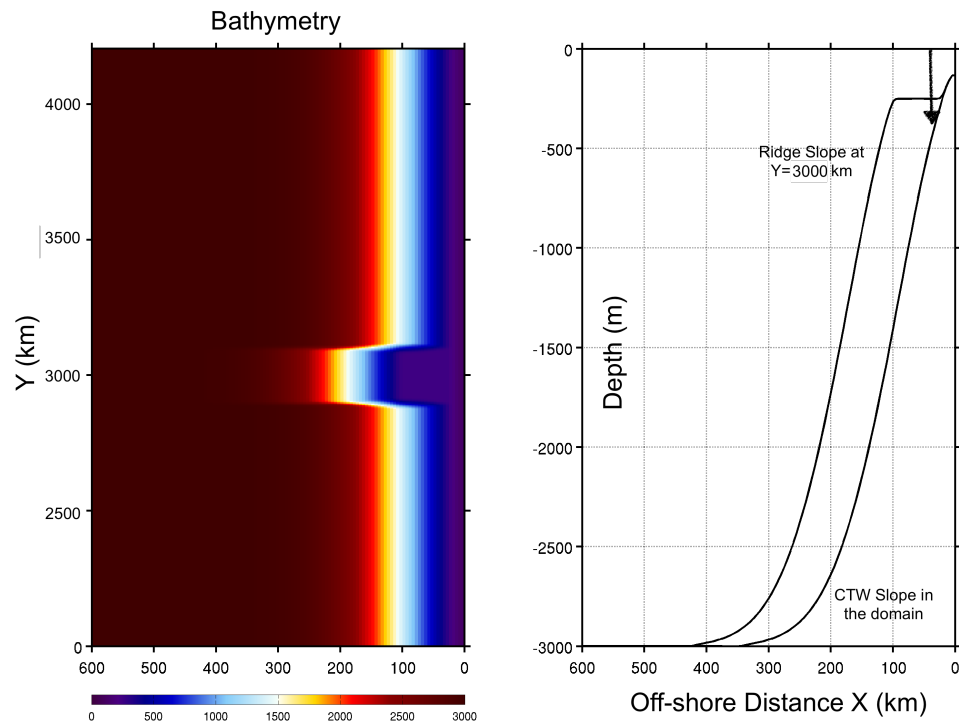


Figure 4.15: Figure to the left shows a bathymetry of the CTW domain with a 200 km wide and 80 km long ridge. The Figure to the right shows the coastal decay slope overlapped on top of ridge slope at $y = 3000$ kms.

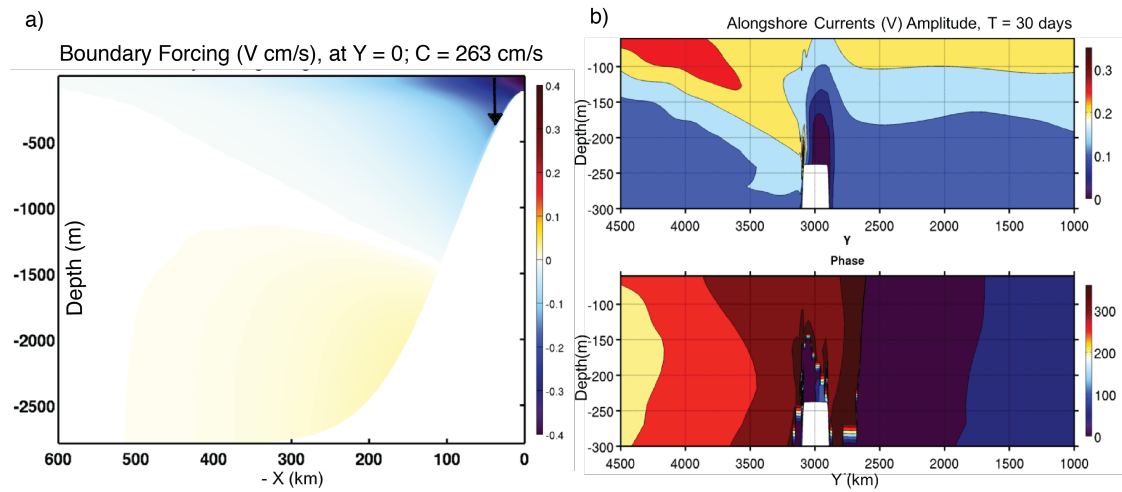


Figure 4.16: a) The cross-shore amplitude structure of alongshore current boundary forcing for a clean mode 1 CTW b) The CTW model output in terms of Amplitude and Phase for alongshore currents (V) at Kollam Mooring Depth (KMD) in Y-Z cross-section. T represents the time period (30 days), used to extract the sinusoidal Amplitude and Phase

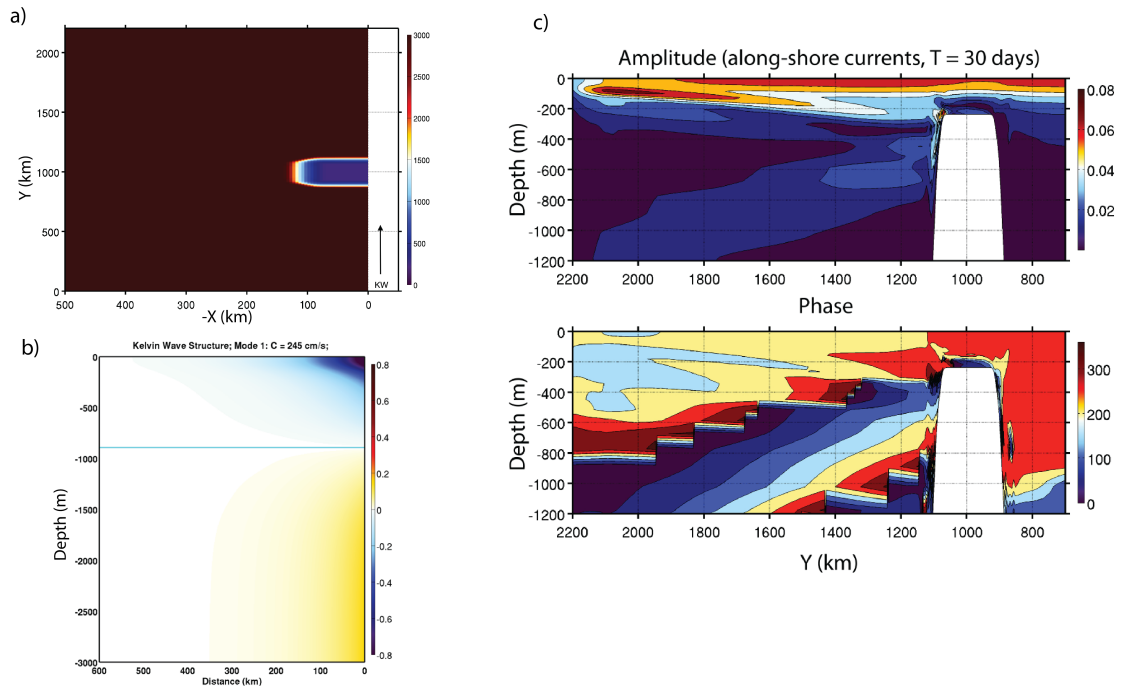


Figure 4.17: a) Bathymetry of KW domain with a 200 km wide and 80 km long ridge b) The cross-shore amplitude structure of alongshore current boundary forcing for a mode 1 KW c) KW model output in terms of Amplitude and Phase for alongshore currents (V) at wall. T represents the time period (30 days), used to extract the sinusoidal Amplitude and Phase

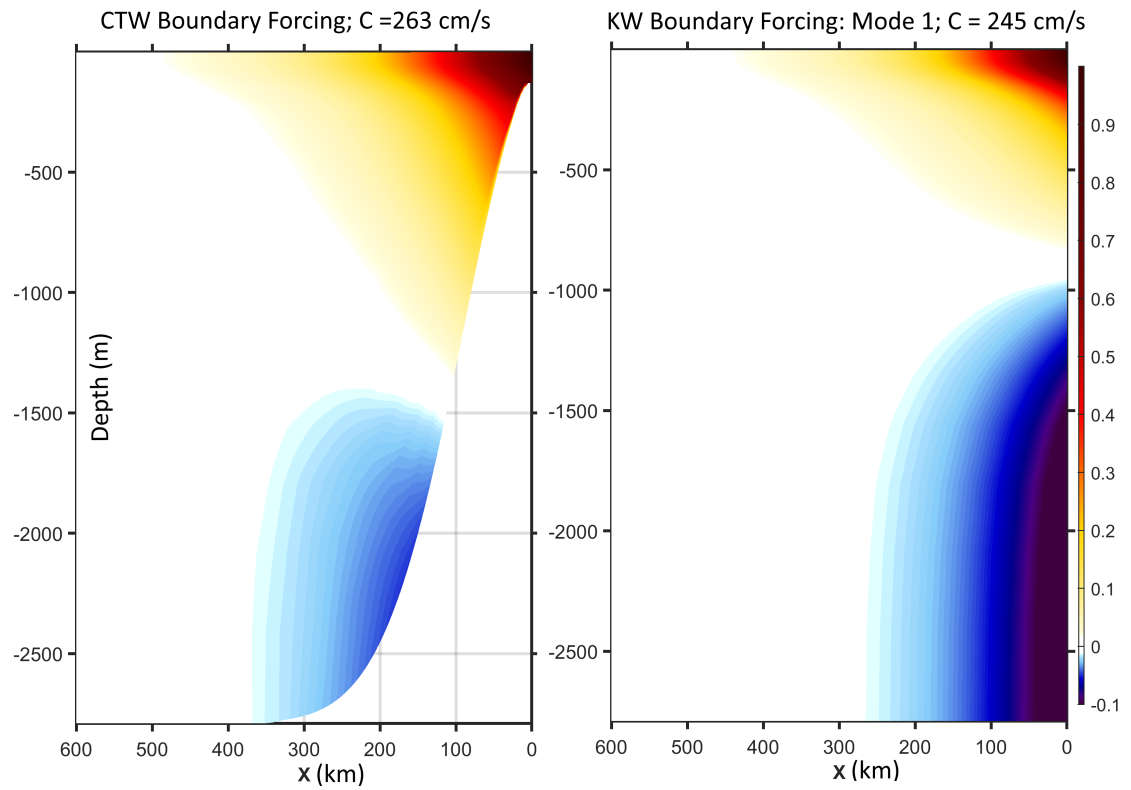


Figure 4.18: The amplitude of alongshore current boundary forcing for CTW and KW domain is plotted with a unit amplitude normalization for the maximum amplitude.

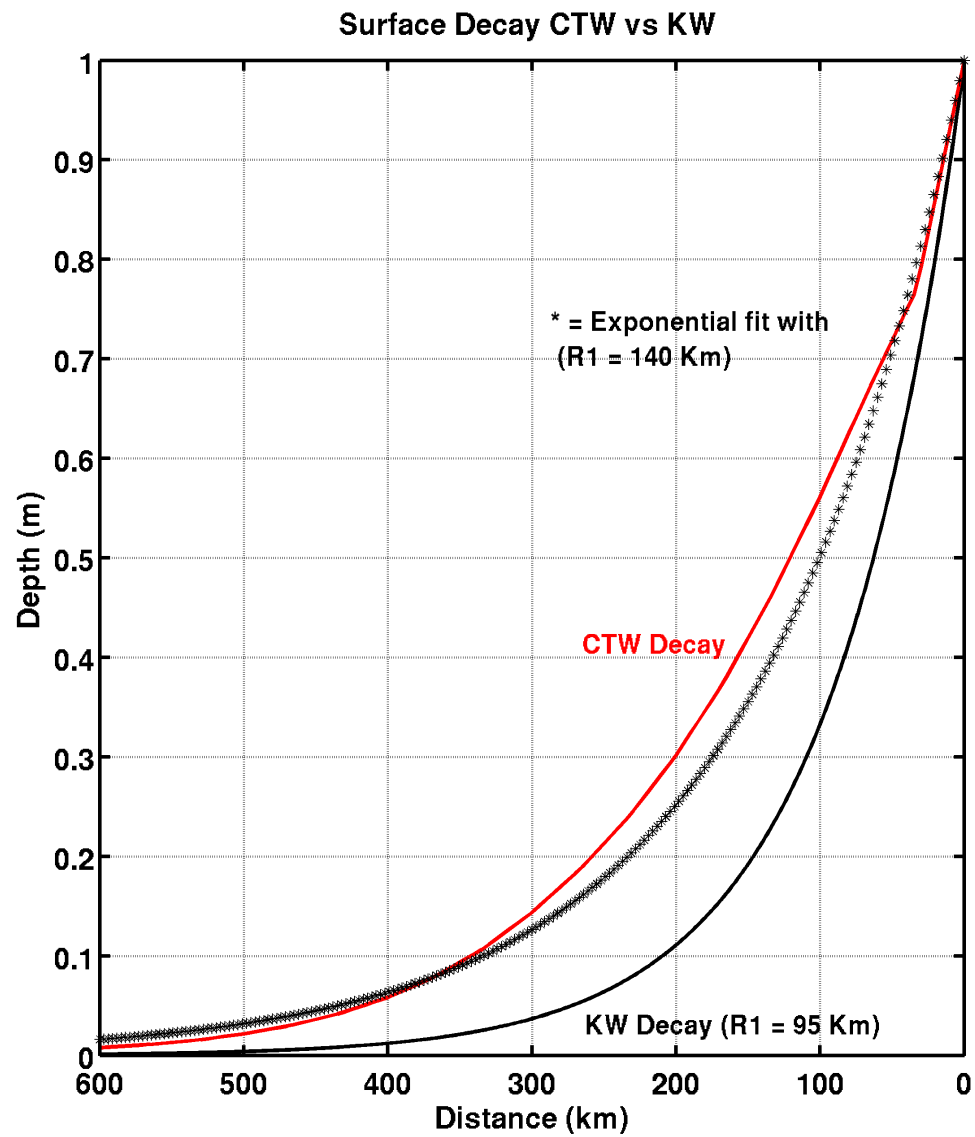


Figure 4.19: The surface amplitude decay of alongshore current boundary forcing for CTW and KW mode 1.

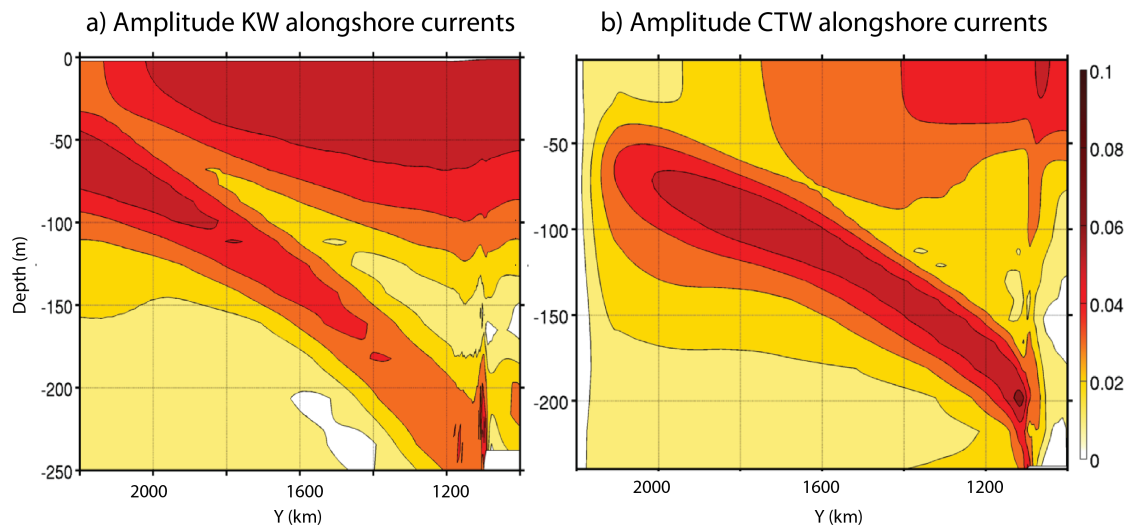


Figure 4.20: Comparison of alongshore currents 30 day period Amplitude for a) KW model run b) CTW model run

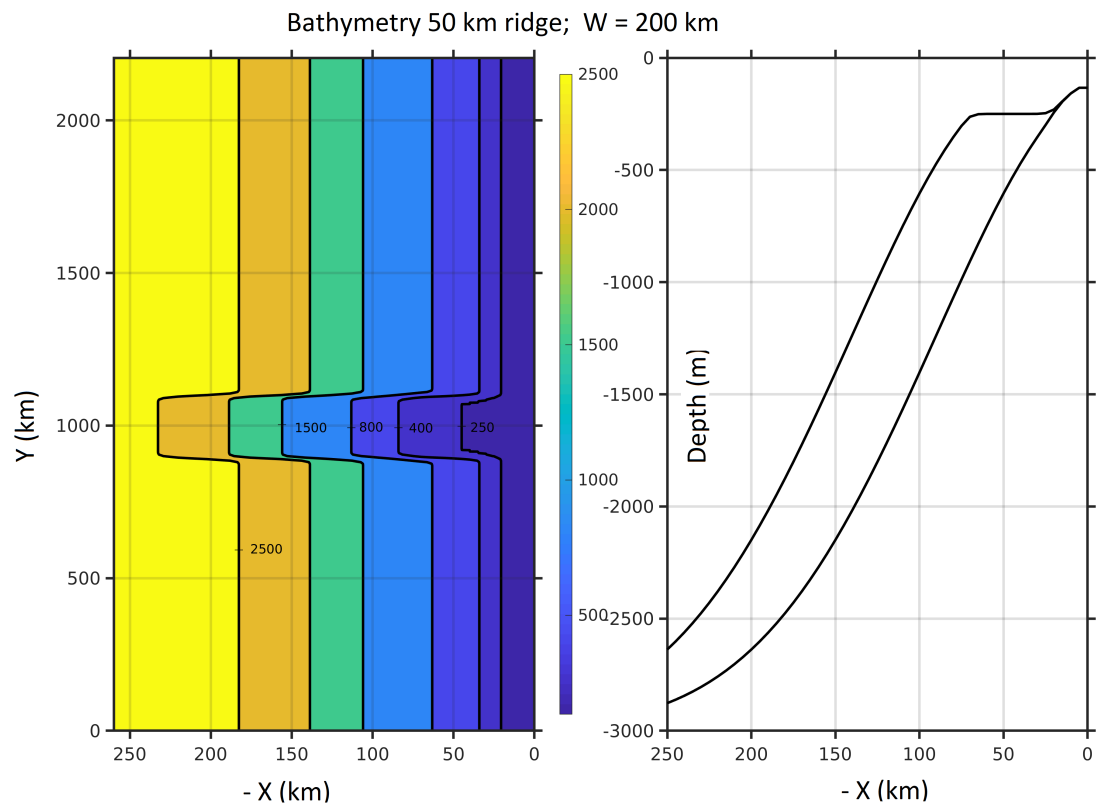


Figure 4.21: Bathymetry of a 50 km long and 200 km wide Ridge

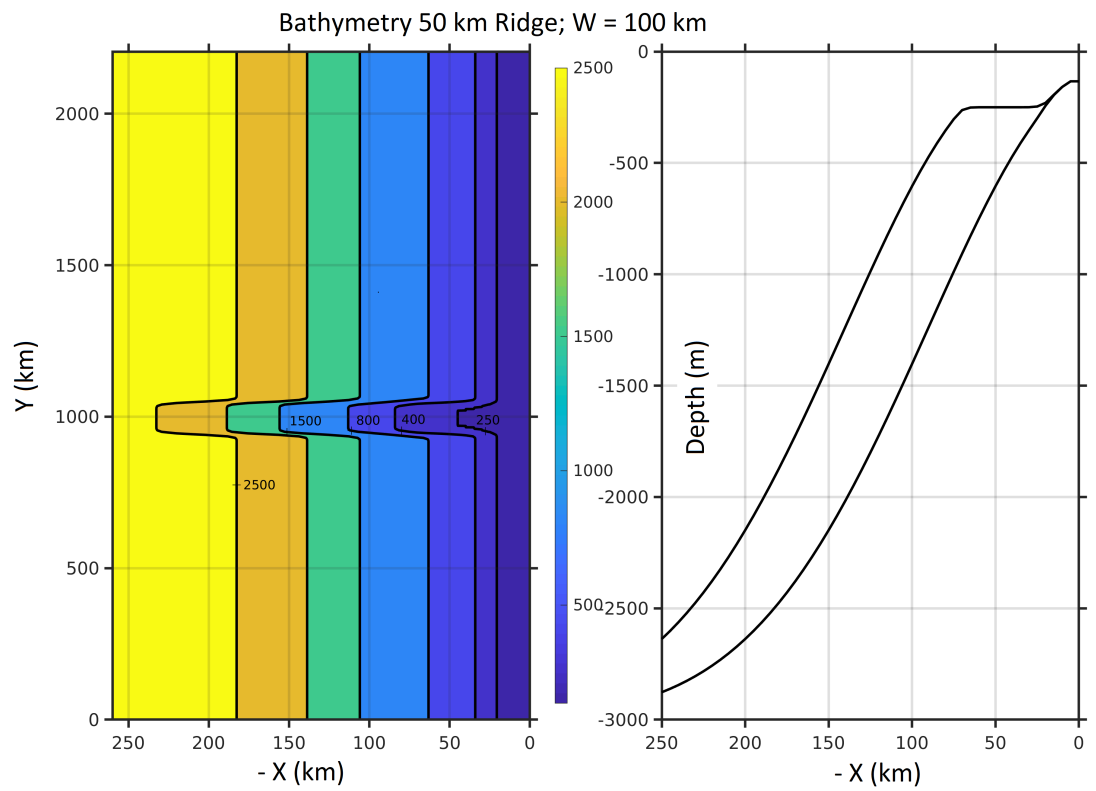


Figure 4.22: Bathymetry of a 50 km long and 100 km wide Ridge

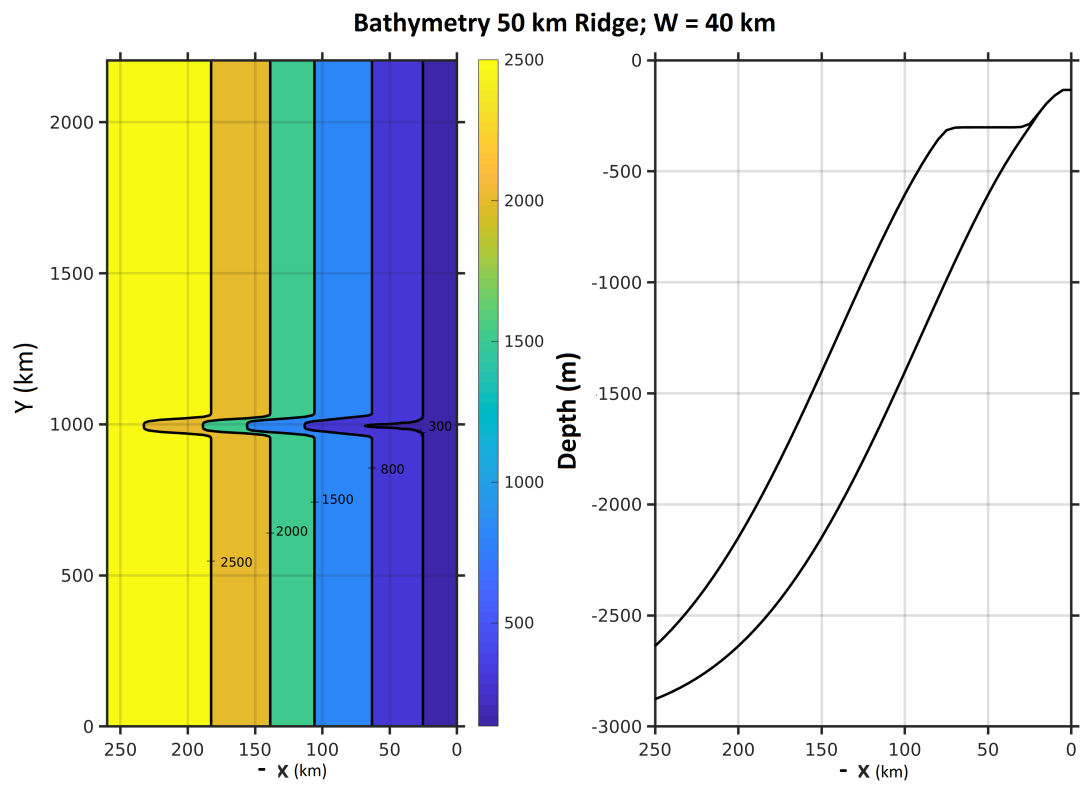


Figure 4.23: Bathymetry of a 50 km long and 40 km wide Ridge

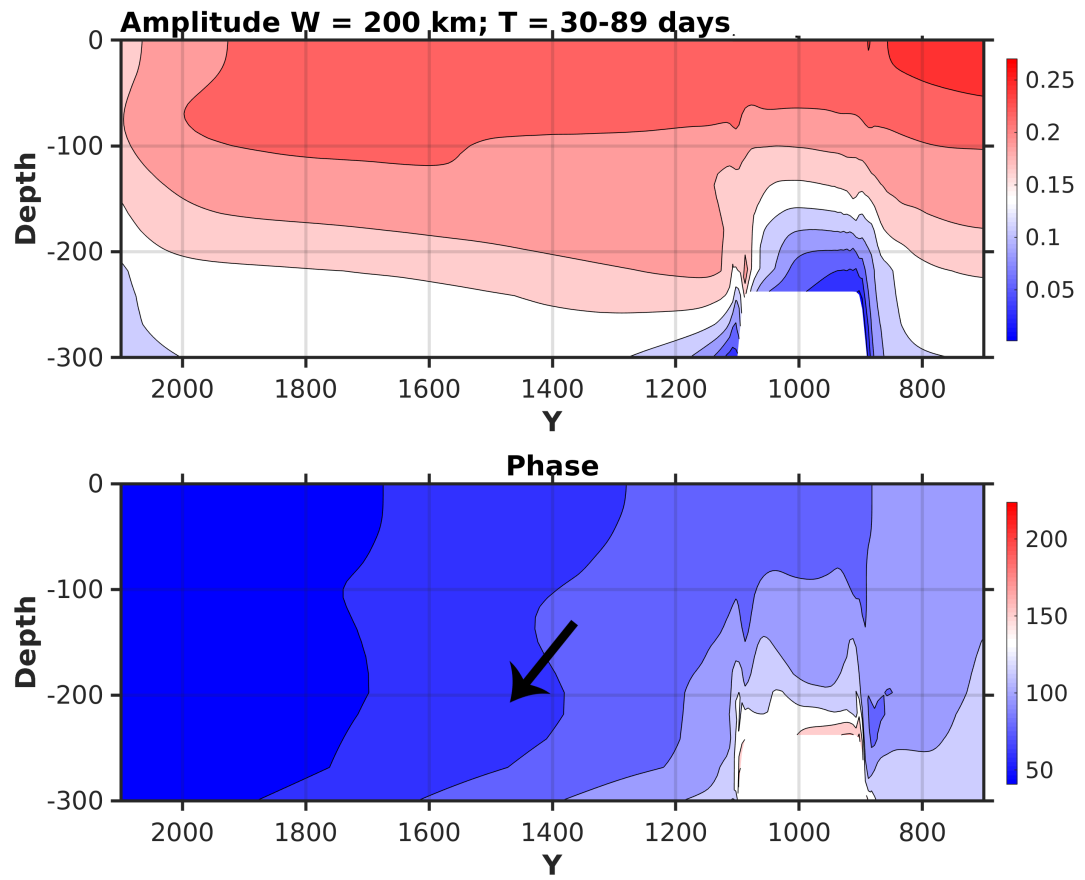


Figure 4.24: ROMS Amplitude and Phase of alongshore currents at a certain depth off-shore transect in YZ for a 50 km long and 200 km wide Ridge. Black Arrow show the direction of phase propagation

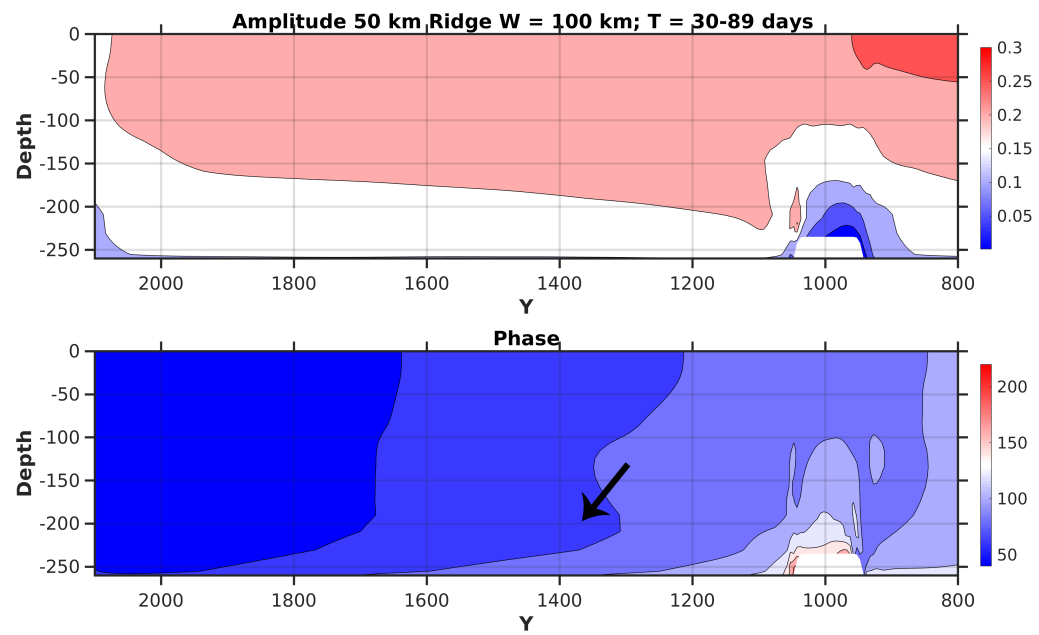


Figure 4.25: ROMS Amplitude and Phase of alongshore currents at a certain depth off-shore transect in YZ for a 50 km long and 100 km wide Ridge. Black Arrow show the direction of phase propagation.

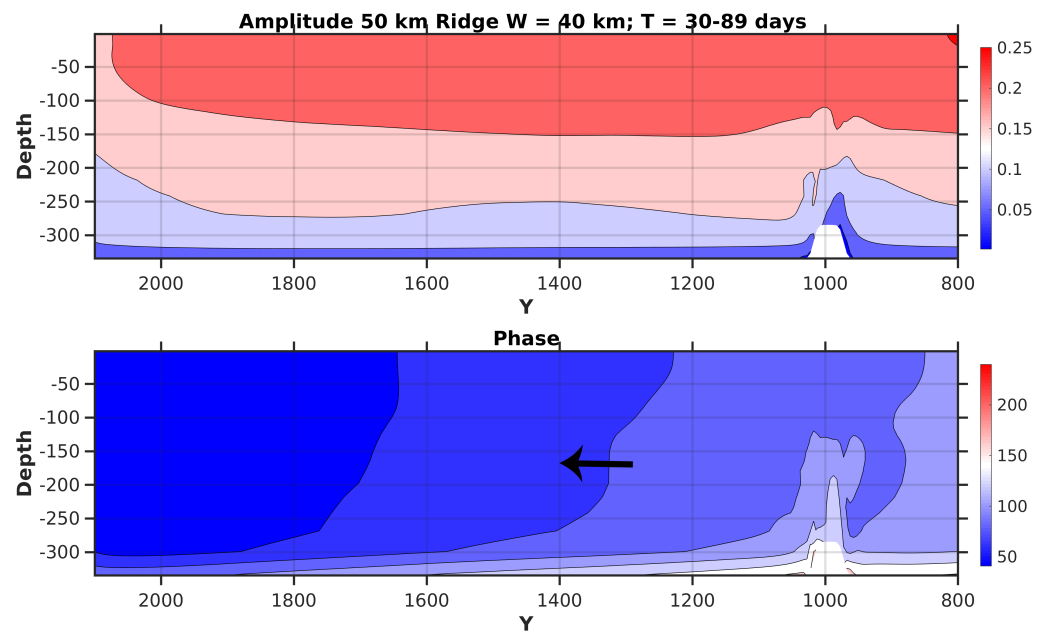


Figure 4.26: ROMS Amplitude and Phase of alongshore currents at a certain depth off-shore transect in YZ for a 50 km long and 40 km wide Ridge. Black Arrow show the direction of phase propagation.

Chapter 5: Conclusions

In the research described in this thesis our overall focus is on aspects of ocean circulation along the west coast of India. Periodic and propagating signals are examined with the intra-seasonal frequencies. In Chapter 2 we examine the relative importance of different sources of energy for signals that propagate along the west coast of India. These include local wind forcing and remote forcing in the form of waves trapped next to the coast. These waves may be generated at the tip of India and Sri-Lanka, along the east coast of India, the mid-Bay of Bengal or even from the wave-guide extending from the equator north into the Bay of Bengal.

In Chapter 3 we look more closely at waves with a single frequency and investigate a possible mechanism for the observed upward and downward propagation of energy along the west coast of India. The focus is the scattering of a single vertical mode KW by a subsurface ridge. Chapter 4 extends the study in Chapter 3 to look at the effects of a sloping bottom (Coastal Trapped Waves) in comparison to a vertical wall (Kelvin Waves) for the vertical propagation of energies.

5.1 Summary of Chapter 2

Chapter 2 investigates the importance of different forcing factors, remote versus local, for the sea level variability in the intra-seasonal band of periods (30-120 days).

Analysis of 10 years of altimeter SLA data and the ECMWF winds on intra-seasonal time scales of 30-120 days are consistent with previous studies that report the presence of Coastal Trapped Wave (CTW) dynamics along the west coast of India. Sea level at H1 (the west coast of India) is highly correlated with sea level and alongshore winds farther south along the coastal wave guide. Sea level at H1 is also moderately well correlated with the sea level east of Sri-Lanka and along the Sumatra coast, implying a more distant connection to the Equator. Sea level at H1 is also weakly correlated with sea level and winds along the south east coast of India. Leads of 3 to 4 weeks are found for sea level between Sumatra and Sri Lanka, followed by a lead of several days between Sri Lanka

and H1. Between the south-east coast of India and H1, the leads are 11 to 12 days for sea level.

The highest correlation for the wind forcing when correlated with SLA at H1 comes from the winds at the tip of India(TA3) with a lead of 6 days, which is too long to represent the creation of CTWs at the tip of India that propagate to H1. Wind forcing from other key locations also produce a lead close to 6 days when correlated with SLA at H1, suggesting the large scale nature of wind forcing. However, a multivariate regression model and coherence calculations give more realistic leads due to the interaction of SLA and winds within a narrower band of 40-60 day periods. In this narrow band, high coherences between H1 and local alongshore winds identify lags of 0-2 days, more realistic for a coastal response to local winds. High coherences between H1 and the south-east coast of India correspond to lags of 8-12 days for the same band. A final band-pass filtering of winds and sea levels to reduce periods outside of the 40-60 day band brings the lags from the correlation calculations of H1 sea level and winds into agreement with the coherence calculations and the regression model. In particular, the lead between local winds and sea level at H1 reduces to a more realistic 0-2 days lead.

Hovmöller diagrams illustrate the propagation of signals through a Rossby wave pathway and an east coast pathway. Rossby wave phase speeds estimated from the slope of Hovmöller plots are around 57 cm/s which is consistent with the previous observations by Webber et al. (2012) for intra-seasonal periods. The observed phase speed produces a lead of 3 to 4 weeks for SLA signals near Sumatra(X8) to travel to a location south of Sri-Lanka(X4), and then to travel quickly in the form of CTWs to reach H1. The phase speed of CTWs along the west coast of India is also estimated from the Hovmöller plots to be around 178 cm/s . Propagation on the east coast pathway is not robust and does not occur as often as along the Rossby wave pathway. This result provides a possible explanation for the modelling study by Suresh et al. (2013), in which the contribution of equatorial forcing for intra-seasonal SLA variability decreases as we move along the coastal wave guide from the northern Bay of Bengal to the eastern coast of Sri Lanka. The correlations then increase along the wave guide from south of Sri Lanka to the west coast of India. The Hovmöller diagrams provide evidence that the increased connection between the west coast of India and the equator is explained by the signals arriving along the Rossby wave pathway.

5.2 Summary of Chapter 3

Numerical process modeling supplemented by analytical approximations show that submerged ridges projecting from the shoreline can scatter a horizontally propagating single baroclinic mode Kelvin wave into both upward and downward propagating Kelvin wave beams, emanating from the ridge top. Numerical model experiments in the form of semi-infinite (fully-extended) ridges are designed to prevent the ridge waves from traveling around the ridge to affect the basin responses. These are compared with the analytical approximate solutions. The semi-infinite shelf response to the incident single mode KW reveals alongshore dependence of the vertical structure in the form of multi-modal ridge-top KWs, suggesting that the width of the ridge is an important factor in determining the basin response past the ridge. The approximate analytical solutions confirm that the upward propagating beam becomes weaker and narrower as the width of the ridge gets narrower (approaching the order of two Rossby radii of deformation on the shelf-top).

A series of numerical model runs further demonstrate the effects of varying the widths of the extended ridges. Decreasing the ridge width from 600 km to 120 kms greatly reduces the strength of the upward propagating beam. We hypothesize that over narrow ridges, the trapped solutions at the edges of the ridges overlap and interact to transmit horizontally propagating energy into the surface layer of the downstream basin. At the same time narrow ridges result in a weaker subsurface peak in velocity next to the ridge top in the downstream basin. This decreases the amplitude of vertically propagating KW beams.

The relative strengths of horizontally propagating KW modes to that of vertically propagating KW modes, is explored with the help of broad surface maxima and sharp subsurface peaks in the alongshore KW velocity profiles as a boundary condition next to edge of the ridge in the downstream basin. When the strength of the subsurface peaks in the vertical profile of alongshore currents is greater the basin response includes relatively stronger amplitudes of vertically propagating KW beams. On the other hand, when the strength of the surface maximum is greater, the strength of the horizontal propagation of energy at the surface is higher relative to the amplitudes of upward propagating KW beams in the downstream basin.

Numerical model runs are carried out for somewhat more realistic case scenarios in the form of finite ridges for an incoming single mode baroclinic KW. The basin response

past the ridge contains additional energy coming in the from of ridge waves. For the wide ridge considered here, the ridge wave strengthen the upward propagating KW beam compared to a semi-infinite ridge where the ridge waves are eliminated in the basin response. The qualitative nature of the upward propagating beam in the semi-infinite ridge, however, is not changed for the wide ridges.

5.3 Summary of Chapter 4

Chapter 4 analyzes the vertical propagation of energy by modeling the west coast of India with a sloping bottom. This is preliminary work done to assess how a more realistic sloping coastal boundary would affect the solutions in Chapter 3.

The differences between the flat-bottom KWs and sloping bottom CTWs in response to a sudden change in bathymetry in the form of a submerged ridge are investigated with the help of numerical model runs. The west coast of India near Kollam has a comparable shelf-slope width to that of that of the first mode Rossby radius of deformation. The scale ratio S in this region suggests that free wave solutions close to Kollam mooring behave more like IKWs. The corresponding phase speed and modal structure of IKWs however, does not accurately represent the hybrid mode 1 CTW phase speed and cross-shore structure.

In this study, we put-forth step by step procedures used to obtain a clean CTW mode 1 eigen function when the Brink and Chapman routines fail for the cases of steep bottom slopes and wide domains in cross-shore directions. Two different models runs in terms of a CTW domain and a KW domain, with a similar ridge dimensions, yield qualitatively similar upward propagating energy beams.

The effect of varying widths on the upward propagation of energy for CTWs is carried out using three different model runs of the widths of 200 km, 100 km and 40 kms by keeping all other dimensions the same. The upward propagation of energy gets weaker as the width of ridge gets narrower.

APPENDICES

Meridional Energy Flux Near an Eastern Boundary Within the
Turning Latitudes of an Equatorial Basin

Ted Durland, Dennis W. Moore, Julian P. McCreary and Laxmikant Dhage

Term paper based on 2014 Fall AGU Poster

Appendix A: Meridional Energy Flux Near an Eastern Boundary Within the Turning Latitudes of an Equatorial Basin

A.1 Introduction

Interaction of the atmosphere with the ocean plays an important role in the ocean dynamics and vice versa. The changes in the properties of the ocean, such as sea surface temperature (SST), sea surface height (SSH) etc. affect the atmosphere by altering the boundary layer above the surface of the ocean (Sweet et al., 1981). These air sea interactions act as a feedback mechanism for each other. For instance, strong SST fronts in the ocean affect the atmospheric thermal boundary layer, altering the wind stress experienced by Ocean surface (DB Chelton et al., 2004). Similarly, wind stress on the ocean acts as a forcing term in the momentum equation, altering the properties of the ocean through different dynamics processes. Hence, atmosphere and ocean communicate with each other by changing the properties of one another.

Another important phenomenon regarding air sea interactions is El-Niño Southern Oscillation (ENSO) events in the Pacific Ocean. Instability in the coupled interaction of ocean and atmosphere may help to trigger these events (Philander et al., 1984). Consistent easterly winds on the equator pile up the warm water on the west. However the relaxation of these winds triggers packets of equatorial trapped Kelvin waves (Cane, 1983). During an El-Niño event a strong downwelling Kelvin wave is generated along the equator which then reflects from the American continents leading to westward propagating Rossby waves and poleward propagating coastal Kelvin waves (McPhaden and Yu, 1999). Poleward propagating Coastal Kelvin waves, linked to these ENSO events, bring the warm waters to the coast, deepening the thermocline on the large scale (Alexander et al., 2012). Changes in the SST anomalies induced due to distant equatorial air-sea dynamics thus can alter the local air sea properties.

A similar phenomenon occurs in the Indian ocean, where changes in the Equatorial trade winds in the form of Madden Julian oscillation (MJO) can trigger equatorial trapped oceanic Kelvin waves. Rao et al. (2010) showed how these Equatorial Kelvin waves can

then alter the distant oceanic conditions, all the way to the west coast of India, through poleward propagating Coastal Kelvin waves.

Thus it shows that air-sea coupling in the equatorial region can alter the distant atmospheric and oceanic condition in the form of propagating Coastal Kelvin waves. However, it is unclear how the energy is transferred from eastward propagating Kelvin wave into the poleward propagating Coastal Kelvin waves, after they are reflected from the boundary.

When a low frequency Kelvin wave on an equatorial beta plane reflects from an eastern meridional boundary, it generates a finite number of westward propagating Rossby modes and infinite number of evanescent modes. Moore (1968) showed that poleward of the turning latitude, the sum of these evanescent modes is equivalent to a coastal trapped wave. However, within the turning latitudes, the meridional energy flux associated with evanescent modes is significantly less than to the poleward energy flux in Coastal Kelvin Waves. The net energy flux (referred solely as period averaged fluxes) associated with individual (finite and real) Rossby modes is due westwards(zonal), as the meridional velocity associated with these modes is orthogonal to pressure signals, implying no meridional energy flux associated with Rossby modes (Clarke, 1983). The above scenario of energy fluxes leads to an important and fundamental question: How does the energy flux from the incident Kelvin wave gets transferred through the narrow strip within the turning latitude, where there is negligible poleward energy flux, to the turning latitude, where there is strong poleward energy flux in the form of coastal Kelvin wave? This work will try to answer the above question by analytical computation of the energy fluxes linked to the interactions of different modes with each other.

This study will thus focus on understanding this fundamental dynamics in more depth, as these poleward propagating Kelvin waves carry the information from the Equator to large distances along the wave-guide.

A.2 Methods

In order to gain the deep understanding of the dynamics we will look into the the energy fluxes due to interactions of different modes with one another.

Equatorial Rossby waves

We assume a shallow water model on an equatorial β -plane ($f = \beta y$) with the Boussinesq approximations. Linearised momentum equations are as follows:

$$\frac{\partial u^*}{\partial t^*} - f^* v^* = g \frac{\partial \eta^*}{\partial x^*} \quad (\text{A.1})$$

$$\frac{\partial v^*}{\partial t^*} + f^* u^* = g \frac{\partial \eta^*}{\partial y^*} \quad (\text{A.2})$$

$$\frac{\partial \eta^*}{\partial t^*} + \frac{g}{c^2} \left(\frac{\partial u^*}{\partial x^*} + \frac{\partial v^*}{\partial y^*} \right) = 0 \quad (\text{A.3})$$

Here u^* and v^* are zonal and meridional velocities respectively where as η^* is the sea level fluctuations from the mean and c is the gravity wave speed. Non-dimensionalisation of the above variables using Matsuno (1966) :

$$(x^*, y^*) = \sqrt{\frac{c}{\beta}} (x, y)$$

$$(t^*) = \sqrt{\frac{1}{\beta c}} (t)$$

$$(u^*, v^*) = c (u, v)$$

$$(\eta^*) = \frac{c^2}{g} (\eta)$$

$$(h) = \frac{c^2}{g}$$

Substituting the above non-dimensionalised variables in Equations 1, 2 and 3, we obtain:

$$\frac{\partial u}{\partial t} - y v = \frac{\partial \eta}{\partial x} \quad (\text{A.4})$$

$$\frac{\partial v}{\partial t} + y u = \frac{\partial \eta}{\partial y} \quad (\text{A.5})$$

$$\frac{\partial \eta}{\partial t} + \left(\frac{\partial u}{\partial x} + \frac{\partial v}{\partial y} \right) = 0 \quad (\text{A.6})$$

Re-arranging the above three equations in terms of the meridional velocity we obtain:

$$\left(y \frac{\partial}{\partial t} (4) - \frac{\partial^2}{\partial t^2} (5) + \frac{\partial^2}{\partial t \partial y} (6) + \frac{\partial^2}{\partial x^2} (5) - \frac{\partial^2}{\partial x \partial y} (4) \right)$$

$$\frac{\partial^3 v}{\partial^3 t} + y^2 \frac{\partial v}{\partial t} + \frac{\partial}{\partial t} \left(\frac{\partial^2 v}{\partial^2 x} + \frac{\partial^2 v}{\partial^2 y} \right) - \frac{\partial v}{\partial x} = 0 \quad (\text{A.7})$$

Using the Fourier Transform in time and zonal direction, i.e. substituting in the above equation $v = V_0(y) e^{i(kx - \omega t)}$, We obtain :

$$\frac{\partial^2 V_0}{\partial^2 y} + \left(\omega^2 - k^2 - \frac{k}{\omega} - y^2 \right) V_0 = 0 \quad (\text{A.8})$$

The above equation is very well known in mathematics as a Hermite equation. It has a solution bounded at infinity in the form of meridional modes as a function of Hermite polynomials. Thus the n^{th} meridional mode can be written as $v_n = A_n \psi_n(y) e^{i(k_n x - \omega t)}$. Substituting in above equation we get :

$$\frac{\partial^2 \psi_n}{\partial^2 y} + \left(\lambda_n^2 - y^2 \right) \psi_n = 0 \quad (\text{A.9})$$

Where λ_n is an eigen value and $\lambda_n^2 = \omega^2 - k_n^2 - \frac{k_n}{\omega}$. For an unbounded basin $\lambda_n^2 = 2n + 1$; and $n = 0, 1, 2, \dots$ such that $\lim_{y \rightarrow \pm\infty} \psi_n(y) = 0$

Thus we obtain the dispersion relation for Equatorial waves

$$\omega^2 - k_n^2 - \frac{k_n}{\omega} = \lambda_n^2 \quad (\text{A.10})$$

Solving for k_n

$$k_n = -\frac{1}{2\omega} \pm \sqrt{\omega^2 + \frac{1}{4\omega^2} - \lambda_n^2} \quad (\text{A.11})$$

ψ_n are Hermite functions, related to Hermite polynomials by

$$\psi_n(y) = \frac{e^{(-y^2/2)}}{\sqrt{2^n n!} \sqrt{\pi}} H_n(y) \quad (\text{A.12})$$

Where as Hermite polynomials can be generated by Rodrigues formula:

$$H_n(y) = (-1)^n \exp(y^2) \frac{\partial^n (e^{-y^2})}{\partial^n y} \quad (\text{A.13})$$

Hence the obtained solution can be written as :

$$\begin{bmatrix} u \\ v \\ \eta \end{bmatrix} = \sum_n \begin{bmatrix} u_n(y) \\ v_n(y) \\ \eta_n(y) \end{bmatrix} e^{i(k_n x - \omega t)} \quad (\text{A.14})$$

Using Equations 4, 5 and 6 we can write u and η in terms of v as follows:

$$\left(\frac{\partial^2}{\partial^2 t} + \frac{\partial^2}{\partial^2 x} \right) \begin{bmatrix} u_n \\ \eta_n \end{bmatrix} = \begin{bmatrix} y \frac{\partial}{\partial t} + \frac{\partial^2}{\partial x \partial y} \\ -y \frac{\partial}{\partial x} + \frac{\partial^2}{\partial t \partial y} \end{bmatrix} v_n \quad (\text{A.15})$$

Substituting Equation 14 in Equation 13 and using the Fourier transform we can get

$$\begin{bmatrix} u \\ v \\ \eta \end{bmatrix} = \sum_n \frac{-i A_n}{k_n^2 - \omega^2} \begin{bmatrix} \omega y - k_n \partial y \\ i(k_n^2 - \omega^2) \\ k_n y - \omega \partial y \end{bmatrix} \psi_n(y) e^{i(k_n x - \omega t)} \quad (\text{A.16})$$

Assuming $B_n = \frac{-i A_n \sqrt{2n}}{k_n + \omega}$; $\alpha_n = \frac{k_n + \omega}{k_n - \omega}$, We obtain:

$$\begin{bmatrix} u \\ v \\ \eta \end{bmatrix} = \sum_n \frac{B_n}{\sqrt{2n}} \begin{bmatrix} (\alpha_n - 1) y - (\alpha_n + 1) \partial y \\ 2 i (k_n + \omega) \\ (\alpha_n - 1) y - (\alpha_n + 1) \partial y \end{bmatrix} \psi_n(y) e^{i(k_n x - \omega t)} \quad (\text{A.17})$$

Rearranging the above equation

$$\begin{bmatrix} u \\ v \\ \eta \end{bmatrix} = \sum_n \frac{B_n}{\sqrt{2n}} \begin{bmatrix} \alpha_n(y - \partial y) - (y + \partial y) \\ 2 i (k_n + \omega) \\ \alpha_n(y - \partial y) + (y + \partial y) \end{bmatrix} \psi_n(y) e^{i(k_n x - \omega t)} \quad (\text{A.18})$$

Using the property of Hermite functions that is $(y - \partial y)\psi_n = \sqrt{2(n+1)}\psi_{n+1}$ and $(y + \partial y)\psi_n = \sqrt{2n}\psi_{n-1}$, we get

$$\begin{bmatrix} u \\ v \\ \eta \end{bmatrix} = \sum_n \frac{B_n}{\sqrt{2n}} \begin{bmatrix} \alpha_n \sqrt{2(n+1)} \psi_{n+1} - \sqrt{2n} \psi_{n-1} \\ 2 i (k_n + \omega) \psi_n \\ \alpha_n \sqrt{2(n+1)} \psi_{n+1} + \sqrt{2n} \psi_{n-1} \end{bmatrix} e^{i(k_n x - \omega t)} \quad (\text{A.19})$$

Assuming $\gamma_n = \sqrt{\frac{n+1}{n}} \alpha_n$ We get,

$$\begin{bmatrix} u \\ v \\ \eta \end{bmatrix} = \sum_n B_n \begin{bmatrix} \gamma_n \psi_{n+1} - \psi_{n-1} \\ i \sqrt{\frac{2}{n}} (k_n + \omega) \psi_n \\ \gamma_n \psi_{n+1} + \psi_{n-1} \end{bmatrix} e^{i(k_n x - \omega t)} \quad (\text{A.20})$$

Kelvin Waves

Another way to satisfy the above sets of equations and the boundary condition, is to have no meridional velocity through out the domain. Using Equations 4, 5 and 6 and substituting $v = 0$ we get eastward and westward propagating Kelvin Waves (Rattray, 1965). The eastward propagating solution is referred as an equatorial Kelvin Wave.

$$\begin{bmatrix} u \\ v \\ \eta \end{bmatrix}_{Kelvin} = B_\kappa \begin{bmatrix} 1 \\ 0 \\ 1 \end{bmatrix} \psi_0(y) e^{i(k_\kappa x - \omega t)} \quad (\text{A.21})$$

$$k_\kappa = \omega \quad (\text{A.22})$$

A.2.1 Reflection from Eastern Boundary

Assume a Kelvin wave with an amplitude of B_κ reflects from an Eastern Boundary at $x = 0$, generating finite real Rossby modes and infinite evanescent Rossby modes. Considering the symmetry of the problem about the equator we will consider only odd Rossby modes which can provide the symmetric solutions for u and η about the equator.

Incident Kelvin Wave at $(x, t) = 0$:

$$\begin{bmatrix} u(y) \\ \eta(y) \end{bmatrix}_{Kelvin} = B_\kappa \begin{bmatrix} 1 \\ 1 \end{bmatrix} \psi_0(y) \quad (\text{A.23})$$

Reflected Rossby waves:

$$\begin{bmatrix} u(y) \\ \eta(y) \end{bmatrix}_{Rossby} = \sum_{n=0}^{\infty} B_{2n+1} \begin{bmatrix} \gamma_{2n+1} \psi_{2n+2} - \psi_{2n} \\ \gamma_{2n+1} \psi_{2n+2} + \psi_{2n} \end{bmatrix} \quad (\text{A.24})$$

Here the value of γ_n is computed such that k_n is appropriate for an eastern boundary reflection, i.e., the reflected Rossby modes have westward group velocity or decay; given by:

$$\gamma_n = \sqrt{\frac{n+1}{n}} \frac{k_n + \omega}{k_n - \omega}; \quad k_n = -\frac{1}{2\omega} - i \sqrt{2n+1 - \left(\omega^2 + \frac{1}{4\omega^2}\right)} \quad (\text{A.25})$$

Combining Equation 23 and 24:

$$\begin{bmatrix} u(y) \\ \eta(y) \end{bmatrix}_{Kelvin} + \begin{bmatrix} u(y) \\ \eta(y) \end{bmatrix}_{Rossby} = \begin{bmatrix} u(y) \\ \eta(y) \end{bmatrix}_{(x=0, t=0)} \quad (\text{A.26})$$

$$\begin{bmatrix} u \\ \eta \end{bmatrix}_{EB, x=0} = B_\kappa \begin{bmatrix} 1 \\ 1 \end{bmatrix} \psi_0(y) + \sum_{n=0}^{\infty} B_{2n+1} \begin{bmatrix} \gamma_{2n+1} \psi_{2n+2} - \psi_{2n} \\ \gamma_{2n+1} \psi_{2n+2} + \psi_{2n} \end{bmatrix} \quad (\text{A.27})$$

Rearranging Equation (27) and re-indexing as a Hermite Series we obtain:

$$\begin{bmatrix} u \\ \eta \end{bmatrix}_{EB, x=0} = \begin{bmatrix} B_\kappa - B_1 \\ B_\kappa + B_1 \end{bmatrix} \psi_0 + \sum_{n=1}^{\infty} \begin{bmatrix} \gamma_{2n-1} B_{2n-1} - B_{2n+1} \\ \gamma_{2n-1} B_{2n-1} + B_{2n+1} \end{bmatrix} \psi_{2n} \quad (\text{A.28})$$

The boundary condition $u_{EB}(y) = 0$ requires the co-efficient of each Hermite function to vanish. Hence from Equation (28) we get:

$$B_1 = B_\kappa \quad (\text{A.29})$$

$$B_{2n+1} = \gamma_{2n-1} B_{2n-1} \quad (\text{A.30})$$

Incorporating Equation (29) and (30) together we obtain:

$$B_{2n+1} = B_\kappa \prod_{m=1}^n \gamma_{2m-1} \quad (\text{A.31})$$

such that for $n = 0$

$$\prod_{m=1}^n \gamma_{2m-1} = 1 \quad (\text{A.32})$$

A.2.2 Energy Flux

Time averaged energy fluxes are computed separately for zonal and meridional directions. Interaction of each mode with one another is looked upon to get corresponding energy fluxes. We categorized Rossby modes broadly into 2 classes 1) Real Finite Rossby modes (real wave number) 2) infinite evanescent modes (imaginary wave number). Energy fluxes are categorized broadly into two categorizes according to the interaction of modes with one another.

1) Energy flux due to interaction of a mode with itself (individual) 2) Energy flux due to interaction of distinct modes (distinct). The above two categories are then further sub-categorized as follows:

[E^K = Incident kelvin mode, $E^{(m/n)}$ = evanescent distinct Rossby modes, $E^{(M/N)}$ = real distinct Rossby modes, involved in computation of energy flux]

1) Energy flux due to interaction of a mode with itself (Individual)

- (a) Incident Kelvin mode interacting with itself (\mathbf{E}^{KK})
- (b) Real Rossby mode interacting with itself ($\mathbf{E}^{MM}/\mathbf{E}^{NN}$)
- (c) Evanescent Rossby mode interacting with itself ($\mathbf{E}^{mm}/\mathbf{E}^{nn}$)

2) Energy flux due to interaction of distinct modes (distinct)

- (a) Incident Kelvin mode interacting with Rossby modes ($\mathbf{E}^{KN}/\mathbf{E}^{Kn}$)
- (b) Real Rossby mode interacting with distinct real Rossby mode (\mathbf{E}^{MN})
- (c) Evanescent Rossby mode interacting with distinct evanescent Rossby mode (\mathbf{E}^{mn})
- (d) Real Rossby mode interacting with evanescent Rossby mode (\mathbf{E}^{Mn})

A.2.3 Zonal Energy Flux Computation

Zonal energy flux is computed by integrating the period averaged zonal flux, meridionally over the entire domain.

$$E_x = \Re \left\{ \int_{-\infty}^{\infty} dy \frac{\omega}{2\pi} \int_0^{2\pi/\omega} dt u \eta \right\} \quad (\text{A.33})$$

For all of the above cases we will compute the flux for individual modes first and then sum them up.

A.2.3.1 Kelvin Wave Interaction with Rossby modes

For the case of a Kelvin wave mode (k) interacting with the n^{th} Rossby mode, this can be computed as follows:

$$E_x^{Kn} = \int_{-\infty}^{\infty} dy \frac{\omega}{2\pi} \int_0^{2\pi/\omega} dt \Re\{(u_k \eta_n + u_n \eta_k)\} \quad (\text{A.34})$$

Assume,

$$\overline{u_k \eta_n} = \frac{\omega}{2\pi} \int_0^{2\pi/\omega} dt (u_k \eta_n) \quad (\text{A.35})$$

$$\Re\{\overline{u_k \eta_n}\} = \overline{\left(\frac{u_k^* + u_k}{2}\right) \left(\frac{\eta_n^* + \eta_n}{2}\right)} \quad (\text{A.36})$$

Where u_k^* and η_n^* are complex conjugates of u_k and η_n respectively. Using the expression for u_k and η_n from equations (20) and (21) we obtain:

$$\overline{u_k^* \eta_n^*} = \overline{u_k \eta_n} = 0 \quad (\text{A.37})$$

$$\overline{u_k^* \eta_n} = \overline{u_k \eta_n^*} \quad (\text{A.38})$$

From Equation (36),(37) and (38) we get:

$$\Re\{\overline{u_k \eta_n}\} = \frac{1}{2} \Re\{u_k \eta_n^*\} \quad (\text{A.39})$$

Similarly,

$$\Re\{\overline{u_n \eta_k}\} = \frac{1}{2} \Re\{\eta_k u_n^*\} \quad (\text{A.40})$$

Hence from Equation (34),(39) and (40)

$$E_x^{Kn} = \int_{-\infty}^{\infty} dy \frac{1}{2} \Re\{u_k \eta_n^* + \eta_k u_n^*\} \quad (\text{A.41})$$

Substituting the expressions for u_k and η_n from equations (20) and (21) and neglecting

the meridional integration of the flux we get:

$$E_x^{Kn} = \sum_{n=1}^{\infty} \psi_0 \psi_{n+1} \Re\{B_n B_n^* \gamma_n^* e^{i(\omega-k_n^*)x}\} \quad (\text{A.42})$$

A.2.3.2 Rossby mode Interaction with itself (Individual)

Following the similar procedure to obtain the energy flux due to interaction of Rossby modes with itself we get (Includes E^{MM}/E^{nn}):

$$E_x^{nn} = \int_{-\infty}^{\infty} dy \frac{\omega}{2\pi} \int_0^{2\pi/\omega} dt \Re\{u_n \eta_n\} \quad (\text{A.43})$$

$$E_x^{nn} = \int_{-\infty}^{\infty} dy \frac{1}{2} \Re\{\eta_n u_n^*\} \quad (\text{A.44})$$

Substituting the expressions for u_n and η_n we obtain:

$$E_x^{nn} = \sum_{n=1}^{\infty} \Re\{B_n B_n^* [\gamma_n^* \gamma_n \psi_{n+1}^2 - \psi_{n-1}^2] e^{i(k_n-k_n^*)x}\} \quad (\text{A.45})$$

A.2.3.3 Rossby mode Interaction distinct Rossby mode

This includes interactions of real Rossby modes with distinct real Rossby modes (E^{MN}), interactions of evanescent rossby modes with real Rossby modes(E^{mN}) and interactions of evanescent Rossby modes with distinct Evanescent Rossby modes (E^{mn}). However we will represent all the above categorize by a generalized form as E^{mn} .

$$E_x^{mn} = \int_{-\infty}^{\infty} dy \frac{\omega}{2\pi} \int_0^{2\pi/\omega} dt \Re\{(u_m \eta_n + u_n \eta_m)\} \quad (\text{A.46})$$

$$E_x^{mn} = \int_{-\infty}^{\infty} dy \frac{1}{2} \Re\{u_m^* \eta_n + \eta_m^* u_n\} \quad (\text{A.47})$$

Substituting the expressions for u and η we obtain:

$$E_x^{mn} = \sum_{n=1}^{\infty} \sum_{m=n+1}^{\infty} \Re\{B_n B_m^* [\gamma_m^* \gamma_n \psi_{m+1} \psi_{n+1} - \psi_{n-1} \psi_{m-1}] e^{i(k_n-k_m^*)x}\} \quad (\text{A.48})$$

A.2.3.4 Kelvin Mode Interaction with itself

This includes the incident energy that has been brought into the system by incoming Kelvin wave. Kelvin wave will only have the zonal component as the meridional velocity vanishes for the Kelvin wave. Following the similar steps we can get the expression for the Energy flux which is given by:

$$E_x^{KK} = \int_{-\infty}^{\infty} dy \frac{\omega}{2\pi} \int_0^{2\pi/\omega} dt \Re\{u_\kappa \eta_\kappa\} \quad (\text{A.49})$$

$$E_x^{KK} = \int_{-\infty}^{\infty} dy \frac{1}{2} \Re\{u_\kappa \eta_\kappa^*\} \quad (\text{A.50})$$

Substituting values for u_κ and η_κ we get:

$$E_x^{KK} = \frac{1}{2} \Re\{B_\kappa B_\kappa^* \psi_0^2\} \quad (\text{A.51})$$

A.2.4 Meridional Energy Flux Computation

Meridional Energy fluxes are computed in the similar manner as discussed above in case of Zonal fluxes. Instead of going into detail expression for the meridional Energy fluxes are directly given in same order as the Zonal Energy flux.

A.2.4.1 Kelvin Wave Interaction with Rossby modes

Kelvin wave mode (k) interacting with n^{th} Rossby mode can be computed as follows:

$$E_y^{Kn} = \int_{-\infty}^{\infty} dx \frac{\omega}{2\pi} \int_0^{2\pi/\omega} dt \Re\{(v_n \eta_\kappa\} \quad (\text{A.52})$$

$$E_y^{Kn} = \int_{-\infty}^{\infty} dy \frac{1}{2} \Re\{(v_n \eta_\kappa^*\} \quad (\text{A.53})$$

Substituting the expressions for v_n and η_κ from equations (20) and (21) and neglecting

the meridional integration of the flux we get:

$$E_y^{Kn} = \sum_{n=1}^{\infty} \frac{\psi_0 \psi_n}{\sqrt{2n}} \Re\{i B_n B_{\kappa}^* (k_n + \omega) e^{i(k_n - \omega)x}\} \quad (\text{A.54})$$

A.2.4.2 Rossby mode Interaction with itself (Individual)

Following the similar procedure to obtain the energy flux due to interaction of Rossby modes with itself we get (Includes E^{MM}/E^{nn}):

$$E_y^{nn} = \int_{-\infty}^{\infty} dx \frac{\omega}{2\pi} \int_0^{2\pi/\omega} dt \Re\{v_n \eta_n\} \quad (\text{A.55})$$

$$E_y^{nn} = \int_{-\infty}^{\infty} dx \frac{1}{2} \Re\{v_n \eta_n^*\} \quad (\text{A.56})$$

Substituting the expressions for u_n and η_n we obtain:

$$E_y^{nn} = \sum_{n=1}^{\infty} \frac{\psi_0 \psi_n}{\sqrt{2n}} \Re\{i B_n B_n^* (k_n + \omega) \psi_n [\gamma_n^* \psi_{n+1} + \psi_{n-1}] e^{i(k_n - k_n^*)x}\} \quad (\text{A.57})$$

A.2.4.3 Rossby mode Interaction with distinct Rossby mode

Similar to the zonal Energy fluxes, this includes interactions of real Rossby modes with distinct real Rossby modes (E^{MN}), interactions of evanescent rossby modes with real Rossby modes(E^{mN}) and interactions of evanescent Rossby modes modes with distinct Evanescent Rossby modes (E^{mn}).

$$E_y^{mn} = \int_{-\infty}^{\infty} dx \frac{\omega}{2\pi} \int_0^{2\pi/\omega} dt \Re\{(v_m \eta_n + v_n \eta_m)\} \quad (\text{A.58})$$

$$E_y^{mn} = \int_{-\infty}^{\infty} dx \frac{1}{2} \Re\{v_m^* \eta_n + \eta_m^* v_n\} \quad (\text{A.59})$$

Substituting the expressions for v and η we obtain:

$$E_y^{nn} = \sum_{n=1}^{\infty} \sum_{m=n+1}^{\infty} \frac{1}{\sqrt{2}} \Re \left\{ i B_n B_m^* \left[\frac{(k_n + \omega) \psi_n}{\sqrt{n}} (\gamma_m^* \psi_{m+1} + \psi_{m-1}) - \frac{(k_m^* + \omega) \psi_m}{\sqrt{m}} (\gamma_n \psi_{n+1} + \psi_{n-1}) \right] e^{i(k_n - k_m^*)x} \right\} \quad (\text{A.60})$$

A.2.5 Analytical Model Description

Energy fluxes due to interaction of different modes are computed using a simple linear analytical model. For all the computations, it is assumed that a Kelvin wave of unit energy flux i.e. an amplitude of square root of 2 with a given frequency is incident onto the boundary at $x=0$. East and north are assumed to be positive axes in x and y directions respectively. All the parameters used in the analysis are non-dimensionalised with values typical of the equatorial Pacific or Indian Ocean, for which c being 2.7 m/s and β being $2.28 \times 10^{-11} \text{ m}^{-1} \text{ s}^{-1}$. The same analysis is carried for a few different frequencies.

Moore (1968), showed that for a given frequency there exist a latitude ($Y_{T\pm}$), poleward of which the solution of u and η have exponential behavior in at-least one direction.

$$Y_{T\pm} = \pm \sqrt{\omega^2 + \frac{1}{4\omega^2}} \quad (\text{A.61})$$

Equator-ward of the turning latitude, the solution is oscillatory in both x and y directions. Also using a different frequency for the analysis leads to a different number of real Rossby modes that are reflected from the wall (Eq 25; the dispersion relation for Equatorial Rossby waves).

A.3 Results

This section encompasses all the results obtained from the analytical model described in the above section. Energy fluxes are computed using the summation of first 801 modes. The final solution for u , η and v at the wall approaches the asymptote as the number of modes used increases. We choose 801 modes for this computation as the structure of u , p and v approaches to asymptote (Figure A.1, for $T=90$ days).

Zonal Energy flux for individual modes has eastward fringes as we go poleward. Figure

A.2 shows the zonal Energy flux for individual Rossby modes for the incident Kelvin wave with a period of 60 days. On the equator all the energy is propagating to the west, however as we move away from the equator we get a flux of energy going to the east. Figure A.3 shows the meridional energy flux for individual modes for the same case. There is no meridional energy flux for individual real (long Rossby or real wave numbers) modes (top panel of Figure A.3). We can also see this from Equation (20) itself: v and η are in quadrature with each other for real wave numbers. The meridional energy flux due to the evanescent modes feeds the coastal Kelvin wave at the wall; however there is no meridional flux at the equator close to the wall. This leads to the question how does the westward energy flux at the equator turns back to eastward fringes as we move away from the equator ?

To answer the above question we looked into the energy fluxes that occur due to interactions of two different distinct modes. Figure A.4 shows the quiver plot of meridional and zonal energy flux due to interactions of distinct Rossby modes (Equation (48) and (60)). We can see the circulation pattern in the energy flux that takes the energy from the equator and feeds into the eastward going energy flux fringes, away from the equator. These eastward energy fringes then transfer the energy into the coastal trapped waves propagating away from the Equator. The important point to remember is that we are looking only at the linear interactions between different modes for a single frequency.

The number of such circulating patterns differs with changes in the frequency. Higher period(lower frequency) waves have more long Rossby (real) modes leading to more of such circulating patterns. Figure A.5 and Figure A.6 shows the zonal and meridional energy fluxes respectively for an incident Kelvin wave with a period of 60 days. This frequency gives rise to just 2 long Rossby modes after reflection from the wall. Figure A.7 shows the quiver plot of the zonal and meridional energy fluxes for the same. This figure shows that there is less energy flux adjacent to the wall within the turning latitude, away from the turning latitude we get poleward energy flux indicating the CTW. The large percentage of the energy which is being extracted efficiently from the equator to feed this CTW is away from the wall. Figure A.7 shows that for the period of 60 days most of the energy is extracted at around -2.5° . This can also be seen in Figure A.5 and Figure A.6 where we can see that around the same longitude, meridional energy flux takes the energy away from the equator where as the zonal energy flux take the energy to the east and then ultimately feeding to the CTWs through meridional energy fluxes

close to the turning latitudes.

The longitude at which the energy is extracted the most efficient way from the equator to feed the CTWs changes with change in frequency of the incident Kelvin wave. Figure A.8 - A.10 show the comparisons of these different circulating patterns. The periods 41, 55 and 67 days are chosen as these periods are critical for 1, 2 and 3 long Rossby (real) modes respectively. At 41 days, there is only one reflected long Rossby mode. The mode interaction terms circulate the energy flux from the narrow equatorial band poleward to the fringes of the long Rossby wave, from whence it feeds into the beginning of the coastal Kelvin wave. The circulating pattern extracts the energy around a latitude of -2^0 to feed the CTWs however the patterns close to the boundary of this latitude are more of a trapped nature trying to direct the energy towards this latitude. At 55 days, (Figure A.9), two long Rossby modes are available, and the circulation pattern becomes more complex. This complexity increases with increasing numbers of available long Rossby modes (i.e., decreasing frequency) as we can see for 67 day period with three long Rossby modes. However the fundamental picture of energy flux transfer from the incident equatorial Kelvin wave to the poleward coastal Kelvin waves remains the same. At 55 days, the circulating pattern seems to extract the energy in the direction of CTW at around -3^0 (Figure A.9, last column), where as for 67 days it happens around (Figure A.10) -4^0 .

A.4 Summary

Incident Kelvin wave on an eastern boundary reflects back as a sum of infinite Rossby modes. This infinite sum leads up to a Coastal Trapped wave (CTW) poleward of the turning latitudes (Moore, 1968). However within the turning latitude this summation leads up to a negligible meridional energy flux compared to that of CTW, poleward of turning latitude. This study focuses on understanding the dynamics equator-ward of turning latitudes where the meridional energy flux adjacent to the eastern boundary is negligible. Interactions of different Rossby modes with each other and with the incident Kelvin wave leads to certain circulating patterns of the energy fluxes which takes out the energy from the equator and transfer it to the poleward propagating CTWs. The complexity of these circulating patterns increases with increase in the period of incident Kelvin wave. The distance from the eastern boundary where the extraction of energy from the equator to direct the energy towards the CTWs is most efficient, also increases

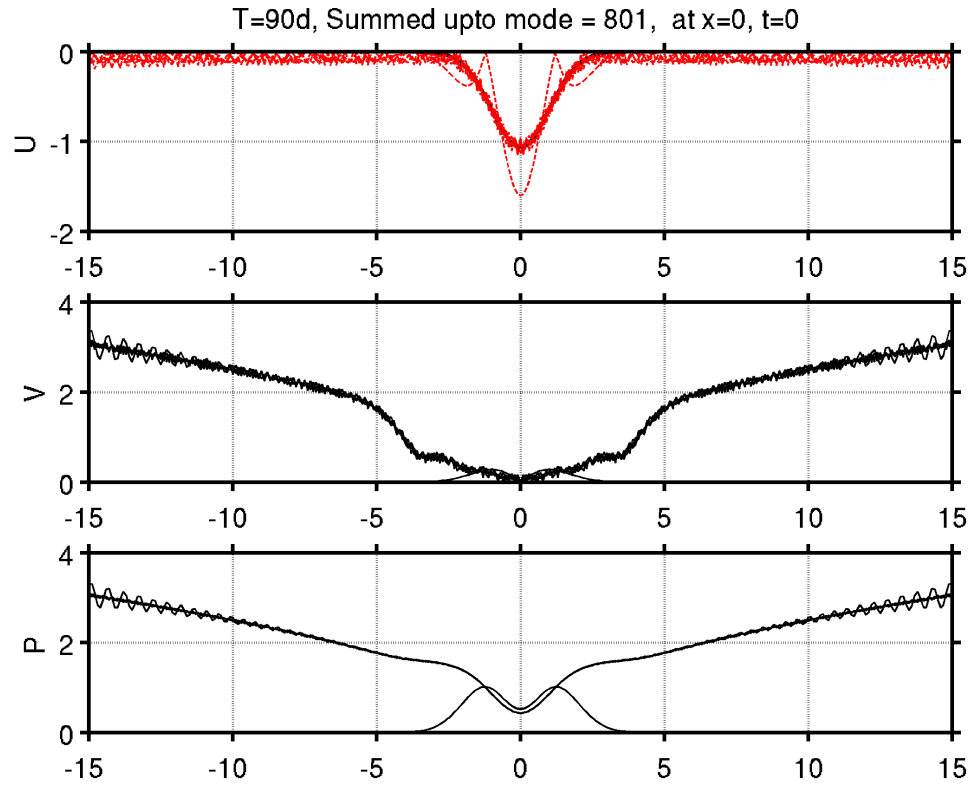


Figure A.1: Structure of U , V and P for the summation of modes at different stages with the final stage being $n=801$

with increment in the period of Kelvin wave. This simple analysis reveals the possibility of transferring the energy from the equator towards the CTWs simply due to linear interaction of different modes.

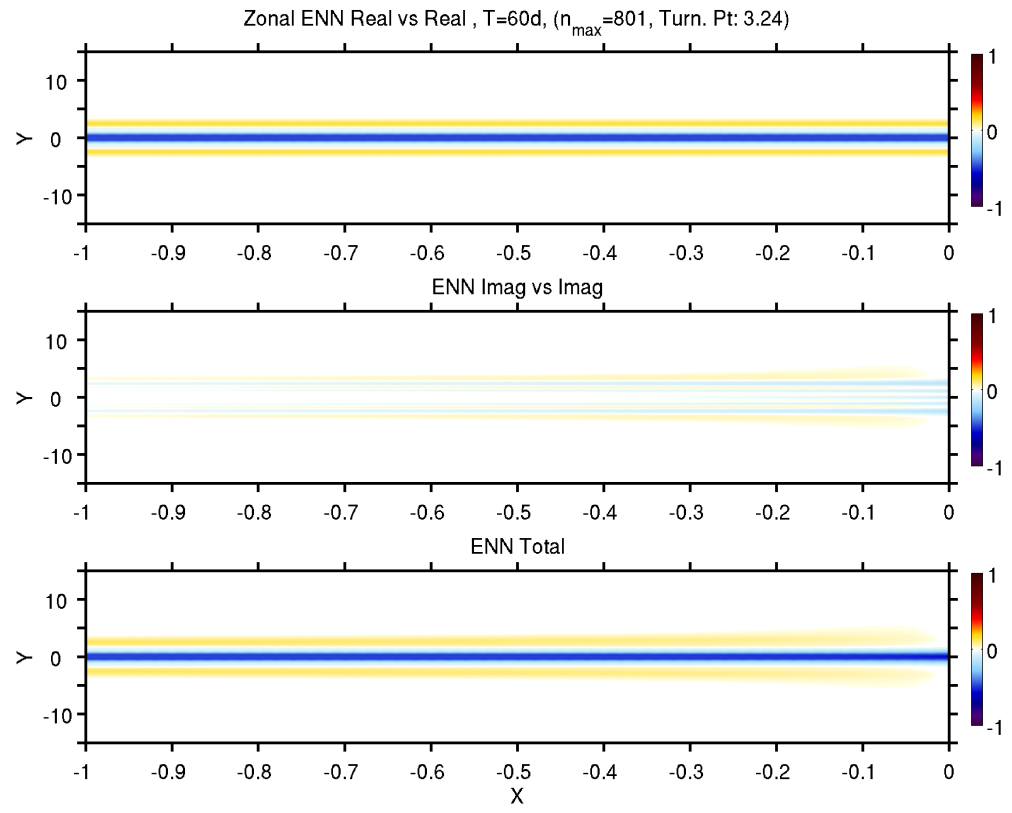


Figure A.2: Zonal Energy flux for single mode at $T=60$ days.

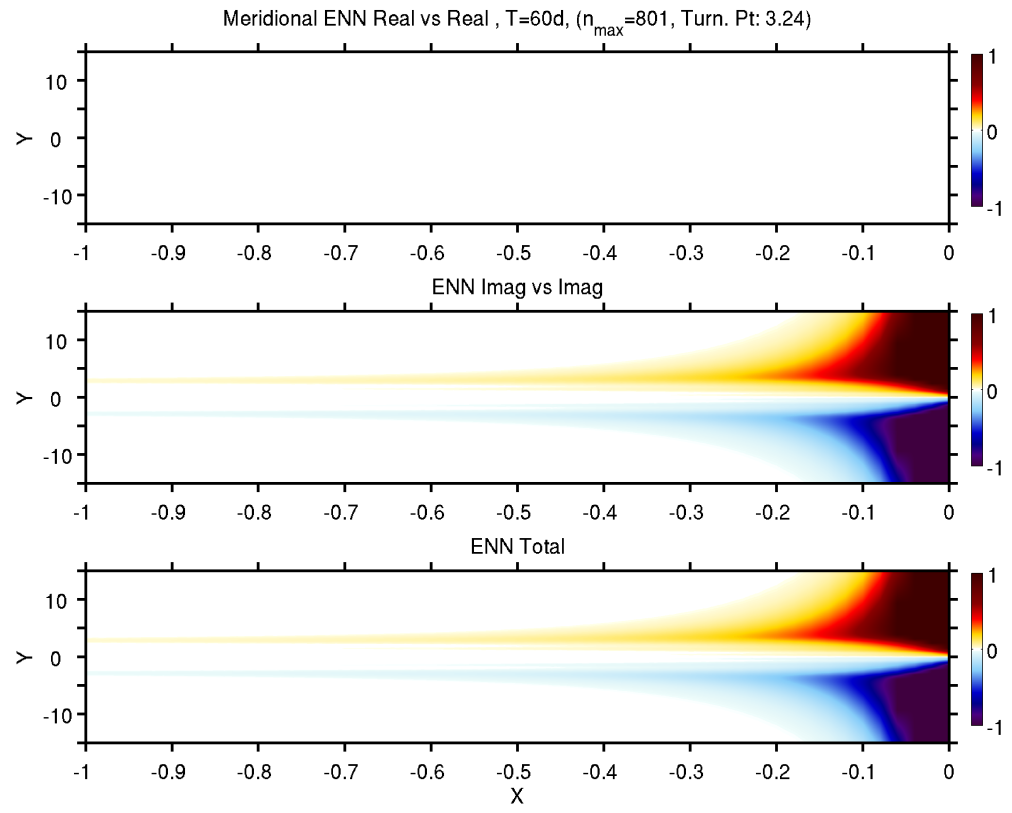


Figure A.3: Meridional Energy flux for individual mode at $T=60$ days.

Distinct Rossby Interactions(EMN): Zonal and Meridional Energy Flux, T=60d, Turn. Pt: 3.24

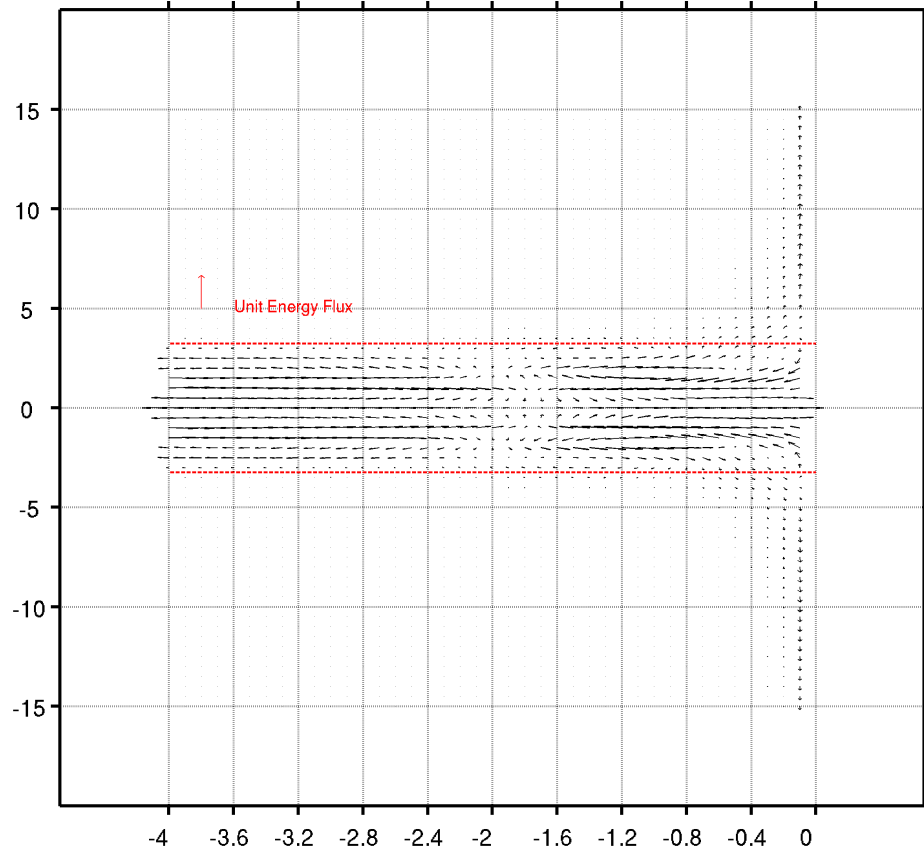


Figure A.4: Quiver plot of Energy Flux due to interaction of distinct Rossby modes(Arrows indicating the direction of the energy flux and dotted red lines represent the turning latitude)

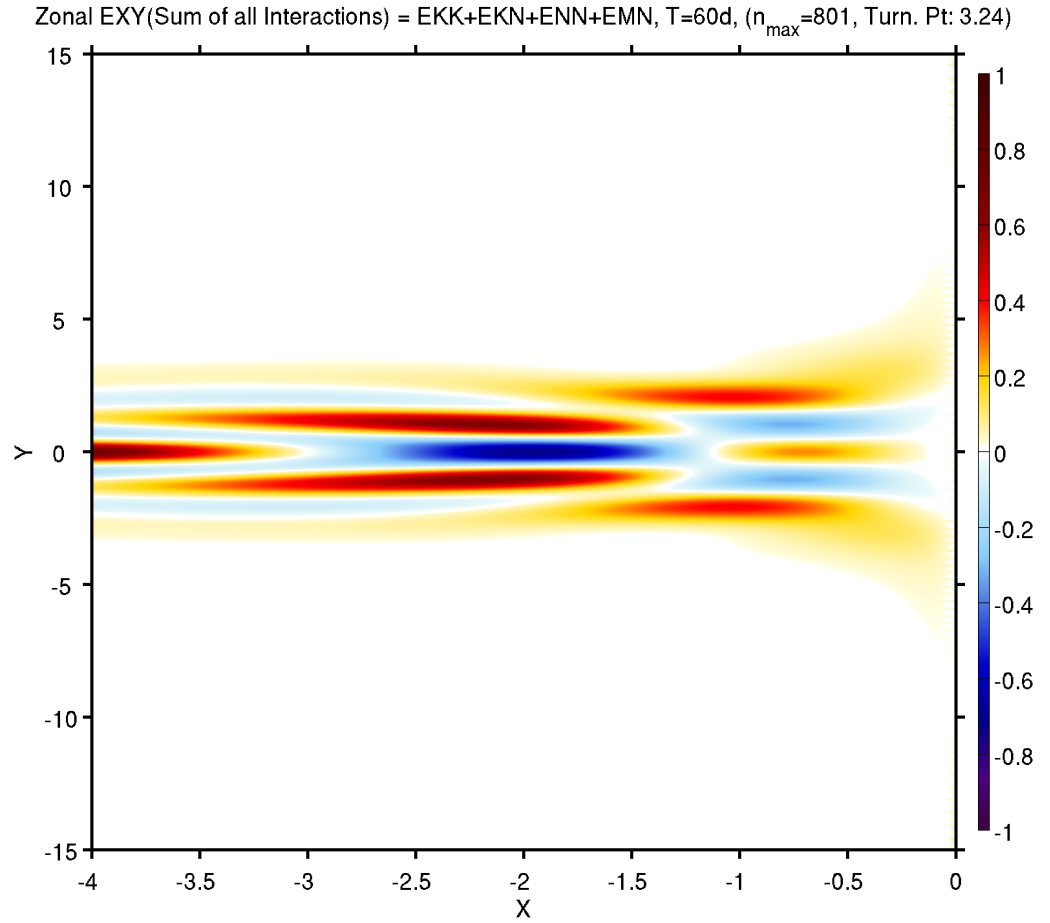


Figure A.5: Net Zonal Energy Flux: EKK (Incoming Incident Kelvin Wave) + EKN (Interaction of Kelvin wave with Rossby modes) + ENN (Individual Rossby modes) + EMN (Interaction of distinct Rossby modes)

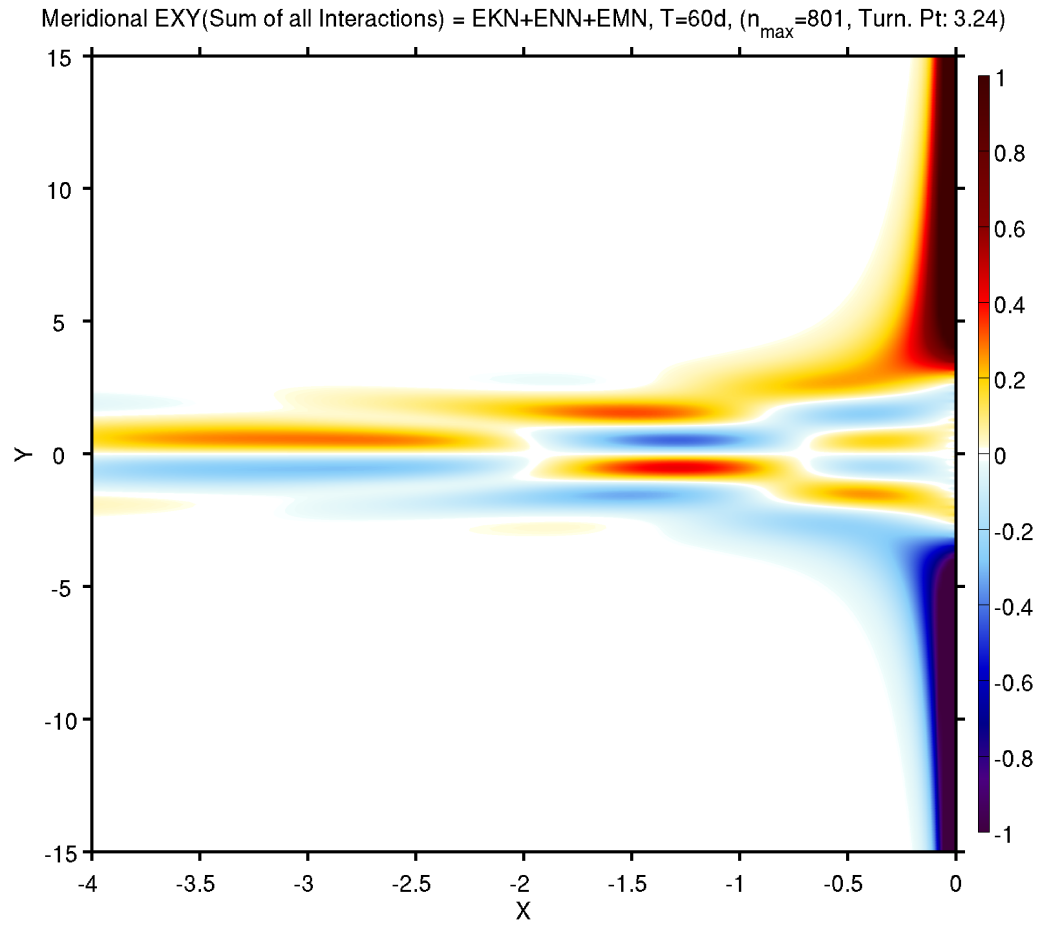


Figure A.6: Net Meridional Energy Flux: EKN (Interaction of Kelvin wave with Rossby modes) + ENN (Individual Rossby modes) + EMN (Interaction of distinct Rossby modes)

Total EKK+EKN+ENN+EMN: Zonal and Meridional Energy Flux, $T=60d$, $N_{\max}=801$

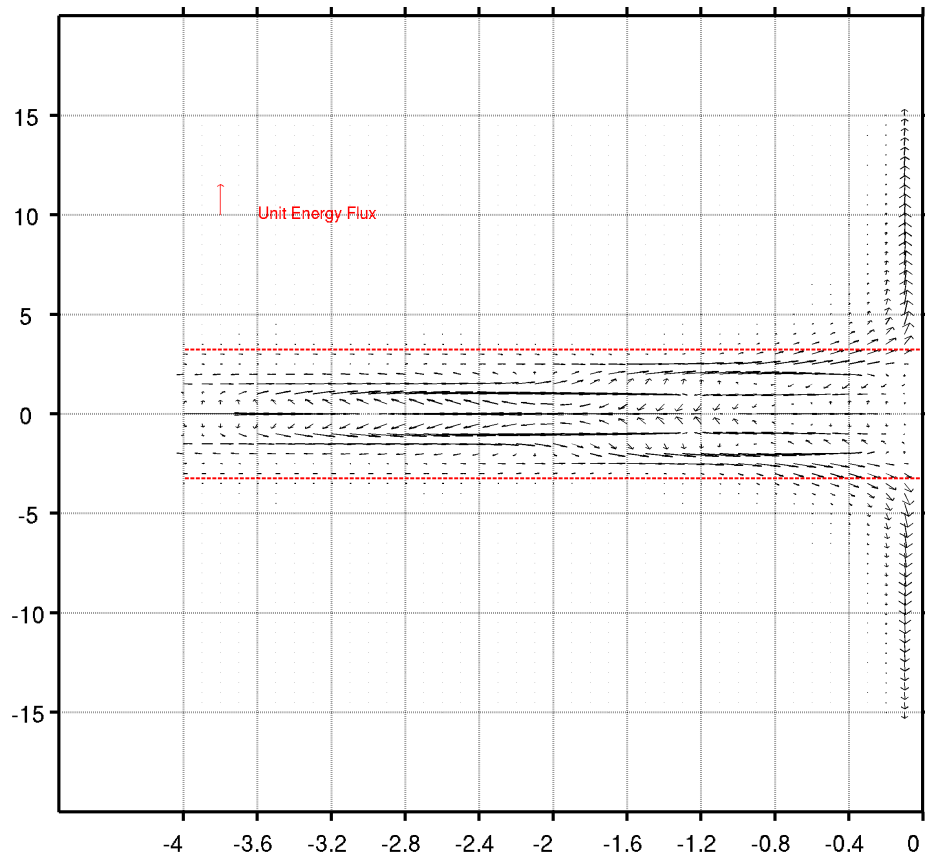


Figure A.7: Quiver plot of total Energy Flux (dashed red lines indicate the turning latitude for a period of 60 days)

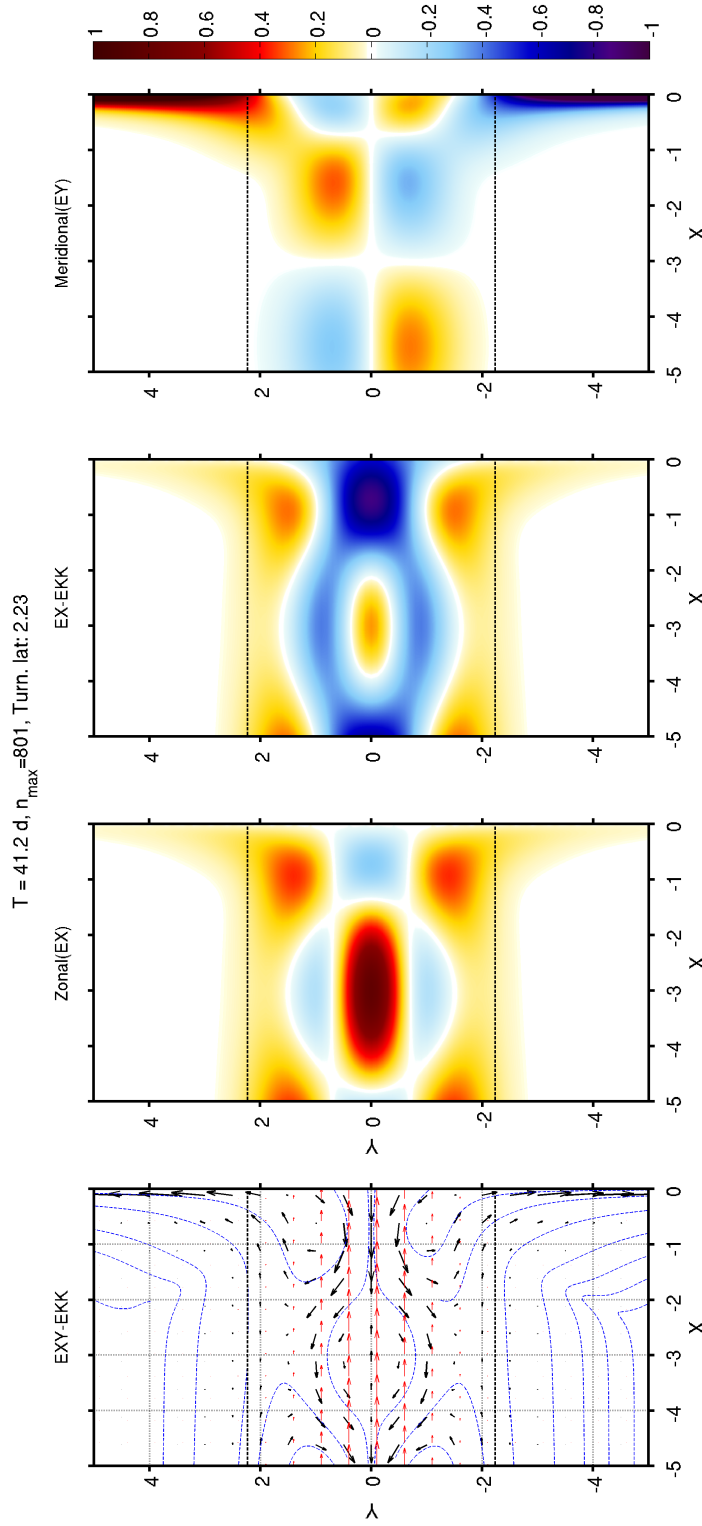


Figure A.8: From Left: 1) Quiver plot of total Energy flux (Red arrows indicate Energy flux from Incident Kelvin Wave, Black arrows indicate the Energy flux due to Rossby modes after reflecting back from the boundary, Blue lines are the contours of the energy fluxes due to interaction of Rossby modes) 2) Zonal Energy flux including the Incident Kelvin wave (dotted black line indicates the turning latitude) 3) Zonal Energy flux without the Incoming Kelvin Wave 4) Meridional Energy (T=41 days with only one real Rossby mode after reflecting from the boundary)

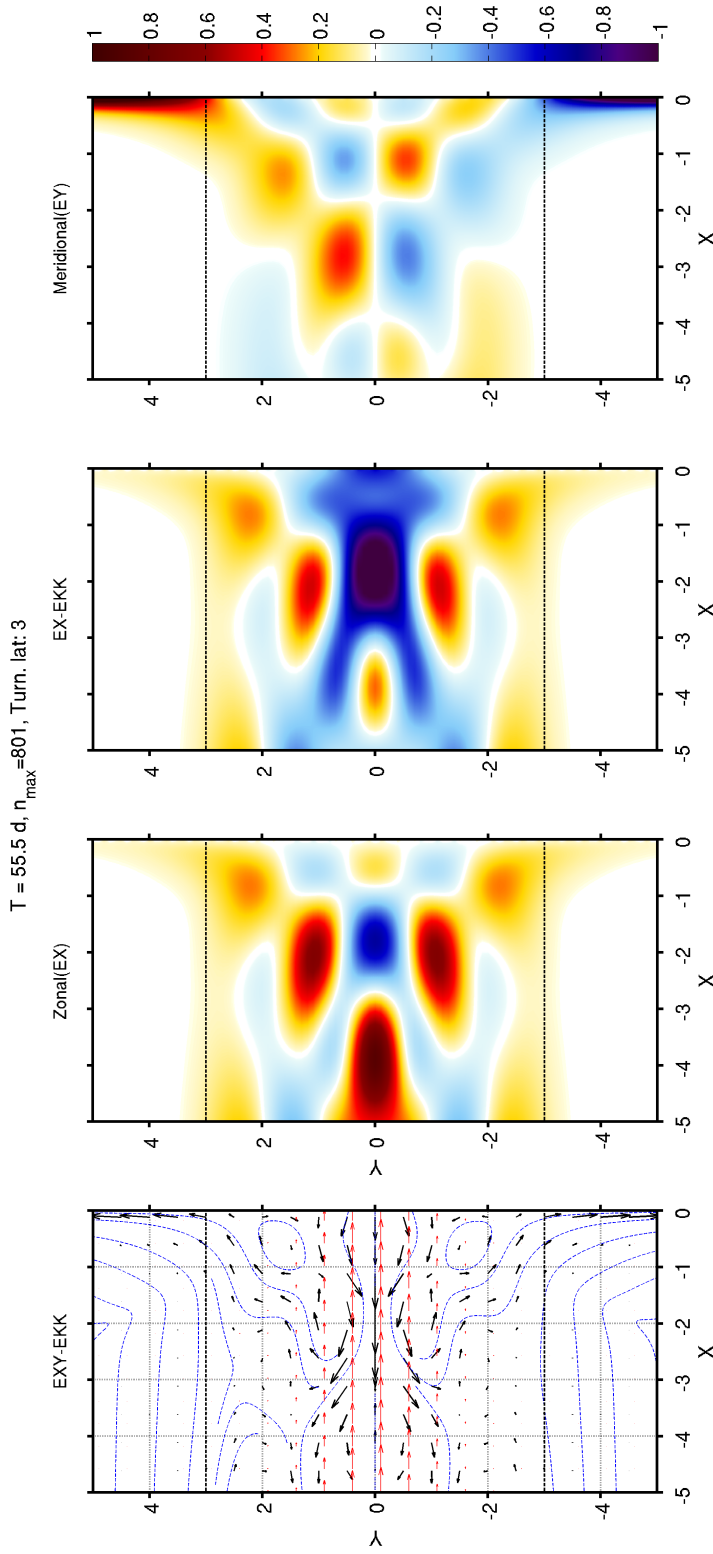


Figure A.9: From Left: 1) Quiver plot of total Energy flux (Red arrows indicate Energy flux from Incident Kelvin Wave, Black arrows indicate the Energy flux due to Rossby modes after reflecting back from the boundary, Blue lines are the contours of the energy fluxes due to interaction of Rossby modes) 2) Zonal Energy flux including the Incident Kelvin wave (dotted black line indicates the turning latitude) 3) Zonal Energy flux without the Incoming Kelvin Wave 4) Meridional Energy (T=55 days with only two real Rossby modes after reflecting from the boundary)

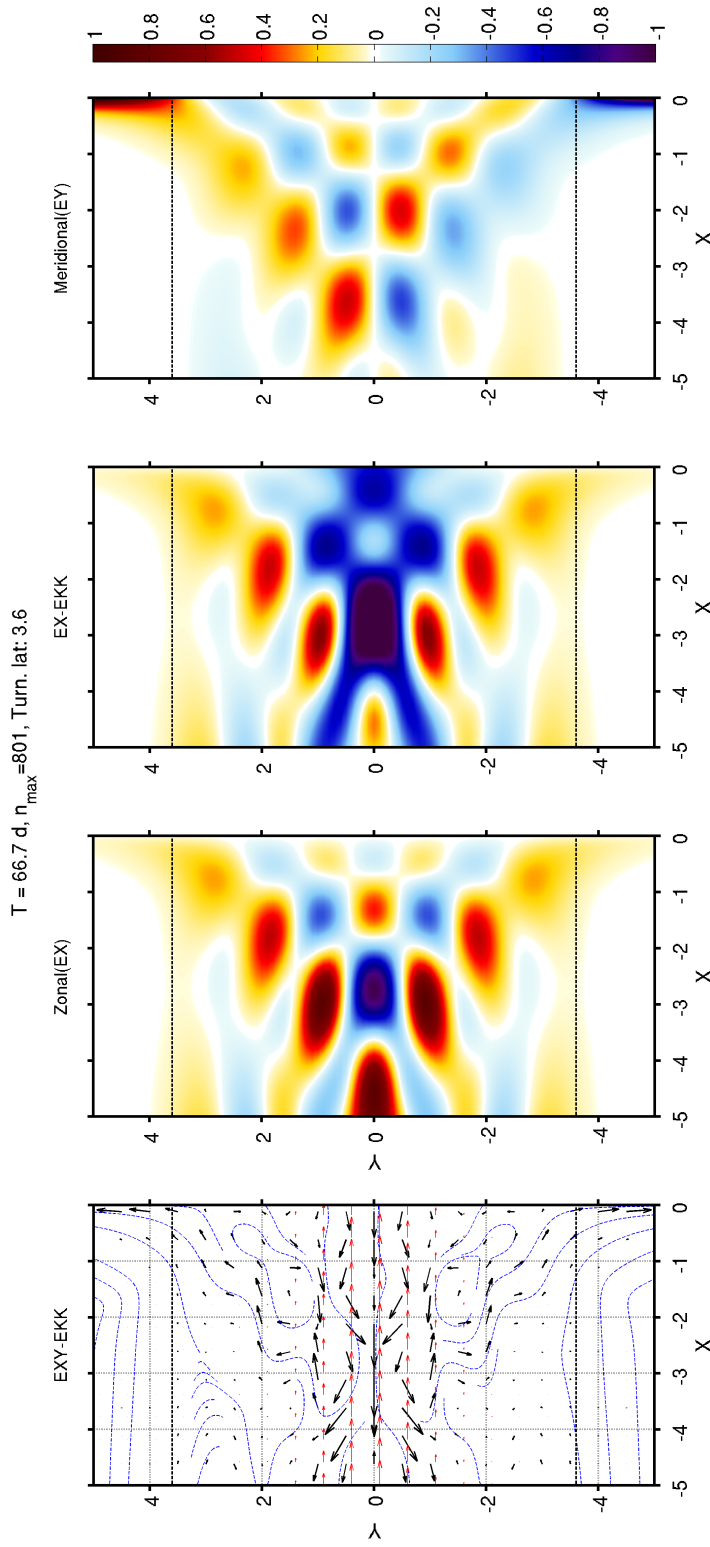


Figure A.10: From Left: 1) Quiver plot of total Energy flux (Red arrows indicate Energy flux from Incident Kelvin Wave, Black arrows indicate the Energy flux due to Rossby modes after reflecting back from the boundary, Blue lines are the contours of the energy fluxes due to interaction of Rossby modes) 2) Zonal Energy flux including the Incident Kelvin wave (dotted black line indicates the turning latitude) 3) Zonal Energy flux without the Incoming Kelvin Wave 4) Meridional Energy (T=67 days with only two real Rossby modes after reflecting from the boundary)

Appendix B: Computation of N^*

Assigning confidence limits to our calculated correlations and regression models requires estimates of the effective sample sizes (degrees of freedom). Because of the decorrelation scales associated with large-scale oceanic phenomena, this is not a straightforward procedure. Here we use the Artificial Skill Method (ASM), described by DB Chelton (1983), to compute the effective sample size (N^*). Assuming that N^* is proportional to the record length, we can define a proportionality between N^* and the total number of observations, N :

$$N^* = \nu N \quad (\text{B.1})$$

where ν represents the degrees of independence of the observations which is an intrinsic property of the process of interest.

Consider a lagged regression Model with a lag $\tau_k (= k \Delta t)$:

$$y(t_n) = \sum_{m=0}^M \beta_{mk} X_m(t_n + \tau_k) + \hat{\varepsilon}_k(t_n) \quad (\text{B.2})$$

where, M is the total number of input parameters used in the model and the ε_k represents the error associated with the model corresponding to the lag τ_k . The expected value of skill (fraction of variance explained by the model) of the regression model can be written as:

$$\langle \hat{S}_k \rangle = S_k + S_A(\tau_k) \quad (\text{B.3})$$

Here, sample skill $\langle \hat{S}_k \rangle$ is a positively biased estimate of the true skill S_k of the postulated model, whereas $S_A(\tau_k)$ represents artificial skill due to sampling errors. At long lags τ_k , the true skill S_k is assumed to go to 0, so that the sample skill at those lags is purely due to sampling errors, given by (ibid.):

$$\langle \hat{S}_k \rangle = S_A(\tau_k) \simeq \frac{M}{N^*} = \frac{M}{\nu N_k} \quad (\text{B.4})$$

where, N_k represents the total number of observations at a long lag τ_k . We can thus estimate the value of ν as follows:

$$\nu = \frac{M}{\langle N_k \hat{S}_k \rangle} \quad (\text{B.5})$$

The above expression is valid only at long lags where the true skill of the postulated model is assumed to be 0. The expected value in the denominator can be estimated by the arithmetic average over a range of long lags, from k_1 to k_2 , both positive and negative:

$$\langle N_k \hat{S}_k \rangle = \frac{1}{2(k_2 - k_1 + 1)} \sum_{k=k_1}^{k_2} [N_k \hat{S}_k + N_{-k} \hat{S}_{-k}] \quad (\text{B.6})$$

The lower cut-off (k_1) has to be such that true skill of the lagged regression model is zero, and the upper cut-off (k_2) should avoid very long lags at which S_k can be very noisy because of the small number of samples, N_k . In this analysis we assume 20-70% of the record length to be an approximation for making the arithmetic average of $N_k \hat{S}_k$ which constitutes *long* lags.

For the case of estimating the confidence intervals over the lagged correlation between two time series, the ASM is used with a 2 parameter univariate regression model (M=1) to compute the effective size of independent samples (N^*).

Bibliography

- [1] MA Alexander, H Seo, SP Xie, and JD Scott, “Enso’s impact on the gap wind regions of the eastern tropical pacific ocean”, *Journal of Climate* **25**, 3549–3565 (2012) [10.1175/JCLI-D-11-00320.1](#).
- [2] JS Allen and RD Romea, “On coastal trapped waves at low latitudes in a stratified ocean”, *Journal of Fluid Mechanics* **98**, 555–585 (1980) [10.1017/S0022112080000286](#).
- [3] J Allen, “Coastal trapped waves in a stratified ocean”, *Journal of Physical Oceanography* **5**, 300–325 (1975).
- [4] P Amol et al., “Observed intraseasonal and seasonal variability of the West India Coastal Current on the continental slope”, *J. Earth Syst. Sci.* **123**, 1045–1074 (2014) [10.1007/s12040-014-0449-5](#).
- [5] P Amol et al., “Observational evidence from direct current measurements for propagation of remotely forced waves on the shelf off the west coast of India”, *J. Geophys. Res.* **117** (2012) [10.1029/2011JC007606](#).
- [6] M Babu, Y Sarma, V Murty, and P Vethamony, “On the circulation in the Bay of Bengal during northern spring inter-monsoon (March–April 1987)”, *Deep Sea Res. Part II* **50**, 855–865 (2003) [10.1016/S0967-0645\(02\)00609-4](#).
- [7] P Baines, “On internal tide generation models”, *Deep Sea Res. Part A.* **29**, 307–338 (1982) [10.1016/0198-0149\(82\)90098-X](#).
- [8] P Baines, “The generation of internal tides by flat-bump topography”, in *Deep sea res. and oceanographic abstracts*, Vol. 20, 2 (Elsevier, 1973), pp. 179–205, [10.1016/0011-7471\(73\)90050-8](#).
- [9] A Bakun and CS Nelson, “The seasonal cycle of wind-stress curl in subtropical eastern boundary current regions”, *J. Phys. Oceanogr* **21**, 1815–1834 (1991).

- [10] A Bakun, C Roy, and S Lluch-Cota, “Coastal upwelling and other processes regulating ecosystem productivity and fish production in the western Indian Ocean”, (1998).
- [11] K Brink, “A comparison of long coastal trapped wave theory with observations off peru”, *Journal of Physical Oceanography* **12**, 897–913 (1982).
- [12] MA Cane, “Oceanographic events during el nino”, *Science* **222**, 1189–1195 (1983) [10.1126/science.222.4629.1189](#).
- [13] SY Chao, LJ Pietrafesa, and GS Janowitz, “The scattering of continental shelf waves by an isolated topographic irregularity”, *J. Phys. Oceanogr* **9**, 687–695 (1979).
- [14] DC Chapman, “On the influence of stratification and continental shelf and slope topography on the dispersion of subinertial coastally trapped waves”, *Journal of physical oceanography* **13**, 1641–1652 (1983).
- [15] D Chelton, M Schlax, J Lyman, and G Johnson, “Equatorially trapped Rossby waves in the presence of meridionally sheared baroclinic flow in the Pacific Ocean”, *Progr. Oceanogr.* **56**, 323–380 (2003) [10.1016/S0079-6611\(03\)00008-9](#).
- [16] DB Chelton, “Effects of sampling errors in statistical estimation”, *Deep Sea Res. Part A* **30**, 1083–1103 (1983) [10.1016/0198-0149\(83\)90062-6](#).
- [17] DB Chelton, RA Deszoeke, MG Schlax, K El Naggar, and N Siwertz, “Geographical variability of the first baroclinic Rossby radius of deformation”, *J. Phys. Oceanogr.* **28**, 433–460 (1998).
- [18] DB Chelton, MG Schlax, MH Freilich, and RF Milliff, “Satellite measurements reveal persistent small-scale features in ocean winds”, *science* **303**, 978–983 (2004) [10.1126/science.1091901](#).
- [19] DB Chelton, MG Schlax, and RM Samelson, “Global observations of nonlinear mesoscale eddies”, *Progr. Oceanogr.* **91**, 167–216 (2011) [10.1016/j.pocean.2011.01.002](#).
- [20] AJ Clarke, “The reflection of equatorial waves from oceanic boundaries”, *Journal of Physical Oceanography* **13**, 1193–1207 (1983).

- [21] AJ Clarke and K Brink, “The response of stratified, frictional flow of shelf and slope waters to fluctuating large-scale, low-frequency wind forcing”, *Journal of Physical Oceanography* **15**, 439–453 (1985).
- [22] D Denbo and JS Allen, “Large-scale response to atmospheric forcing of shelf currents and coastal sea level off the west coast of North America: May-July 1981 and 1982”, *J. Geophys. Res.* **92**, 1757–1782 (1987) [10.1029/JC092iC02p01757](https://doi.org/10.1029/JC092iC02p01757).
- [23] L Dhage and PT Strub, “Intra-seasonal sea level variability along the west coast of india”, *J. Geophys. Res. Oceans* **121**, 8172–8188 (2016) [10.1002/2016JC011904](https://doi.org/10.1002/2016JC011904).
- [24] F Durand, D Shankar, F Birol, and S Shenoi, “Spatiotemporal structure of the East India Coastal Current from satellite altimetry”, *J. Geophys. Res.* **114** (2009) [10.1029/2008JC004807](https://doi.org/10.1029/2008JC004807)..
- [25] T Durland, D Moore, J McCreary Jr, and L Dhage, “Meridional energy flux near an eastern boundary within the turning latitudes of an equatorial basin”, in *Agu fall meeting abstracts* (2014).
- [26] T Durland, J Pedlosky, and MA Spall, “Response to a steady poleward outflow. part i: the linear, quasigeostrophic problem”, *Journal of Physical Oceanography* **39**, 1541–1550 (2009) [10.1175/2008JP03999.1](https://doi.org/10.1175/2008JP03999.1).
- [27] M Girishkumar, M Ravichandran, and W Han, “Observed intraseasonal thermocline variability in the Bay of Bengal”, *J. Geophys. Res. Oceans* **118**, 3336–3349 (2013) [10.1002/jgrc.20245](https://doi.org/10.1002/jgrc.20245).
- [28] V Gopalakrishna et al., “Observed anomalous upwelling in the Lakshadweep Sea during the summer monsoon season of 2005”, *J. Geophys. Res. Oceans* **113** (2008) [10.1029/2007JC004240](https://doi.org/10.1029/2007JC004240).
- [29] R Grimshaw, P Baines, and R Bell, “The reflection and diffraction of internal waves from the junction of a slit and a half-space, with application to submarine canyons”, *Dynamics of atmospheres and oceans* **9**, 85–120 (1985) [10.1016/0377-0265\(85\)90001-6](https://doi.org/10.1016/0377-0265(85)90001-6).
- [30] PE Holloway and MA Merrifield, “Internal tide generation by seamounts, ridges, and islands”, *J. Geophys. Res. Oceans* **104**, 25937–25951 (1999) [10.1029/1999JC900207](https://doi.org/10.1029/1999JC900207).

- [31] JM Huthnance, “On coastal trapped waves: analysis and numerical calculation by inverse iteration”, *Journal of Physical Oceanography* **8**, 74–92 (1978).
- [32] ER Johnson, “Low-frequency scattering of Kelvin waves by continuous topography”, *J. Fluid Mech.* **248**, 173–201 (1993) [10.1017/S0022112093000734](#).
- [33] ER Johnson, “The low-frequency scattering of Kelvin waves by stepped topography”, *J. Fluid Mech.* **215**, 23–44 (1990) [10.1017/S0022112090002531](#).
- [34] ER Johnson, “The scattering at low frequencies of coastally trapped waves”, *J. Phys. Oceanogr* **21**, 913–932 (1991).
- [35] PD Killworth, “How much of a baroclinic coastal Kelvin wave gets over a ridge?”, *J. Phys. Oceanogr* **19**, 321–341 (1989).
- [36] PD Killworth, “Transmission of a two-layer coastal Kelvin wave over a ridge”, *J. Phys. Oceanogr* **19**, 1131–1148 (1989).
- [37] M Longuet-Higgins, “On the trapping of waves along a discontinuity of depth in a rotating ocean”, *J. Fluid Mech.* **31**, 417–434 (1968) [10.1017/S0022112068000236](#).
- [38] U Manjusha, J Jayasankar, R Remya, T Ambrose, and E Vivekanandan, “Influence of coastal upwelling on the fishery of small pelagics off Kerala, south-west coast of India”, *Indian J. Fish.* **60**, 37–42 (2013).
- [39] T Matsuno, “Quasi-geostrophic motions in the equatorial area”, *Journal of the Meteorological Society of Japan. Ser. II* **44**, 25–43 (1966) [10.2151/jmsj1965.44.1_25](#).
- [40] J McCreary, W Han, D Shankar, and S Shetye, “Dynamics of the East India Coastal Current: 2. Numerical solutions”, *J. Geophys. Res.* **101**, 13993–14010 (1996) [10.1029/96JC00560](#).
- [41] J McCreary, PK Kundu, and RL Molinari, “A numerical investigation of dynamics, thermodynamics and mixed-layer processes in the Indian Ocean”, *Progr. Oceanogr.* **31**, 181–244 (1993) [10.1016/0079-6611\(93\)90002-U](#).
- [42] MJ McPhaden and X Yu, “Equatorial waves and the 1997–98 el niño”, *Geophysical Research Letters* **26**, 2961–2964 (1999) [10.1029/1999GL004901](#).
- [43] DW Moore, “Planetary gravity waves in an equatorial ocean”, Ph. D. Thesis, Harvard University, 207 (1968).

- [44] D Nethery and D Shankar, “Vertical propagation of baroclinic Kelvin waves along the west coast of India”, *J. Earth Syst. Sci.* **116**, 331–339 (2007) [10.1007/s12040-007-0030-6](#).
- [45] S Philander, T Yamagata, and R Pacanowski, “Unstable air-sea interactions in the tropics”, *Journal of the Atmospheric Sciences* **41**, 604–613 (1984).
- [46] R Rao, MG Kumar, M Ravichandran, A Rao, V Gopalakrishna, and P Thadathil, “Interannual variability of Kelvin wave propagation in the wave guides of the equatorial Indian Ocean, the coastal Bay of Bengal and the southeastern Arabian Sea during 1993–2006”, *Deep Sea Res. Part I* **57**, 1–13 (2010) [10.1016/j.dsr.2009.10.008](#).
- [47] M Rattray, *Time-dependent motion in an ocean: a unified two-layer, beta-plane approximation* (University of Washington Department of Oceanography, 1965).
- [48] RD Romea, “On coastal trapped waves at low latitudes in a stratified ocean”, PhD thesis (Oregon State University, 1983).
- [49] D Shankar, “Seasonal cycle of sea level and currents along the coast of India”, *Curr. Sci.* **78**, 279–288 (2000).
- [50] D Shankar and S Shetye, “On the dynamics of the Lakshadweep high and low in the southeastern Arabian Sea”, *J. Geophys. Res.* **102**, 12551–12562 (1997) [10.1029/97JC00465](#).
- [51] D Shankar, P Vinayachandran, and A Unnikrishnan, “The monsoon currents in the north indian ocean”, *Progress in oceanography* **52**, 63–120 (2002) [10.1016/S0079-6611\(02\)00024-1](#).
- [52] AF Shchepetkin and JC McWilliams, “The regional oceanic modeling system (roms): a split-explicit, free-surface, topography-following-coordinate oceanic model”, *Ocean Modell.* **9**, 347–404 (2005) [10.1016/j.ocemod.2004.08.002](#).
- [53] S Shenoi, “Intra-seasonal variability of the coastal currents around India: a review of the evidences from new observations”, *Indian J. Geo-Mar. sci.* **39**, 489 (2010).
- [54] S Shetye, A Gouveia, D Shankar, S Shenoi, P Vinayachandran, D Sundar, G Michael, and G Nampoothiri, “Hydrography and circulation in the western Bay of Bengal during the northeast monsoon”, *J. Geophys. Res.* **101**, 14011–14025 (1996) [10.1029/95JC03307](#).

- [55] S Shetye, A Gouveia, S Shenoi, G Michael, D Sundar, A Almeida, and K Santanam, “The coastal current off western India during the northeast monsoon”, *Deep Sea Res. Part A*. **38**, 1517–1529 (1991) [10.1016/0198-0149\(91\)90087-V](#).
- [56] S Shetye, A Gouveia, S Shenoi, D Sundar, G Michael, A Almeida, and K Santanam, “Hydrography and circulation off the west coast of India during the southwest monsoon 1987”, *J. Mar. Res.* **48**, 359–378 (1990) [10.1357/002224090784988809](#).
- [57] I Suresh, J Vialard, T Izumo, M Lengaigne, W Han, J McCreary, and P Muralleedharan, “Dominant role of winds near Sri Lanka in driving seasonal sea level variations along the west coast of india”, *Geophys. Res. Lett.* **43**, 7028–7035 (2016) [10.1002/2016GL069976](#).
- [58] I Suresh, J Vialard, M Lengaigne, W Han, J McCreary, F Durand, and P Muralleedharan, “Origins of wind-driven intraseasonal sea level variations in the North Indian Ocean coastal waveguide”, *Geophys. Res. Lett.* **40**, 5740–5744 (2013) [10.1002/2013GL058312..](#)
- [59] W Sweet, R Fett, J Kerling, and P La Violette, “Air-sea interaction effects in the lower troposphere across the north wall of the gulf stream”, *Monthly Weather Review* **109**, 1042–1052 (1981).
- [60] J Vialard, S Shenoi, J McCreary, D Shankar, F Durand, V Fernando, and S Shetye, “Intraseasonal response of the northern Indian Ocean coastal waveguide to the Madden-Julian Oscillation”, *Geophys. Res. Lett.* **36** (2009) [10.1029/2009GL038450..](#)
- [61] BG Webber, AJ Matthews, and KJ Heywood, “A dynamical ocean feedback mechanism for the Madden–Julian oscillation”, *Q.J.R. Meteorol. Soc.* **136**, 740–754 (2010) [10.1002/qj.604..](#)
- [62] BG Webber, AJ Matthews, KJ Heywood, and DP Stevens, “Ocean Rossby waves as a triggering mechanism for primary Madden–Julian events”, *Q.J.R. Meteorol. Soc.* **138**, 514–527 (2012) [10.1002/qj.936](#).
- [63] JL Wilkin and DC Chapman, “Scattering of coastal-trapped waves by irregularities in coastline and topography”, PhD thesis (1990), pp. 396–421.
- [64] JL Wilkin and DC Chapman, “Scattering of continental shelf waves at a discontinuity in shelf width”, *J. Phys. Oceanogr* **17**, 713–724 (1987).

